THERMODYNAMICS OF VOLTAGE-DEPENDENT GATING OF ION CHANNELS

By

Sandipan Chowdhury

A dissertation submitted in partial fulfillment of the requirements for the degree of

Doctor of Philosophy

(Biophysics)

at the

UNIVERSITY OF WISCONSIN-MADISON

2014

Date of Final Oral Examination: 05/30/2014

The dissertation is approved by the following members of the Final Oral Committee:

Dr. Baron Chanda, Associate Professor, Neuroscience

Dr. Meyer Jackson, Professor, Neuroscience

Dr. Qiang Cui, Professor, Professor, Chemistry

Dr. Mathew Jones, Associate Professor, Neuroscience

Dr. Martin Zanni, Professor, Chemistry

ACKNOWLEDGEMENTS

I thank Dr. Baron Chanda for giving me the opportunity to work in his lab as a graduate student and for introducing me to the exciting and captivating field of ion channels, which I have grown to love deeply in the past several years, and for mediating my tryst with experimental science which I had yearned for as an undergraduate student of engineering. The one-on-one discussions that I have had with him on different topics related to ion channels, over the past six years have been a crucial part of the my graduate training and I am very grateful for them. I am also thankful to all the present and past members of the Chanda lab who have been great friends and colleagues, who have helped me grow scientifically as well as personally. I would especially like to thank Dr. Vadim Klenchin (Dima), who in spite of being in the lab for just one year now, has thoroughly influenced the way I think about science and experiments. Also, Kevin Oelstrom – "…you've been the absolute best of friends and a lab-mate that I could've hoped for!"

I am grateful to my high school physics teacher – Mr. Supriyo Ghosh, under whose tutelage I began to love and appreciate science in the first place. He is the person who taught me how to think scientifically. He impressed upon me that it takes a lot of patience and determination to learn something and master it and a great amount of discipline and sincerity to not forget what one has learnt. It is because of him that I still remember the physics and mathematics that he taught me almost a decade ago, which has served me very well throughout graduate school.

Most of all, I thank my father, Dwijen Chowdhury, and mother, Dr. Snigdha Chowdhury, for all that they have done for me over the past three decades. My mother, in particular, has been my rock. She has been my most vicious critic as well as my most

relentless supporter. She is the most passionate human being I know and over the years I have realized that my success, well-being and happiness are the sole objects of her passion. She has fought for me and with me, for my own good, and made me who I am today. Much to my chagrin, she continues to be on my case, even today, although she is 40000 miles away in India – but honestly, I don't know what I would do without her.

I have thoroughly enjoyed and relished graduate school, all the ups and downs, and I am eager and apprehensive to see what lies ahead of me. I hope that the uncountable good wishes that my friends and family have showered on me, which filled my graduate school life with unbridled excitement, help me find happiness, stability and peace of mind doing whatever I do.

ABSTRACT

Voltage-gated ion channels (VGICs) constitute an evolutionary diverse family of integral membrane proteins that transport ions across the hydrophobic membrane bilayers, when triggered by changes in membrane potential. This thesis examines the manifestations of the fundamental laws of thermodynamics on this family of proteins to understand how they operate at the molecular level.

In the first few Chapters of this thesis, I describe an analytical approach to extract the energetics of voltage-dependent activation of ion channels and use it to determine the interaction energies between residues in the exemplar Shaker K_V channel. The approach involves extracting a special parameter, the median voltage of activation (V_M) from experimentally measured gating-charge displacement *vs* voltage (QV) curves. Next, I use this approach to determine the interaction energies between residues comprising an intersubunit gating nexus, which is likely to be crucial for the relay of structural and energetic information, from the voltage-sensors to the pore. Additionally, I describe how these thermodynamic principles can be extended to deconstruct the allosteric linkage pathways between voltage and ligand dependent activation pathways of polymodal allosteric channels.

In the final chapter of this thesis, I study the mechanism by which temperature modulates voltage-dependent gating of ion channels. Gating of some members of the VGIC superfamily is exquisitely sensitive to changes in temperature, however we lack an understanding of the molecular mechanisms underlying temperature sensation and modulation of voltage-dependent channel function. I use a heuristic approach to systematically engineer mutations into the relatively temperature insensitive Shaker K_V

channel to design a temperature modulated voltage-dependent channel. From the characterization of the relative open probability *vs* voltage curves of over fifty mutants of the channel at two different temperatures, I propose that thermal sensitivity is mediated by state dependent changes in the solvation status of critical residues, which governs ΔC_P of channel gating. I also demonstrate that voltage-sensing charges play a crucial although indirect role in governing the effect of temperature on channel gating. These principles could be very useful to deconstruct the temperature sensing mechanisms of natively thermosensitive channels, such as the thermoTRPs and other structurally unrelated channels, such as Anoctamins.

PUBLICATIONS

#1. Chowdhury, S., and Chanda, B., *Free-energy relationships in ion channels activated by voltage and ligand.* The Journal of General Physiology, 2013, 141(1):11-28.

#2. Chowdhury, S., and Chanda, B., *Thermodynamics of electromechanical coupling in voltage-gated ion channels*. (Perspective article) The Journal of General Physiology, 140(6): 613-23

#3. Chowdhury, S., and Chanda, B., *Estimating the voltage-dependent free energy change of ion channels using the median voltage for activation.* The Journal of General Physiology, 2012, 139(1):3-17. (Research article)

#4. Chowdhury, S., and Chanda, B., *Deconstructing thermodynamic parameters of a coupled system from site-specific observables*. Proceedings of the National Academy of Sciences U S A, 2010, 2;107(44):18856-61. (Research article)

#5. Arcisio-Miranda, M., Muroi, Y., Chowdhury, S, Chanda, B., *Molecular mechanism of allosteric modification of voltage-dependent sodium channels by local anesthetics.* The Journal of General Physiology, 2010, 136(5):541-54. (Research article)

#6. Muroi, Y., Arcisio-Miranda, M., Chowdhury, S., Chanda, B., Molecular determinants of coupling between domain III voltage sensor and pore of a sodium channel. Nature Structural & Molecular Biology, 2010, 17(2):230-7. (Research article)

Manuscripts under review

#1 Chowdhury, S., Haehnel, B. M., and Chanda, B., *An exact approach for determining residue-specific coupling interactions that underlie channel activation.* (Research article)

#2 Chowdhury, S., Haehnel, B. M., and Chanda, B., *Interfacial gating triad is crucial for electromechanical transduction in voltage-activated potassium channels.* (Research article)

#3 Chowdhury, S.*, Jarecki, B. W.*, and Chanda, B., *Interfacial gating triad is crucial for electromechanical transduction in voltage-activated potassium channels.* (Research article) (* denotes equal contribution).

#4 Chowdhury, S., and Chanda, B., *Basic Voltage sensing mechanisms*. (Book Chapter, Publisher: Taylor and Francis; Editors: Matthew C. Trudeau and Jie Zheng)

TABLE OF CONTENTS

CHAPTER ONE

INTRODUCTION

General Overview

Voltage-dependent changes in the permeability of the membrane bilayer to different ions underlie the initiation and propagation of action potentials in electrically excitable cells (Hille, 2001b). Classical electrophysiological studies, now more than half-a-century old, were able to convincingly demonstrate that such voltage-dependent changes in membrane conductance originate due to special proteins embedded in the membrane which quickly respond to membrane potential changes by catalyzing the transport of ions across the membrane. Many of these proteins were found to exhibit exquisite ion selectivity, being able to discriminate between Na^+ and K^+ ions whose ionic radii differ by < 0.5 Å (Hille, 1971, 1972, 1973). Ion transport mediated by these proteins occurred in the direction of the electrochemical gradient of permeant ions and at rapid rates in the range of $10^4 – 10^6$ ions/sec. These characteristic features distinguish this class of proteins, from other transport proteins that mediate ion flux, across the membrane, at much slower rates and/or require additional sources of energy (such as ATP hydrolysis or co-transport of other ions), and are known as voltage-gated ion channels (VGIC).

Since the early pioneering studies by Bernstein, Cole, Hodgkin, Huxley and others, VGICs have been extensively studied because of their primary roles in neuroscience and cardiovascular physiology (Bernstein, 1902, 1912; Cole and Curtis, 1939; Hodgkin and Huxley, 1952d, e, c, a, b; Hagiwara and Saito, 1959; Hagiwara, 1966; Hagiwara and Nakajima, 1966). However, VGICs are important in a plethora of

additional physiological processes. For instance, calcium influx through calcium channels can also act as a second messenger which initiates various processes such as muscle contraction (Hagiwara et al., 1971; Hagiwara and Kidokoro, 1971). Isoforms of voltage-dependent potassium channels are involved in diverse physiological processes that include volume regulation, secretion, proliferation and migration (Nelson and Quayle, 1995). Apart from their occurrence at the plasma membrane, members of VGICs are also found in different cellular organelles, where they perform important functions. For instance, mitochondrial potassium channels are deemed to be important for mitochondrial respiration and maintenance of membrane potential, and are also believed to play cytoprotective roles in injured cardiac tissues (O'Rourke, 2004). A further testament to the physiological importance of VGICs is the plethora of genetically inherited pathological mutations that have been linked to members of this family of membrane proteins.

For more than half a century, voltage-clamp experiments have been the bedrock of electrophysiological methods to analyze biophysical properties of voltage-gated ion channels. In this technique, the amount of current flowing through the membrane expressing channels in response to step changes in potential is measured. From their time-dependent current responses, it is possible to deduce the rates of channel opening and closing and the fraction of open channels when a new equilibrium is established. The analysis of voltage-dependence of open probabilities provides a measure of the relative stability of the open versus closed state of the channel.

From a physical perspective, voltage-dependent change in channel open probability (P_O) can be thought of as a simple two state process wherein the channel

exists either in the closed or the open state and voltage biases the equilibrium towards one state or the other. For instance, in channels that open in response to depolarization, the equilibrium is biased towards the closed state at resting membrane potentials (~ –90mV) and depolarization results in a shift in the bias in favor of the open state (Fig. 1a) resulting in increase occupancy of the open state at higher depolarized membrane voltages. In addition to the energy difference between the closed and open states, membrane potential also alters the energy barrier between the closed/open states and the transition state (Fig. 1a**)**. Upon membrane depolarization, the forward energy barrier decreases while the reverse energy barrier increases with the result that channel opening becomes faster at higher membrane voltages while channel closing becomes slower.

For any voltage-gated ion channel, the open probability (P_O) *vs* voltage (V) relationship can be plotted (P_OV curve) and the curve is sigmoid (Fig. 1b) and can be described by a simple logistic equation, commonly referred to as the Boltzmann equation:

$$P_o = \frac{1}{1+\exp\{zF(V_{1/2}-V)/RT\}} \quad \ldots (1)$$

The latter equation has two parameters – *z*, which is a measure of the steepness of the curve and $V_{1/2}$, which is the voltage that elicits half-maximal response (i.e. $P_O = 0.5$). The free-energy difference between the closed and open states, at 0 mV (ΔG_c), can be estimated from the Boltzmann fit parameters as:

$$\Delta G_c = zFV_{1/2} \quad \ldots (2)$$

Clearly, a more negative value of $V_{1/2}$ or a steeper P_oV curve (larger z) will imply that at zero membrane potential, the open state is energetically more favorable than the closed state and vice-versa.

Based on the assumption that the transition energy barrier for channel opening and closing scales linearly with voltage, the rate constant for channel opening (k_O) and closing (k_C) will have exponential dependence on voltage, i.e.

$$k_o = \alpha \exp(z_o FV / RT) \ldots (3a)$$

$$k_c = \beta \exp(-z_c FV / RT) \ldots (3b)$$

where α and β indicate the rate of channel opening and closing, respectively, at 0 mV and z_O and z_C governs the voltage dependence of the rate constants of channel opening and closing, respectively. The negative sign in Eq. 3b dictates that the rate constant of channel closing reduces as voltage is increased.

In this simple two-state scenario, the time-dependent open-probability in response to a depolarization pulse, from a hyperpolarizing holding potential (when all channels are closed), can be derived to be:

$$P_O = \frac{k_O}{k_O + k_C}(1 - e^{-(k_O + k_C)t}) \ldots (4)$$

An important result of Eq. 4 is that the time constant of channel opening, τ_O, will vary non-monotonically with voltage (Fig. 1c) i.e. initially, upon small depolarizations, τ_O will increase with voltage, reach a peak and subsequently decrease with voltage. This occurs due to the reversibility of the closed-open transitions. At small depolarizations, k_O is less than k_C and hence τ_O (= $(k_O + k_C)^{-1}$) will be dominated by k_C, while at larger depolarizations, when k_C becomes small, k_O dominates τ_O. Experimentally, ionic current activation traces are often fitted with mono-exponential equations to extract τ_O and asymptotic limits of an ln τ_O *vs* V plot, at large depolarizations, give an estimate of α and

z_O. In a similar way, time constant of channel closing, extracted from deactivating currents elicited by very hyperpolarizing pulses, from highly depolarizing voltages, are used to obtain estimates of β and z_C. The basic relationships described in Eqs. 1-4 are some of the most commonly used approaches to deduce basic functional characteristics of voltage-dependent channel gating from electrophysiologically assayed channel activity.

Multi-state nature of channel gating

The first order time derivative of Eq. 4 gives an expression for the 'initial rate' of channel opening in response to depolarization, which comes out to be simply k_O. The implication is that P_O, and thus the current, will begin to rise immediately after a depolarization pulse. Very interestingly, classical electrophysiological studies observed a distinct time-delay before the ionic currents begin to rise. This time-delay was found to become longer with increasing hyperpolarization of the pre-pulse (voltage before the depolarizing pulse). This feature, now known as the Cole-Moore shift (Cole and Moore, 1960), cannot be explained using monoexponential rate equations. The implication of this observation was that channel activation involved voltage-dependent transition via multiple closed states.

In their classical studies on voltage-dependent sodium and potassium permeabilities in squid axons, Hodgkin and Huxley had postulated, "…it seems difficult to escape the conclusion that the changes in ionic permeability depend on the movement of some component of the membrane which behaves as though it had a large charge or dipole moment" (Hodgkin and Huxley, 1952d). The temporal pattern of this charge movement which is known as gating currents, was first demonstrated independently by

two groups in the early seventies (Armstrong and Bezanilla, 1973; Schneider and Chandler, 1973). Gating currents are observable as (relatively) small transient currents, when all ionic currents are blocked by the application of a channel blocker or depleting permeant ions (Fig. 2a). Gating-charge displaced at a particular voltage is obtained by integrating the gating currents over the time period of depolarization. A plot of the displaced gating charges at various voltages generates a charge-voltage curve (QV) (Fig. 2b). Comparison of the QV and P_oV curves shows that there is a significant displacement of gating charges prior to channel opening, a phenomenon that has been observed in all known VGICs till date. This is contrary to the predictions of a two-state model according to which the QV and P_OV curves should have been superimposable.

With development of electrophysiological methods permitting measurements of stochastic gating behavior of single ion channels and analytical methodologies to construct detailed multi-state Markov models, the multi-state nature of channel activation was described with great precision. Using a Drosophila potassium selective voltage-gated channel as a model system, three groups in the nineties generated detailed kinetic models of voltage-dependent activation, using single channel measurements, macroscopic ionic and gating currents as constraints (Bezanilla et al., 1994; Zagotta et al., 1994a; Schoppa and Sigworth, 1998). The key feature of these models was that there were several strongly voltage-dependent transitions preceding a single transition, with a relatively low voltage-dependence, which ushers the channel into an open state. While the multi-state nature of channel activation was well known, the structural events in the channel during this process remained unknown.

Basic Structural features

Molecular cloning of voltage-dependent ion channels stimulated mechanistic thinking in terms of chemical structures and their role in determining function. Numa and coworkers in a series of landmark papers described the primary structure of voltage-dependent sodium and calcium channels (Noda et al., 1986; Tanabe et al., 1987; Suzuki et al., 1988). Voltage-gated potassium channels were cloned by molecular genetic analysis of a Drosophila *Shaker* mutant (Papazian et al., 1987; Tempel et al., 1987; Timpe et al., 1988). Expression of these genes in heterologous expression system enabled functional analysis of a relatively homogenous population of these ion channels. The primary structure in combination with biochemical and functional analysis revealed that while the voltage-gated potassium channels are homotetrameric built from four identical subunits, the voltage-gated sodium and calcium channels consist of four homologous domains on a single polypeptide. Each subunit or domain comprise six transmembrane helices (Fig. 3a**)**, S1 through S6 with a membrane re-entrant P-loop intervening the S5 and S6 helices. The P-loop harbors the selectivity filter of the channel (Heginbotham et al., 1994; Favre et al., 1996) but more recently has been implicated in channel gating (Zheng and Sigworth, 1998; Cuello et al., 2010; Sauer et al., 2011; Capes et al., 2012).

In all voltage-gated ion channels, the fourth transmembrane (S4) segment is strikingly conserved and contains multiple repeats of RXXR motif where X in general represents a hydrophobic residue (Fig. 3b). Neutralization of these charges reduced the slope of the conductance-voltage curves (Papazian et al., 1991) but so did mutations of hydrophobic residues in the intracellular loops between S4 and S5 (Lopez et al., 1991; McCormack et al., 1991b; Smith-Maxwell et al., 1998b). To unequivocally establish that

these residues are gating charges, it is necessary to measure their contribution to the total charge associated with the gating of the channel.

To date three different approaches have been exploited to measure the total gating charge per channel. Almers showed that for a sequential mode of channel opening, the slope of the ln P_O versus voltage plot at hyperpolarized voltages becomes equal to the total charge during channel activation (Almers, 1978; Sigg and Bezanilla, 1997). Using this limiting slope method, Schoppa and Sigworth calculated that for the Shaker potassium channels 12.8 electronic charges are transferred during activation (Schoppa et al., 1992). Mackinnon and Bezanilla group independently corroborated these values by an alternate approach which involved calculating the total charge by measuring the gating currents and then independently estimating the number of channels in the same preparation (Aggarwal and MacKinnon, 1996; Seoh et al., 1996), using either noise-analysis or radioactively labeled toxins. Both groups found that the first four arginines in the S4 segment of the Shaker potassium channel were the primary gating charge carrying residues. These results directly imply that the S4 helix, along with its positive charge bearing arginine residues, move across the membrane electric field during voltage-dependent activation of the channel.

Limiting slope analysis methods have also been used to measure the charge transferred per channel (Q_{max}) of voltage-gated calcium channels (Noceti et al., 1996) as well as sodium channels (Hirschberg et al., 1995), although it remains unknown whether the four homologous (but non-identical) domains of each channel transfer equal amount of gating charge during activation. Another approach which has been utilized to determine the contribution of a particular residue to gating charge movement is the

"charge add back" experiment (Ahern and Horn, 2004). In this approach the gating-charge displacement curves of cysteine mutant channels, before and after modification with a positive charge bearing, thiol modifying reagent (MTSET), and the difference is attributed to the gating charge contribution of the site in question. While logical, such an experimental strategy has important caveats arising out of uncertainties related to completeness of MTSET modification and/or structural distortion introduced upon MTSET modification, etc. Identification of the gating-charge determining residues remains an unanswered question in Na_Vs and several other voltage-gated ion channels. Neutralization of the S4 charges in several other voltage-gated channels strongly perturb gating, however, as discussed before this is not sufficient evidence to argue that the perturbing sites are the voltage-sensing charges.

The location of the channel gates in the Shaker K_V channel was identified using substituted cysteine accessibility studies (Liu et al., 1997; Holmgren et al., 1998). Yellen and colleagues showed that some residues in the S6 segment, when mutated to cysteines were promptly modified by thiol modifying reagents, such as MTSET (as judged by extent of current block upon exposure to MTSET), but only when the channels were open. In contrast, other sites, which were closer to the intracellular (C-terminal) end of the S6, did not exhibit any significant change in the rates of MTSET accessibility between the closed and open states. Furthermore, it was shown that in the closed state, cysteines introduced, deep in the S6, were protected from modification by Ag^+ ions (del Camino and Yellen, 2001). These results thus demonstrated that in the prototypical Shaker K_V channel the S6 segments line the ion permeation pathway, that the channel gates were formed by confluence of the intracellular ends of the S6 which was tightly packed to

prevent access of Ag^+ ions into the inner pore and that channel opening is associated with dilation of the gating constriction, presumably resulting from splaying open of the S6 helices (Fig. 3c).

The solution of the high-resolution structure of a full-length eukaryotic potassium (K_V) channel was a remarkable achievement (Long et al., 2005a; Long et al., 2007) and offered a solid framework to understand the mechanisms of voltage-dependent gating (Fig. 4a). The structure revealed that voltage-sensors of the different subunits, each comprising the S1-S4 helices arranged as a four-helical bundle, are located symmetrically around the central pore domain, which is formed by the association of the S5-S6 segments from each of the four domains. The voltage-sensors of each subunit shares limited contacts with pore domain, except at an intracellular interface, constituted primarily by the S4-S5 linker helix and the tail end of the S6 segment. It has been proposed that this interface is crucial for relaying voltage-dependent structural changes in the S4 helix to the channel gates (Long et al., 2005b). In the structure, the channel gates were dilated to >12Å in radius, which is large enough to allow solvated potassium ions to flow through. In other words, the structure of the channel putatively represents an open/activated state of the channel. In last several years, multiple structures of the voltage-dependent potassium and prokaryotic sodium channels (Payandeh et al., 2011; Payandeh et al., 2012; Zhang et al., 2012) have become available and in all cases, the quaternary structure is remarkably similar.

Before the structures of the voltage-sensing domain became available, scanning mutagenesis studies had suggested that the voltage sensor comprised four α-helical segments (Monks et al., 1999; Hong and Miller, 2000; Li-Smerin et al., 2000a). In

particular these studies had proposed that the S3 helix is kinked at a specific site, which features a proline residue, conserved in the K_V channel family. In other VGICs the analogous position is occupied by serine residue (whose hydroxyl side-chain can hydrogen-bond with the backbone), which are known to be potential 'helix-breakers'. In the post-structural era, when the existence of such a kink was confirmed in the K_V channels, the S3 helix was further subdivided into two parts – the S3a (below the kink) and the S3b helix (above the kink). Structure-function studies which followed suggest that a tight complementarity between the S3b helix and the S4 helix is important for voltage-sensing (Ruta et al., 2005). Several studies have also suggested that the S3a helix remains static during voltage-dependent structural changes, but the S3b helix undergoes relatively greater conformational changes (Nguyen and Horn, 2002; Banerjee and MacKinnon, 2008; Henrion et al., 2012). This helix-turn-helix motif, comprised most of the voltage-sensing charges of the S4, and is referred to as the paddle motif (Swartz, 2008) (Fig. 4b). This motif is also an important and selective target for a large number of gating-modifier toxins in different channels (Li-Smerin and Swartz, 1998; Winterfield and Swartz, 2000; Li-Smerin and Swartz, 2001).

In a series of important experiments, Swartz and colleagues showed that the paddle motif was portable across different channels (Alabi et al., 2007; Kalia and Swartz, 2013). By transferring the paddle motif of different ('source') channels onto a common structural template of $K_V2.1$, they showed that the chimeric channels were not only functional but were also imbued with some of the macroscopic voltage-dependent properties of the source channels. Additionally, they also became sensitive to gating-modifier toxins that target the source channels (Bosmans et al., 2008; Milescu et al.,

2009). More recent experiments performed by Lu and colleagues reveal that a tight complementarity between S3b and S4 is not essential for voltage-dependent motions (Xu et al., 2010; Xu et al., 2013). They also find that the channels retain their basic voltage-dependence even after deletion of nearly the entire paddle motif. Together, these experiments imply that the paddle motif is modular and moves relatively unconstrained in response to depolarization.

Another interesting feature of the structures is that the first charge seems to face away from proteinaceous environments and points outwards towards the membrane-water interface (Long et al., 2005a). Functional reconstitution of purified proteins in bilayers with different headgroups suggest that the lipid charge may profoundly alter channel function (Schmidt et al., 2006). Modification of the lipid headgroups in native membranes by specific lipases, which alter the nature of the lipid headgroup leaving them positively or negatively charge or electroneutral, also alter the function of voltage-dependent channels (Ramu et al., 2006). Structural studies utilizing NMR spectroscopy have shown that the first charge is in close proximity to the lipid headgroups (Krepkiy et al., 2012). These findings indicate that some of the outermost arginines of the S4 segment may interact with the negative charges on the phospholipid head groups and this may be an important mechanism by which the lipid environment alters the voltage-dependent gating behavior.

Basic voltage-sensing mechanisms

The structural underpinnings of voltage-sensing mechanism have been a focus of investigation since the cloning of the first voltage-dependent ion channels. One of the

earliest models of S4 helix movement was the ‘sliding helix’ model (Catterall, 2000) in which voltage change causes a vertical displacement of the S4 helix perpendicular to the membrane plane. A related structural model is the ‘helical screw’ model (Guy and Seetharamulu, 1986; Broomand and Elinder, 2008) (Fig. 5) in which apart from a sliding motion, the S4 helix also undergoes a rotation about its helical axis. One of the central aspects of this model is the proposition that stabilizing salt-bridge interactions of the positive charges on S4 with conserved negative charges in the surrounding S1, S2 and S3 helices facilitate vertical translocation of the S4 helix. In functional studies, perturbation of these negative charges caused significant effects on protein expression and function (Tiwari-Woodruff et al., 1997). Disulphide and metal bridging assays have demonstrated that these ion pairs are in close proximity in functional channels consistent with their position in the crystal structure (DeCaen et al., 2008; DeCaen et al., 2009; DeCaen et al., 2011).

A central feature in the structures of the voltage-sensing domains is the presence of water accessible crevices. In the years leading up to the crystal structure, the presence of these water-filled crevices was proposed based on multiple lines of evidence. Cysteine accessibility studies by Yang and Horn (Yang and Horn, 1995; Yang et al., 1996) on voltage-gated sodium channels show that the 3rd charge on the S4 segment is accessible to a modifying reagent applied on the outside whereas the 4th gating charge was accessible from the inside. This was the first evidence that there is a septum between the third and the fourth charge. Similar studies performed on the model Shaker K_V channel also demonstrated that the modification of substituted cysteines, at the gating charge positions, to extracellularly or intracelullarly applied thiol reactive reagents, depended on

the membrane potential. These studies indicated that not only was there a septum within the voltage-sensing domain, but also that the position of the S4 helix, relative to the septum changed with voltage.

In the three-dimensional structure, the 'septum' can be deduced to be roughly 7-8 Å in length packed with hydrophobic residues (Chen et al., 2010). As a consequence the majority of the electric field drops across a much smaller thickness inside the protein although the potential difference is applied across the entire membrane width. Thus voltage-dependent activation can occur with S4 helix moving across a much smaller distance. Demonstrating the existence of such a focused electric field within the voltage-sensing domain is an intensely challenging problem. However, some important studies have strongly suggested such a principle. Firstly, by carefully examining the effect of ionic strength on gating-charge movement combined with electrostatic field calculations, Islas and Sigworth (Islas and Sigworth, 2001) were able to argue in favor of the existence of a septum of low dielectric constant, 3-10 Å thick, within the voltage-sensing domain. Secondly, using electrochromic probes tethered to residues within the voltage-sensor, Bezanilla and colleagues (Asamoah et al., 2003) observed a Stoke's shift in the fluorescence emission properties of the probes in response to voltage-sensor activation. Thirdly, using charged MTS reagents of different lengths as molecular rulers, Ahern and Horn (Ahern and Horn, 2005) demonstrated that modification of cysteine at the position of the first arginine on S4, increased the magnitude of experimental measured gating charge displacement, but only when the molecular probes were short (<4 C-C bonds). They hypothesized probes longer than the thickness of the septum would allow the voltage sensor to move without the additional gating charge and thus the thickness of

septum should be ~ 4Å. While these experiments all have multiple underlying assumptions and caveats (such as usage of simplified geometries for the electrostatic calculations by Islas and Sigworth, size and orientation of fluorophores in the spectroscopic investigations of Bezanilla and colleagues and the uncertainty of the structure and gating dynamics, post MTS modification, in the studies of Ahern and Horn), they converge on the central idea that the membrane electric field, instead of being spread across the full thickness of the membrane bilayer, is focused across a much narrow, putatively hydrophobic septum.

In a remarkable set of experiments, Bezanilla and colleagues were first to show that mutating the S4 arginines to histidines allowed protons to go through the voltage-sensing domains in a pH dependent manner (Starace et al., 1997; Starace and Bezanilla, 2001, 2004) – while the second and third argine substitutions leads to formation of a proton transporter, which is at its highest activity at intermediate voltages, the first arginine mutation results in a proton pore which actively permeates protons, but only at hyperpolarizing voltage conditions. Furthermore, neutralizing the first S4 charge with small, non-histidine residues made the voltage-sensing domains permeable to alkali metal cations in a relatively non-selective manner (Starace et al., 1997; Starace and Bezanilla, 2001, 2004; Tombola et al., 2005; Sokolov et al., 2007) (Fig. 6a**)**. This current, now called the gating pore current, further substantiates the idea that there is a narrow septum which bifurcates the extracellular and intracellular crevices of the voltage-sensing domain and the septum can be ‘dissolved’ through a relatively small number of mutations (Campos et al., 2007).

As mentioned above, the gating pore currents have a unique state-dependence - mutation of the R1 charge elicits inwardly rectifying currents (Starace and Bezanilla, 2004) whereas R4 neutralization generates outwardly rectifying currents (Starace et al., 1997). This observation can be reconciled by considering that the R1 is closest to the gating pore septum in the resting configuration whereas R4 is the most proximal in the activated state and the presence of these charges prevent permeant ions from accessing this pore. Strikingly, mutation of non-S4 residues were also shown to generate state-dependent gating pore currents (Campos et al., 2007) which may be interpreted as that the septum itself undergoes reorganization between the resting and activated conformations. Based on this observation and spectroscopic measurements (Chanda et al., 2005), it has been proposed (Fig. 6b) that the voltage-sensing domain undergoes a "transporter" like motion wherein the septum moves from an outside position to an inside position upon activation. As a result, the region across which the electric field is focused changes between conformations and rather than the charges physically moving a large distance through the electric field, the electric field also moves through the charges. This sort of a movement recapitulates the alternating access model of the transporters in which the opening switches between an outward facing and inward facing configuration during the transport cycle. (Jardetzky, 1966).

Despite intense focus by many groups, the exact structural details of voltage-gating remain unresolved in large part due to the absence of a well-defined structure of a fully resting voltage-sensor. In the activated state structure of a voltage-gated potassium channel, the first four charges are in a water accessible external crevice and/or lipid headgroups and the remaining charges are in an internal crevice separated by a

phenylalanine residue in the S2 segment (Tao et al., 2010). This residue is conserved in >99% voltage-gated channels indicating that it has a crucial role in voltage-dependent gating. Size and hydrophobicity of this site has been suggested to be crucial for channel activation as indicated by perturbation experiments using natural and unnatural amino acids (Tao et al., 2010; Lacroix and Bezanilla, 2011; Pless et al., 2011). Given its functional role and structural location, this conserved phenylalanine, which is referred to constitute a 'gating charge transfer center', quite possibly constitutes the hydrophobic septum. However, it is only one of the many hydrophobic residues that separate the water filled crevices in the voltage-sensing domains. Further work will be required to determine the specific role of this and other residues in the hydrophobic septum (Lacroix et al., 2014) in focusing the membrane electric field.

Structural and functional diversity of voltage-gated ion channel superfamily

VGICs are an incredibly diverse family of membrane proteins which are ubiquitous in all kingdoms of life, although their physiological roles in lower organisms, such as prokaryotes, is much less understood. While the general architecture and the structural principles of voltage-dependent gating are in all likelihood similar across the different family members, some of them possess unique structural and gating properties which enable them to perform distinct physiological functions.

A phylogenetic tree of some of the important members of this superfamily (Fig. 7), based on a multiple sequence alignment of the voltage-sensing domains, shows that the different members can be broadly grouped into four different clades. One of the clades (cyan) comprise the potassium selective channels, which are possibly the most well

studied clade, in terms of structure and biophysics. They have served as model systems on which much of the theories of voltage-dependent gating have been developed. A unique member of this clade is the Slo1 channel, alternatively known as the BK or the maxiK channel (Fig. 7b**)**. At a functional level, Slo1 channel is different from other members of this clade (and VGICs in general) in two important ways. First, its single channel conductance is a whopping 300pS, which is 10-50 times higher than most known VGICs. Second, voltage-dependent gating of this channel is exquisitely sensitive to intracellular calcium ions, which cause large leftward shifts (~50-100 mV) in the open-probability *vs* voltage relationships of these channels. At a structural level, these channels are also unique. C-terminal to the S6 segment, these channels have two RCK (regulators of potassium conductance) domains which hang in the cytoplasm and house the calcium regulatory sites of the channel. Structural studies of the RCK domains of these channels (and other prokaryotic homologs of this channel, such as MthK) have suggested that they form a 'gating-ring' at the cytoplasmic mouth of the ion permeation pathway, which expands laterally (along the membrane plane) upon calcium binding and allosterically facilitates voltage-dependent gating. The second unique feature of these channels is the presence of an additional transmembrane segment, S0, N-terminal to S1 segment (the first transmembrane helix of general VGICs). This results in the N-terminal of the S0 segment being extracellular which is in contrast to other VGICs. Low resolution cryoelectron microscopy structures and disulfide bridging assays have indicated that the S0 lies at the interface between two subunits of the channel, which in turn suggests that it can modulate voltage-dependent gating in ways, unperceivable from the currently known structures of VGICs. The BK channels have been argued to play crucial roles in muscle

contraction and are considered to be one of the most prominent targets for drugs for asthma, blood pressure control, etc.. A structurally related member of the Slo1 channel is the Slo3 channel, which apart from being voltage-modulated, is modulated by intracellular pH and has been shown to play crucial roles in sperm motility in mouse and is considered to be an important target for the design of male contraceptives.

The second clade (red) depicted in the phylogenetic tree represents a relatively new members of the VGIC family, the voltage-sensor only proteins (VSOPs) **(**Fig. 7b**)**. These include the voltage-sensing phosphatase (VSP) in which the S1-S4 voltage-sensor is tethered to a PTEN phosphatase domain and is a protein which catalyzes the hydrolysis of membrane phospholipids (such as PIP_2) in a voltage-dependent manner. Another member of the VSOP clade is the voltage-dependent proton-selective, H_V, channel, which is simply an S1-S4 voltage-sensor C-terminally linked to a cytoplasmic coiled-coil domain (which mediates channel dimerization). The discovery of both these proteins confirmed earlier propositions that the voltage-sensing domain of the canonical VGICs is modular and can fold and function, independent of the pore domain. The H_V channels additionally were strongly reminiscent of the gating-pore conducting mutants of the K_V/Na_V channels, in which ions were able to flux right through the voltage-sensing domains. A central difference between H_V currents and the gating-pore currents is that while in the former currents are outwardly rectifying, currents in the latter are inwardly rectifying. This in all likelihood arises due to some crucial, albeit currently unknown, structural differences between H_V channel and gating-pore current conducting voltage-sensing domains of K_V/Na_V channels. Recently, the crystal structures of the voltage-sensing domains of a VSP and H_V have been independently determined (Li et al., 2014a).

The structures show that the S4 segment is more intracellular than previously determined structures of K_V and prokaryotic Na_V channels and putatively represent a "pre-activated" conformation of the voltage-sensor. However, whether these structures represent *bona fide* intermediate or resting states, representative of what happens in other VGICs is not clear.

The third clade of the phylogeny tree (green) comprises unique members of VGICs which are appended with a cyclic nucleotide binding domain at their C-termini (Fig. 7b). Members of this clade are incredibly diverse and include: (i) HCN channels, which are hyperpolarization activated monovalent-cation conducting, non-selective channels, whose gating is modulated by intracellular cyclic nucleotides (particularly cAMP) and, in higher organisms, are important for the heart pacemaking activity, learning and memory; (ii) the potassium selective hERG channel, which opens upon membrane depolarization, and mediates the repolarizing potassium currents in the cardiac action potential, but is not modulated by cyclic nucleotides. These channels further possess N-terminal, cytoplasmic domains, part of which is a PAS domain, which is crucial for their characteristic slow deactivation gating. Over 500 genetic mutations have been linked to the hERG gene which lead to life-threatening pathophysiological conditions such as long QT syndrome and cardia arrhythmias; (iii) the non-selective CNG channels, which are non-voltage gated channels, despite the structural and sequence similarity of their transmembrane segments with those of other VGICs. They are gated by binding of cyclic nucleotides (particularly cGMP) which underlie their physiological roles in vision and olfaction; (iv) KAT channels, which are potassium selective plant channels, activated upon membrane hyperpolarization, modulated by binding of cyclic

nucleotides. The functional diversity of the channels within this clade thus arises, in part, due N- and C-terminal appendages which are believed to interact with various regions of transmembrane core and thereby modulate the voltage-dependent activity of these channels.

The final clade comprises the voltage-gated Na and Ca channels, from eukaryotes and prokaryotes. The ultrafast activation of the eukaryotic Na_V channels (<~1ms) underlies the rising phase of the action potentials. The eukaryotic Ca_V channels on the other hand have been implicated in a variety of physiological processes because they lead to an increase in cytosolic levels of calcium which activates other calcium activated ion channels (such as the BK channels) or triggers other signal cascades. From an architectural standpoint, the prokaryotic Na_Vs, studied so far, are similar to the members of previous clades in that, functional channels are formed by homo- (or hetero- in case of CNG/HCN channels) tetrameric assembly. In contast, eukaryotic Na_V and Ca_V channels arise from a single polypeptide chain encoding all four domains. Extracellularly, the four domains are arranged in a clockwise orientation. The four different domains are deemed to have unique roles in voltage-dependent gating of these channels. For instance, the Domain II (and III) voltage-sensors of the Na_V seem to be especially important for voltage-dependent channel opening, while Domain IV voltage sensor seems to be the most important for channel inactivation (which is a process by which the currents through these channels decline to baseline levels even in the presence of sustained depolarization). Gating of these channels is further modulated by accessory subunits. For instance, the Ca_V channels are known to have at least three different accessory subunits, which

associate with specific domains of the channel and alter the Q_{max} of the channel, rates of channel activation/deactivation, etc.

Members of VGICs activate over different voltage ranges. For instance, BK channels (in absence of calcium) activates at ~+100 mV whereas the prokaryotic Na_V channel (Na_VAb) activates at ~ -100 mV (Gamal El-Din et al., 2013). In addition, some members such as the Na_Vs activate within 1 ms whereas others such as HCN channels take more than 1 sec to open. What might be the origin of this incredible functional diversity in the VGIC superfamily? The overall transmemembrane architecture of the voltage-sensors and pore domains of all VGICs are likely to be similar. However, local differences in amino acid residues might alter the energy landscape of voltage-dependent gating contributing to the profound variation in the voltage-dependent activation characteristics. Visual inspection of high resolution structures might not offer the necessary information to realize the energy differences underlying the functional differences in gating behavior. Molecular dynamics simulations might offer a means to determine these energies. However not only would such an exercise be computationally intensive, experimental validation of such computational hypotheses is necessary to assuage concerns related to accuracy of force-fields and uncertainties arising from durations and protocols of molecular simulations. Currently, accurate determination of the energetics of activation requires construction of detailed well-constrained multi-state Markov models. Implementing such an approach for large scale perturbation studies of ion channels, while possible (as demonstrated by studies of Auerbach and colleagues (Purohit et al., 2013)), is extremely tedious and resource-intensive. Thus deconstructing

the specific roles of protein residues and their interactions that shape the energy landscape of voltage-dependent gating remains an extremely challenging problem.

FIGURES

Figure 1. A simple two-state voltage-dependent gating of an ion channel.

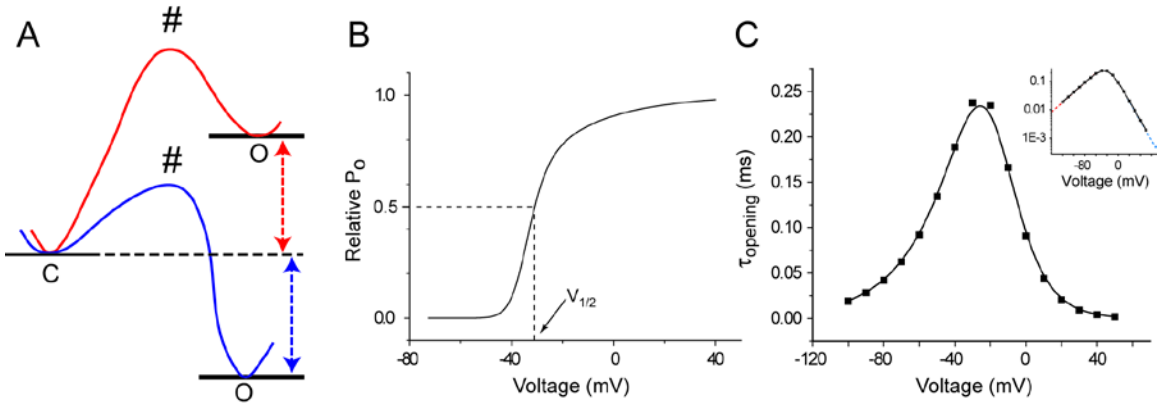

(A) Energy profile diagram of a closed (C) to open (O) transition for a VGIC involving a single transition state (#). At a hyperpolarizing voltage, (red profile), the closed state is energetically more favorable than the open state. At a depolarizing voltage, (blue profile), the open state is more stable than the closed state. The net energy difference between the closed states under the two conditions are indicated using arrows. **(B)** The open-probability *vs* voltage curve for non-inactivating mutant of Shaker potassium channel. The voltage at which half the channels are open is indicated by $V_{1/2}$. **(C)** The time-constant of channel opening ($\tau_{opening}$) *vs* voltage curve for an arbitrary channel. Inset shows the same plot on a semi-logarithmic scale (the slopes of the hyperpolarizing and depolarizing asymptotes of the plot in the inset give the voltage-dependence of the rate constant of channel closing and opening respectively).

Figure 2. Gating-charge displacement in voltage-gated ion channels.

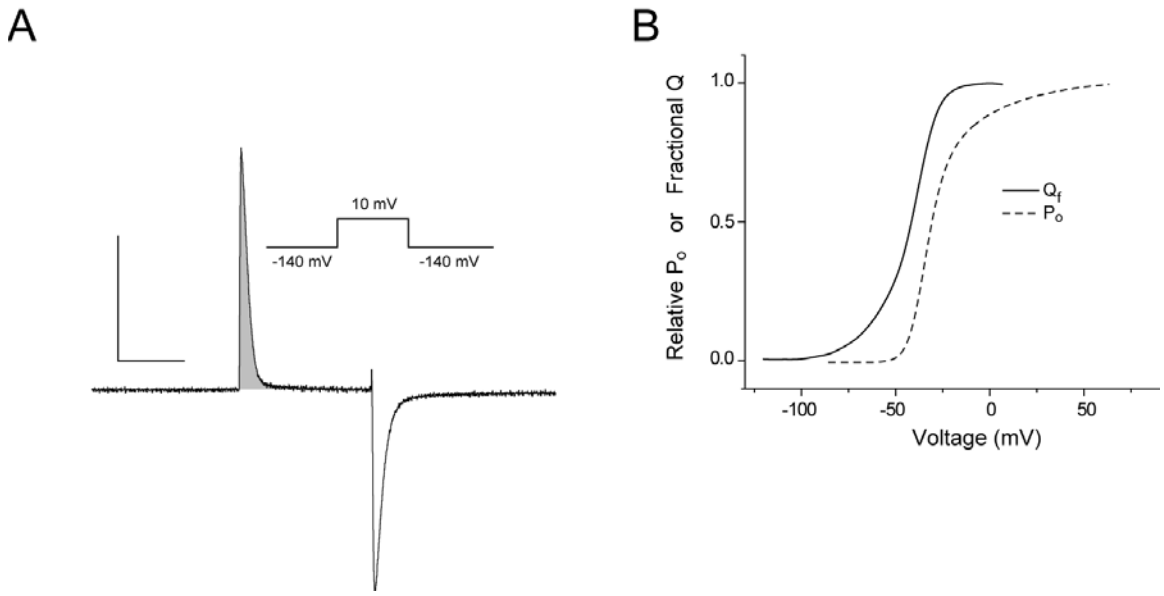

(A) An example of a gating current trace for the Shaker potassium channel (in the background of the non-conducting W434F and inactivation-removing mutations) obtained in response to a depolarizing pulse. The shaded area represents the gating-charge transferred during the depolarization. Scale bars represent 1 μA and 25 ms. **(B)** Comparison of the normalized gating-charge displacement (Q_f) and relative open-probability curves for the Shaker potassium channel (inactivation removed mutant).

Figure 3. Basic structural features of voltage-gated ion channels.

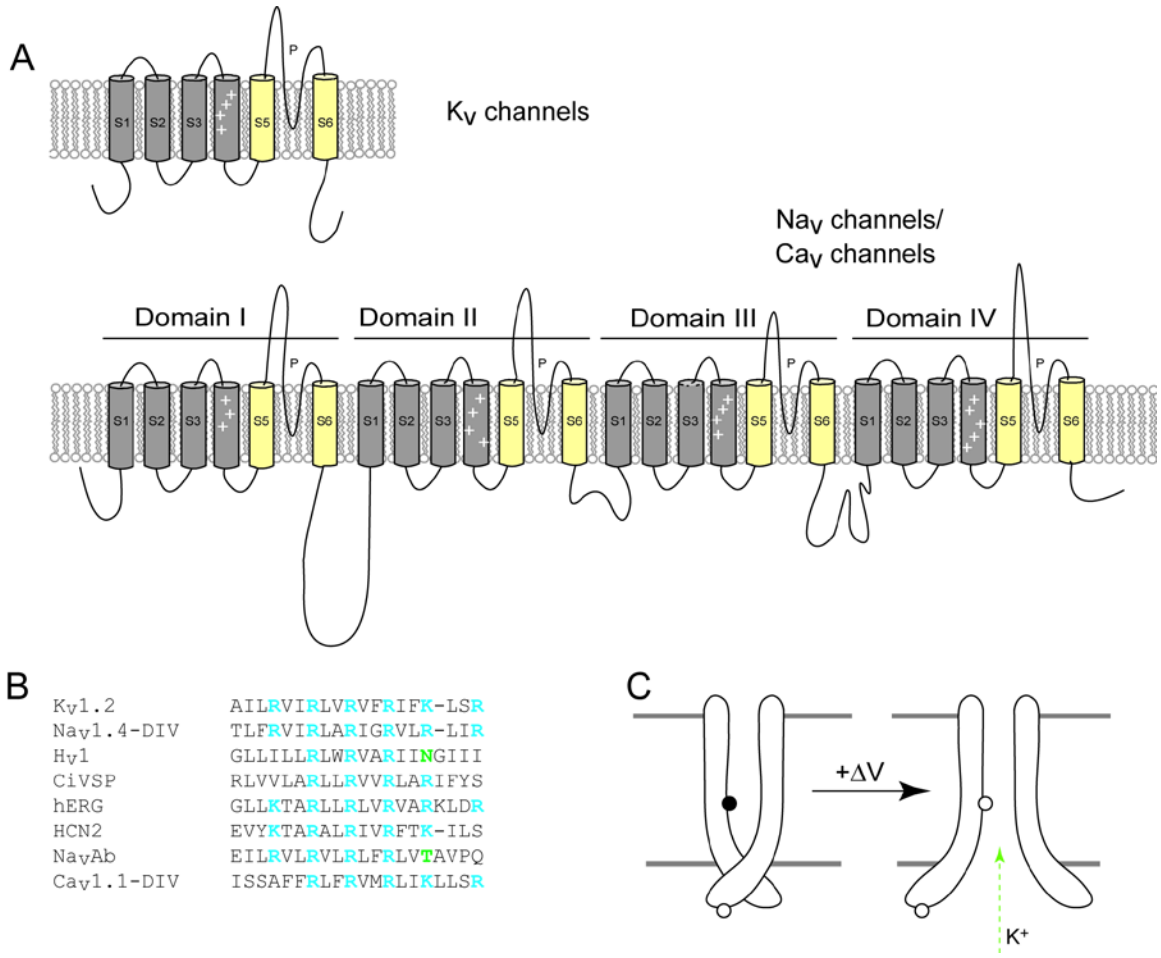

(A) Membrane topology of the voltage-gated potassium, sodium and calcium channels. The potassium channels are homotetrameric and each subunit comprises six transmembrane helixes, S1 through S6. The fourth transmembrane segment carries a series of regularly spaced positively charged residues. Between the S5 and S6 segments is the membrane re-entrant loop which houses the residues which confer potassium selectivity to these channels. The eukaryotic Na_V and Ca_V channels are heterotetrameric comprising four homologous domains (Domains I-IV). Each domain shares the same membrane topology as a single subunit of the potassium channels. **(B)** Sequence alignment of the S4 segments of different members of the voltage-gated ion channels.

The conserved positively charged residues are shown in blue. **(C)** Cartoon showing the opening and closing of channel gates (in response to change in depolarization). Cystein residue introduced above the channel gate is inaccessible to internally applied thiol modifying reagents in the closed state (indicated by black circle) and accessible in the open state, while at sites below the channel gate, thiol-modifying reagent accessibility is state-independent.

Figure 4. Structural features of voltage-gated ion channels revealed by x-ray crystallography.

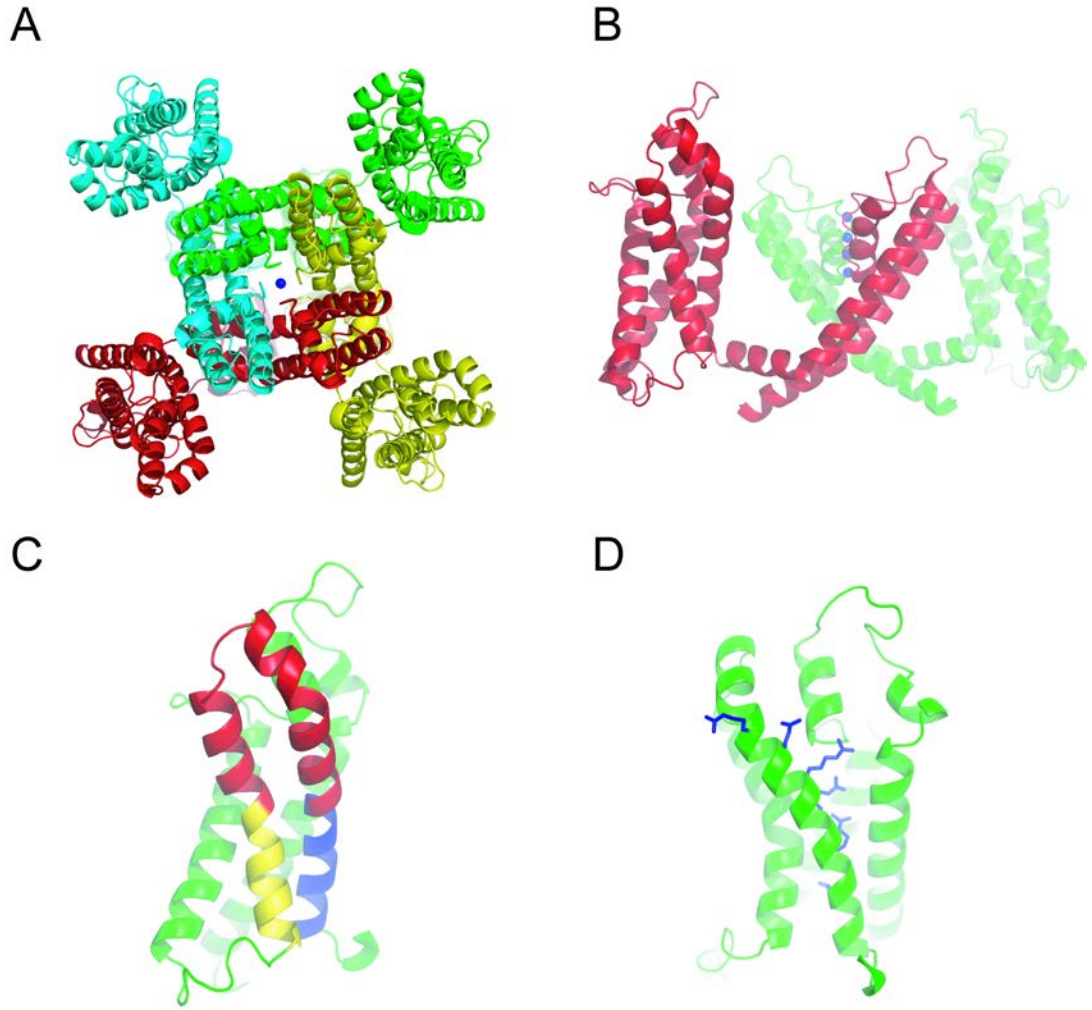

(A) and (B) The high resolution crystal structures of the mammalian voltage-gated potassium channel (PDB-ID: 2R9R) showing a top view (from the extracellular side) **(A)** of the tetrameric channel and a side view **(B)** of two non-adjacent subunits of the channel. The four voltage-sensing domains of the different subunits are arranged symmetrically around the central pore domain. Potassium ions bound to the selectivity filter are shown as blue circles. The structures represent a putative open-activated state of the channel. **(C)** The paddle motif of the voltage-gated potassium channel (PDB-ID: 2R9R) is shown in

red, while the S1/S2 helices are in green, S3a helix is in yellow and the intracellular portion of the S4 segment is in blue. **(D)** The position of the gating-charges on the S4 segment are shown in (blue) stick representations (PDB-ID: 2R9R). The first two side-chains are seen to face in the opposite direction from the remaining sidechains. The latter point towards the interior of the voltage-sensing domain (crevices) while the former are exposed to the lipid-protein interface. (Note that in this paddle-chimera structure the first gating charge position is occupied by a glutamine and not an arginine (or lysine), which aligns with the position and orientation of the first arginine residue seen in the crystal structures of $K_V1.2$ (PDB-ID: 2A79) and the isolated voltage-sensing domain of the prokaryotic channel, K_VAP (PDB-ID: 1ORS)).

Figure 5. The helical screw model of voltage-sensor activation.

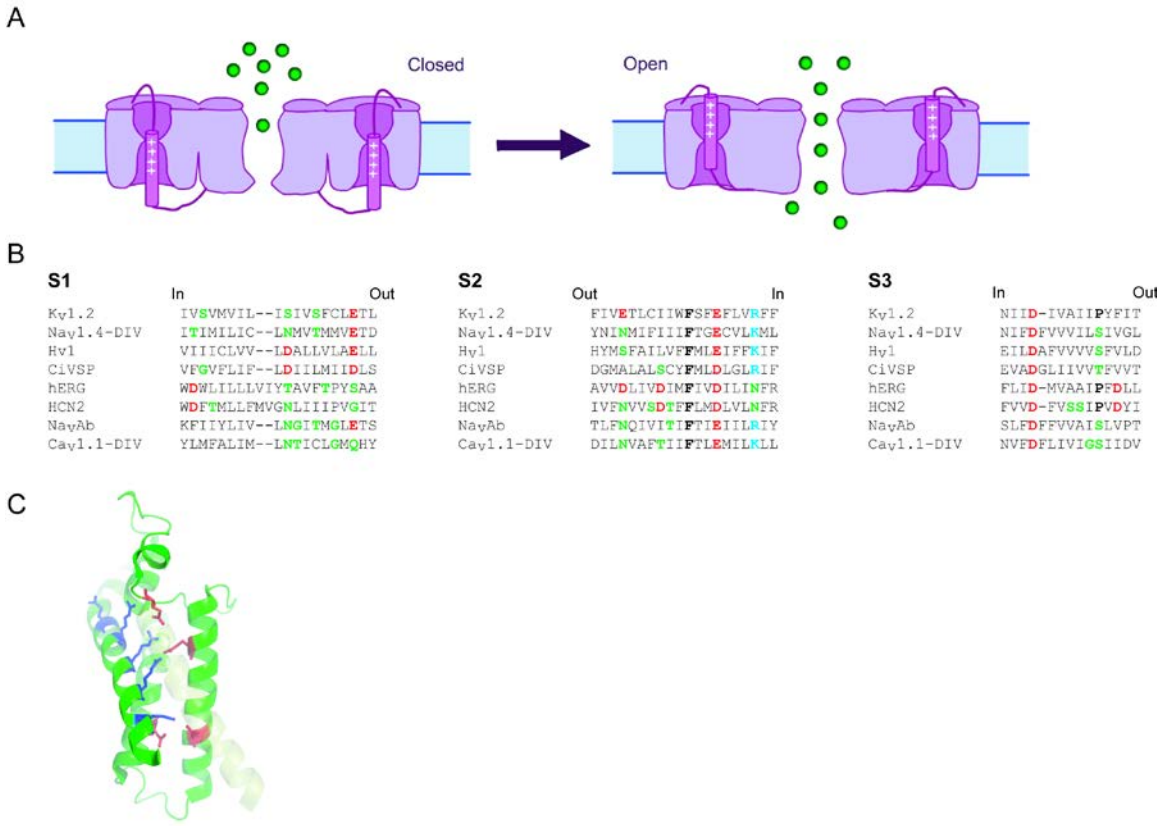

(A) Cartoon depicting the sliding helix/helical screw model of movement of the S4 helix. Voltage-dependent activation, by this model, involves a vertical translation of the S4 helix, accompanied by a rotation of the helix about its axis. **(B)** Sequence alignment of the S1, S2 and S3 helices of different VGICs. The intracellular and extracellular ends of helical segments are indicated. The positions of the conserved negative charges are shown in red bold characters. Negative charges close to the intracellular ends of the S2 and S3 helices are highly conserved, while those close to the extracellular ends of S1 and S2 segments are more variable. A conserved phenylalanine residue intracellular end of the S2 segment is shown in black bold characters. **(C)** The voltage-sensing domain of the Kv1.2/2.1 paddle chimera structure (PDB-ID: 2R9R) showing the positions of the conserved positive charges (on the S4 segment) and the negative countercharges in the S1,

S2 and S3 helices in a putatively activated state of the voltage-sensor. (For clarity of depiction, the S1 helix is depicted in a transparent mode.) The third and fourth positive charges (from the top of S4) are clearly involved in a salt-bridge interaction while the fifth positive charge (which a lysine residue in most Kv channels) is in close proximity to two conserved negative charges on the S2 and S3 segments.

Figure 6. Gating-pore currents and the transporter model of voltage-sensor activation.

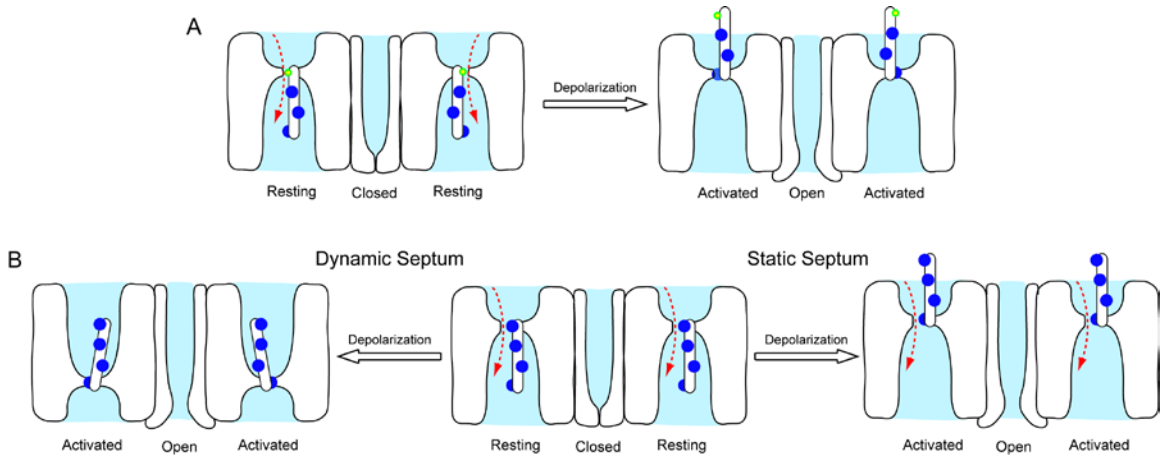

(A) A cartoon depicting the origin of gating-pore currents in the VGICs. At hyperpolarizing voltages, when the channel is closed and the voltage-sensor is in a resting conformation, the first arginine (R1) occludes a narrow (gating) pore between the external and internal crevices within the voltage-sensor and repels small cations preventing them permeating. Mutation of R1 to small/neutral amino acids removes the pore-occluding moiety allowing ions to pass through the voltage-sensor. **(B)** Comparison of the static and dynamic septum models of voltage-sensor activation. Mutations in the non-S4 segments (at sites constituting the hydrophobic septum, referred to as "wall mutants") elicit gating-pore currents only at hyperpolarizing voltages, when the voltage-sensor is in a resting conformation. If the septum remains static, gating-pore currents should be elicited when the voltage-sensor is in resting (hyperpolarizing voltages) as well as activated (depolarizing voltages) conformations. In the dynamic septum model, the hydrophobic septum undergoes reorganization during voltage-dependent activation such that the sites which constitute the primary constriction in the gating-pore, in the resting state, are not the same as the sites which make up the septum in the activated state. The

result is septum is different in the resting and activated states. The dynamic septum model explains the rectification behavior of the gating-pore currents elicited by wall mutants (80). The feature of the dynamic septum is embodied in the transporter model of the voltage-sensor activation.

Figure 7. Diversity in the voltage-gated ion channel family.

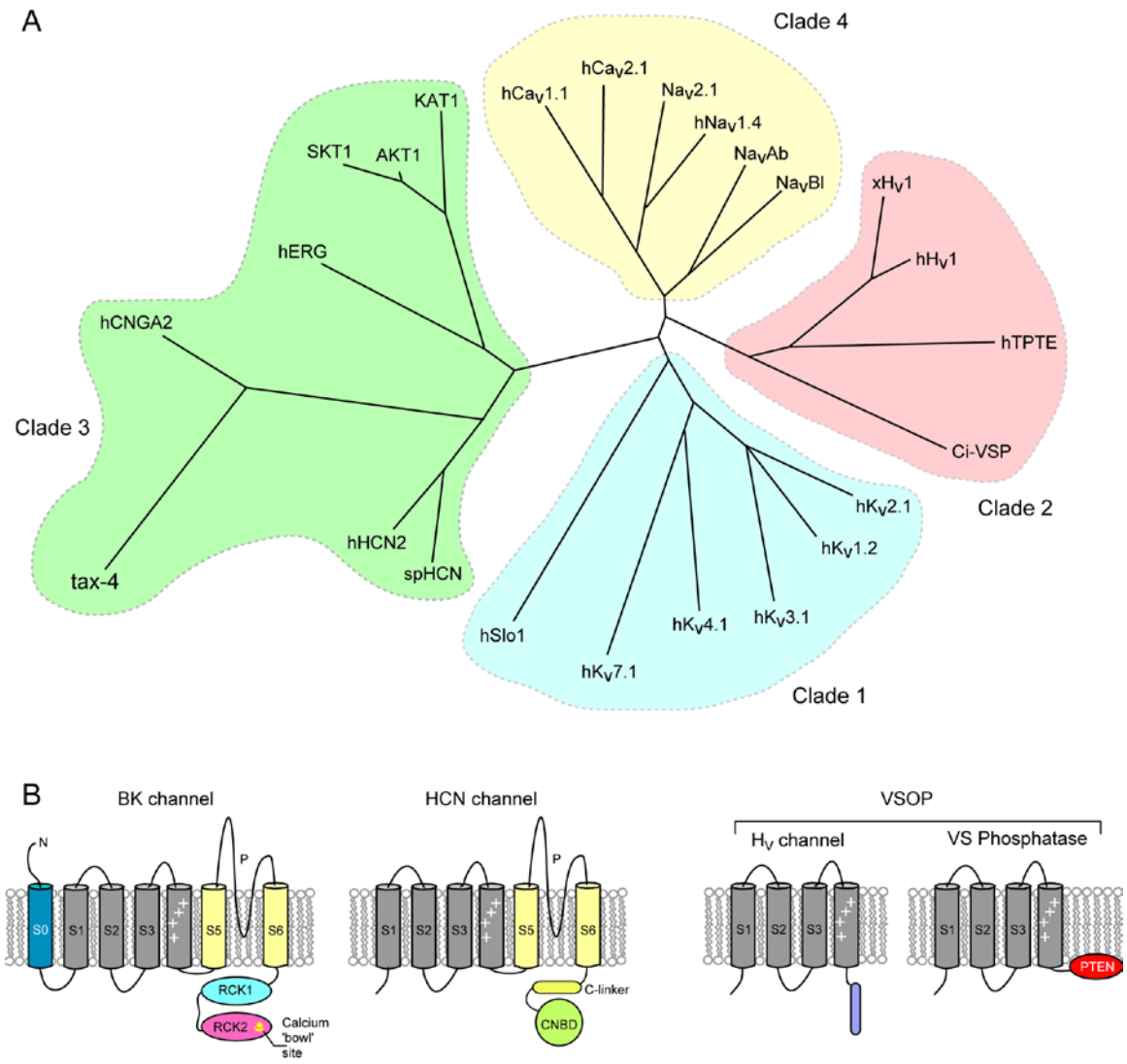

(A) The cladogram shows the sequence diversity of 24 voltage-sensing domains (VSDs) from different members of VGIC family, created from a multiple sequence alignment of the VSDs (obtained using MUSCLE (138)). The phylogenetic tree calculation was performed using BioNJ (139). Four distinct clades are directly observable. Clade1 comprises the different voltage-gated potassium channels members of which form homotetrameric channels. Clade 2 comprises the voltage-sensor only proteins (VSOP) –

the proton selective H_V channel (human and Xenopus) and the PTEN phosphatase domain containing VSOP from Ciona intestinalis and its human orthologue (hTPTE). Clade 3 comprises members of the VGIC family containing a cyclic nucleotide binding domain at their C-termini. Members of this clade include the depolarization activated hERG channels, hyperpolarization activated channels from metazoans (hHCN2 and spHCN), the inwardly rectifying plant channels (SKT1, AKT1 and KAT1) and the very weakly voltage-sensitive CNG channels (human and C. elegans orthologues). Clade 4 comprises the voltage-gated sodium and calcium channels from eukaryotes (which are heterotetrameric; $Na_V2.1$ represents the sodium channel from Nematostella vectensis) and prokaryotes (NavAb and NavBl). **(B)** Membrane topology and functional domains of structurally distinct members of the VGIC superfamily – the BK channel (the calcium "bowl" site is an important calcium regulatory site); the HCN channel (C-linker links the membrane core to the cyclic nucleotide binding domain (CNBD) and is essential for allosteric regulation of channel gating by cyclic nucleotides); two members of the VSOP clade – the H_V channel (the C-terminal cytoplasmic structural motif is the coiled-coil domain of the channel) and the voltage-sensing phosphatase (VSP).

CHAPTER TWO

Experimental procedures

Materials

Methanesulfonic acid (MES) was purchased from Acros organics (Geel, Belgium). N-methyl D-glucamine (NMG) was purchased from Sigma-Aldrich. Collagenase A was purchased from Roche (Madison, WI). One 1 kb DNA ladder was purchased from New England Biolabs (Ipswich, MA) and the low mass ladder was purchased from Invitrogen (Life Technologies, Madison, WI). All restrictions used for molecular biology purposes were purchased from New England Biolabs. Fast AP dephosphatase was purchased from Fermentas (Glen Burnie, MD). Primers were synthesized by Integrated DNA Technologies (East Providence, RI). The PFU-Ultra DNA polymerase, from Agilent Technologies (Santa Clara, CA) was used for PCR. All other chemicals were obtained either from Fisher Scientific (Fitchburg, WI) or from Sigma Aldrich.

Oocyte preparation

Oocytes were extracted for *Xenopus laevis*, obtained from Xenopus Express (Brooksville, FL) or Nasco (Fort Atkinson, WI). Following removal of oocytes, they were mechanically dissociated using sterile forceps. Following two rinses in SOS (standard oocyte solution) (100 mM NaCl, 2 mM KCl, 1 mM $MgCl_2.6H_20$, 5 mM HEPES, at pH 7.2), the oocytes were placed in 1mg/ml Collagenase A dissolved in SOS and placed on a turntable (VWR, Radnor, PA) for 20 minutes. After three rinses with SOS, the oocytes were again manually separated with sterile forceps and then they were

returned to the collagenase for another 15 minutes. Following three rinses in SOS the oocytes were observed under a dissection microscope (Ningbo Yong Jing Science and Education Equipments Co., Ningbo, China). If oocytes were still in their follicular layers, they were treated with the collagenase solution for additional 5-10 minutes. This process was repeated until ~70% oocytes were defolliculated. Next, oocytes were stored in SOS, supplemented with 1.8 mM $CaCl_2.2H_2O$, 0.1mg/ml Gentamycin and 1 mg/ml bovine serum albumin (Sigma Aldrich). Oocytes were stored in an 18°C incubator (VWR). All oocyte solutions were measured for the correct osmolarity (190-210 mmol/kg) using a Wescor Vapro 5520 Osmometer (Logan, UT).

Mutagenesis and DNA preparation

All clones used in this study were derived from a cDNA of the inactivation-removed Shaker K_V channel (Δ6-46) cloned into the pBSTA vector, which is optimized for oocyte expression and contains an ampicillin resistance marker. Mutations were introduced by PCR using mismatch mutagenic primers (QuikChange; Agilent Technologies). All mutations were confirmed by sequencing the whole cDNA at the Biotechnology Center at the University of Wisconsin Madison. For gating current measurements, mutations were introduced in the background of the W434F mutation which knocks off all ion conduction without compromising other aspects of channel gating (Perozo et al., 1993). Constructs were transformed into chemically competent XL1-Blue or XL10-Gold cells prepared in the lab. Plasmid purification was carried out using Qiagen Plasmid purification (mini-prep) kits and final concentration of purified

DNA was measured on Nanodrop 2000x spectrophotometer (Thermo Scientific, Wilmington, DE).

RNA preparation and injection

DNA was linearized using a NotI enzyme (New England Biolabs, Inc.) and then the linearized DNA was purified (and concentrated) using PelletPaint (EMD Millipore, Billerica, MA). In vitro transcription reactions were performed using mMESSAGE mMACHINE T7 kit (Life Technologies, Grand Island, NY), following manufacturer's instructions and transcribed mRNA was precipitated using lithium chloride. Precipitated mRNA was washed with 70% ethanol and resuspended into nuclease free water at concentrations 1-5 μg/μl and stored at -80°C until needed.

For oocyte injection, healthy oocytes were selected from the collagenase treated oocytes by manual inspection and placed in sterile SOS (no calcium ions to be present) and a micropipette was pulled using the PP-83 puller (Narishige, East Meadow, NY). The tip of the pipette was chipped off using fine forceps and back loaded with light mineral oil. The pipette was attached to a Nanoliter 2000 microinjector (World Precision Instruments, Sarasota, FL). The pipette was loaded with RNA and 50nL of cRNA at a concentration of 50-200ng/μl was injected into each oocyte. After injection, the oocytes were kept at 18°C in a solution containing 100 mM NaCl, 2 mM KCl, 1.8 mM $CaCl_2$, 1 mM $MgCl_2$, 5 mM Hepes, 0.1 mM DTT, and 0.2 mM EDTA, supplemented with 100 μg/ml gentamicin and 100 mg/ml bovine serum albumin for 12hrs – 5 days (with the storage solution being replenished every day).

Electrophysiological experiments

Ionic current measurements

Ionic currents were measured on a cut-open oocyte voltage clamp (COVC) set-up (CA-1B; Dagan Corporation) 12-72hr post-injection (during which injected oocytes were stored at 18°C). Oocytes were first placed in external solution (115 mM K-MeS (potassium methanesulfonate), 2 mM Ca-MES, and 10 mM Hepes, pH 7.4) and seated in the central recording chamber, positioned over a hole leading into the lower chamber. Suction was applied to the lower chamber to create a negative pressure which allows the oocyte to sit tightly on the hole. Next, the top chamber was carefully placed on top of the oocyte such that the oocyte partially protruded through the hole into the top chamber. The top chamber was next filled with the same external solution and the bridges were connected to the top, middle and bottom chambers. Subsequently, the lower chamber was filled with the internal solution (105 mM K-Mes (*N*-methyl-d-glucamine methanesulfonate), 2 mM EGTA, and 10 mM Hepes, pH 7.4). With this combination of external and internal solutions, the reversal potential was ~ 0mV which leads to large inward tail currents (used to measure the relative open probability of the channel) but also lead to much larger steady-state currents, which was problematic while characterizing mutants with left-shifted conductance-voltage relationships (owing to series resistance errors which become increasingly problematic with increasing inward currents). To circumvent this problem, in many experiments, an alternate external solution was used (105 mM NMG-Mes (*N*-methyl-d-glucamine methanesulfonate), 10 mM K-MeS, 2 mM Ca-MES, and 10 mM Hepes, pH 7.4). With the latter external solution the reversal potential was ~ -60 mV and thus was used for characterization of such mutants.

Voltage clamping on a COVC set-up has been described in detail elsewhere (Stefani and Bezanilla, 1998). Briefly, 3M KCl agar bridges with platinum wire are placed in wells containing an AgCl wire and 3M KCl. The top recording chamber is connected to three bridge electrodes – P1, P2 and CC. These electrodes are used to voltage-clamp the oocyte membrane to the command potential and to minimize capacitive transient currents. Two other electrodes, GS1 and GS2 (referred to as the guard bridges) connect the respective electrodes to the central guard chamber. These serve to reduce leak cuurents from the top chamber into the lower bath chamber by electrically isolating the chamber. The bottom chamber is connected to I bridge which is the current injection electrode. Following the set-up of the oocyte in the recording chamber, the internal solution is replaced with a mild detergent (0.3% wt/vol saponin prepared in the standard internal solution) to permeabilize the inner oocyte membrane. This allows a low resistance path for current injection, via the I electrode, into the oocyte. Following permeabilization, the internal chamber is quickly washed and replenished with the internal recording solution. Micropipettes were pulled using a P-97 flaming brown microelectrode puller (Sutter Instrument Co., Novato, CA). This was filled with KCl and a AgCl wire, installed on a micromanipulator, is inserted through the top membrane of the oocyte and then the membrane may be clamped to the command potential. The pipette resistance is 0.2 – 0.7 MΩ. Using a CA-1B clamp (Dagan Instruments, Minneapolis, MN) the membrane was clamped to -80mV. To minimize the capacitive currents, capacitance compensation was carried out at voltages stepping from -100 to -90 mV (or in a voltage-range where currents from expressed channels are unlikely). Following compensation, the oocyte is equilibrated at -80mV (or the appropriate holding

voltage for the experiment) for 5minutes and then electrophysiological measurements are made.

In general, ionic currents were obtained by applying 100 ms long depolarizing pulses from -120 to + 80 mV in 5 mV (or in some cases 2.5 mV or 10 mV) increments, with 1sec between each pulse. The holding potential was -120 mV. Capacitive transients and linear leak currents were subtracted online using the P/-4 method, during which the holding potential was -120 mV (or set at the same voltage as the holding voltage). Analogue signals were sampled at 20-250 kHz with a Digidata 1440 or 1320 interface (Molecular Devices) and low-pass filtered at 10 kHz. After baseline subtraction, peak tail current amplitudes, elicited by repolarization pulses to -120 mV, were used to generate the relative open probability *vs* voltage (I/I_{max}) curves. The holding voltage was in general -120 mV. The duration of depolarization pulse and the voltage-range over which ionic currents were elicited were varied while characterizing some mutants (e.g. slowly activating mutants). Data was collected using pClamp 10 software (Molecular Devices, Sunnyvale, CA).

Gating Current measurements

For gating currents, setting the oocyte and COVC voltage-clamp was performed as described above. The difference was in the solutions used for electrophysiological measurements. The external solution used for gating current measurements was: 105 mM NMG-MES (*N*-methyl-d-glucamine methanesulfonate), 2 mM Ca-MES, and 10 mM Hepes, pH 7.4. The internal solution used for gating current measurements on the COVC set-up was 105 mM NMG-MES, 2 mM EGTA, and 10 mM

Hepes, pH 7.4. The recording pipette resistance for all electrophysiological measurements was 0.2–0.5 MΩ.

Gating currents were obtained by applying 50 ms long depolarizing pulse to voltages from −120 to 20 mV (in 5-mV intervals). The capacitive transient and linear leak currents were subtracted online using the P/-4 method, with a subsweep holding potential of -120 or -90 mV (on COVC or TEV respectively). Following baseline readjustments, the on-gating current records were integrated over the duration of the depolarization pulse to obtain the gating charge displaced, which was used to compute the fractional gating charge displacement *vs* V curve (Q/Q_{max} *vs* V or Q_f-V).

Temperature control

The recording temperature was changed using an in-house fabricated temperature controlling device. The recording chamber was placed in a metal block (with heat conducting paste sealing contacts between the chamber and the block) which was connected to a Peltier device. The Peltier device was in turn connected to an industrial controller on which the temperature set-point was entered. A feedback loop further connected the controller and the solution in top recording chamber (the tip of the feedback loop was placed very close to the oocyte).

For measuring the temperature dependent shifts in the conductance-voltage curves, after compensation of the capacitive transients, the oocyte was equilibrated to holding temperature for at least 15 minutes (during which the oocyte was voltage clamped). To check for temperature equilibration, short depolarizing pulses (50 ms long to +60 mV from a hyperpolarizing holding voltage of -120mV) were applied every 30 sec. Once the

drift in the magnitude of outward currents was <5-10%, the train of step depolarizations were applied.

For measurements at the lower temperature (8°C), after temperature equilibration, voltage pulses to +60mV were applied, first for 100 ms and then in increments of 50 ms. If the magnitude of current at the end of a pulse of duration 't' is >85-90% of currents for pulses of duration 't+50', then for conductance voltage curve measurements, the duration of the depolarizing pulses was fixed at 't+50'. It must be mentioned that in many cases it was not possible to accurately determine this time 't' because increasing the duration of the depolarizing pulse lead to progressive decline in oocyte quality (e.g. leak currents begin to rise enormously with longer depolarizing pulses), in which case a standard depolarizing pulse duration of 150 ms was used for measuring ionic currents, to deduce conductance voltage curves at the lower temperature. It needs to be mentioned that ionic current measurements at the two different temperatures were not always paired – i.e. not always obtained from the same oocyte. This was because it the oocytes frequently became leaky due to the stringent test protocols to which they were subject, thereby allowing us to obtain the full conductance voltage trace at only one temperature (from each oocyte). However, in the event that the oocyte remained healthy after measurements at a single temperature, the same oocyte was oocyte to obtain the conductance voltage curve at the second temperature as well.

In the temperature ramp experiments, after setting up the system, the oocytes were held at -120 mV, 28°C until equilibration. Next, a temperature ramp was applied by switching the temperature controller to 8°C. The ramp speed, as assessed using the feedback loop (and independently assessed using an electronic thermometer, whose probe

was placed at a similar location as the feedback loop), was 1°C/15sec. At each temperature, 100 ms long depolarizing pulses were applied from -120 mV holding voltage to -20 mV (which is close the half-activation voltage of the wild-type inactivation removed Shaker K_V channel). The outward currents elicited by these pulses were used to determine temperature sensitivity of some of the mutants and compare it with the Shaker K_V channel.

Gating current measurements in Two Electrode Voltage Clamp (TEVC)

For some mutants, which did not express well enough, TEVC was used to measure gating currents. As before mRNA injected oocytes were injected and incubated at 18°C for 2-6 days. Oocyte was placed in the recording chamber, filled with full NMG solution (105 mM NMG-Mes (*N*-methyl-d-glucamine methanesulfonate), 10 mM K-MeS, 2 mM Ca-MES, and 10 mM Hepes, pH 7.4). Two micropipettes, of resistance 0.2 – 0.7 MΩ each, were filled with 3M KCl solution and fixed to microelectrodes with a AgCl wire. Oocyte was impaled using the two electrodes and voltage clamped at -90 mV using an OC-725C Oocyte Clamp (Warner Instruments). After 5 minutes of equilibration, gating currents were measured using a voltage-protocol identical to that used on the COVC set-up, except that depolarization pulses followed 100 ms prepulse to -120 mV and were also followed by a repolarization pulse to -120 mV. Data was collected using pClamp 8 software (Molecular Devices, Sunnyvale, CA).

Data Analysis

Electrophysiological traces were analyzed using Clampfit 10.2 (Molecular Devices, Sunnyvale, CA). The I/I_{max} curve for each mutant was obtained by averaging the curves obtained (in general) from 3-6 oocytes. The curve was fitted to the Boltzmann Equation:

$$\frac{I}{I_{\max}} = \frac{1}{\exp\{z_{app}F(V_{1/2} - V)/RT\}}$$

where z_{app} is the Boltzmann slope and $V_{1/2}$ is the voltage that elicits half-maximal response. Fitting was performed on Microsoft Excel, by minimizing the mean-squared error between data points and Boltzmann predicted points using the Solver Plug-in. The Boltzmann measure of free-energy change, ΔG_{app}, for each mutant was calculated as: $\Delta G_{app} = z_{app}FV_{1/2}$. The uncertainty associated with ΔG_{app} estimation ($\delta\Delta G_{app}$) was calculated as:

$$\delta\Delta G_{app} = F\sqrt{\left(\delta z_{app}V_{1/2}\right)^2 + \left(z_{app}\delta V_{1/2}\right)^2}$$

where δz_{app} and $\delta V_{1/2}$ is the standard error associated with estimation of z_{app} and $V_{1/2}$, respectively.

The non-additivity in a functional mutant cycle (FMC), $\Delta\Delta G_{FMC}$, was calculated as:

$$\Delta\Delta G_{FMC} = \{z_{app}FV_{1/2}\}_{WT} + \{z_{app}FV_{1/2}\}_{S12} - \{z_{app}FV_{1/2}\}_{S1} - \{z_{app}FV_{1/2}\}_{S2}$$

where the subscripts indicate the wild-type channel (WT), double mutant (S12) or the two single mutants (S1 or S2). The uncertainty associated with $\Delta\Delta G_{FMC}$ ($\delta\Delta\Delta G_{FMC}$) was calculated as:

$$\delta\Delta\Delta G_{FMC} = \sqrt{\left(\delta\Delta G_{app\|W}\right)^2 + \left(\delta\Delta G_{app\|S12}\right)^2 + \left(\delta\Delta G_{app\|S1}\right)^2 + \left(\delta\Delta G_{app\|S2}\right)^2}$$

where the terms in the brackets indicate the uncertainty associated with the ΔG_{app} estimates of the WT, double and two single mutants.

For evaluating temperature dependent shifts in the relative open-probability *vs* voltage ($P_O V$) curves, the median voltage of channel opening (V_M) was calculated. This was done as in many cases (especially at lower temperatures), the $P_O V$ curves are not adequately fitted by single Boltzmann curves and required superposition of multiple Boltzmann components:

$$\frac{I}{I_{\max}} = \frac{1}{\sum_{i=1}^{n} A_i} \sum_{i=1}^{n} \frac{A_i}{\exp\{z_{app}^{(i)} F\,(V_{1/2}^{(i)} - V)/RT\}}$$

where A_i indicates the 'amplitude' of the i^{th} Boltzmann component (i=1…n). Such fitting routines required estimation of 3n parameters (n representing the number of Boltzmann components) from a single curve and which in all likelihood is ill-constrained. In addition this introduces confusion comparing temperature-sensitization between cases where only one Boltzmann component is sufficient and in other cases where multiple components are required.

The V_M of channel opening is calculated from the $P_O V$ curves as:

$$V_M = \sum_{i=1}^{n-1} \frac{(P_O^{(i+1)} - P_O^{(i)})(V_{i+1} + V_i)}{2}$$

where $P_O^{(i)}$ and V_i is the i^{th} point on the $P_O V$ curve having 'n' points. Uncertainty of V_M measurement is described as the standard error of the V_M estimate across replicate measurements from multiple oocytes.

The fractional gating-charge displacement curves for all the mutants were obtained by averaging measurements performed on 3-6 oocytes. The median voltage of

activation, V_M, for each Q_f V curve was extracted by calculating the area between the Q_f V curve and the ordinate axis, using the trapezoid method. For a Q_f V curve with 'n' points, the V_M is calculated as:

$$V_M = \sum_{i=1}^{n-1} \frac{(Q_{i+1} - Q_i)(V_{i+1} + V_i)}{2}$$

where Q_i and V_i is the i^{th} point on the Q_fV curve. The net free-energy of activation of the channel is calculated as: $\Delta G_C = Q_{max} F V_M$, where Q_{max} is the maximum number of charges transferred during voltage-dependent activation of the channel. For all our calculations, we used a Q_{max} of 13.2 (Schoppa et al., 1992; Aggarwal and MacKinnon, 1996; Seoh et al., 1996). Although, Q_{max} for each of the mutations were not measured individually it is unlikely that any of the mutants studied in this paper alters Q_{max} as they are not the primary gating charge determining residues of the channel (Aggarwal and MacKinnon, 1996; Seoh et al., 1996). The uncertainty in ΔG_C was calculated as: $Q_{max} F \delta V_M$, where δV_M is the standard error of the V_M estimation.

The non-additivity in a mutant cycle analysis was calculated using the median measure of free-energy change – this non-additivity, $\Delta\Delta G_{GIA}$, was calculated as:

$$\Delta\Delta G_{GIA} = Q_{\max} F (V_{M\|W} + V_{M\|S12} - V_{M\|S1} - V_{M\|S2})$$

The standard error associated with $\Delta\Delta G_{GIA}$ ($\delta\Delta\Delta G_{GIA}$) was calculated as: $\delta\Delta\Delta G_{GIA} = Q_{\max} F \sqrt{\{\delta(V_M)_{WT}\}^2 + \{\delta(V_M)_{S1}\}^2 + \{\delta(V_M)_{S2}\}^2 + \{\delta(V_M)_{S12}\}^2}$, where $\delta(V_M)_{WT}$, $\delta(V_M)_{S1}$, $\delta(V_M)_{S2}$ and $\delta(V_M)_{S12}$ are the uncertainties (standard error of the mean) associated with V_M measurement of the wild-type channel and the single and double mutant channels, respectively.

Equilibrium Simulations

All simulations were performed with MATLAB version R2012b. The equilibrium responses simulated for different multi-state Markov models were directly obtained from the algebraic expressions of equilibrium occupancies of the different states. In Chapter Four a random sampling approach was used to test our theories (on determining non-additive energies). The simulations were performed follows. First we assume that all the three mutants and the wild-type channel constituting the mutant cycle undergo voltage-dependent activation following the same scheme. Each gating scheme is described by 'n' equilibrium parameters whose magnitude as 0 mV are K_1, K_2, …, K_n and all of which have standard exponential voltage-dependence determined by parameters z_1, z_2,…, z_n respectively. For the i^{th} equilibrium constant, the range of values (i.e. the parameter space) is determined to be: $K_i^{\min}$ to $K_i^{\max}$ and similarly the voltage-dependent parameters also have a defined range of values $z_i^{\min}$ to $z_i^{\max}$. In each mutant cycle the model parameters for the wild-type is fixed but those of mutants were randomly selected within the given parameter space. For each mutant in the cycle '2n' random numbers between 0 and 1 (a uniform random number generating function was used) were generated, each of which specifies the extent of perturbation on the equilibrium constants or the voltage-dependence parameters for each. The equilibrium constants of the mutant was assigned as: $K_{i,mut} = K_i^{\min}\left(K_i^{\max}/K_i^{\min}\right)^R$, where R is the random number while the voltage-dependence parameters were assigned as: $z_{i,mut} = z_i^{\min} + R(z_i^{\max} - z_i^{\min})$ (the random numbers used for perturbation of K_i and z_i were independently generated). This process was repeated for all three mutants of the cycle and represents a situation where single and double mutants have multiple effects on channel energetics. The P_OV and QV curves of

the mutants were generated from which ΔG_{app} and ΔG_{net} was extracted. These parameters were then used to compute $\Delta\Delta G_{FMC}$ and $\Delta\Delta G_{GIA}$ for the cycle. This process was repeated for more >600 cycles in two instances – first were the channel and its mutants follow a ZHA activation scheme and second where they follow an MWC activation scheme. This strategy allowed us vigorously test the accuracy of $\Delta\Delta G_{GIA}$ since a large parameter space was sampled.

The parameter range sampled for the simulations performed using the ZHA scheme was: K_1^0: [0.005 – 5000], K_2^0: [0.1 100000], L_0 : [0.01 – 10000], z_1 : [0.5 – 3.5], z_2: [0.5 – 3.5], z_L: [0.25 – 2.5]. The parameters for the wild-type channel was fixed at: K_1^0: 5, K_2^0: 100, L_0 : 10, z_1 : 2, z_2: 1.5, z_L: 0.5 (which are close to the parameters for the Shaker K_V channel reported previously (Zagotta et al., 1994a; Ledwell and Aldrich, 1999)). The parameter space sampled for the simulations performed using the MWC scheme was: J_0 : [0.00001 10], L_0 : [10^{-9} 10^{-3}], D : [1 100], z_J : [0.1 4], z_L : [0.1 2] (D was maintained voltage-dependent in all > 1800 cases). The parameters for the wild-type channel was fixed at: J_0 : 0.03, L_0 : 10^{-6}, D : 25, z_J : 0.6, z_L : 0.3 (which are close to the parameters for the BK channel model reported previously (Horrigan and Aldrich, 2002)).

Molecular Dynamics simulation for generation of a model of a hydrated voltage-sensor

The hydrated model of the voltage-sensor (see Chapter Seven) was generated using molecular dynamics simulations, performed using NAMD (Phillips et al., 2005) with CHARMM 36 force-field parameters. The VSD of the K_V 1.2/2.1 paddle-chimera

structure (PDB-ID: 2R9R, residues 159-310, along with crystallographic waters within 5 Å of the aforesaid region of the protein) was embedded in a POPC membrane, with additional layers of water molecules bathing the bilayer using VMD (Humphrey et al., 1996). After energy minimization (1ns), a 2ns equilibration run was performed during which a harmonic constraint (of spring constant, 1 kcal/mol/$Å^2$) was applied to the protein atoms and the crystallographic water molecules, while the remaining water molecules were kept outside of the membranous space using user defined forces. This allows melting of lipid tails. Subsequently, in a second equilibration run of 2ns, all constraints were eliminated. Next, a 5 ns production run was performed in an NPT ensemble, with the area in the x-y plane maintained constant over the duration of the simulation. In all steps of the simulation, the temperature was maintained at 25°C, periodic boundary conditions were imposed, the time-step of simulation was 1fs and no external electric field was imposed. The model of the VSD shown in Chapter Seven, Fig. 3a, is a snapshot from the last 1 ns of the production run.

CHAPTER THREE

Estimating the voltage-dependent free energy change of ion channels using the median voltage of activation.

INTRODUCTION

Voltage-gated ion channels are integral membrane proteins which, upon sensing a change in membrane electric field open a passage for ions to flux through the membrane. Site-specific mutagenesis has been one of the most commonly used approaches to identify critical residues which are crucial for voltage-dependent activity of these proteins. To understand the mechanisms of ion channel gating and function, it is necessary to obtain an accurate estimate of energetic effects of site-specific mutations. One widely used approach to quantify the perturbation effects of mutations involves measurements of macroscopic ionic currents for a series of voltage steps from which one can derive the relative fraction of open channel at various potentials (P_O-V). These responses show a sigmoidal voltage-dependence and are typically characterized by fitting to a single Boltzmann equation. For such a curve, the chemical free-energy difference between the open and the closed state is defined by $\Delta\overline{G}_C$ which is characterized by two parameters, *z*, the Boltzmann slope and $V_{1/2}$ which is the voltage that elicits the half-maximal response. This free-energy difference is also referred to as the free-energy of channel opening at zero voltage.

The voltage-gated ion channels, however, are known to transit through a number of intermediates to reach their final open states (Cole and Moore, 1960; Vandenberg and Bezanilla, 1991; Bezanilla et al., 1994; Zagotta et al., 1994a; Schoppa and Sigworth,

1998). The slope factor which for a two-state process is the charge translocated, in the case of a multi-state process depends not only on the charge displaced during activation but also on stabilities of the intermediate states (McCormack et al., 1991a; Sigworth, 1993; Bezanilla, 2000; Villalba-Galea et al., 2008). Thus, mutations which affect only the energies of the intermediate states would generate erroneous values of the net free energy difference between the initial closed and the final open states when derived from Boltzmann fits.

Furthermore, when the central pore opens, the channel molecule has already undergone significant conformational transitions as evidenced by separation in the charge-voltage (Q-V) and conductance-voltage (G-V) curves (Armstrong and Bezanilla, 1973; Perozo et al., 1993). Therefore, the free energy associated with the activation process cannot be fully captured from conductance-voltage relationships. Single Boltzmann fits of G-V curves for Shaker potassium ion channel give an estimate of -2 to -3 kcal/mol in the chemical free-energy difference between the open and closed state (Monks et al., 1999; Li-Smerin et al., 2000a; DeCaen et al., 2008). This estimate which corresponds to a single hydrogen bond or salt-bridge interaction is surprising and seems to suggest that a single interaction site could tip the balance between the two states.

Perhaps the most confounding observation is the fact that during activation of Shaker potassium channels, ~14 charges are transferred across the membrane electric field, which translates to an electrical free-energy change of >15 kcal/mol for a 50 mV change in the membrane potential. If the chemical free energy difference between the resting and activated state is 3 kcal/mol, then what happens to the remaining energy? The

process of conversion of electrical energy into a conformational change would thus seem to be very inefficient.

Finally, calculating the free-energy change using single Boltzmann fits becomes even more problematic when mutations result in discernibly multi-phasic P_O-V curves (Li-Smerin et al., 2000b; Yifrach and MacKinnon, 2002). Boltzmann fits to the P_O-V curve also neglects the energetic effect of non-unity values of the maximum open probability, which has been observed in voltage-dependent ion channels (Schoppa et al., 1992). These observations prompted us to carefully analyze the free-energy principles associated with a voltage-dependent process at a theoretical level. Our objective was to derive a more general, physically consistent measure of free-energy change which is easily obtainable from experimental observables and not limited by the two-state assumption inherent to Boltzmann fit derived energy estimates.

In this chapter, we analyzed the fundamental basis of free-energy change in a voltage-dependent system from the standpoint of classical statistical mechanics. The pioneering work of Wyman and colleagues on theoretical thermodynamics has greatly furthered our understanding of ligand binding equilibria (Wyman and Gill, 1990). Of specific interest to us was the concept of median ligand activity. Wyman's elegant derivation shows that from the knowledge of the maximum number of ligands which bind a macromolecule and the median ligand activity one can obtain an accurate estimate of the average ligand binding affinity (Wyman, 1964a, 1967). Here, we adopted a similar approach to analyze the free-energy relationships of voltage dependent ion channels. We found that a comparable parameter, the median voltage of activation, as calculated from QV curve, can be related to the net chemical free-energy change associated with voltage-

dependent activation of these proteins. Specifically, this procedure yielded a value of -14.6 kcal/mol associated with full-scale channel activation of the Shaker potassium channels and -16.1 kcal/mol for the voltage-gated sodium channels. We have discussed several characteristic models of ion channel activation such as those with inactivation, cooperativity, voltage-independent steps, latent charge movement between multiple open states, etc. and illustrate the validity and robustness of our proposed method.

THEORY

Free-energy change in a two state process is obtained from a Boltzmann fit

Consider a voltage-dependent ion channel which can exist in two states – closed (C) and open (O). On increasing the voltage, the open state of the channel becomes increasingly populated. The associated free-energy difference between the closed and open states can be written as: $\Delta\overline{G}_C - qV$, where V is the membrane electric field gradient, $\Delta\overline{G}_C$ is the chemical (non-electrical) free-energy difference between the two states or the free-energy change associated with the transition in the absence of an electrical driving force (V = 0). q is the gating-charge translocated when the ion channel activates and is responsible for an electrical component in the net free-energy change associated with activation. The equilibrium constant for such a transition at any voltage will be: $\frac{P_O}{P_C} = K^0 \exp(qV\beta)$, where P_O and P_C are the fractional occupancy of the open and closed states respectively and K^0 is the voltage-independent component of the equilibrium constant which is related to $\Delta\overline{G}_C$ as, $\Delta\overline{G}_C = -RT \ln K^0$. The voltage-dependent probability of occupancy of the open state, in this situation, will be:

$P_O = \frac{P_O}{P_O + P_C} = \frac{1}{1 + (P_C / P_O)} = \frac{1}{1 + \frac{\exp(-qV\beta)}{K^0}}$. Re-writing K^0 as $\exp(-qFV_{1/2})$, where $V_{1/2}$ (Stevens, 1978)is the voltage at which half of the channels are open, P_O can be re-expressed as:

$$P_O = \frac{1}{1 + \exp\{q(V_{1/2} - V)\beta\}} \quad \text{... (1)}$$

By fitting an experimentally derived, P_O-V curve to Eq. 1, one can derive the parameters of the Boltzmann fit, $V_{1/2}$ and q and thereby estimate $\Delta\overline{G}_C$ as $qFV_{1/2}$. A similar equation can be derived for the gating-charge displacement vs V relation. If a channel can access only two states, the normalized QV and P_O-V curves will superimpose on each other. Also, the Boltzmann slope of the curves will equal the exact number of gating charges displaced during channel activation. Voltage-gated ion channels are however known to transit through a large number of intermediates during activation- the experimentally derived P_O-V and QV curves do not superpose, with the latter almost always preceding the P_O-V curve on the voltage axis. Also the Boltzmann slope of either curves are much lower than the actual amount of gating charge displaced during channel activation (Schoppa et al., 1992; Aggarwal and MacKinnon, 1996; Seoh et al., 1996). Thus it is likely that free-energy estimates of ion channel activation via a Boltzmann fit to activation response are inaccurate.

Area under the QV curve is a measure of the free-energy of activation

Consider that the voltage-gated ion channel exists in N different conformational states, with each state '*i*' associated with a gating-charge (or valence), given by:

$$q_i = \sum_j z_j \lambda_{ji} \quad ...(2)$$

where the summation is over all the charges z_j of the channel protein in state *'i'*, which are informed principally by the charges on the side chains of specific ionizable residues of the protein. λ_{ji} is a state-dependent parameter representing the fraction of the membrane electric field sensed by the j^{th} charge of the protein in the state *'i'* (Stevens, 1978; Roux, 1997). q_i essentially governs the voltage-dependence of the energy of a given conformational state, E_i, i.e.

$$\frac{\partial E_i}{\partial V} = -q_i \quad ...(3)$$

The negative sign in Eq. 3 implies that states with a more positive valence become more stable with increasing voltage.

The average gating-charge of the entire ensemble of conformational states at any given voltage is (Sigworth, 1993):

$$\overline{Q}(V) = \sum_i q_i P_i(V) \quad ...(4)$$

where P_i(V) is the equilibrium occupancy of the i^{th} state at voltage V, which is assumed to follow a Boltzmann distribution. Thus, $P_i = exp(-E_i \beta)/Z$, where $\beta = 1/k_B T$ and Z is the partition function of the system, $Z = \sum_i exp(-E_i \beta)$. The mean free-energy of the ensemble, assuming that temperature is held constant, is:

$$\overline{G} = -k_B T \ln Z \quad ...(5)$$

Changing the electrical potential (V) will alter the distribution of the channel states and thus the mean ensemble free energy. At a constant temperature, differentiating Eq. 5 with respect to voltage gives:

$$\frac{\partial \overline{G}}{\partial V} = \sum_i \frac{\partial E_i}{\partial V} P_i \quad ...(6)$$

Now using Eqs. 3 and 4, the differential change in the free-energy of the system with voltage can be expressed as:

$$\frac{\partial \overline{G}}{\partial V} = -\overline{Q} \quad ...(7)$$

Thus net work done or net change in free-energy of the system as the voltage is changed from V_1 to V_2, can be given by:

$$\Delta \overline{G} = \overline{G}\Big|_{V_1}^{V_2} = -\int_{V_1}^{V_2} \overline{Q} dV \quad ... (8)$$

The gating charge displacement measured when the voltage is switched from a reference voltage (V_{ref}) to a voltage V is essentially the difference: $\overline{Q}(V) - \overline{Q}(V_{ref})$. V_{ref} is usually a hyperpolarizing voltage when all protein charges are retracted to their initial resting configuration and, without any loss of generality, $\overline{Q}(V_{ref})$ can be taken to be 0. Taking V_1 as V_{ref} and using V instead of V_2, Eq. 8 can be integrated by parts giving:

$$\Delta \overline{G} = -(\overline{Q}V)\Big|_{V_{ref}}^{V} + \int_{\overline{Q}(V_{ref})}^{\overline{Q}(V)} V d\overline{Q} \quad ... (9)$$

Suppose, gating charge movement is measured experimentally from a hyperpolarizing reference potential, where all the charges are retracted, to a potential V at which all charge movement saturates. Thus $\overline{Q}(V)$ at highly depolarized voltages is Q_{max}, which makes Eq. 9,

$$\Delta \overline{G} = -Q_{\max} V + \int_0^{Q_{\max}} V d\overline{Q} \quad ...(10)$$

From above, the net free-energy change in the process thus comprises two terms – the first $(-Q_{max}V)$ scales linearly with voltage and the second component ($\Delta\overline{G}_C$) equals the area between the gating-charge displacement vs. voltage (QV) curve and the ordinate (Q) axis. A hypothetical QV curve for a voltage-dependent ion channel is shown in Fig.1a, where the shaded region represents $\Delta\overline{G}_C$. The linear component is the change in the net electrical energy of the system as it undergoes a complete transformation. The second component, unlike its linear counterpart, is convergent and will be shown to lead to an expression for the net change in the chemical free-energy of the system. In the next section we derive a parameter, the median voltage of activation, which is directly related to $\Delta\overline{G}_C$.

The median voltage of activation

Following the definition of median ligand activity proposed by Wyman (1967), we define the median voltage of activation, V_M, as the voltage at which:

$$\int_{-\infty}^{V_M} \overline{Q}dV = \int_{V_M}^{\infty} (Q_{max} - \overline{Q})dV \quad ...(11)$$

Also let Q_M be the gating-charge displacement at V_M.

By definition, $\Delta\overline{G}_C$ is:

$$\Delta\overline{G}_C = \int_0^{Q_{max}} Vd\overline{Q} = \int_0^{Q_{max}} (V - V_M)d\overline{Q} + Q_{max}V_M \quad ...(12)$$

The integral on the right-side of Eq. 11 can be broken down into two integrals:

$$\int_0^{Q_{max}} (V - V_M)d\overline{Q} = \int_0^{Q_M} (V - V_M)d\overline{Q} - \int_{Q_M}^{Q_{max}} (V - V_M)\,d(\overline{Q}_{max} - \overline{Q}) \quad ... (13)$$

Integrating each of the two integrals in Eq. 13, by parts, and using the definition of V_M V_m (Eq. 11) and fact that $\overline{Q}(V_M) = Q_M$, it can be shown that the integral on the right of Eq. 12 is zero. The result is:

$\Delta\overline{G}_C = Q_{\max} V_M$ ... (14)

Fig.1b shows the QV curve intersected by the V = V_M axis, with the two shaded regions being equal in area. The areas on the right and left of the V_M axis correspond to the integrals on the right and left hand side of Eq. 11, respectively. The area of the rectangle shaded in Fig. 1c is equal to the sum of the two areas shaded in Fig. 1a, taking the sign of the latter areas into consideration.

A physical interpretation of $\Delta\overline{G}_C$ and V_M

Thus far, we have shown that the area under an experimentally measured QV curve can be separated into two components - a linear and a saturating (converging) component, both being dependent on the total charge moved between the initial and final states of the system. The saturating component, $\Delta\overline{G}_C$, can be described by a parameter, the median voltage of activation, given by Eq. 11. In this section we will show that $\Delta\overline{G}_C$ is the change in chemical free energy of the system associated with the activation of the system.

Following Eq. 3, the energy of each state of the system can be written as, $E_i = E_i^0 - q_i V$, where E_i^0 is the chemical energy of the i^{th} state. The Boltzmann weight of each of these states can be expressed as, $K_i \exp(q_i V\beta)$, where $K_i = \exp(-E_i\beta)$. We assume that at sufficiently hyperpolarizing voltages, the system occupies just one

(reference) state for which $q_r = 0$ and $E_r^0 = 0$. With this normalization, the Boltzmann weights of the different states become $K_{r\to i}^0 \exp(q_i V\beta)$, where $K_{r\to i}^0$ (= $\exp(-\{E_i - E_r^0\}\beta)$) is the chemical component of the equilibrium constant of the transition from the reference state to state *i*. The partition function of the system is now:

$$Z = \sum_i K_{r\to i}^0 \exp(q_i V\beta) \quad \ldots (15)$$

For our reference state, $K_r^0 = 1$.

Now we turn to Eq. 11 and rewrite it as:

$$\int_{-\infty}^{\infty} \overline{Q} dV = \int_{V_M}^{\infty} Q_{\max} dV \quad \ldots (16)$$

Combining Eqs. 5, 7 and 16, we get:

$$k_B T \int_{-\infty}^{\infty} \frac{\partial \ln Z}{\partial V} dV = \int_{V_M}^{\infty} Q_{\max} dV \quad \ldots (17)$$

or, $k_B T \ln Z\big|_{-\infty}^{\infty} = (\lim_{V\to\infty} Q_{\max} V) - Q_{\max} V_M \quad \ldots (18)$

At hyperpolarizing voltages ($V \to -\infty$), only the reference state will be populated and thus $\lim_{V\to-\infty} \ln Z = 0$. Dividing the equation by k_BT and re-writing Q_{max}Vβ as, ln exp (Q_{max}Vβ), where (k_BT = 1/β), Eq. 18 becomes,

$$\lim_{V\to\infty} \ln\left(\frac{Z}{\exp(Q_{\max} V\beta)}\right) = -\frac{Q_{\max} V_M}{k_B T} \quad \ldots (19)$$

Now, we substitute Z from Eq. 15 into Eq. 19. At very high voltages, all the terms of Z are dominated by the (final) state. Thus,

$$Q_{\max} V_M = -k_B T \ln K_{r\to f}^0 \quad \ldots (20)$$

where $K^0_{r\to f}$ is the chemical component of the equilibrium constant for the transition from the reference state to the final state of the system. Two fundamentally crucial points emerge from this relation. First, $\Delta\overline{G}_C$, which is equal to $Q_{max}V_M$, is thus the measure of chemical free-energy difference between the initial resting state of the system and the final activated state of the system i.e. the free-energy difference between the initial and final states of the system in the absence of any electric field (0 mV). Second, at V_M, the Boltzmann weight of the fully activated state of the system, $K^0_{r\to f}\exp(Q_{max}V_m\beta)$, is 1, which is same as the Boltzmann weight of the reference state (for which the valence is 0). This implies that at V_M, the state(s) where all charge has moved (fully activated) and that where none has moved (fully resting state) are equally populated.

The relations established are independent of the pathway connecting the initial and final states of the system and the number of possible states of the system. Measurement of the QV can thus directly be related to the change in the free energy without elaborate model fitting procedures or assumptions about the nature of the conformational transitions (such as two-state process assumption required by Boltzmann fits). The relations remain valid even when the QV curves show biphasic or asymmetric behavior. It requires the knowledge of Q_{max}, which, at least for the voltage-gated potassium (K_V) channels, is known with reasonable certainty (Schoppa et al., 1992; Aggarwal and MacKinnon, 1996; Seoh et al., 1996). Thus at a first level of approximation, the measurement of the median voltage of activation would facilitate a straightforward and accurate calculation of the free-energy changes associated with the voltage dependent activation of any system.

RESULTS

Accuracy of $Q_{max}V_M$ as a measure of free-energy change

`To compare the free-energy values derived from $Q_{max}V_M$ and the Boltzmann fits for real systems, we experimentally recorded the gating currents in the inactivation-removed Shaker W434F potassium channel construct (Sh-IR W434F) and in the voltage-gated sodium channel ($Na_V1.4$), with the ionic currents blocked with tetrodotoxin (TTX), and evaluated their normalized QV curves (Fig. 2). $V_{1/2}$ for each was obtained by fitting the Boltzmann equation (Eq. 1) while V_m was obtained by calculating the area between the curve and the Q axis (see Methods). Previously published values of Q_{max} for each channel (Schoppa et al., 1992; Hirschberg et al., 1995; Aggarwal and MacKinnon, 1996; Seoh et al., 1996) was used for the free-energy calculations using the median method. We find that the free-energy values computed via the median method were 4-8 times the values computed via the Boltzmann method (Table I).

Occasionally for potassium channels, the sigmoid activation curves have been fitted to a fourth-power Boltzmann equation (Zagotta et al., 1994b; Smith-Maxwell et al., 1998b; Gonzalez et al., 2000, 2001), assuming that identical conformational changes occur in a single step in each of the four identical voltage-sensors, which "move" independent of the other. This fit provides a much closer value of the free-energy change to that obtained from the median method for the Sh-IR W434F but for $Na_V1.4$ the difference between the two estimates continues to be large (Table I). Fitting the QV curve of $Na_V1.4$ to the product of four non-identical Boltzmann terms (which takes into consideration the four non-identical domains of the protein) would be ill constrained. We fitted two other model dependent sigmoidal functions (Perozo et al., 1994; Rodriguez et

al., 1998), both of which resulted in free-energy estimates significantly different from the median method for Sh-IR W434F as well as $Na_V1.4$ (Table I).

For the Shaker potassium channel, elaborate multi-step kinetic models have been proposed by various groups (Bezanilla et al., 1994; Zagotta et al., 1994a; Schoppa and Sigworth, 1998) based on single channel conductances, gating currents and macroscopic ionic currents. Here, we consider the model proposed by Aldrich and colleagues (ZHA model (Zagotta et al., 1994a)).

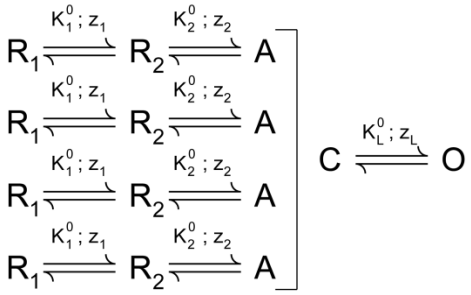

According to this model, each voltage sensor independently activates in two discrete steps (with equilibrium constants K_1 and K_2) and when all the voltage-sensors are activated a concerted transition gates the ion channel pore open (equilibrium constant K_L). All the equilibrium constants have an exponential voltage-dependence: $K_i = K_i^0 \exp(z_i F V \beta)$ (i = 1, 2 or L). The net chemical free-energy change in going from the reference state to the final open state, $\Delta\overline{G}_C$, will be: $-RT \ln\{(K_1^0 K_2^0)^4 K_L^0\}$. (Note the use of R, the universal gas constant, instead of k_B and the inclusion of Faraday constant (F) in the numerical free energy calculations). Using the parameters reported, we find that the free-energy estimate from the ZHA model parameters and the median method are nearly identical (Table II). Next, we considered the ILT mutant of the Shaker potassium channel (Smith-Maxwell et al., 1998a; Ledwell and Aldrich, 1999) which is characteristic in that it results in a QV curve with a secondary phase, widely separated

from the primary (Fig. 2), and thus cannot be fitted to a Boltzmann curve. However the value of chemical free-energy change for this mutant computed using the median method from the numerically simulated QV curve is again almost the same as that obtained from the kinetic model parameters. The fitting exercise described herein, thus shows that the median method is a physically consistent, experimentally feasible method to accurately estimate voltage-dependent energetics in the system.

Free-energy estimation using the median method in the case where certain steps are voltage-independent

Next we consider models of ion channel activation with voltage-independent steps to illustrate how our inferred energetics can be modified by consideration of such transitions. Let us assume that a voltage-independent transition occurs in the middle of a linear transition pathway, involving six states with the final state being the open state O_f (Fig.3a, Scheme I). Since all the steps beyond it are voltage-driven, as we increase the voltage the system will be pushed further and further to the right until it finally saturates in O_f. For this system the chemical free-energy difference between the initial and final states, $\Delta\overline{G}_C$, will be equal to $Q_{max}V_M$ as described previously (Section III, Theory).

To test this numerically, we generated a large number of QV curves, based on this model, for different values of z_2 and $K_3^0 K_3^0$. The former is the voltage-dependence of the equilibrium constant for the second step, and the latter is the equilibrium constant for voltage-independent third step. For this Scheme $Q_{max} = \sum_i z_i$ and thus changing z_2 alters the maximum gating-charge transferred in the process of activation. From each

simulated curve, we computed the median voltage of activation, V_M, by integrating the area between the curve and the ordinate (Q) axis ($\int_0^1 V d\overline{Q}_f$). Plotting $Q_{max}FV_M$ against $\Delta\overline{G}_C$ (Fig. 3b), shows that they are identical to each other and independent of Q_{max}. The surface plot of $\Delta\overline{G}_C$ for varying z_2 and $\log K_3^0$ (Fig. 3c) shows that it has logarithmic dependence on K_3^0 and is independent of z_2. However, V_M shows a logarithmic dependence on K_3^0 but an inverse dependence on z_2 (Fig. 3d). $\Delta\overline{G}_C$, which is the chemical free-energy difference between the final and initial states of the system, will be independent of the magnitude of gating-charge translocated between the two states. For a fixed value of Q_{max} in the system, V_M is linearly related to $\Delta\overline{G}_C$ and both will have a proportional dependence on the equilibrium constants. When Q_{max} is altered without changing any of the equilibrium constants, $\Delta\overline{G}_C$ remains unchanged, but V_m will be altered, since $Q_{max}FV_M = \Delta\overline{G}_C$.

Next, we modify Scheme I by making the last (rather than the middle) step of the pathway voltage-independent (Scheme II, Fig. 4a). Now at saturating depolarization, both the final states, C_5 and O_f will be occupied, their relative occupancies being determined by the voltage-independent equilibrium constant of the last transition (K_5^0). Invoking Eq. 19 for Scheme II, we see that,

$$Q_{\max}V_m = -k_BT \lim_{V\to\infty} \ln\left(\frac{Z}{\exp(Q_{\max}V\beta)}\right) = -k_BT \ln(K^0_{C_1\to C_5} + K^0_{C_1\to O_f}) \quad \ldots (21)$$

Eq. 21 tells us that if the system does not saturate to a single state, $Q_{max}V_M$ reports the change in chemical free-energy in taking the system from its initial reference state to a

saturating condition, which is an ensemble rather than a single state. This brings us to an important point – there are two non-equivalent definitions of free-energy change in the system. One is the change in the free-energy of the ensemble while the other is the free-energy difference between the unique final and initial states of the system ($\Delta\overline{G}_C$, which in this case is: $-k_BT\ln K^0_{C_1\to O_f}$). The former is estimated simply via $Q_{max}V_M$ whereas to estimate the latter, we re-write Eq. 21:

$$Q_{\max}V_M = -k_BT\left\{\ln K^0_{C_1\to O_f} - \ln\left(\frac{K^0_5}{1+K^0_5}\right)\right\} \quad \ldots (22)$$

If K^0_5 is not large, then the second logarithmic term in Eq. 22 would have a non-vanishing contribution to the overall equation. In this situation, however, $P_O^{\max}$ will be equal to $K^0_5/(1+K^0_5)$. This gives:

$$\Delta\overline{G}_C = Q_{\max}V_M - k_BT\ln P_O^{\max} \quad \ldots (23)$$

Thus when the final step is voltage independent, the knowledge of the maximum open probability, along with Q_{max} and V_M, would let us estimate the net free-energy change associated with the transferring the channel from its initial state C_1 to its final state O_f.

We illustrate this point through numerical simulations. We calculated the V_M for a number of QV curves, based on Scheme II, using different values of K^0_5 and plot $Q_{max}FV_M$ against $\Delta\overline{G}_C$ (Fig. 4b). In each case we also calculated $P_O^{\max}$ (Fig. 4c). Fig. 4b shows that for large values of K^0_5, $Q_{max}FV_M$ and $\Delta\overline{G}_C$ are identical and $-RT\ln P_O^{\max} \sim 0$ (since $P_O^{\max} \sim 1$). This is expected since, under these conditions, the final saturated state of the ensemble is populated by a single state so that the change in the chemical

free-energy of the ensemble and the chemical free-energy difference between the final and the initial state are equivalent. For smaller values of K_5^0, where $P_O^{\max} < 1$, these two free-energy measures are different and the value of $-RT \ln P_O^{\max}$ increases as the difference between the two free-energy quantities.

Next, we consider Scheme III, which is a 6 state linear model with two final open states, the transition between them being voltage-independent (Fig. 4a). For this case, the $Q_{max}V_M$ measure is equal to:

$$Q_{\max}V_M = -k_BT \ln (K^0_{C_1 \to O_1} + K^0_{C_1 \to O_f}) \quad \text{... (24)}$$

This Scheme yields $P_O^{\max} = 1$ and $Q_{max}V_M$ will be the free-energy change of the ensemble but not the chemical free-energy difference between the first and last states ($-k_BT \ln K^0_{C_1 \to O_f}$). Unlike our previous case (terminal voltage-independent step between a closed and open state), here, the two free-energy measures cannot be distinguished using $P_O^{\max}$ values.

Effects of cooperativity and ion channel inactivation

In the models considered thus far the median measure of the chemical free-energy change of the system correlates well with the model based estimates. To further check and validate these correlations we performed numerical simulations on an allosteric model of ion channel activation. Such models have been used with success to understand the voltage-dependent gating of the BK channels (Horrigan and Aldrich, 1999, 2002). We use an MWC model (Monod et al., 1965a) for our simulations here.

Consider Scheme IV, a 10 state MWC model of ion channel activation as shown in Fig. 5a. The channel is assumed to comprise 4 identical voltage-sensing modules and a single pore domain. K_V is the equilibrium constant of activation of each of the 4 voltage-sensing modules while K_P is the equilibrium constant of the pore-opening transition. Both the equilibrium constants are assumed to have an exponential voltage-dependence: $K_i = K_i^0 \exp(z_i FV\beta)$, ($i$ = V, P) where z_i reflects the voltage-dependence of each transition and K_i^0 is the chemical component of the equilibrium constant of each transition. This model is different from those discussed previously, in part, due to the presence of multiple open states with different valences which will manifest itself as a latent charge movement between the open states (Sigg and Bezanilla, 1997). θ is the cooperativity parameter which represents the facilitation experienced by the pore-opening process due to activation of a voltage-sensor and vice-versa. θ is assumed to be voltage-independent. In this Scheme, if all the steps are voltage-dependent, the system will start from state C_1 at hyperpolarizing voltages and end in state O_f at highly depolarizing voltages. The chemical free-energy difference between the states C_1 and O_f, $\Delta\overline{G}_C$, will be given by $-RT\ln\{(\theta K_V^0)^4 K_P^0\}$.

We generated a number of QV curves for this Scheme with different values of z_V and θ when z_P is not zero. The free-energy change calculated from median voltage of activation in each case was compared to $\Delta\overline{G}_C$. Q_{max} for this Scheme is $4z_V + z_P$. The plot of $Q_{max}FV_M$ against $\Delta\overline{G}_C$ (Fig. 5b) shows that, as long as the pore opening transition is voltage-dependent ($z_P \neq 0$), the two free-energy measures are equal, dependent on θ but independent of Q_{max}. This illustrates that the presence of multiple open states or latent

charge movement between the open states does not limit the applicability of the median method to estimate the chemical free-energy change.

When the pore-opening process is voltage-independent, at saturating voltages both states C_f and O_f will be populated, their relative proportions being determined by the magnitude of the equilibrium constant: $K_P^0\,\theta^4$. In addition at hyperpolarizing voltages, both the states C_0 and O_0 will be populated, their relative proportions being determined by K_P^0. Thus at both hyperpolarized and depolarized conditions, the system does not exist in a unique state but rather in an ensemble of states. From Eq. 18 and assuming C_0 to be our reference state, we see that:

$$\mathbf{Q_{max}V_M} = -\mathbf{k_BT\ln Z}\Big|_{-\infty}^{\infty} + (\lim_{\mathbf{V}\to\infty}\mathbf{Q_{max}V}) = -\mathbf{k_BT\ln}(\mathbf{K^0_{C_0\to C_f}} + \mathbf{K^0_{C_0\to O_f}}) + \mathbf{k_BT\ln}(1 + \mathbf{K^0_{C_0\to O_0}}) \ldots (25)$$

In terms of the model parameters for Scheme IV, the above equation may be re-written as:

$$Q_{\max}V_M = -k_BT\ln\{K_P^0\,(K_V^0\theta)^4\} - k_BT\ln\left(1+\frac{1}{K_P^0\,\theta^4}\right) + k_BT\ln(1+K_P^0) \quad \ldots (26)$$

For such an MWC model, $P_O^{\max}$ at highly depolarized voltages will be $K_P^0\,\theta^4/(1+K_P^0\,\theta^4)$ while at very low hyperpolarizing voltages, $P_O^{\min}$ will be $K_P^0/(1+K_P^0)$. Using these definitions in Eq. 26 we obtain:

$$\Delta\overline{G}_C = Q_{\max}V_M - k_BT\ln P_O^{\max} + k_BT\ln(1-P_O^{\min}) \quad \ldots (27)$$

For illustration purposes, we compared numerically simulated values of $Q_{max}FV_M$ and $\Delta\overline{G}_C$ in the case when the pore-opening is voltage-independent (i.e. $z_P = 0$) at different values of the model parameters. When K_P^0 is small (thus $P_O^{\min} \sim 0$), and θ is

large, $P_O^{\max} \sim 1$ and the two free-energy measures are equal (Fig. 5C). For smaller values of θ adding the correction factor $-RT\ln P_O^{\max}$ to $Q_{max}FV_M$ gives us $\Delta\overline{G}_C$. Alternatively, when both θ and K_P^0 are large (thus $P_O^{\min}$ is significant), the deviation between the two free-energy measures can be accounted for by the correction factor, $RT\ln(1-P_O^{\min})$ (Fig. 5D). Thus, using the median measure along with the appropriate correction factors, the chemical free-energy difference between the terminal states can be estimated for systems undergoing voltage-dependent activation following an MWC scheme of activation.

We finally consider the case of channels which undergo inactivation on sustained depolarization (Fig. 6a, Scheme V). The system can be modeled by considering that there are 3 specialized units $\boldsymbol{V}$, $\boldsymbol{P}$ and $\boldsymbol{I}$, each capable of existing in two conformations. Conformational change of $\boldsymbol{V}$ ($\boldsymbol{V_R}$ to $\boldsymbol{V_A}$) governs the initial voltage-sensing steps of the channel, that of P ($\boldsymbol{P_C}$ to $\boldsymbol{P_O}$) is the gate opening transition and that of $\boldsymbol{I}$ ($\boldsymbol{I_R}$ to $\boldsymbol{I_A}$) controls the inactivation process. Scheme IV has 12 parameters. This cubic model of an inactivating channel can be represented as a nested coupled model as depicted in Fig. 6b. Each of three structural units has an intrinsic activation constant described by a voltage independent component, K_i^0, and voltage-dependence z_i (where i is V, P or inact). Additionally there are three coupling parameters θ_{VP}, θ_{PI} and θ_{IV}, which are voltage-independent and depict the pairwise interactions between the structural units. Each of the 12 parameters of the cubic model (Fig. 6a) can be uniquely related to the parameters of Fig. 6b using the principle of microscopic reversibility.

If all the equilibrium constants in this model have a positive voltage-dependence, then at highly depolarizing voltages the system will saturate in the state $\boldsymbol{V_A P_O I_A}$ while at

very low voltages only the initial reference state, $\boldsymbol{V_R P_C I_R}$, will be populated. $Q_{max}V_m$ (V_m being obtained from the QV curve) will thus be the chemical free-energy difference between the initial and final states of the system.

Next, assume that the inactivation process is voltage-independent. As a result all the equilibrium constants between two connected states differing in the conformation of $\boldsymbol{I}$ (in Fig. 6a) will be voltage-independent i.e. K_9, K_{10}, K_{11} and K_{12} do not change with voltage. Since all other transitions are voltage-dependent, both states $\boldsymbol{V_A P_O I_R}$ and $\boldsymbol{V_A P_O I_A}$ will be populated at depolarized potentials and at very low voltages, both $\boldsymbol{V_R P_C I_R}$ and $\boldsymbol{V_R P_C I_A}$ will exist. This situation is similar to our description of the MWC model, with voltage-independent pore opening transitions, in that multiple states are populated at both hyperpolarized and depolarized voltages.

Thus, Eq. 18 here transforms to:

$$-k_B T \ln\left(\frac{K_1^0 K_2^0 + K_1^0 K_2^0 K_{11}^0}{1 + K_{10}^0}\right) = Q_{\max} V_M \quad \text{... (28)}$$

Even in this scenario, $Q_{max}V_M$ is the change in the chemical free-energy of the ensemble but not the chemical free-energy difference between a unique final and initial states of the system, $\Delta\overline{G}_C$. The latter will be equal to: $-k_B T \ln(K_1^0 K_2^0 K_{11}^0)$. The relation between the two measures of free-energy can be expressed as:

$$Q_{\max} V_M = \Delta\overline{G}_C - k_B T \ln\left\{\frac{1 + K_{11}^0}{K_{11}^0 (1 + K_{10}^0)}\right\} \quad \text{... (29)}$$

The maximum fraction of inactivating channels (I_{max}) in this system, at depolarizing voltages, is $K_{11}^0/(1 + K_{11}^0)$. In most inactivating ion channels, inactivation is coupled to activation which would mean that $K_{11}^0 >> K_{10}^0$. Thus, Eq. 29 can be re-expressed as:

$$\Delta\overline{G}_C = Q_{\max}V_M - k_BT \ln I_{\max} \quad \ldots (30)$$

Eq. 27 is very similar to the relation which we derived for the case when the terminal voltage-dependent opening transition of a non-inactivating ion channel is voltage-insensitive (Eq. 23, Scheme II). The difference between $\Delta\overline{G}_C$ and $Q_{max}V_M$ is small when I_{max} is close to unity and continues to increase with decreasing values of I_{max}. These points are illustrated through simulations performed using Scheme V. $Q_{max}FV_M$ is plotted against $\Delta\overline{G}_C$ for different values of K^0_{inact} in two situations – when inactivation is voltage-dependent and when it is voltage-independent (Fig. 6c). In the former case, they are equal, while in the latter case they are equal only at relatively large values of K^0_{inact}, where $I_{max} \sim 1$ (Fig. 6d). Thus our overall proposition that $Q_{max}FV_M$ is the chemical free-energy of the ensemble remains valid even in inactivating channels.

DISCUSSION

In summary, we have derived a general expression for the change in the chemical free-energy change associated with the activation of a voltage-dependent ion channel, $\Delta\overline{G}_C$: $\Delta\overline{G}_C = Q_{\max}FV_M$, where Q_{max} is the maximum amount of gating charge displacement, F is the Faraday constant and V_M is the median voltage of activation estimated from a QV curve. V_M is mathematically defined by Eq. 11. It is the voltage where the area bounded by the Q-V curve, V_M axis and Q = 0 axis becomes equal to that bounded by the QV curve, V_M axis and the $Q = Q_{max}$ axis as depicted pictorially in Fig. 1b. We have considered various classes of models with cooperativity, voltage-independent transitions, multiple open states and latent charge movement etc. and

discussed the measures of free-energy change in each case. We demonstrate that the V_M measure of free-energy change is independent of the nature of the transition pathway and of the symmetry relations within the protein (i.e. whether parts of them are identical or not). In some instances where initial or terminal steps of the transition pathway are voltage-independent, certain correction factors need to be added to the V_M measure to calculate the free-energy difference between the first and last state of the channel. General relations between the median estimates of free-energy changes and the chemical free-energy differences between the first and last states of the system in six broad classes of ion channel gating models are listed in Table III.

Although these relations are fairly general their application to understand the energetic relationships in ion channels should be performed with careful deliberation of the assumptions on the basis of which the relations are derived and the behavior of the specific system of interest. The median estimate of free-energy is no substitute for full quantitative models of channel gating. However, it might serve as a useful check/constraint of the parameters for details models of ion channel gating. Also this measured free-energy change includes free-energy contributions from the intrinsic stabilities of the different structural units as well as interactions between them. Parsing out these individual components via measurement of QV curves alone is not straightforward and might require the application of site-specific measurements along with more detailed analyses.

The median voltage of charge movement (V_M) is a more accurate and physically meaningful free-energy correlate than $V_{1/2}$. The two parameters will be identical when the QV curve is symmetric but the difference between them can be easily appreciated in

cases where the QV curve is non-symmetric and/or shows multiple phases (Perozo et al., 1994; Ledwell and Aldrich, 1999; Tao et al., 2010; Lacroix and Bezanilla, 2011). We estimate that the chemical free-energy change for the Shaker potassium channels is ~ -14kcal/mol which suggests that most electrical energy is being efficiently utilized to drive conformational change in the ion channel.

An alternate way to understand the principle of median transformation, is to consider the slope of the QV curve (generally referred to as the slope function) in a voltage-dependent channel. The total gating-charge translocated over a voltage range can be written as:

$$\overline{Q} = \int_{-\infty}^{V} \frac{\partial \overline{Q}}{\partial V} dV \quad \ldots (31)$$

Similarly we can write:

$$Q_{\max} V_M = \int_{-\infty}^{\infty} V \frac{\partial \overline{Q}}{\partial V} dV \quad \ldots (32)$$

We divide both the equations with Q_{max}, noting that fractional gating charge moved, $\overline{Q}_f$, is $\overline{Q} / Q_{\max}$. As a result, we land up with the following pair of equations:

$$\int_{-\infty}^{\infty} \frac{\partial \overline{Q}_f}{\partial V} dV = 1 \ldots (33)$$

and

$$\int_{-\infty}^{\infty} V \frac{\partial \overline{Q}_f}{\partial V} dV = V_M \ldots (34)$$

The important consequence of Eqns. 33 and 34, is that, since $\frac{\partial \overline{Q}_f}{\partial V}$ is continuous and differentiable and its infinite limit integration over voltage is unity, it represents a

probability density function (pdf) and the median voltage is mean of the pdf. More interestingly, it can be realized that the $V_{1/2}$ (the voltage at which half of all the gating-charges have moved) is:

$$\int_{-\infty}^{V_{1/2}} \frac{\partial \overline{Q}_f}{\partial V} dV = 0.5 \quad \text{... (35)}$$

which is the definition of the median of a pdf. Thus (by Eq. 35) $V_{1/2}$ of the QV curve is the median of the pdf and V_M of the QV curve (by Eq. 34) is the mean of the pdf. In a similar manner, $\ln x_m$ can be shown to be the mean of the pdf describe by the slope of the fractional ligand binding curve and $\ln x_{1/2}$ is the median of the pdf. These pdfs (the slope functions) encapsulate several thermodynamic details, for example about cooperativity (Di Cera et al., 1988; Di Cera and Chen, 1993), and are beyond the scope of our current discussion.

Our derivations establish QV as the direct free-energy correlate of the free-energy change in a voltage-dependent system. In many instances, P_O-V curves have been used to obtain empirical estimates of free-energy of activation of voltage-dependent ion channels (Monks et al., 1999; Li-Smerin et al., 2000a; Hackos et al., 2002; Yifrach and MacKinnon, 2002; Sadovsky and Yifrach, 2007). Such energy measures are substantially different from those proposed in this study. Operationally, a P_O-V based estimate of the free-energy change can be interpreted as the free-energy difference between the ensemble of closed states of the system at the threshold voltage of pore opening and the final ensemble of open states. This also implies that a P_O-V curve does not fully capture the activation energetics of a voltage-dependent ion channel which activates in multiple steps.

On a final note it must be mentioned that, in a case where the Q_{max} of a channel is not measured, the energetic effect of a mutation on the activation energetics can be

enumerated via the V_M of its QV curve alone, under the assumption that Q_{max} is unaltered by the mutation. If the QV curve of the mutant channel is symmetric, $V_{1/2}$ might be used instead of V_M (both will be identical). This implies that considering the Boltzmann slope in the energy terms introduces a theoretical anomaly in the expression for the change in free-energy in cases beyond the realm of a two-state approximation. Therefore when Q_{max} is not measured an empirical estimate of the energetic effect of a mutation on the voltage-gated ion channel can be assessed simply via comparison of the V_M value of its QV curve with that of a control (Soler-Llavina et al., 2006; Gagnon and Bezanilla, 2010; Muroi et al., 2010; Xu et al., 2010). The obvious caveats to this approach are cases where mutations affect Q_{max}. In such scenarios, to quantify the magnitude of energetic perturbation, apart from the QV curve, Q_{max} for each charge altering mutation needs to be measured separately.

CHAPTER CONTENT

Significant portions of this chapter (text, figures and tables) are adapted from: "Chowdhury, S., and Chanda, B., *Estimating the voltage-dependent free energy change of ion channels using the median voltage for activation.* The Journal of General Physiology, 2012, 139(1):3-17"

FIGURES

Figure 1 Free-energy measures from a QV curve

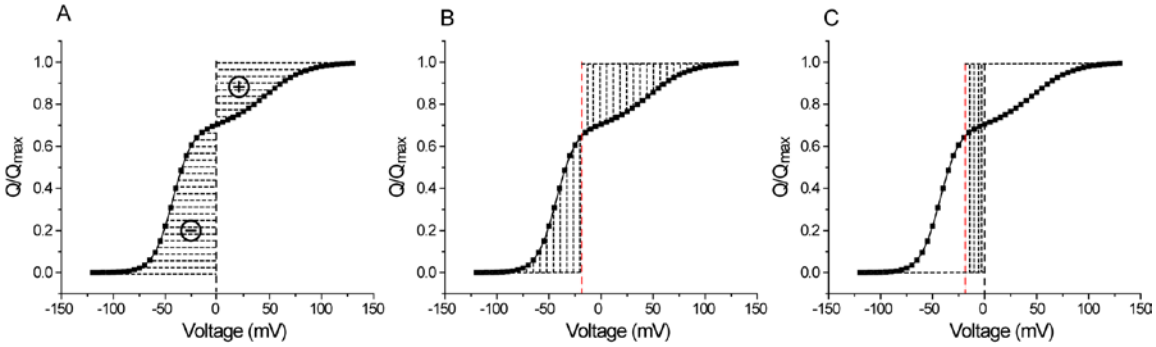

(A) A hypothetical normalized QV curve. The vertical dashed line is the V = 0 axis. The shaded area is the integral: $\int_0^1 V\, d\overline{Q}_f$ ($\overline{Q}_f = \overline{Q}/Q_{\max}$), which equals $\Delta\overline{G}_C / Q_{\max}$. The integral is negative on the left of the V = 0 axis and positive on the right, as indicated by the '–' and '+' signs. **(B)** The same QV curve with the median voltage of charge movement (V_M) marked by the vertical dashed lines. The areas on either side of the V_M axis are equal and are both positive. **(C)** The QV curve intersected by the V = 0 and V = V_M axes. The area of the shaded rectangle is equal to the sum of the two areas shaded in (A), taking their respective signs into consideration.

Figure 2 QV curves of the Shaker potassium channel and the rNav 1.4 channel.

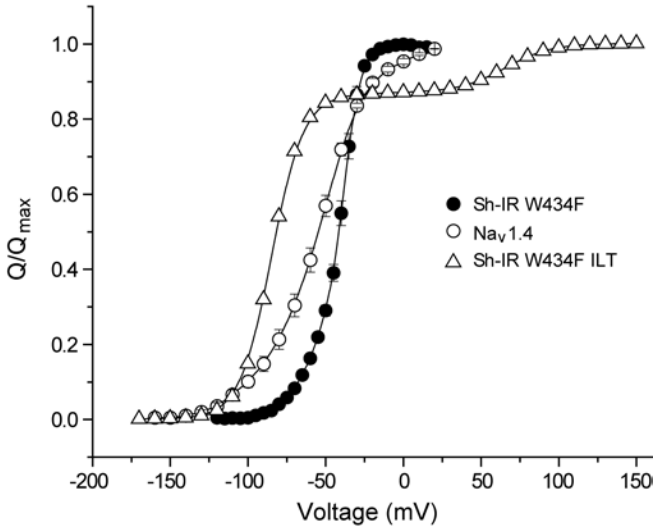

Normalized QV curves for Sh-IR W434F and $Na_V1.4$. Each curve is an average of independent measurements from 5 oocytes. The normalized QV curve for the ILT mutant was simulated according to the kinetic model proposed by Aldrich and colleagues (Ledwell and Aldrich, 1999)

Figure 3 Effect of an intermediate voltage-independent step on the free-energy estimates

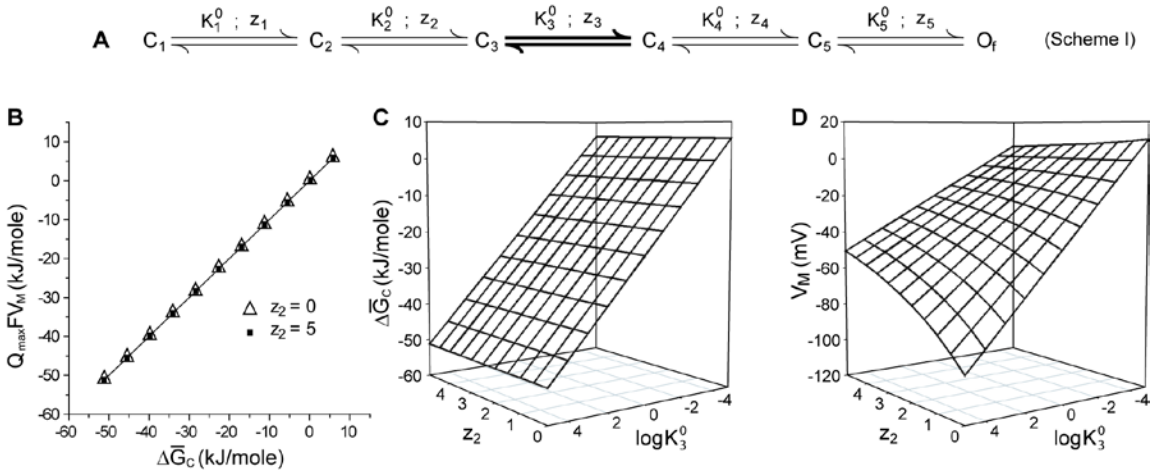

(A) A 6 state linear model of activation of a voltage-dependent ion channel with 5 closed state and a single final open state. The voltage-dependence of the equilibrium constants is given by: $K_i = K_i^0 \exp(z_i F V \beta)$ (i=1, 2, 3, 4, or 5), where K_i^0 is the chemical component of the equilibrium constant K_i and z_i is its voltage-dependence. The third step (shown in bold) is voltage-independent and thus $z_3 = 0$. $\Delta\overline{G}_C$ is the sum of the chemical free-energy change of each of the steps and will equal: $-RT \ln \prod_{i=1}^{5} K_i^0$ **(B)** $Q_{max}FV_M$ is plotted against $\Delta\overline{G}_C$ for different values of log K_3^0 (-5 to +5) and 2 values of z_2 (filled squares: $z_2 = 5$ and open triangles: $z_2 = 0$). The remaining parameters of the model were arbitrarily chosen as: $K_1^0 = 1$; $K_2^0 = 75$; $K_4^0 = 25$; $K_5^0 = 5$; $z_1 = 2$; $z_3 = 0$; $z_4 = 2.5$; $z_5 = 1$. **(C)** and **(D)** Variation of $\Delta\overline{G}_C$ (C) and V_M (D) with changing values of z_2 (0 to 5) and log K_3^0.

Figure 4 Effect of terminal voltage-independent steps on the free-energy estimates

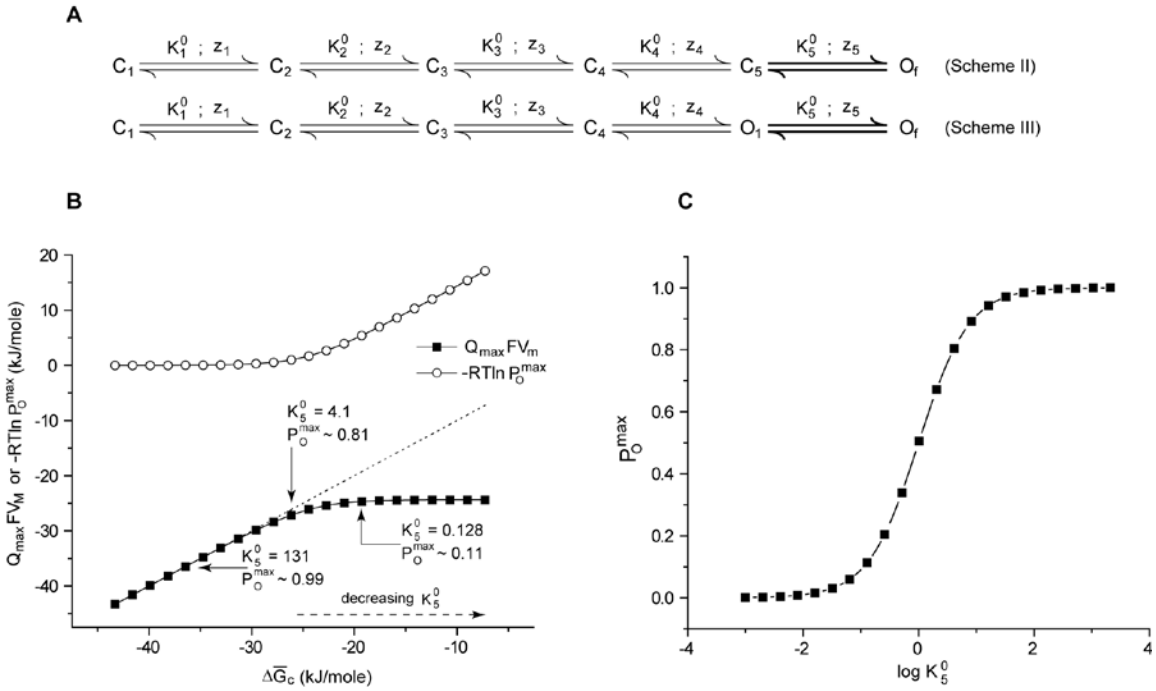

(A) Two 6 state linear Schemes of voltage-dependent activation of a channel. In both Schemes, except for the final transition (in bold), all other steps are voltage dependent. Scheme II has 1 open state while Scheme II has 2 open states. The voltage-dependence of each of the equilibrium parameters in Schemes II and III are defined similar to those in Scheme I. For Schemes II and III, z_5 = 0. **(B)** Results of the numerical simulations performed using Scheme II. K_3^0 = 10; z_2 = 1.5; z_3 = 1; z_5 = 0. Remaining parameters were same as those in Scheme I. K_5^0 was varied from 0.001 to 2097.15. Relation between the free-energy difference between the initial and final states, $\Delta\overline{G}_C$, ($-RT\ln\prod_{i=1}^{5}K_i^0$) and the free-energy change in the ensemble, $Q_{max}FV_M$ (filled symbols) and $-RT\ln P_O^{max}$ (open symbols), for different values of K_5^0. Adding

$Q_{max}FV_M$ and the correction factor, $-RT\ln P_O^{max}$, gives $\Delta\overline{G}_C$, as depicted by the dashed line. **(C)** P_O^{max} values calculated at different values of K_5^0 for Scheme II.

Figure 5 Influence of latent charge movement and cooperativity on inferred energetics

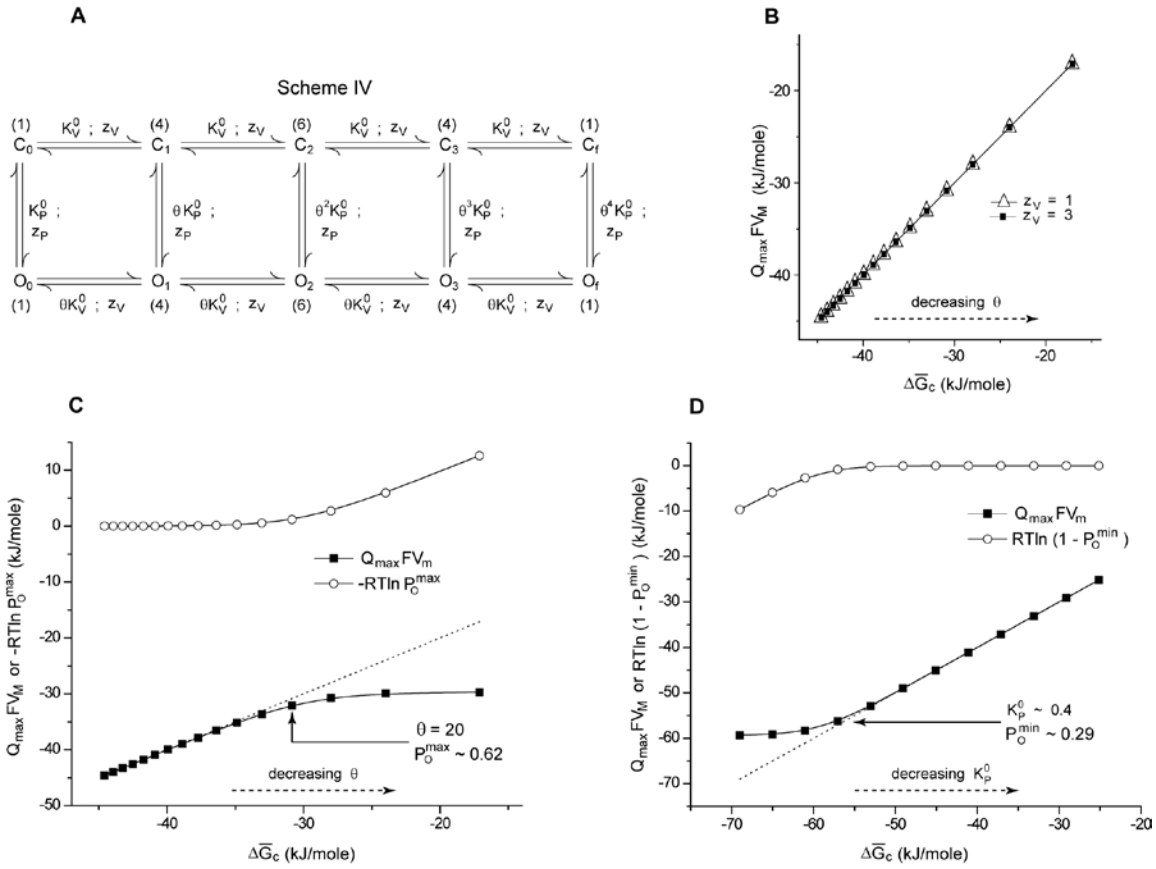

(A) A 10 state MWC cooperative scheme of voltage-dependent ion channel activation. The channel comprises of 4 identical voltage-sensing modules and one pore domain, each capable of existing in two conformations. States C_i and O_i differ in the conformational status of the pore domain, while the different C_is and O_is differ among each other in the number of activated voltage-sensing modules (i = 0,1,…,4). Activation of the each of the voltage-sensors facilitate the opening transition of the pore and vice-versa. The number alongside each state indicates its multiplicity. The voltage-dependence of the equilibrium constant for activation of the pore and voltage-sensors follow the relation: $K_i = K_i^0 \exp(z_i F V \beta)$ (i = V, P). **(B)** Plot of $Q_{max}FV_M$ against $\Delta\overline{G}_C$ for different values

of θ (varied between 5 and 80) and 2 values of z_V (open triangles: z_V = 1 and filled squares: z_V = 3). The other model parameters were chosen to be: K_V^0 = 20, K_P^0 = 10^{-5}, z_P = 1.5. Different values of z_V leads to different latent charge movement. **(C)** Plot of $Q_{max}FV_M$ and $-RT\ln P_O^{max}$ against $\Delta\overline{G}_C$ for different values of θ (varied between 5 and 80) when z_P = 0. The arrow mark shows the value of θ and P_O^{max} beyond which $\Delta\overline{G}_C$ and $Q_{max}FV_M$ deviate. For these simulations, K_V^0 = 20, K_P^0 = 10^{-5} and z_V = 3. P_O^{min} in each case was ~ 0. Adding $Q_{max}FV_M$ and the correction factor, $-RT\ln P_O^{max}$, gives $\Delta\overline{G}_C$, as depicted by the dashed line. **(D)** Plot of $Q_{max}FV_M$ and $-RT\ln(1-P_O^{min})$ against $\Delta\overline{G}_C$ for different values of K_P^0 (varied between 10^{-5} and 50) when z_P = 0. The arrow mark shows the value of K_P^0 and P_O^{min} below which $\Delta\overline{G}_C$ and $Q_{max}FV_M$ deviate. For these simulations, K_V^0 = 20, θ = 20 and z_V = 3. P_O^{max} in each case was ~ 1. Adding $Q_{max}FV_M$ and the correction factor, $-RT\ln(1-P_O^{min})$, gives $\Delta\overline{G}_C$, as depicted by the dashed line.

Figure 6 Influence of inactivation on the median estimate of free-energy change

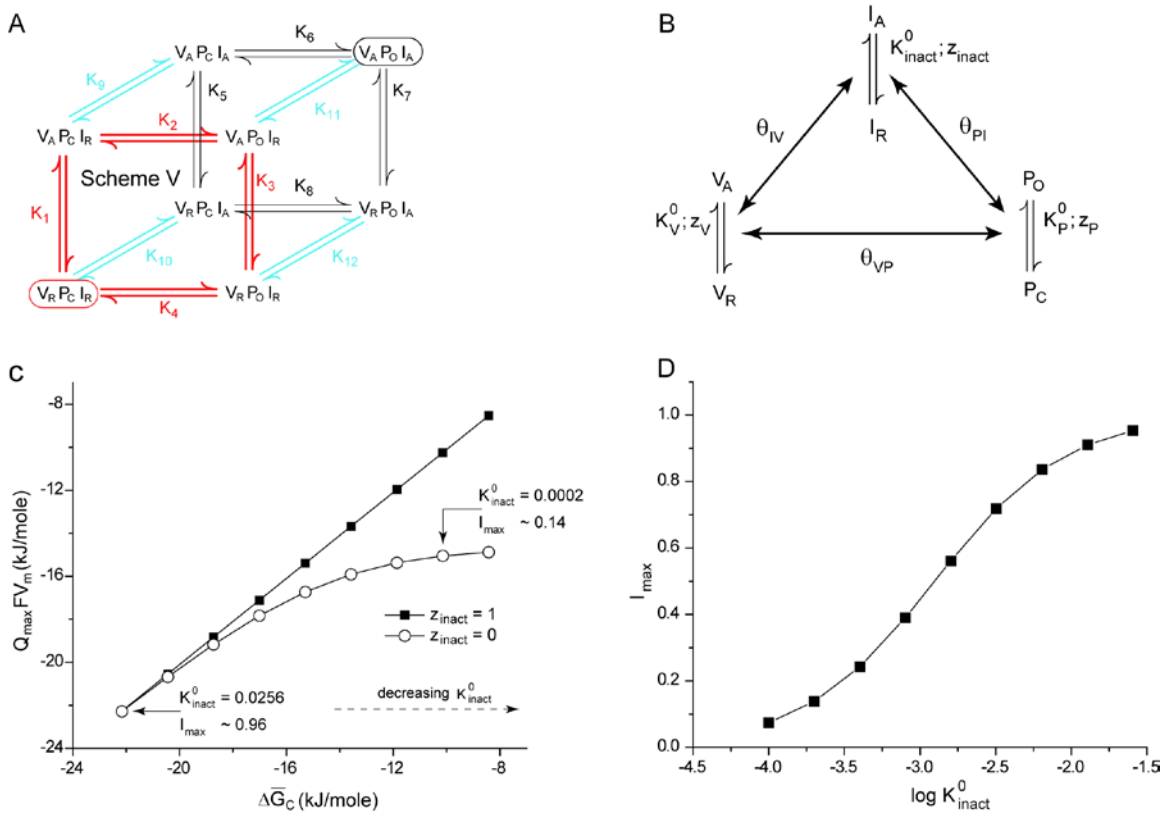

(A) An 8 state model for an inactivating channel. The encircled states represent the initial reference state ($\boldsymbol{V_R P_C I_R}$, red) and the final state ($\boldsymbol{V_A P_O I_A}$, black) of the system. In the final state all the units of the system are in their activated/open conformations while the reference state all are in their resting/closed conformations. The equilibrium constants are assumed to have an exponential voltage dependence, $K_i = K_i^0 \exp(z_i F V \beta)$, ($i$ = 1, 2, …, 12). **(B)** An equivalent nested coupled model of inactivation. The conformational transitions in each of the structural units are $K_i = K_i^0 \exp(z_i F V \beta)$, where i is V, P or inact. The pairwise coupling parameters, θ_{VP}, θ_{PI} and θ_{IV}, denote the voltage-independent coupling between units ***V*** and ***P***, ***P*** and ***I*** and ***I*** and ***V*** respectively. The parameters of the cubic model can be related to those of the nested model. For instance,

$K_{10} = K_{inact}$ and $K_{11} = K_{inact}\theta_{PI}\theta_{IV}$. **(C)** Plot of $Q_{max}FV_m$ against $\Delta\overline{G}_C$ for different values of K_{inact}^0 (varied between 0.0001 to 0.0256) and 2 values of z_{inact}. The remaining parameters were arbitrarily chosen to be: $K_V^0 = 75$, $K_P^0 = 1$, $\theta_{VP} = 5$, $\theta_{PI} = 8$, $\theta_{IV} = 100$, $z_V = 3$, $z_P = 1$.

$$\Delta\overline{G}_C = -RT \ln K^0_{V_R P_C I_R \rightarrow V_A P_O I_A} = -RT \ln (K_1^0 \, K_2^0 \, K_{11}^0) = -RT \ln (K_V^0 \, K_P^0 \, K_{inact}^0 \theta_{VP} \, \theta_{PI} \, \theta_{IV})$$

(D) Maximum fraction of inactivated channels at depolarizing voltages for different values of K_{inact}^0.

Table I Estimation of free-energy change from QV.

Fitting Function	Para-meter	Shaker-IR		rNa$_V$1.4	
		Val.	$\Delta\bar{G}_C$	Val.	$\Delta\bar{G}_C$
$\frac{1}{1+\exp\{zF(V_{1/2}-V)\beta\}}$ [a]	$V_{1/2}$	-45.9	-3.2	-56.5	-1.8
	z	3.03		1.4	
$\frac{1}{[1+\exp\{zF(V_{1/2}-V)\beta\}]^4}$ [b]	$V_{1/2}$	-64.6	-13.9	-97.2	-9.6
	z	2.35		1.08	
$\frac{1}{z_1+z_2}\left(\frac{z_1}{1+\exp\{z_1F(V_{1/2}^{(1)}-V)\beta\}}+\frac{z_2}{1+\exp\{z_2F(V_{1/2}^{(2)}-V)\beta\}}\right)$ [c]	$V_{1/2}^{(1)}$	-58.2	-7.1	-71.6	-3.9
	z_1	1.99		1.1	
	$V_{1/2}^{(2)}$	-42.4		-49.6	
	z_2	4.5		1.85	
$\frac{1}{z_1+z_2}\left(\frac{z_1\exp(z_1F(V_{1/2}^{(1)}-V)\beta+(z_1+z_2)\exp[\{z_1V_{1/2}^{(1)}+z_2V_{1/2}^{(2)}-(z_1+z_2)V\}F\beta]}{1+\exp(z_1F(V_{1/2}^{(1)}-V)\beta)+\exp[\{z_1V_{1/2}^{(1)}+z_2V_{1/2}^{(2)}-(z_1+z_2)V\}F\beta]}\right)$ [d]	$V_{1/2}^{(1)}$	-56.6	-6.4	-71.0	-3.6
	z_1	2.02		1.15	
	$V_{1/2}^{(2)}$	-42.6		-48.2	
	z_2	3.89		1.58	
$F\int_0^{Q_{max}} VdQ = Q_{max}FV_M$ [e]	V_M	-46.8	-14.6	-56.3	-16.5
	Q_{max}	13.6		12.8	

The table lists the different functions used to fit the QV curve and the values of the corresponding parameters derived from the fits to the QV curves of the Sh-IR W434F and Na$_V$1.4 channels. $V_{1/2}$ parameters have units in mV and z parameters have units of electronic charges. The free-energy changes ($\Delta\bar{G}_C$) calculated from each of the fits are also listed (kcal/mol). **[a]** A simple two state model and the fitting function is a Boltzmann function. **[b]** A model where the channel activates in 4 independent single-step transitions – the fitting function is the 4th power of the Boltzmann function and $\Delta G_C = 4zFV_{1/2}$. **[c]** A model where the channel activates via two energetically independent steps – the fitting function is the sum of two Boltzmann terms and $\Delta G_C = z_1FV_{1/2}^{(1)} + z_2FV_{1/2}^{(2)}$. **[d]** A three state model where the channel activates in two sequential steps - $\Delta G_C = z_1FV_{1/2}^{(1)} +$

$z_2 FV_{1/2}^{(2)}$. [e] The free-energy change calculated via the median method of channel activation. The Q_{max} values for each channel was obtained from previously published literature (Schoppa et al., 1992; Hirschberg et al., 1995; Aggarwal and MacKinnon, 1996; Seoh et al., 1996).

Table II Comparison of free-energy estimates from kinetic models and median method.

Channel	K_1^0	z_1	K_2^0	z_2	K_L^0	z_L	$\Delta G_C = -RT \ln\{(K_1^0 K_2^0)^4 K_L^0\}$	Q_{max}	V_M (mV)	$Q_{max} F V_M$
Sh-IR	3	1.8	132.07	1.4	12	0.4	-15.58 kcal/mol	13.2	-46.8	-14.19 kcal/mol
ILT	74.67	1.7	466.67	1.3	0.014	1.8	-22.17 kcal/mol	13.8	-67.4	-21.37 (kcal/mol)

The table lists the parameters of the ZHA model for the Sh-IR channel and the ILT mutant. V_m value for the ILT mutant was calculated from the QV curve, generated using the model parameters published previously (Ledwell and Aldrich, 1999) (Fig. 2). The Q_{max} values used in both cases are those specified in the ZHA model.

Table III Relation between $\Delta\bar{G}_C$ and $Q_{max}FV_M$ for ion channel gating models.

Model	Reference state (r)	Final State (f)	Relation
Non-inactivating; All steps voltage-dependent or intermediate step voltage-independent	C_1	O_f	$\Delta\bar{G}_C = -RT \ln K^0_{C_1 \to O_f} = Q_{max}FV_M$
Non-inactivating; Last step voltage-independent	C_1	O_f	$\Delta\bar{G}_C = -RT \ln K^0_{C_1 \to O_f} = Q_{max}FV_M - RT \ln P_O^{max}$
Inactivating; All steps voltage-dependent or intermediate step voltage-independent	C_1	I_f	$\Delta\bar{G}_C = -RT \ln K^0_{C_1 \to I_f} = Q_{max}FV_M$
Inactivating; Voltage-independent inactivation	C_1	I_f	$\Delta\bar{G}_C = -RT \ln K^0_{C_1 \to I_f} = Q_{max}FV_M - RT \ln I_{max}$

The table lists the relationship between the median measure of free-energy (derived from a QV plot) and the chemical free-energy difference between the unique initial and final states of the system $\Delta\bar{G}_C$ for four broad classes of gating modes of the ion channel.

CHAPTER FOUR

A self-consistent approach for determining residue-specific coupling interactions that underlie channel activation.

INTRODUCTION

Allosteric control of functional activity of multi-domain proteins is a well-known phenomenon in biological systems (Goodey and Benkovic, 2008). In classical examples of allosteric proteins, such as hemoglobin or aspartate transcarbomylase, binding of a ligand induces a change in the quarternary structure of the proteins which alters its ability to binding other molecules/ligands or catalyze other biomolecular processes (Wyman and Gill, 1990). Allosteric regulation, however, is not just limited to stimuli that exert chemical potential but also include regulation by different physical stimuli such as voltage, mechanical stretch or even heat (Hille, 2001b). In this light, ion channels are *bona fide* examples of allosteric proteins in which changes in ambient stimuli levels lead to structural changes in their stimulus sensing domains which modulate quarternary changes in the protein structure, underlying the transition between conducting and non-conducting states of the channel. Understanding the molecular mechanisms underlying energy transduction in proteins require identification of specific pathways involved in transmission of information from sensory modules to catalytic centers. Structural methods like NMR and X-ray crystallography provides us high-resolution snapshots of conformational changes that underpin molecular communication but ultimately direct determination of energetic coupling is necessary to prove and elucidate these pathways.

Mutant cycle analyses is a perturbation based approach which can be used to experimentally determine the interaction energies between specific residues and thus

elucidate their roles in governing the fold of a protein or conformational changes associated with the proteins' transitions between functionally active and passive forms(Ackers and Smith, 1985; Horovitz and Fersht, 1990; Horovitz et al., 1994; Di Cera, 1998b) (Fig. 1a). In this approach, perturbation energies are evaluated when a specific site (say X) is perturbed in the native protein and in the background of a secondary perturbation (say Y). If the two perturbation energies are equal then it implies that the two sites are energetically independent whereas unequal perturbation energies imply that the two sites interact. This methodology was first used to study protein-protein interactions in tRNA synthetase (Carter et al., 1984) and has now seen widespread application in the study of protein folding and conformational changes (Serrano et al., 1990; Schreiber and Fersht, 1995; Ranganathan et al., 1996). Of central importance, however, is the question – how is the perturbation energy in each step evaluated?

In the case of a binding reaction such as those involving protein-protein or protein-ligand interaction, free-energy changes associated with perturbations can be evaluated directly by directly monitoring binding. In many cases, however functional activity is used as a surrogate measure of free-energy of conformational transition. For instance, free-energy of activation of voltage-gated and ligand activated ion channels are frequently evaluated based on their functional responses as evidenced in conductance-voltage (G-V) (Yifrach and MacKinnon, 2002; Sadovsky and Yifrach, 2007; Zandany et al., 2008; Yifrach et al., 2009) or conductance-ligand (Shanata et al., 2012) (typically referred to as dose response) relationships. In the event that the channel possesses a single dominant conducting state, these relationships reflect the channel open probabilities (P_O) at different voltages or ligand concentrations and are fitted to a

Boltzmann function or Hill equation, respectively. For voltage-activated processes, the free-energy of activation of the channel is estimated as: $\Delta G_{app} = zFV_{1/2}$ ($V_{1/2}$ is the voltage that elicits half-maximal response and z reflects the number of charges transferred during channel activation) (Fig. 1b). The functional mutant cycle (FMC) approach conventionally uses ΔG_{app} to measure the perturbations along each path of the cycle. This is not unlike other proteins in which a sigmoid functional response is fitted to a quasi-empirical logistic equation, often derived by invoking simplistic assumptions about their functional behavior (such as 'the two-state assumption').

In most known voltage-gated ion channels, however, the process of channel activation comprises multiple intermediate closed states, before the channels finally open (Bezanilla et al., 1994; Zagotta et al., 1994a; Schoppa and Sigworth, 1998). The occupancies of the ensemble of non-conducting states are not adequately captured by the GV curves, and their energetic contributions remain indeterminate. More significantly, the uncertainty associated with the values of these interaction energies prevents a direct comparison to molecular simulations based on high-resolution structures with experimental free-energy measures. In some instances, multi-state kinetic models are fitted to experimental behavior of proteins and the model parameters are directly used for mutant cycle analyses (Lee and Sine, 2005; Gupta and Auerbach, 2011). While such an approach is likely to be better than simply measuring GV curves, it's use is limited to systems whose gating-behavior can be adequately described by a well-constrained gating scheme.

In Chapter three, an alternative methodology has been described to estimate the voltage-dependent change in free-energy in proteins. Gating-charge movement is the

'conjugate displacement' for a voltage-driven transformation and governs the work done in the process (which, in a reversible limit, is the free-energy change) (Chowdhury and Chanda, 2012a, 2013). This enables us to extract the net free-energy change (ΔG_{net}) associated with the full-scale voltage-dependent activation of a channel directly from experimentally measured gating-charge displacement *vs* voltage (QV) curves. ΔG_{net} can be expressed in terms of the median voltage of activation, V_M (Fig. 1c) as: $\Delta G_{net} = Q_{max} F V_M$, where Q_{max} is the maximum number of gating charges transferred during activation of the channel and V_M is the voltage such that the shaded areas on either side of the V_M axis are equal. The most important advantage of this approach is that virtually no assumptions are made about how the channel undergoes voltage-dependent activation (i.e. number of intermediate states and how the states are connected to each other in the gating process, etc.). A corollary to this proposition is that we should be able to use this approach to measure residue specific interaction energies that underlie gating transitions in a completely model-independent manner by using ΔG_{net}, derived from the QV curve, to quantify the energetic consequences of the single and double mutants. In this study, we test this approach, which we call the Generalized Interaction energy Analysis (GIA), and compare it with functional mutant cycle (FMC) analysis. Previous studies on the Shaker K_V channel have identified several putative interactors in the pore domain which have been proposed to govern the energetics of the last concerted transition which opens the channel pore (Yifrach and MacKinnon, 2002; Sadovsky and Yifrach, 2007). However, using GIA we find that a majority of these interaction pairs have little to no net contribution on the overall free-energy of activation of the channel. Only a single residue pair, A391-T469, exhibits a significant energetic non-additivity which in all likelihood

reflects a long range interaction between them mediated by networks in intervening residues. Extensive numerical simulations, using different multi-state gating models, clearly show that GIA but not FMC yields an accurate estimation of energetic non-additivities, and thus interactions. The inaccuracy in FMC stems forth from the uncertainty of the references states which makes it impossible to compare perturbation energies across different mutants.

As a further demonstration of the approach, GIA was used to understand the molecular mechanisms of electromechanical coupling in the Shaker K_V channel. High-resolution structures and structure-function studies on potassium and sodium channels have shown that the residues in the S4-S5 linker connecting the voltage-sensing domain (VSD) and the pore domain (PD) are important for coupling voltage-sensing and pore gates. However, the energetic contribution of specific residues in this crucial interface remains unclear in large part due to a lack of general methods to measure free-energy of interactions. Specific networks of residues in this region maybe especially important for the great diversity in 'coupling mechanisms' of VGICs. For example, the exemplar Shaker K_V channel, the coupling of the VSD is putatively obligatory such that the channel gates can open only after all VSDs have activated. On the other hand, in the well characterized BK channels, the coupling is relatively much weaker, allowing for the channel gates to open even when all the VSDs are not activated (albeit with a low probability). In contrast, in the hyperpolarization activated HCN channel, activation of the VSDs causes the channel gates to close. The different modes of coupling arise in these proteins, despite the fact that they are built on a common structural template.

GIA was used to determine the energetic contributions of specific residues that are at the interface of the pore domain and voltage-sensors. The study focused on a group of conserved residues clustered at an intersubunit interface between the S4-S5 linker and the tail end of the S6 segment. Previous studies have shown the perturbations at these positions profoundly alter the functional activity of the channel (Soler-Llavina et al., 2006; Batulan et al., 2010). However, it remains to be determined whether these sites truly interact with each other and if so, how strongly. Our experimental measurements reveal that three residues in this cluster, R394, E395 and Y485, exhibit strong inter-residue coupling (3-5 kcal) and that the pairwise (or binary) coupling between the residues are sensitive to the ternary perturbation. The three residues are structurally oriented in a way that the Tyr residue intercalates itself between the Arg and Glu residues and putatively prevents them from interacting. Taken together, our data strongly suggests that this conserved interfacial gating triad constitutes a critical electromechanical transducer which mediates coupling between structural transitions in the voltage-sensor to those in the pore.

In summary, the results argue that GIA might prove to be a very useful approach to accurately, reliably and rapidly deconstruct the interaction networks underlying the conformational changes in voltage-gated ion channels as well as for other proteins where the conjugate displacements can be experimentally measured.

RESULTS

Principle of the Generalized Interaction-energy Analysis (GIA)

Let us consider a protein which exists in a passive form S_1, which upon action of an external stimulus (such as ligand, voltage, etc.) undergoes a series of conformational changes to reach its final active form, S_{n+1}, via 'n' sequential transitions (involving n-1 intermediate states, S_i, i=2, 3,…, n-1). The free-energy of each conformational state is G_i. On such a system we implement the mutant cycle analysis (Fig. 1a and d) to deduce the interaction energy between two residues, X and Y.

The residue X is perturbed in the native protein and in the background of the secondary perturbation, Y. As a consequence of these perturbations, the free-energies of multiple intermediates may change. The interaction energy between the two residues in the state S_i (i=1, 2,…,n), $G_{\text{int}}^{(i)}$, can be described by the equation:

$$G_{\text{int}}^{(i)} = \left(G_i^{(X,Y)} - G_i^{(0,Y)}\right) - \left(G_i^{(X,0)} - G_i^{(0,0)}\right) \quad \text{... (1)}$$

where the superscripts on the free-energy terms on the right side of the equation indicate the unperturbed, singly and doubly perturbed systems, as shown in Fig. 1d. Equations, analogous to Eq. 1, may be written for each of the conformational states of the protein. However, absolute free-energies of biomolecular systems cannot be derived via experimental measurements thereby making it impossible to obtain the absolute interaction energies between residues.

From an experimental standpoint, we can measure the free-energy change associated with a conformational change, say between states S_i and S_{i+1}, by measuring the equilibrium constant, K_i, for the transition. This allows us to evaluate the difference in the interaction energies between the two states in two different conformations as:

$$G_{\text{int}}^{(i+1)} - G_{\text{int}}^{(i)} = \left\{\left(G_{i+1}^{(X,Y)} - G_{i+1}^{(0,Y)}\right) - \left(G_{i+1}^{(X,0)} - G_{i+1}^{(0,0)}\right)\right\} - \left\{\left(G_{i}^{(X,Y)} - G_{i}^{(0,Y)}\right) - \left(G_{i}^{(X,0)} - G_{i}^{(0,0)}\right)\right\}$$

which may be re-written as:

$$\Delta\Delta G_i = \left(\Delta G_{i\to i+1}^{(X,Y)} - \Delta G_{i\to i+1}^{(0,Y)}\right) - \left(\Delta G_{i\to i+1}^{(X,0)} - \Delta G_{i\to i+1}^{(0,0)}\right) = -RT\ln\left(\frac{K_i^{(X,Y)}K_i^{(0,0)}}{K_i^{(0,Y)}K_i^{(X,0)}}\right) = -RT\ln\Omega_i \quad \text{... (2)}$$

In Eq. 2, $\Delta\Delta G_i$ reflects $G_{\text{int}}^{(i+1)} - G_{\text{int}}^{(i)}$ and $\Delta G_{i\to i+1}$ is the free-energy difference between the states S_i and S_{i+1} which can be written as $-RT\ln K_i$. Ω_i reflects the non-additivity of the equilibrium constants in the mutant cycle.

Next, suppose the non-additive perturbation energy associated with each of the 'n' conformational transitions ($\Delta\Delta G_i$, i=1,2,…,n) are evaluated and we sum all the $\Delta\Delta G_i$ measures to obtain the net non-additivity of the two perturbations, $\Delta\Delta G_{net}$:

$$\Delta\Delta G_{net} = \sum_{i=1}^{n}\Delta\Delta G_i = \left(\Delta G_{1\to n+1}^{(X,Y)} - \Delta G_{1\to n+1}^{(0,Y)}\right) - \left(\Delta G_{1\to n+1}^{(X,0)} - \Delta G_{1\to n+1}^{(0,0)}\right) = -RT\sum_{i=1}^{n}\ln\Omega_i \quad \text{... (3)}$$

where $\Delta G_{1\to n+1}$ is the free-energy difference between the states, S_1 and S_{n+1}. This net energetic non-additivity reflects the difference in the interaction energies between X and Y in the initial passive conformation and the final active conformation. A protein might transit between its two limiting states following multiple pathways. Since most biological macromolecules obey the principle of microscopic reversibility, the net free-energy changes across all such pathways are necessarily identical. This implies that $\Delta\Delta G_{net}$ is path independent and thus Eq. (3) holds for systems activating via a multi-state transitions, in sequential or parallel modes or combinations thereof.

How can we extract $\Delta\Delta G_{net}$ from experimental measurements? In Chapter three, we have described an approach to extract the ΔG_{net} for conformational change in proteins,

driven by an external stimulus, in a model independent manner (Chowdhury and Chanda, 2012a, 2013). The approach involves measuring the 'conjugate displacement' associated with the stimulus, followed by an integral transformation of the 'conjugate displacement' *vs* 'stimulus intensity' which directly yields the total work done (and thus ΔG_{net}, in a reversible limit) during the conformation change in the protein. The approach was described in detail for voltage-gated ion channels, for which the conjugate-displacement curve is the gating-charge displacement *vs* voltage (QV) curve. From the measured QV curves we extract, the median voltage of activation, V_M, and evaluate ΔG_{net} as $Q_{max}FV_M$, where Q_{max} is the maximum amount of gating charges transferred during channel activation (or in other words the charge per channel). By incorporating such a free-energy measure in Eq. 3, we can obtain a measure of $\Delta\Delta G_{net}$ (Eq. 3). This approach of combining the mutant cycles with energies of perturbation evaluated by measuring the conjugate displacement curves is what we refer to the 'Generalized Interaction-energy Analysis' (GIA) - $\Delta\Delta G_{net}$ in Eq. 3, is thus referred to as $\Delta\Delta G_{GIA}$.

Experimental comparison of Functional Mutant Cycle analysis and Generalized Interaction-energy Analysis

Functional mutant cycle analysis (FMC) and Generalized Interaction-energy Analysis (GIA) use orthogonal experimental measurements to estimate the interaction energies between two sites. How do the interaction energies computed by these two methods compare against each other? In the prototypical Shaker K_V channel, previous FMC analysis has identified several strongly interacting residues (Yifrach and MacKinnon, 2002; Sadovsky and Yifrach, 2007). Some of the interaction partners lie

more than 10 Å away in the protein structure which has led to the view that voltage-dependent channel opening involves dynamic rearrangements of long-range interaction networks. To estimate these interaction energies accurately, we reevaluated them using the GIA approach.

We focused on four residues (A391, E395, T469 and V476) located in the pore domain of the channel, a region likely to undergo significant conformational changes during channel gating (Fig. 2a) (Yifrach and MacKinnon, 2002; Sadovsky and Yifrach, 2007). First, we applied FMC to measure the interaction energy between sites E395 and T469. Two single and one double mutant were generated by mutating the sites to Ala and their relative $P_O V$ curves were measured (along with that of the wild-type (WT) channel) by tail current analysis (Fig. 2b and c). Both single mutations result in large shifts in the $P_O V$ curves and, consistent with previous reports (Yifrach and MacKinnon, 2002), FMC analysis shows a large non-additivity ($\Delta\Delta G_{FMC}$ ~ 7.5 kcal) of the two perturbations (Table I) (Fig. 2d). Next, for each of the constructs, we measured the gating currents (Fig. 2e) and extracted their QV curves (Fig. 2f). Perturbation energies for each mutation was calculated by extracting the V_M of each curve (Table II) and the non-additivity of the perturbations at the two sites was calculated using GIA (Table III). Strikingly, GIA showed that the perturbations are almost completely energetically independent ($\Delta\Delta G_{GIA} \approx 0$). (Fig. 2g)

To determine whether contrasting results of GIA and FMC is specific for the E-T pair or a general trend, we calculated all pairwise interaction energies between the residues spanning the four-residue cluster using GIA (Fig. 3, Table II and III). QV curves of single mutants (A391V, E395A, T469A and V476A) and all pairwise combination

(double) mutants were measured to calculate $\Delta\Delta G_{GIA}$. The experimental error associated with $\Delta\Delta G_{GIA}$ estimations was ~ 0.6 kcal (≈ RT) considering which we used a cut-off of 1.8 kcal to determine whether the non-additivite energies were significant or not. An additional justification for such a cut-off value is that, the net free-energy change associated with voltage-dependent activation of the wild-type Shaker K_V channel ($\Delta G_{net, WT}$) being ~ -14 kcal, significant interactions exhibit non-additivities of more than 13% of $\Delta G_{net, WT}$. In all the six possible pairs, we found that that $\Delta\Delta G_{GIA}$ and $\Delta\Delta G_{FMC}$ (reported previously) do not agree with each other. More importantly, except for the AT pair (i.e. A391-T469), all the pairwise non-additivities evaluated by GIA were below the significance level suggesting that they are almost energetic independent, which is in contrast to previous reports.

Numerical simulations of GIA and FMC

This discrepancy in interaction energies evaluated using FMC and GIA prompted us to examine the robustness of the two approaches in measuring energetic non-additivities. We performed numerical simulations using the 16 state ZHA model (Hoshi et al., 1994; Zagotta et al., 1994a; Zagotta et al., 1994b; Ledwell and Aldrich, 1999) (Fig. 4a) which describes the voltage-dependent activation of the Shaker K_V channel. In this model voltage-sensor activation is described as a two step sequential process occurring independently in different subunits and once all voltage-sensors are activated, a final concerted transition opens the channel pore. We constructed a hypothetical mutant cycle in which two mutations were envisioned to affect only the equilibrium constant of the last concerted transition and the double mutant affects the same transition, additively (Fig. 4a).

Thus, by design the cycle ensures that the two perturbations are energetically independent and hence non-additivity measurements should yield a null result. While holding the other equilibrium parameters constant, the magnitude of perturbation of each mutant was varied over 12 orders of magnitude and in each case we calculated the $\Delta\Delta G$ using FMC (by simulating the P_O-V curves) and GIA (by simulating the QV curves). As shown in Fig. 4b, the FMC simulations show strong non-additive energies whereas the GIA simulations show that the non-additivity is zero in all cases. This simulation suggests that even under limiting conditions when perturbations affect a single transition of the gating scheme, FMC analysis may report non-real interaction energies.

Next, we considered a more general scenario where single mutations affect multiple transitions and the double mutants may affect these transitions non-additively. A hypothetical mutant cycle was created wherein the wild-type reference channel and the three mutants constituting the cycle were envisioned to be gated via the ZHA model. For each of the three mutants comprising a thermodynamic cycle, the values of the equilibrium parameters were randomly chosen from within a parameter space (see Methods). The P_OV and QV curves in each case were simulated and the $\Delta\Delta G_{FMC}$ and $\Delta\Delta G_{GIA}$ for the cycle was computed. This process was repeated for a large number (> 600) of mutant cycles and $\Delta\Delta G_{FMC}$ and $\Delta\Delta G_{GIA}$ for each cycle were then compared against the true non-additive energy $\Delta\Delta G_{true}$ (Fig. 5a and b), derived directly from the equilibrium constants. $\Delta\Delta G_{true}$ was calculated as:

$$\Delta\Delta G_{true} = -4RT\ln\left(\frac{K_1^{WT}K_1^{S12}}{K_1^{S1}K_1^{S2}}\right) - 4RT\ln\left(\frac{K_2^{WT}K_2^{S12}}{K_2^{S1}K_2^{S2}}\right) - RT\ln\left(\frac{L^{WT}L^{S12}}{L^{S1}L^{S2}}\right)$$

where the superscripts, WT, S12, S1 and S2 indicate the equilibrium constants for the WT channel, the double and the two single mutant channels respectively. The comparison reveals that $\Delta\Delta G_{GIA}$ and $\Delta\Delta G_{true}$ are identical for all cases (Fig. 5b) whereas $\Delta\Delta G_{FMC}$ is practically uncorrelated with $\Delta\Delta G_{true}$ (Fig. 5a).

Similar simulations were performed envisioning that each of the four constructs comprising the mutant cycle gates via an MWC-type allosteric scheme (Fig. 5c). According to this scheme, voltage-sensor activation and pore opening represent pre-existing equilibria wherein the pore is intrinsically biased towards the closed state and voltage-sensor activation causes a shift in this bias towards the open state, via allosteric interactions. Such an activation scheme has been shown to accurately describe the voltage-dependent gating of the BK channel (Horrigan and Aldrich, 2002). For >600 mutant cycles, generated by a random sampling strategy, we generated $\Delta\Delta G_{FMC}$ and $\Delta\Delta G_{GIA}$ while $\Delta\Delta G_{true}$ was calculated as:

$$\Delta\Delta G_{true} = -4RT\ln\left(\frac{J^{WT}J^{S12}}{J^{S1}J^{S2}}\right) - 4RT\ln\left(\frac{D^{WT}D^{S12}}{D^{S1}D^{S2}}\right) - RT\ln\left(\frac{L^{WT}L^{S12}}{L^{S1}L^{S2}}\right)$$

where J and L represent the intrinsic equilibrium constant of activation, at 0 mV, for the voltage-sensor and the pore and D represents the allosteric interaction factor. We find that $\Delta\Delta G_{FMC}$ and $\Delta\Delta G_{true}$ are highly divergent (Fig. 5d), while $\Delta\Delta G_{GIA}$ and $\Delta\Delta G_{true}$ are equal in all tested cases (Fig. 5e). The discrepancy between $\Delta\Delta G_{GIA}$ and $\Delta\Delta G_{true}$ is thus not just limited to the systems activating via the ZHA model but also extends to other multi-state voltage-dependent systems (see Chapter Addendum for additional examples). These findings establish that GIA but not FMC can report energetic non-additivities (residue-

specific interaction energies) accurately and in a completely self-consistent manner irrespective of whether the perturbations affect single or multiple transitions.

Energetic role of the interfacial gating triad evaluated using GIA

Identifying the molecular mechanism of electromechanical coupling in the Shaker K_V channel is believed to be mediated by an intracellular interface formed between the S4-S5 linker and the intracellular end of the S6 helix. Several studies have shown that perturbation at this interface leads to large shifts of the P_OV curves (Yifrach and MacKinnon, 2002; Soler-Llavina et al., 2006; Batulan et al., 2010). However, identifying the specific interaction networks which mediate coupling and quantifying the strength of such interactions, reliably, has not yet been possible. We focused on the site E395 which lies at the C-terminal end of the S4-S5 linker helix (Fig. 6a), which has been proposed to play an important role in electromechanical coupling. Structural inspection shows that three residues are close to it, namely R394, Y485 (and V476), raising the possibility that these sites might be interacting (see thesis Appendix). Of these Y485 site belongs to an adjacent subunit and previous studies has suggested that interactions between these residues play an important role in mediating slow-components of the OFF gating currents in the Shaker K_V channel (Batulan et al., 2010). Furthermore, the E395 and Y485 sites are strongly conserved in the K_V channel family (Fig. 6b) raising the possibility that the functional role of this residue-network might be evolutionarily conserved. We determined the interactions between these residues using GIA.

Each of the three residues were substituted to Ala individually and in pairwise combination and for each mutant we measured the gating-charge displacement *vs* voltage

(QV) curve. For each pair (EY, RY and RE) we compared the effects of the two single mutants with that of the double mutant. For instance, in the case of the EY pair (Fig. 7a) we observed that while E395A mutation causes a large leftward shift in the QV curve of the wild-type channel, in the background of the Y485A mutation, E395A results in a much smaller shift (Table I). Such a functional response is clearly reflective of non-additivity of the two perturbations. The calculated non-additivity of the perturbations, in this case turns out to be ~ +5 kcal (Table II). Similarly, even in the case of the RY pair (Fig. 7b) we observed a substantial non-additivity of ~ +3.1 kcal (Table II). In contrast for the RE pair we found that the E395 mutation causes a substantial shift in the QV curves both in the presence and absence of the R394A mutation. The calculated non-additivity for the RE pair was found to be ~ 1 kcal which is lower than the cut-off value for significant interactions (1.8 kcal). These results imply that both the Arg and Glu residues strongly interact with the Tyr residue while they do not interact with each other.

Next, we generated the triple mutant where all the three sites were mutated to Ala and we measured its QV curve. This allowed to us to compute each of the three pairwise interactions, in the presence of a third perturbation (Fig. 8). In the presence of the R394A mutation, the E395A mutation caused a prominent leftward shift in the QV curves, whether the Y485A mutation was present or absent (Fig. 8a). The non-additivity calculation shows that in the background of the R394A mutation, $\Delta\Delta G_{GIA}$ for the EY pair is ~ +1.2 kcal. Thus there is a strong reduction in the interaction between E and Y in the background of the R394A mutation. Similarly, for the RY pair (Fig. 8b) we observed that, in the presence of the E395A mutation, $\Delta\Delta G_{GIA}$ for the RY pair is ~ -0.9 kcal, which is 4 kcal lower that the non-additivity calculated in the absence of the mutation (Table II).

However, the RE pair exhibits a strong non-additivity of ~ -3 kcal in the presence of the Y485A mutation (Fig. 8c). These results therefore imply that within the triad, tertiary perturbations strongly influence each of the pairwise non-additivities.

Val476 has no energetic influence on the gating triad

The Val residue (V476), which resides in the pore domain of the channel, lies in close proximity to the gating triad. It has been previously hypothesized to strongly interact with the Glu residue (E395). However, $\Delta\Delta G_{GIA}$ measurements (Fig. 3d) show that the contribution of such an interaction (if present) to the overall free-energy change of the protein is very small (< 1 kcal). We further investigated whether V476 has any additional influence on the interactions in the gating nexus.

First, we generated the double mutant (V476A/Y485A), measured its QV curve and performed non-additivity analysis to measure the interaction between the sites V476 and Y485 (Fig. 9a). Y485A perturbation caused small shifts in the QV curves in the wild-type channel as well as in the background of the V476A mutation and the calculated $\Delta\Delta G_{GIA}$ between the two sites was found to be ~ 0.8 kcal. This indicates that V476 does share any substantial energetic linkage with the site Y485.

Finally, we sought to determine whether V476 modulates the interaction between the sites E395 and Y485. To this end we generated the triple mutant (E395A/V476A/Y485A) and measured its QV curve (Fig. 9b). This was subsequently used to construct a mutant cycle, wherein the reference channel was the V476A mutant and the single and double perturbations (E395A, Y485A and E395A/Y485A) were all in the background of the V476A mutation. For this cycle, $\Delta\Delta G_{GIA}$ was calculated to be ~

+3.9 kcal. This non-additivity reflects the interaction energy between the EY pair in the background of the V476A mutation and is not significantly different from the interaction energy between the EY pair calculated in the wild-type channel background (Fig. 8a). This suggests the V476A does not influence the interactions at the gating nexus.

Mechanistic Role of the Interfacial gating triad

The results of the GIA calculations, summarized in Fig. 10a, reveal that in the native channel the RY and EY pairs of residues interact with each other very strongly (3-5 kcal), but the interaction is likely to be destabilizing towards the open state of the channel. The RE pair on the other hand do not seem to interact with each other in the native channel. Surprisingly, perturbation of the Tyr residue, led to the development of a strong interaction between the RE pair (3 kcal) which favors the open state of the channel. On the other hand, the RY and EY interactions seem to disappear when the E and R sites were perturbed, respectively. These interactions are not modulated by other residues in the vicinity as demonstrated by the GIA measurements performed with the V476 mutant channels.

Guided by the structure of the channel, we can propose a mechanistic basis underlying the origin of these dynamic interactions (Fig. 10b and c). As seen in the structure of the open state of the paddle chimera, the Tyr residue intercalates itself in between the Arg and Glu sites and thereby prevents the two oppositely charge residues from interacting. Upon mutation to Ala, the room created by removal of the bulky phenolic sidechain allows the Arg and Glu to re-orient themselves and interact via a salt-bridge interaction, which accounts for the non-additivity between the RE pair in the

absence of Tyr (but not in its presence). In the native structure, the Tyr itself is held in position by its interaction with the Arg and Glu sidechains – the underlying forces, although repulsive (due to the positive $\Delta\Delta G_{GIA}$) are oppositely directly which holds the Tyr in position. Mutation of the Arg (or Glu) residue might result in a force imbalance causing the Tyr to swing out of position thereby resulting in a disruption of its interaction with Glu (or Arg).

The inter-subunit interactions at the gating-triad, promotes electromechanical coupling at two levels. First, they form a "coupling" cuff around the pore gates which glues the intracellular moving parts of the neighboring subunits together thereby facilitating the final concerted transition that leads to channel opening. (Zagotta et al., 1994a; Ledwell and Aldrich, 1999). Second, this interfacial nexus is also important to maintain the flexibility of the distal gating hinge connecting the S4-S5 linker helix and the S5 transmembrane segment. We speculate that this flexibility is important for electromechanical transduction in voltage-gated ion channels as a flexible hinge would facilitate energy flow to the S6 segment instead of the contiguous S5, thereby allowing the lever-arm movement of the S4-S5 linker to efficiently close and open the channel gates(Chowdhury and Chanda, 2012b). Compromising the flexibility of the distal hinge by forming tight intra-subunit interactions, as observed in the Y485A mutation impairs channel electromechanical coupling(Ding and Horn, 2002; Soler-Llavina et al., 2006; Muroi et al., 2010). By intercalating itself between R394 and E395, the Y485 residue forms a "coupling" nexus allowing for facile transfer of information within and between the subunits of the K_V channel. This gating triad thus is an important electromechanical

tranducer which converts the electrical force acting on the S4 charges into a mechanical force which tags at the tail end of the S6 segment causing it to open/close.

DISCUSSION

In this study we describe an experimental methodology to quantitatively determine the contribution of interaction energies between two sites of a protein to the overall free-energy change associated with a stimulus driven conformational change of the protein. The approach, referred to as the Generalized Interaction-energy Analysis (GIA), is based on determining the energetic consequence of a perturbation in the presence of a secondary perturbation, by measuring the 'conjugate displacement' of the associated process. This is fundamentally different from the canonical mutant cycle analyses, wherein functional activity of a protein is measured and used to empirically quantify the free-energies. We show that the free-energies of perturbation calculated via a median transformation of the conjugate displacement curve, directly allows us to calculate the interaction energies between specific sites of a multi-state protein, in a completely self-consistent manner, even in instances when the perturbations affect multiple transitions of the protein.

We implemented GIA on the voltage-gated Shaker K_V channel, for which the conjugate displacements associated with the voltage-dependent transformation can be conveniently obtained by experimentally measuring the gating charge displacement *vs* voltage (QV) curves. We used GIA to calculate the interaction energies between several pairs of residues, lying along the pore domain of the channel, which undergoes large

conformational changes during channel gating (Yellen, 1998). Many of the perturbed pair of sites are several angstroms distant in the structure and previous functional mutant cycle analyses studies (employing GV curves) have suggested that they constitute a long-range energetically coupled network of residues which are crucial for channel gating. However, using GIA, we found that, except for one pair (A391-T469), the rest of the perturbations were independent of each other. Numerical simulations of allosteric (MWC-type) and the quasi-sequential non-allosteric (ZHA-type) models show that GIA can provide exact estimates of non-additivity in interaction energies over a large parameter space even when mutations affect different transitions during a multi—step activation process, although FMC frequently report false positive interactions.

The false positives that are observed in FMC approach can be rationalized by considering a simple three-state model of a channel with two closed states (C_0 and C_1) and one open state (O) (Fig. 11). A $P_O V$ curve samples the occupancy of only the O state. As a consequence, $P_O V$ based free energy estimate is dominated by the energy difference between the open state and the most stable closed state. Mutations which alter the stability of the intermediate closed state(s) could change the reference closed state. In the example shown, $P_O V$ based energetics is informed by the energy difference between C_1 and O for the WT, while for the three mutants, the GV based energies will mainly reflect the energy difference between C_0 and O. Because of these differences in reference states, GV based perturbation energies are not comparable across mutations and, thus, cannot be used to calculate interaction energies accurately (Fig. 11). This problem is exacerbated as the number of intermediate closed states increase. GIA, on the other hand, is based on V_M measurements from the QV curves which are always informed by the energy

difference between first and last states without any influence of the intermediates. This ensures that in the given example the QV based energies always reflect the energy difference between the states C_0 and O. Hence GIA based non-additivity reflects the true contribution of pairwise interactions to the overall free-energy change between the first and last states of the channel (Fig. 11).

To further demonstrate the applicability of GIA, interactions between three crucial residues constituting an inter-subunit gating interface (R394, E395 and Y485) were quantified by measuring the QV curves of the single, double and triple mutants. Our measurements show that interactions between these residues are crucial for the overall energetics of channel activation and that the structural integrity of this interfacial gating triad is important for electromechanical in the voltage-gated Shaker K_V channel.

It must be mentioned that in GIA, the lack of observed non-additivity will arise in three instances: (i) the sites truly do not interact (ii) the sites interact only in the intermediate states or (iii) the interaction between the two sites does not change between the initial resting and final activated states. Thus, given these caveats, a lack of non-additivity is not a definite proof of lack of interaction but when interaction is observed by GIA one can be certain that those residues synergistically contribute to the gating process.

It is important to note that the QV curves of Shaker K_V channel and many of its mutants exhibit only a slight asymmetry – the QV curve is slightly steeper at depolarized than at hyperpolarizing potentials. As a result, the QV curves can be adequately fitted to the symmetric Boltzmann equation and the median voltage of charge transfer (V_M) will be often similar to the $V_{1/2}$, the voltage at which half of the gating charges have moved. In such situations Boltzmann-fit derived $V_{1/2}$ values can be used instead of V_M values in

computing the energetic non-additivies. However, it must be remembered that adequate fitting of the Boltzmann equation to the QV curve is hardly an argument in favor of a two-state assumption, which underpins the derivation of the Boltzmann equation. In instances, when the QV curves are split, superposition of multiple Boltzmann functions can be used to fit the experimental curve but the energetic estimates obtained from such quasi-empirical fits can be high inaccurate, as has been demonstrated previously in Chapter three (Chowdhury and Chanda, 2012). This might introduce significant inaccuracies in estimating energetic non-additivities. V_M, not being predefined by a model-specific equations, does not lead to such inaccuracies and is thus a more reliable and uniform strategy to extract energies from the QV curves.

Implementation of GIA requires a prior knowledge of the Q_{max} of the channel, the maximum gating charge transferred during full-scale activation of the channel, and its mutants. Measurements of Q_{max} for a channel is a non-trivial problem and cannot be estimated simply from the slope of the QV curve. However, for the system under investigation, the gating-charge determining residues reside in the voltage-sensor and are highly specific (Ahern and Horn, 2004). The specific sites which have been investigated in this study are uncharged, lie outside the electric field and are when perturbed are unlikely to significantly alter the Q_{max} of the channel. However, in implementing GIA to test for interactions between residues in the voltage-sensor, it might be important to calibrate Q_{max} of the mutant channels to establish that Q_{max} is not altered significantly by the perturbations.

For many channels, the maximum open probability ($\mathbf{P_O^{max}}$) at depolarized potentials does not reach unity, because the transitions between their last closed and open

states are voltage-independent. In such situations, a correction factor needs to be added to $Q_{max}FV_M$, to obtain an accurate measure of the free-energy of channel activation. In Chapter three, we have derived the correction factor to be -RTln $\mathbf{P_O^{max}}$, which becomes larger in magnitude with decreasing value of $\mathbf{P_O^{max}}$. However, the magnitude of this correction factor becomes significant (>1 kcal) only when $\mathbf{P_O^{max}}$ drops below ~0.15. For many Shaker K_V channel mutants (in the voltage-sensor and the pore), $\mathbf{P_O^{max}}$ has been measured and found to be similar to that of the wild-type channel, ~ 0.8. This implies that, although $\mathbf{P_O^{max}}$ measurements improve the accuracy of the free-energy estimation and thus of $\Delta\Delta G_{GIA}$, its contribution is likely to be small enough, so as to not interfere with the identification of strongly interacting residue pairs and quantifying the strengths of their interactions.

A final point, particularly relevant for the Shaker K_V channels is the way by gating-charge displacement curves are experimentally measured. In our study, the non-conducting W434F mutant was used to measure the QV curves. This mutant eliminates ion conduction via acceleration of C-type inactivation, putatively resulting in a channel with a permanently collapse outer pore (Yang et al., 1997). Gating charge of different channel mutants can also be obtained in the background of a second non-conducting mutant of the Shaker K_V channels: V478W, which putatively forms a hydrophobic seal close to the channel gates and thereby occludes ion flux (Kitaguchi et al., 2004). A third strategy to measure gating currents is to use a high-affinity peptide toxin (Aggarwal and MacKinnon, 1996), such as Agitoxin (Garcia et al., 1994), which blocks ion conduction. The final alternative is to measure gating currents under conditions when all permeant ions are washed off. The QV curves obtained from each of the four strategies are

generally considered to be equivalent. However, subtle differences between them, especially when studying mutant channels, could potentially lead to uncertainties in quantification of perturbation energies and thus of GIA. A thorough and careful study will be needed to assess and compare these strategies in extracting perturbation energies, which is beyond the scope of the current study.

The importance of the GIA approach lies in its accuracy, reliability and generality. Unlike FMC measurements, GIA is accurate, as has been demonstrated in this study, and unlike conventional multi-state kinetic modeling based on single channel analysis, GIA may more amenable to large scale perturbation studies (Soler-Llavina et al., 2006; Muroi et al., 2010) to accurately determine the dynamic interaction networks which shape the energy landscape governing protein conformational changes and constitute the molecular forces that drive structural changes in the protein.

FIGURES

Figure 1: Functional mutant cycle *vs* Generalized Interaction-energy Analysis in voltage-gated ion channels.

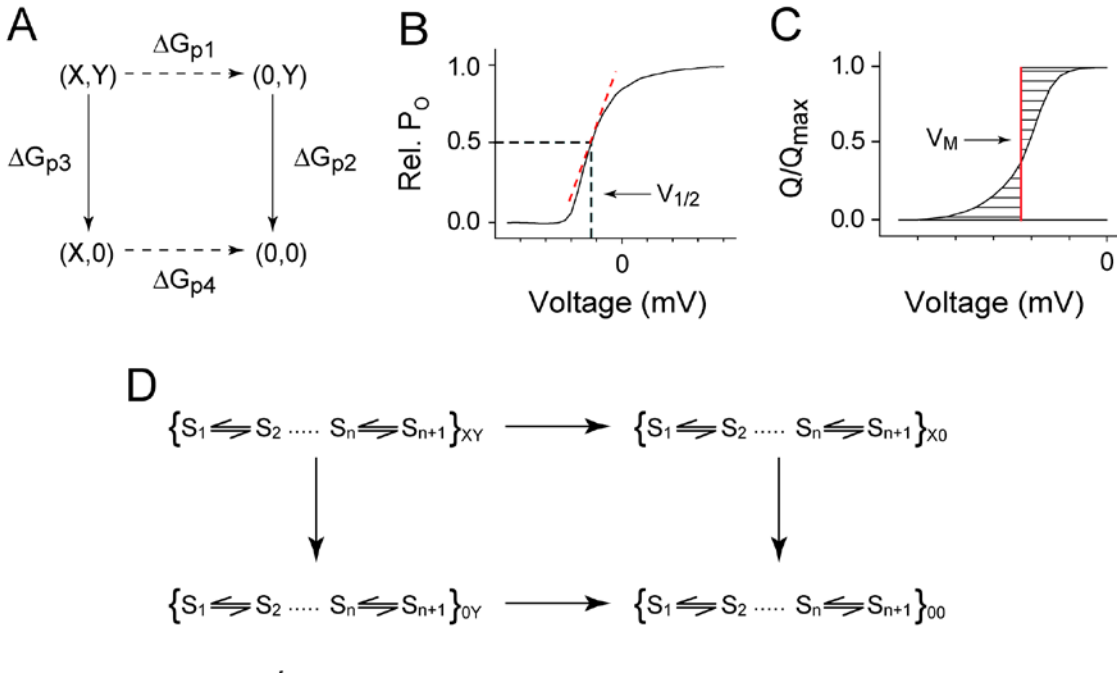

(A) Principle of the mutant cycle analysis, wherein two sites (X,Y) are mutated individually or jointly. By measuring the free-energies of perturbation along each path, the interaction energy between the two sites can be assessed as $\Delta\Delta G_{non\text{-}add} = \Delta G_{p4} - \Delta G_{p1} = \Delta G_{p2} - \Delta G_{p3}$. **(B)** The relative open-probability *vs* voltage curve showing the half-maximal voltage of activation, $V_{1/2}$. The red dashed line is the tangent to the sigmoid curve at $V_{1/2}$ and the slope of this tangent is linearly related to the Boltzmann slope (z_{app}). In FMC, the free-energy of perturbation along each path of the thermodynamic cycle in (A) is computed as $\Delta(z_{app}FV_{1/2})$. **(C)** The QV curve with the median voltage of activation, V_M, depicted by the red vertical line. By definition, the two dashed areas on either side of the median voltage-axis are equal. In GIA, the free-energy of perturbation along each path of the thermodynamic cycle in (A) is computed as $\Delta(Q_{max}FV_M)$.

Figure 2. Experimental comparison of interaction energies evaluated using FMC and GIA.

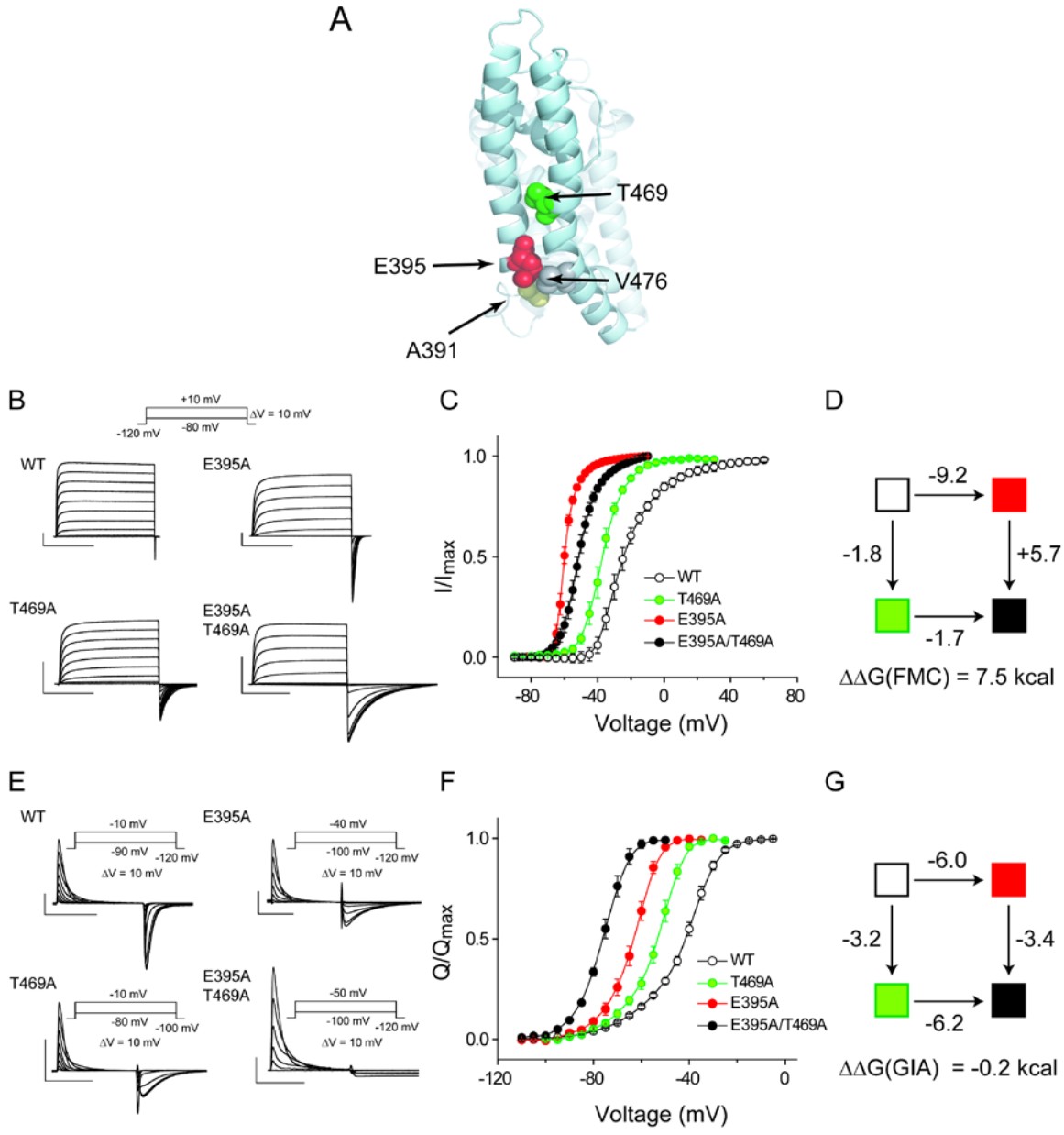

(A) The structure of the pore domain of a single subunit of the $K_V1.2/2.1$ paddle chimera, showing four residue previously proposed to be strongly interacting. **(B)** Raw ionic currents for the WT channel, E395A, T469A and E395A-T469A mutants, in response to the voltage protocol shown. Scale bars represent 1 μA and 50 ms. **(C)** I/I_{max} curves

(reflecting the relative P_O vs. V relationship) for the WT channel and the single (E395A and T469A) and double alanine (E395A-T469A) mutants. **(D)** Functional mutant cycle analysis for the E-T pair with each box colored as in the P_OV curves on the right. The perturbation energy along each path was assessed from the P_OV curves (in kcal). **(E)** Raw gating currents for the WT channel, E395A, T469A and E395A-T469A mutants, in response to the voltage protocol shown alongside each current trace. Scale bars represent 1 μA and 50 ms. **(F)** Normalized gating-charge displacement *vs* voltage curves (QV) for the WT channel and the single (E395A and T469A) and double alanine (E395A-T469A) mutants. **(G)** Generalized Interaction-energy analysis for the E-T pair with each box colored as in the P_OV curves on the right. The perturbation energy along each path was assessed from the V_M of the QV curves (in kcal) (assuming Q_{max} = 13.2 for all the mutations).

Figure 3. Interaction energies evaluated using GIA differ from those evaluated using FMC. (A-E)

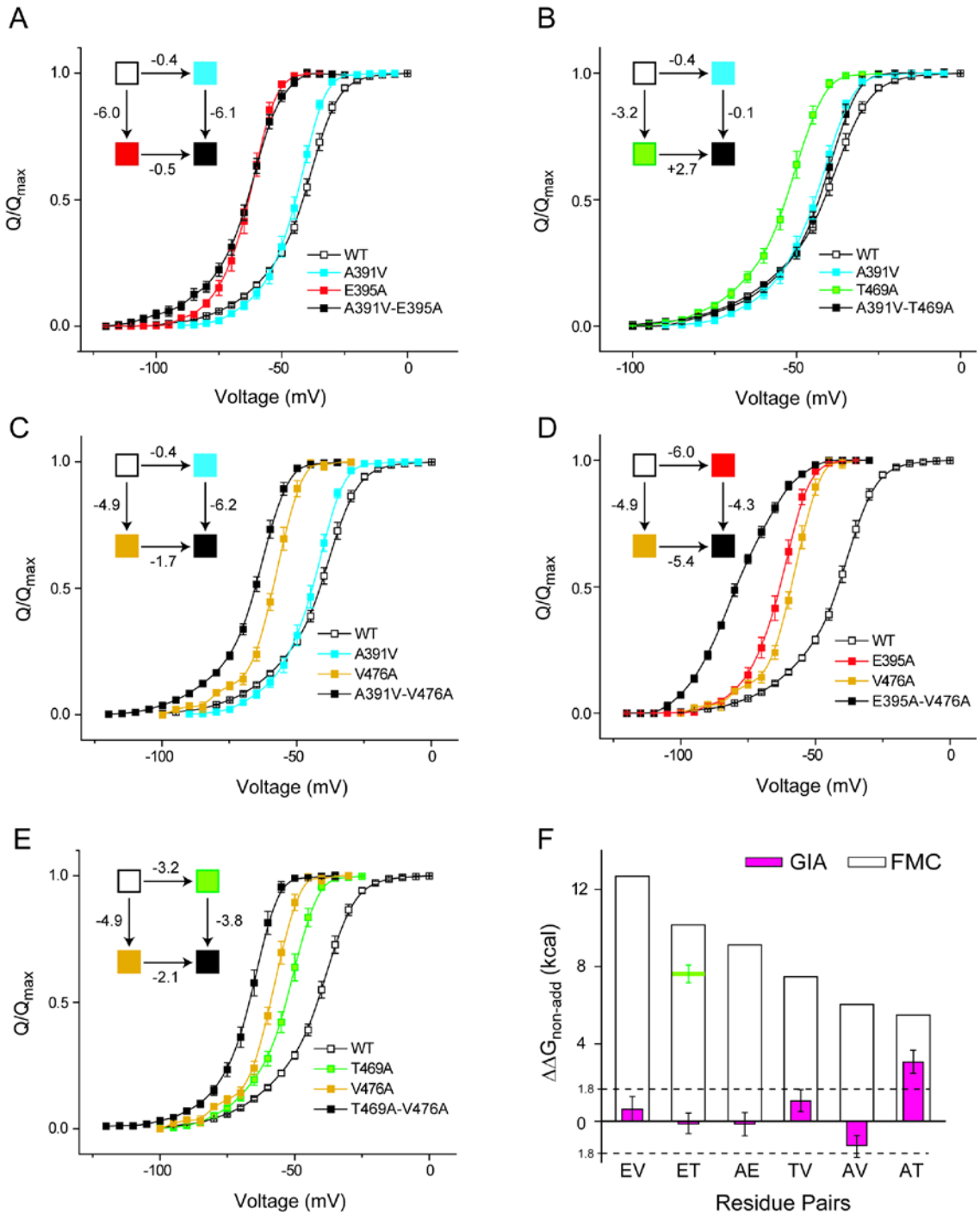

GIA was used to measure the interaction energies between A391-E395 (AE) **(A)**, A391-T469 (AT) **(B)**, A391-V476 (AV) **(C)**, E395-V476 (EV) **(D)** and T469-V476 (TV) **(E)**.

In each case the normalized QV curves of the single and double mutants were measured, from which the V_M was extracted and used to calculate the free-energy of perturbation (assuming Q_{max} = 13.2 for all the mutations). The thermodynamic cycle for each pair is shown in the inset, where each box corresponds to the WT, single or double mutants, colored according to the curves in each panel and the perturbation energy (in kcal) along each path of the cycle is written alongside. **(F)** $\Delta\Delta G_{GIA}$ for each pair was calculated using the QV curves and were compared with $\Delta\Delta G_{FMC}$ calculated using the Boltzmann fit parameters of each of the mutations reported previously by Yifrach and Mackinnon, 2002. For the ET pair, horizontal green bar depicts $\Delta\Delta G_{FMC}$ evaluated in this study.

Figure 4. Numerical analysis of interaction energies computed via FMC and GIA using the ZHA model.

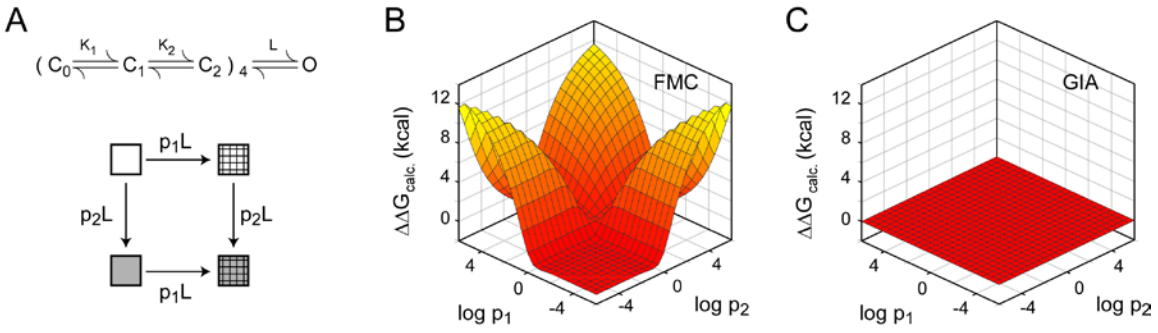

(A) Scheme I shows the ZHA model of activation of the Shaker K_V channel. A mutant cycle is envisioned in which the wild-type channel and the single and double mutants gate via Scheme I. The two single mutants (hashed box and grey box) differ from the wild-type reference channel (white box) only in the value of the last concerted transition (by factors of p_1 and p_2). The effects of the two single mutants are additive such that for the double mutant (grey hashed box) the equilibrium constant of the last transition is p_1p_2L while the other equilibrium constants are same as the wild-type channel. Several such cycles were generated using different values of p_1 and p_2 and for each cycle $\Delta\Delta G_{FMC}$ **(B)** and $\Delta\Delta G_{GIA}$ **(C)** were calculated from simulated P_OV and QV curves respectively and plotted against p_1 and p_2.

Figure 5. Comparison of non-additivities evaluated to GIA and FMC from randomly sampled mutant cycles.

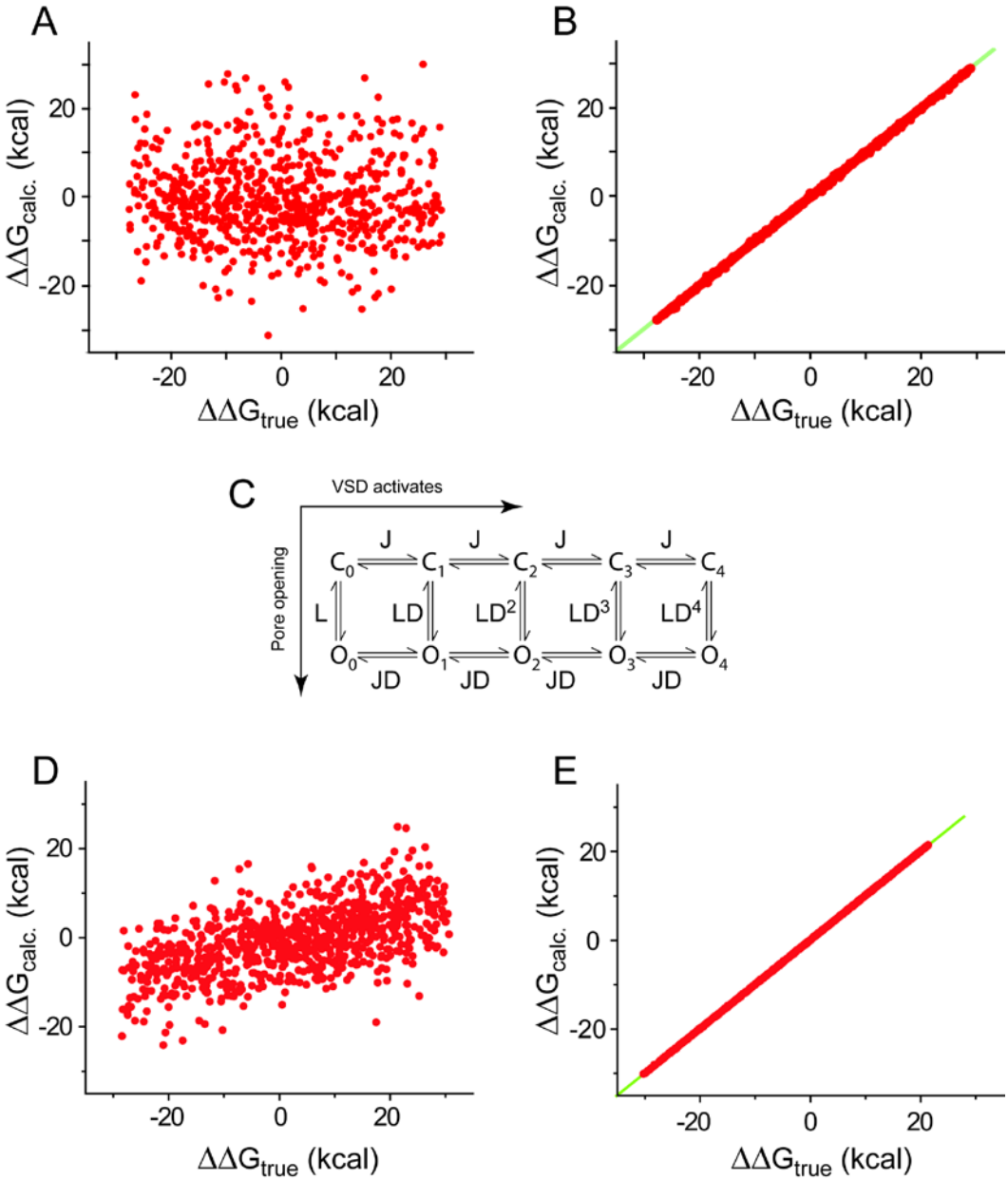

Several mutant cycles were generated via random sampling strategy. For each cycle, $\Delta\Delta G_{FMC}$ **(A, D)** and $\Delta\Delta G_{FMC}$ **(B, E)** were calculated and compared against $\Delta\Delta G_{true}$. In **(A)** and **(B)**, each of the four constructs constituting the cycle follow a ZHA activation scheme while in **(D)** and **(E))**, each of the four constructs constituting the cycle follow an

MWC activation scheme **(C)**, where J represents the intrinsic voltage-dependent activation constant of each voltage-sensor, L is the intrinsic activation constant of the pore and D is the allosteric interaction factor.

Figure 6. Structural location of the conserved inter-subunit gating triad.

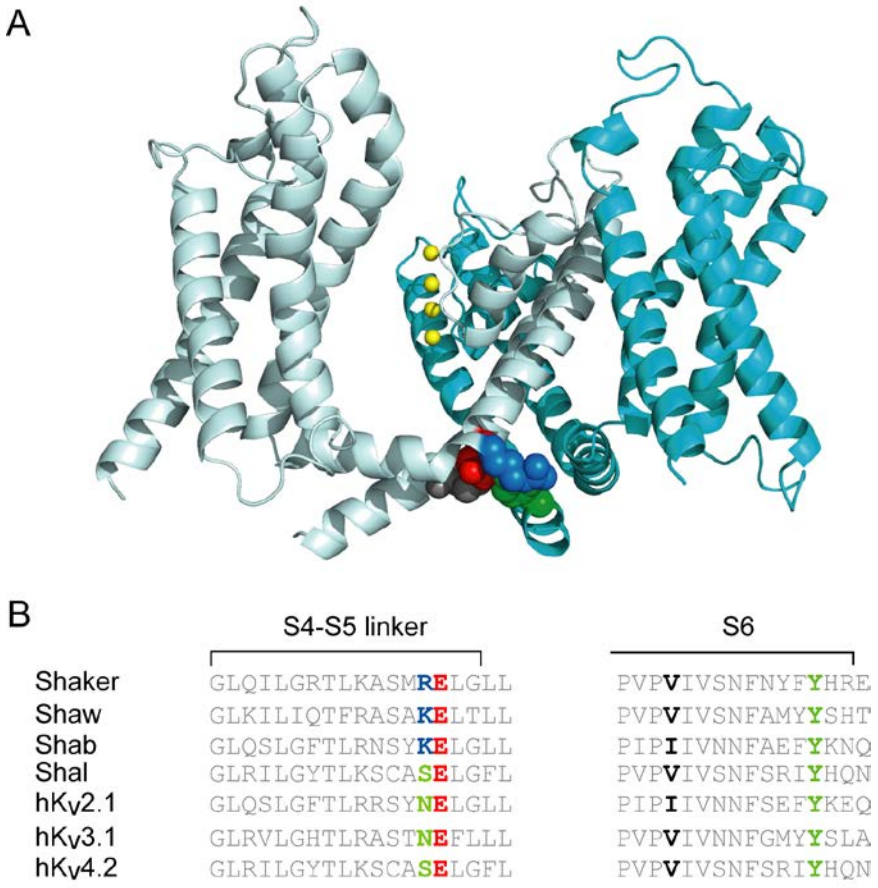

(A) Two subunits of the K_V1.2/2.1 paddle chimera are shown, with the three residues, E395 (red), R394 (blue) and Y485 (green) at the inter-subunit interface, show in van der waal's representation. The residue in gray corresponds to V476 (in the pore domain). **(B)** Sequence alignment of different homologs of the Shaker K_V channel, showing the conservation at sites corresponding to E395 (red), R394 (blue/green), Y485 (green) and V476 (black).

Figure 7. Pairwise interaction energies between residues of the interfacial triad using GIA.

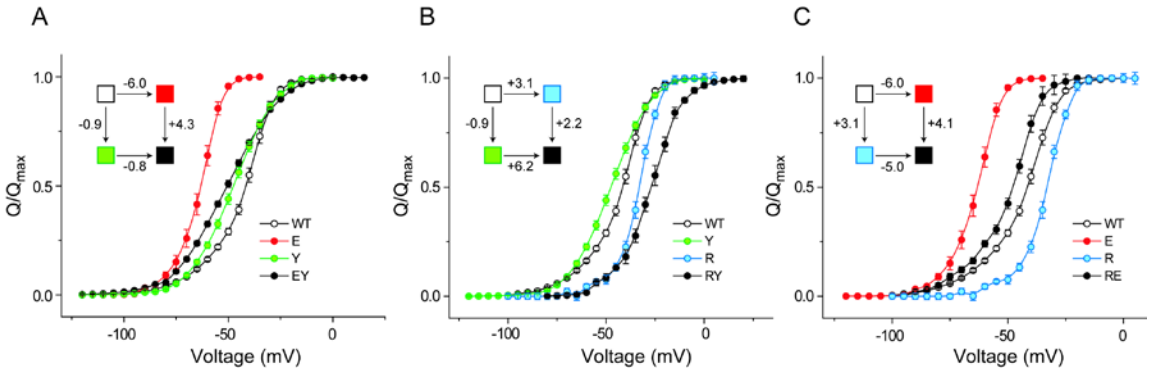

GIA was used to measure the interaction energies between E395-Y485 **(A)**, R394-Y485 **(B)** and R394-E395 **(C)**. For each pair, the normalized QV curves of the single and double (alanine) mutants were measured, from which the V_M was extracted and used to calculate the free-energy of perturbation (assuming Q_{max} = 13.2 for all the mutations). The thermodynamic cycle for each pair is shown in the inset, where each box corresponds to the WT, single or double mutants, colored according to the curves in each panel. The legends correspond to single letter codes of the amino acids perturbed.

Figure 8. Tertiary perturbation affects the pairwise interactions between residues in the interfacial triad.

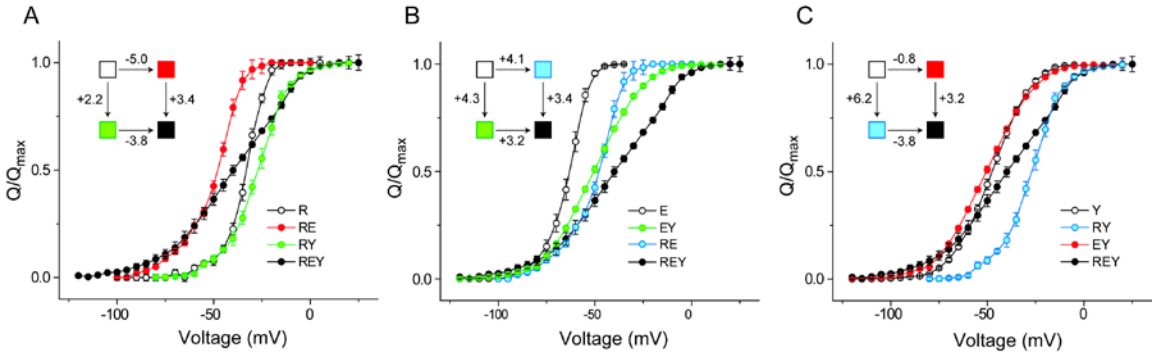

(A) GIA was used to measure the interaction energies between E395-Y485 in the presence of the R394A perturbation. The control or reference channel was the R394A mutant and the single (E and Y) and double mutations (EY) are in the presence of the tertiary perturbation, R394A. For each case of the four mutants, the normalized QV curves are shown along with the thermodynamic cycle in the inset (with each box colored according to the respective curves (mutants)) **(B)** and **(C)** GIA for the R394-Y485 pair in the presence of E395A mutation **(B)** and for the R394-E395 pair in the presence of the Y485A mutation **(C)** showing the respective QV curves of the control/reference channel, the two single and the double mutation and the thermodynamic cycle in the inset. (Q_{max} = 13.2 for all the mutations).

Figure 9. Effect of V476 on the interaction between E395 and Y485.

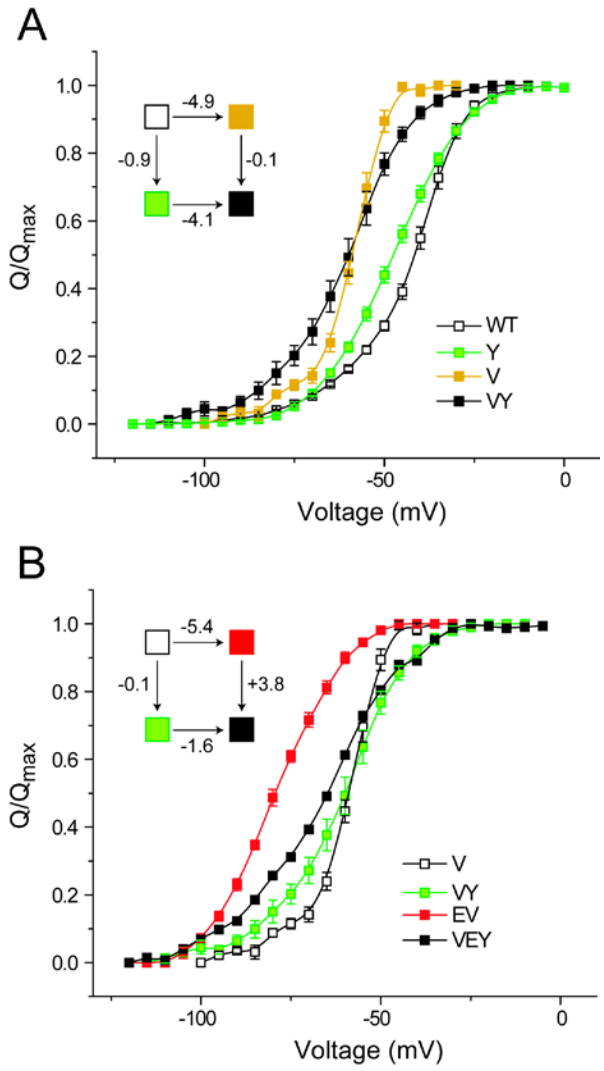

(A) Normalized QV curves to evaluate the interaction energy between V476 and Y485 using GIA, with the corresponding thermodynamic cycle in the inset. **(B)** Interaction energy between E395 and Y485 was assessed in the presence of the V476A mutation. The normalized QV curves for the single (E, Y) and double (EY) mutants, all in the background of the V476A mutation is shown, along with the corresponding thermodynamic cycle.

Figure 10. Speculative role of the interfacial gating triad in electromechanical coupling in K_V channels.

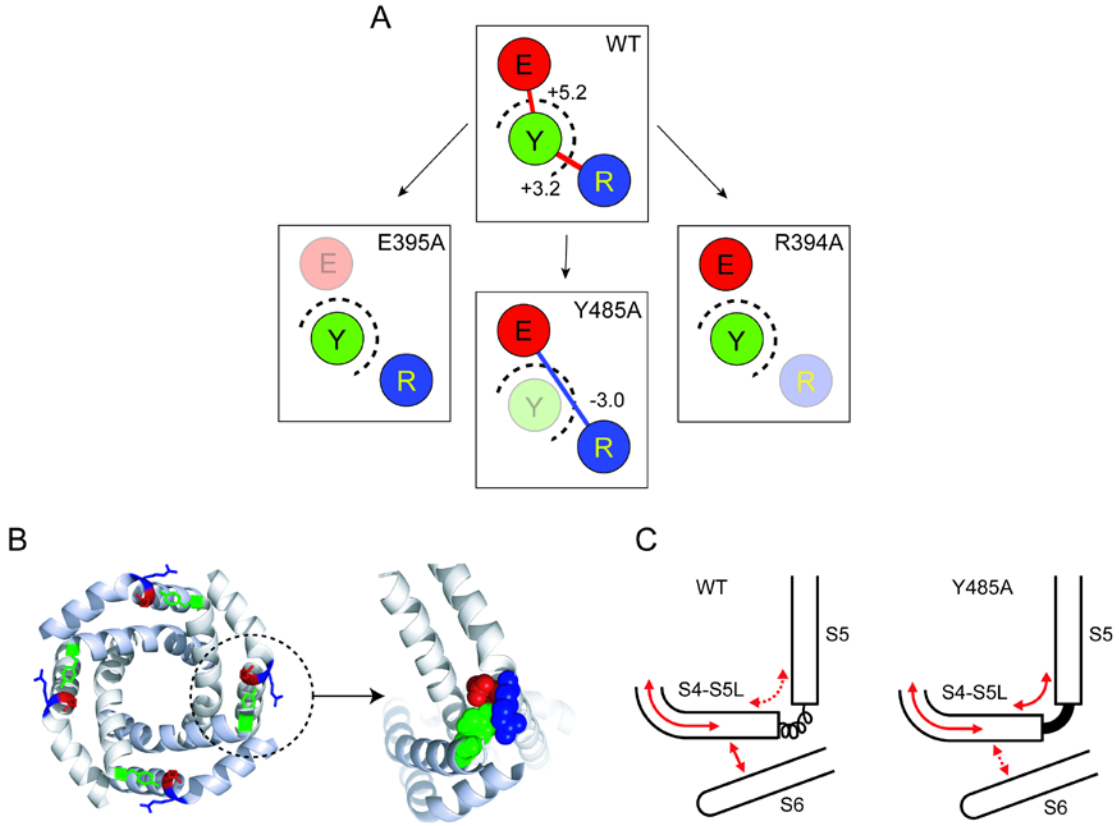

(A) *Right,* A bottom-up view of the pore domains of the $K_V1.2/2.1$ paddle chimera with the non-adjacent pairs of subunits colored similarly. The residues constituting the coupling cuff (R394, E395 and Y485) are depicted in a stick representation (and colored in blue, red and green, respectively). *Left,* An enlarged view of the interfacial triad at a single inter-subunit interface with the residues in a van der waal's representation. **(B)** Cartoon of the S4-S5 linker and S5 hinge region in the wild-type channel and in the Y485A mutant.

Figure 11. Physical explanation behind the discrepancy between FMC and GIA.

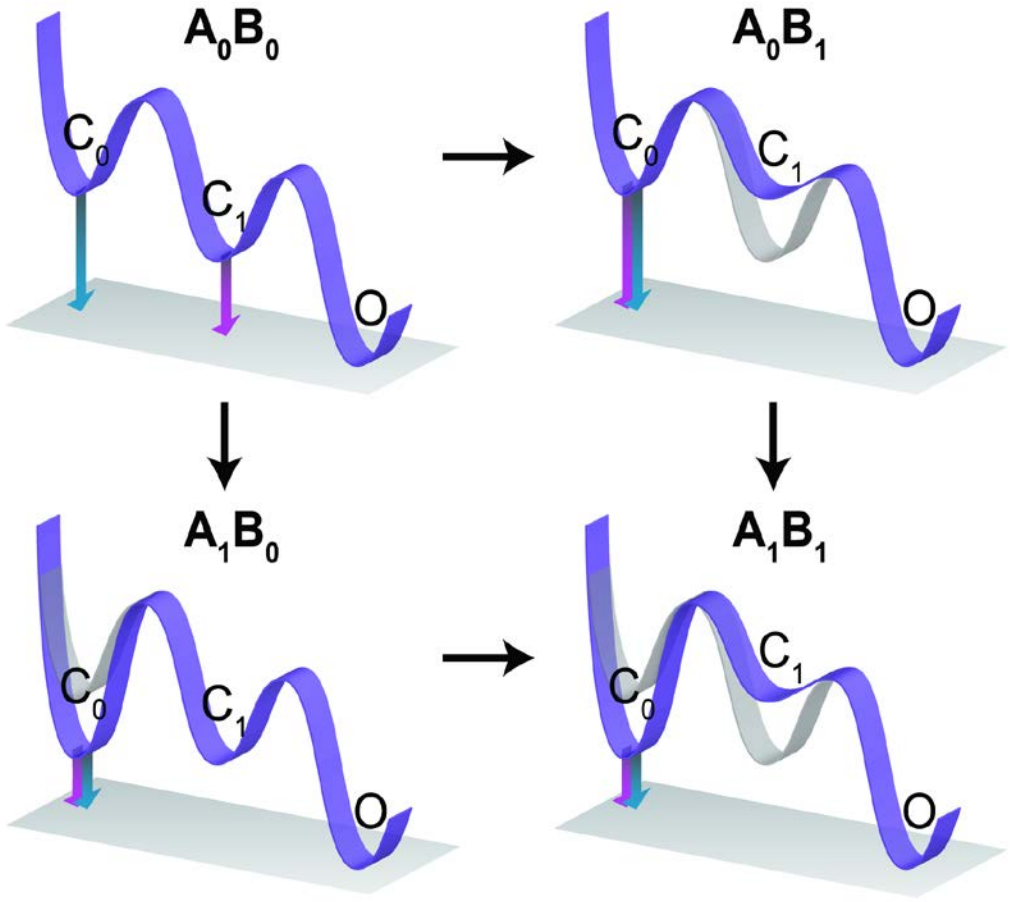

The energy profile diagram represents a thermodynamic mutant cycle for a 3-state sequential gating process involving two closed states (C_0 and C_1) and an open state (O). One of the mutants destabilize the state C_1 (A_0B_1) and the second mutant stabilizes state C_0 (A_1B_0) but the effect is additive on the double mutant (A_1B_1) (i.e. C_1 is destabilized and C_0 is stabilized). The red arrows show the free-energy difference computed by the GV curves (as is done in FMC) while the blue arrows show the free-energy difference computed by the QV curves (as is done in GIA). Note that in GIA, the measured ΔG is that between C_0 and O in all four cases, while in FMC, the measured ΔG is between C_1 and O in A_0B_0 but between C_0 and O in the other three.

Table I: Non-additivity of the perturbations at E395 and T469 evaluated using FMC.

Mutant	$\mathbf{V_{1/2}}$ (± s.e.m.) (mV)	**z** (± s.e.m.)	**n**	$\mathbf{\Delta G_{app}}$ (± s.e.m.) (kcal)
WT	-21.8 (± 1.4)	2.5 (± 0.07)	4	-1.3 (± 0.09)
E395A	-59.3 (± 0.6)	7.7 (± 0.17)	4	-10.5 (± 0.25)
T469A	-36.5 (± 1.3)	3.7 (± 0.32)	4	-3.1 (± 0.29)
E395A-T469A	-50.8 (± 1.0)	4.1 (± 0.28)	3	-4.8 (± 0.34)

The $V_{1/2}$ values of the relative $P_O V$curves of the wild-type Shaker K_V (inactivation removed) channel and the mutants are close to those previous reports[4,5]. However, the Boltzmann slopes (**z**) observed in this study are consistently lower than those reported previously. This can be attributed to the differences in the solutions used for functional measurements of the tail currents (110mM NMG-Mes/10mM KMes *vs* 58mM NaCl/40mM RbCl). As a result of this difference in slopes, the $\Delta\Delta G_{FMC}$ calculated in this study (+7.5 ± 0.52 kcal/mol), despite being very large, is smaller than that reported previously.

Table II: **V_M and the net free-energy of activation of mutants of Shaker K_V channel**

Mutant	V_M (± s.e.m.) (mV)	n	ΔG_{net} (± s.e.m.) (kcal)
WT	-44.7 (± 1.0)	5	-13.6 (± 0.3)
A391V	-46.0 (± 0.9)	5	-14.0 (± 0.3)
E395A	-64.6 (± 0.9)	5	-19.6 (± 0.3)
T469A	-55.4 (± 0.8)	3	-16.8 (± 0.2)
V476A#	-61.0 (± 0.9)	8	-18.5 (± 0.2)
A391V-E395A#	-66.4 (± 0.9)	10	-20.1 (± 0.3)
A391V-T469A#	-46.4 (± 0.8)	6	-14.1 (± 0.2)
A391V-V476A#	-66.7 (± 0.8)	12	-20.2 (± 0.2)
E395A-T469A	-75.7 (± 0.8)	4	-23.0 (± 0.2)
E395A-V476A#	-78.8 (± 1.4)	4	-23.9 (± 0.4)
T469A-V476A#	-68.0 (± 1.0)	5	-20.6 (± 0.3)

Gating currents for the mutants were measured either on a cut-open oocyte voltage clamp (COVC) or a two electrode voltage (TEV) clamp set-up (marked by #). The V_M of the normalized QV curve, for all the mutants (averaged from measurements performed in 'n' oocytes) are reported along with the standard error of the mean (s.e.m., δV_M). ΔG_{net} was

evaluated as $Q_{max}FV_M$ and its standard error, as: $Q_{max}F\delta V_M$. For all mutants, a Q_{max} of 13.2 electronic charges was used for ΔG_{net} calculations.

Table III: Comparison of non-additive perturbation energies, evaluated using GIA and FMC, for different pairwise mutations.

Site-pairs	**$\Delta\Delta G_{GIA}$** (± s.e.) (kcal)	**$\Delta\Delta G_{FMC}$** (kcal)
A391-E395	-0.15 (± 0.56)	9.12
A391-T469	3.12 (± 0.53)	5.49
A391-V476	-1.33 (± 0.55)	6.04
E395-T469	-0.12 (± 0.53)	10.15 (7.5 ± 0.52)
E395-V476	0.64 (± 0.65)	12.68
T469-V476	1.12 (± 0.56)	7.48

$\Delta\Delta G_{GIA}$ for each pair of sites was calculated according to the equation was calculated as described in the Methods. $\Delta\Delta G_{FMC}$ for all pairs was calculated using the Boltzmann fit parameters (of the relative P_OV curves) obtained from Yifrach and Mackinnon (2002). $\Delta\Delta G_{FMC}$ for E395-T469, calculated in this study is shown in ().

Table IV: **Median voltage of activation, V_M and the net free-energy of activation of mutants of the Shaker K_V channel.**

Mutant	V_M (± s.e.m.) (mV)	n	ΔG_{net} (± s.e.m.) (kcal)
WT	-44.7 (± 1.0)	5	-13.6 (± 0.3)
R394A	-34.6 (± 1.0)	5	-14.0 (± 0.3)
E395A	-64.6 (± 0.9)	5	-19.6 (± 0.3)
V476A#	-61.0 (± 0.9)	8	-18.5 (± 0.2)
Y485A	-47.9 (± 0.9)	5	-14.5 (± 0.3)
R394A-E395A#	-51.0 (± 0.9)	6	-15.5 (± 0.3)
R394A-Y485A	-27.4 (± 0.9)	6	-8.3 (± 0.3)
E395A-Y485A	-50.5 (± 1.0)	4	-15.3 (± 0.3)
E395A-V476A#	-78.8 (± 1.4)	4	-23.9 (± 0.4)
V476A-Y485A#	-61.4 (± 1.6)	9	-18.6 (± 0.5)
R394A-E395A-Y485A#	-40.0 (± 1.9)	4	-12.1 (± 0.6)
E395A-V476A-Y485A#	-66.6 (± 0.6)	6	-20.2 (± 0.2)

Gating currents for the mutants were measured either on a cut-open oocyte voltage clamp (COVC) or a two electrode voltage (TEV) clamp set-up (marked by #). The V_M of the normalized QV curve, for all the mutants (averaged from 'n' oocytes), along with its standard error (s.e.m., δV_M) are reported for each mutant. ΔG_{net} was evaluated as

$Q_{max}FV_M$ and its standard error, as: $Q_{max}F\delta V_M$. For all mutants, a Q_{max} of 13.2 electronic charges was used for ΔG_{net} calculations.

Table V. Interaction energies between residue pairs evaluated using GIA.

Site-pairs	**$\Delta\Delta G_{GIA}$** (kcal)	**$\delta\Delta\Delta G_{GIA}$** (kcal)
R394-E395	1.05	0.58
R394-Y485	3.14	0.58
E395-Y485	5.27	0.58
E395-V476	0.64	0.65
V476-Y485	0.84	0.69
R394-E395 (Y485A)	-3.03	0.76
R394-Y485 (E395A)	-0.94	0.76
E395-Y485 (R394A)	1.15	0.76
E395-Y485 (V476A)	3.86	0.72

$\Delta\Delta G_{GIA}$ and its uncertainty ($\delta\Delta\Delta G_{GIA}$) for each pair of sites was calculated as described in Methods. The first five rows correspond to mutant cycles in which the wild-type channel was the reference channel. For the last four rows, the control/reference channel is a mutant indicated in () and reflect the interaction energy between two residues in the presence of a third mutation.

ADDENDUM

An analytical comparison of non-additive energies computed by FMC and GIA in example multi-state systems

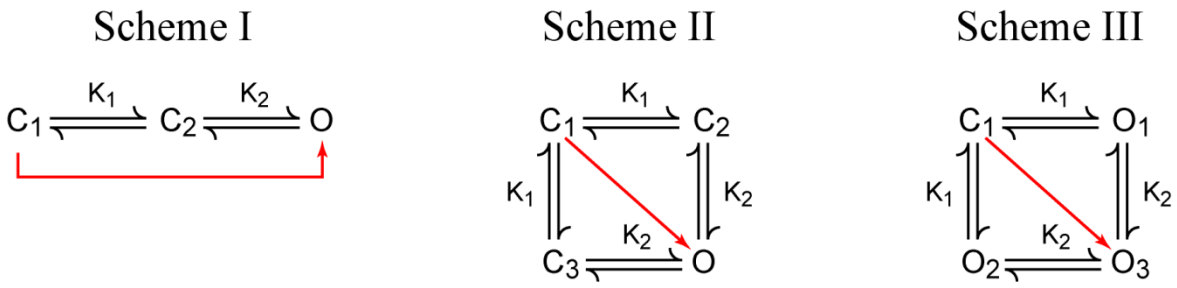

Consider a voltage-dependent ion channel comprising two subunits. For simplicity we assume that the subunits are identical, such that they transfer equal amount of gating charge during voltage-dependent activation. For such a system we envision three different gating schemes as shown above. In **Scheme I**, the two subunits activate sequentially, following a particular order (say subunit 1 activates before subunit 2). The channel is open only when both subunits are activated. The equilibrium constants of the two steps have the same voltage-dependence, q, but differ in their voltage-independent components. In **Scheme II**, the two subunits activate independently, but activation of one subunit allosterically modulates the activation of the other, by a factor, K_2/K_1, and the channels are open only when both subunits are activated. As in Scheme I, both K_2 and K_1 have the same voltage-dependence, q, but differ in their voltage-independent components. **Scheme III**, is similar to Scheme II, but with the central difference that channels are open when any one of the two (or both) subunits are activated (or in other words, the channel is closed only when both subunits are deactivated). For all the three Schemes, K_1 and K_2 are written as: $K_i^0 \exp(qFV/RT)$, where i=1 or 2 and K_i^0 represents the voltage-

independent component of the equilibrium constant. Furthermore, for all the three schemes, the net free-energy change during voltage-dependent activation (i.e. the chemical component of the free-energy difference between the first and last states of the channel, as indicated by the red arrow) is the same: $\Delta G_{net} = -RT\ln\left\{K_1^0 K_2^0\right\}$, and so is the total charge transferred during voltage-dependent activation: $Q_{max} = 2q$.

What is the P_O-V based, Boltzmann metric for the free-energy change in each of the three cases? We use the principle that the Boltzmann slope (obtained through fitting a Boltzmann equation to the P_O-V curve) can be approximated to the slope of the Hill-transformed P_O-V curve at $V_{1/2}$ (Yifrach, 2004), i.e.:

$$z_{app} = \frac{RT}{F}\frac{\partial}{\partial V}\ln\left(\frac{P_O}{1-P_O}\right)\Big|_{V_{1/2}}$$

Using the above equation, the Boltzmann measure of the free-energy change (i.e. $\Delta G_{app} = z_{app}FV_{1/2}$) for the three Schemes can be derived to be:

$$\Delta G_{app-I} = -RT\left(1 + \frac{2K_2^0}{2K_2^0 + K_1^0 + \sqrt{K_1^{0^2} + 4K_1^0K_2^0}}\right).\ln\left(\frac{2K_1^0K_2^0}{K_1^0 + \sqrt{K_1^{0^2} + 4K_1^0K_2^0}}\right)$$

$$\Delta G_{app-II} = -2RT\left(\frac{K_2^0 + K_1^0 + \sqrt{K_1^{0^2} + K_1^0K_2^0}}{K_2^0 + 2K_1^0 + 2\sqrt{K_1^{0^2} + K_1^0K_2^0}}\right).\ln\left(\frac{K_1^0K_2^0}{K_1^0 + \sqrt{K_1^{0^2} + K_1^0K_2^0}}\right)$$

$$\Delta G_{app-III} = -2RT\left(\frac{K_2^0 + K_1^0 + \sqrt{K_1^{0^2} + K_1^0K_2^0}}{K_2^0 + 2K_1^0 + 2\sqrt{K_1^{0^2} + K_1^0K_2^0}}\right).\ln\left(\frac{K_1^0K_2^0}{K_1^0 + \sqrt{K_1^{0^2} + K_1^0K_2^0}}\right)$$

where $\Delta G_{app\text{-}I}$, $\Delta G_{app\text{-}II}$, $\Delta G_{app\text{-}III}$ are the P_OV based Boltzmann measures of free-energy change for Schemes I, II and III respectively. This derivation illustrates two major points.

First, although in all the three Schemes, the total free-energy change associated with full scale activation of the channel is the same, the Boltzmann measure of free-energy change is different in the three cases. Thus, depending on nature of the gating scheme, the free-energy change deduced from the P_OV curves will be different. Second, and more importantly, for each of three Schemes, ΔG_{app} is not related to K_1^0 and K_2^0 by simply logarithmic relations (i.e. unlike ΔG_{net}). The non-linear/non-logarithmic dependence raises the possibility of obtaining false positives when ΔG_{app} is used to compute interaction energies as is done in FMC applications i.e. $\Delta G_{FMC} \neq 0$ when two single mutations affect K_1^0 by factors p_1 and p_2 and the double mutant affects K_1^0, additively, by a factor p_1p_2. However, in GIA, since the median measure of free-energy change accurately captures ΔG_{net} this problem will not arise.

AUTHORSHIP NOTE

This project was designed by Sandipan Chowdhury and Dr. Baron Chanda. Molecular biology and electrophysiological experiments was done by Sandipan Chowdhury and Benjamin M. Haehnel. Equilibrium simulations of gating models was done by Sandipan Chowdhury.

CHAPTER FIVE

Free-energy relationships in ion channels activated by voltage and ligand

INTRODUCTION

Voltage-gated ion channels (VGICs) constitute a superfamily of ion channels which have evolved over millions of years and are known to mediate a variety of physiological processes ranging from electrical and chemical signaling (Hille, 2001a) to gene expression (Dolmetsch, 2003) and cell division (DeCoursey et al., 1984; Day et al., 1993). In addition to membrane potential, some members of this superfamily are regulated by other physical and chemical stimuli, which sometimes involve additional regulatory domains. For instance, the BK channels are also regulated by free calcium (Marty, 1981) while the activity of members of the TRP channel family is regulated by heat, ligands and/or mechanical stretch (Caterina et al., 1997; Clapham, 2003; Voets et al., 2004). This polymodal behavior of many members of VGIC superfamily makes them outstanding models to study the fundamental basis of signal propagation in membrane proteins (Horrigan and Aldrich, 2002).

To gain insight into the mechanisms of how information is transferred between domains, it is necessary to map the network of residues involved in mediating such cross-talk. This appears seemingly straightforward because all it would require is to measure the effect of site-specific of perturbation on interaction energies. In practice, however, domain level interaction energies cannot be directly estimated and require development of detailed discrete state models to fully explain the voltage and ligand dependent

properties of these ion channels. This can be an enormous challenge since even a simple model of a dually regulated tetrameric ion channel requires a minimum of 50 states (Magleby, 2003). Symmetry arguments would reduce the number of free equilibrium parameters to a minimum of six but even this is by no means straightforward. These practical considerations restrict the analyses of interaction networks to a limited set of well-defined sites and to systems where detailed kinetic models have been developed.

In this chapter, we examine the free-energy relationships between ligand and voltage-gating pathways of polymodal ion channels. Our aim is to develop a theoretical framework which will allow us to extract the various free-energies without indulging detailed model fitting routines. Our approach is, to a degree, an extension of Wyman's linkage principles to electrochemical equilibria (Wyman and Gill, 1990). A direct consequence of these ideas is that the total chemical free-energy change of a voltage or ligand-dependent system is directly estimable by extracting the median voltage of activation or the median ligand concentration from the gating-charge displacement (QV) (as discussed in the previous chapters) or the ligand binding curve respectively (Wyman, 1967; Chowdhury and Chanda, 2012a). Here, we show that the ligand binding curve at any voltage can be obtained by measuring the QV curves at multiple ligand concentrations and a single reference ligand binding curve. This information can be further transformed to obtain the net free-energy change of a bimodal system. Finally, we show that the net displacement of the QV curve on the voltage-axis between zero and fully saturating ligand concentrations is linearly related to total interaction energy of the ligand binding sites with the pore and the voltage-sensors. We apply these theoretical propositions on allosteric gating models of the BK channel and hyperpolarization

activated HCN channel, both of which are regulated by voltage and ligand, to estimate the interaction energies between the two regulatory domains. Finally, we discuss the potential of applicability of our theoretical framework to systems of varying size and complexity and even to non-allosteric systems.

THEORY

Free-energy component for the ligand or voltage-dependent pathway

As shown by Wyman, the work done to saturate a macromolecule with a ligand can be directly estimated from the ligand binding curve, by extracting the median ligand concentration (Wyman, 1967; Wyman and Gill, 1990). In his original derivation, however, it was assumed that the free-energy of the macromolecule does not change upon ligand binding (Wyman, 1964b). Here, we show that such an assumption is not essential to deduce energetic information from the binding curves.

Consider a protein which can bind a ligand (X). The protein is presumed to exist in N different conformational states. Each state is associated with a variable n_i, which depicts the number of molecules of ligand X bound to the conformational state. The probability of occurrence of each state is assumed to follow a Boltzmann distribution such that, $P_i = \frac{\exp(-E_i\beta)}{Z}$, where $\beta = 1/k_BT$, E_i is the energy of the state and Z is the partition function of the system ($Z = \sum_i e^{-E_i\beta}$). The Boltzmann weight of each state, B_i (= $e^{-E_i\beta}$) is assumed to have an overall functional form as:

$$B_i = B_i^0 . x^{n_i} \quad ...(1)$$

In Eq. 1, x represents the ligand concentration and B_i^0 is related to the chemical energy of the state (which includes contributions from the intrinsic energies of the different component structural units and the interactions between them). The probability distribution of the conformational states will depend on the ligand concentration. The average number of ligands bound to the protein is:

$$\overline{X}(x) = \sum_i n_i P_i(x) \text{ ... (2)}$$

The free-energy of the system is:

$$\overline{G}(x) = -k_B T \ln Z \text{ ... (3)}$$

For a small change in ligand concentration, the change in the free-energy of system can be obtained through partial differentiation of Eq. 3 and thus:

$$d\overline{G}(x) = \left(\frac{\partial \overline{G}}{\partial \ln x} \right) d \ln x \text{ ... (4)}$$

Using Eqs. 2 and 3, Eq. 4 can be converted to:

$$d\overline{G}(x) = -k_B T \, \overline{X}(x) \, d \ln x \text{ ... (5)}$$

To obtain the net change in free-energy of the system due to a process completely driven by the ligand, we integrate Eq.5 from zero to a specified ligand concentration. Thus:

$$\overline{G}\,|_{x=0}^{x} = -k_B T \int_{-\infty}^{x} \overline{X}(x) d \ln x \text{ ... (6)}$$

Thus the free-energy associated with a ligand binding process is related to the area under a ligand binding curve ($\overline{X}$ vs. $\ln x$). Integrating the right side of Eq. 6, by parts, gives:

$$\Delta\overline{G}(x) = -k_B T \left(\overline{X} \ln x \,|_{x=0}^{x} - \int_0^{\overline{X}(x)} \ln x \, d\overline{X} \right) \text{ ... (7)}$$

In the above integral equation (Eq. 7), we have used the boundary condition that at zero ligand concentration, $\overline{X} = 0$. At saturating ligand concentration, $\overline{X}$ approaches $N_{max}N_{max}$, which is the maximum number of ligands that each protein molecule can bind. Using these limits in Eq. 7, the net free-energy change associated with full-scale transformation of the protein, associated with binding of ligand is:

$$\Delta\overline{G} = -k_B T\, N_{\max} \ln x + k_B T \int_0^{N_{\max}} \ln x \, d\overline{X} \quad \text{... (8)}$$

The free-energy expression in Eq. 8 comprises of two terms – the first is a non-saturating component that increases in magnitude with increasing ligand concentration; the second component is a saturating component which equals the area between the ligand binding curve and the ordinate axis, as shown in Fig. 1.

What do these individual components mean? We take a look at the overall "reaction" that is occurring here:

$$N_{\max}[X] + [P] \rightarrow [P.X_{N_{\max}}]$$

$[P]$ and $[P.X_{N_{\max}}]$ represent the completely unbound and bound states of the protein. The overall free-energy change of this process can be represented as:

$$\Delta\overline{G} = \mu(P.X_{N_{\max}}) - \mu(P) - N_{\max}\mu(X) = [\mu(P.X_{N_{\max}}) - \mu(P) - N_{\max}\mu^0(X)] - k_B T\, N_{\max} \ln x \quad \text{... (9)}$$

μ of each component of the reaction is its chemical potential. The chemical potential of the free/unbound ligand in turn has two components – the standard chemical potential (μ^0) superposed on a secondary term, $k_B T \ln x$, which originates from "mixing" (entropic factors) of the free ligand in solution (Depaula and Atkins, 2010). Comparing Eqs. 8 and 9, thus, tells us that the non-saturating term in Eq. 8 is the mixing term, while the second

term is associated with the full-scale binding of the ligand to the protein. The difference in our derivation, from Wyman's, principally results in the appearance of the non-saturating component in the free-energy change expression (Eq. 8).

Following Wyman's elegant mathematical analysis, the saturating component of Eq. 8 ($\Delta\overline{G}_c$) can be shown to be related to the overall chemical free-energy change of the protein-ligand system using the median ligand activity (x_m) (Wyman, 1964b). The latter is defined as follows (Fig. 1):

$$\int_{-\infty}^{\ln x_m} \overline{X}\, d\ln x = \int_{\ln x_m}^{\infty} (N_{\max} - \overline{X})\, d\ln x \quad \text{... (10)}$$

Using this definition, $\Delta\overline{G_c}$ is:

$$\Delta\overline{G_c} = k_B T \int_0^{N_{\max}} \ln x \, d\overline{X} = k_B T \, N_{\max} \ln x_m \quad \text{... (11)}$$

The thermodynamic equations describing a ligand binding process is strictly analogous to that of a voltage-driven process. In Chapter 3, we have shown (Chowdhury and Chanda, 2012a) that for a purely voltage-driven process, the net change in the chemical free-energy of the system can be estimated directly via the measurement of the gating-charge displacement vs voltage-curves as:

$$\Delta\overline{G_c} = \int_0^{Q_{\max}} V d\overline{Q} = Q_{\max} V_M \quad \text{... (12)}$$

where V is the voltage, $\overline{Q}$ is the mean gating-charge of the ensemble, $Q_{\max}$ is the maximum number of gating-charge translocated in the voltage-dependent activation of the protein and V_M is the median voltage of activation[a]. As discussed in the previous chapters, V_M is defined in a manner similar to Eq. 10:

$$\int_{-\infty}^{V_M} \overline{Q}\, dV = \int_{V_M}^{\infty} (Q_{\max} - \overline{Q})\, dV \quad \text{... (13)}$$

The preceding thermodynamic relations, although esoteric in construction, is simply the consequence of a fundamental thermodynamic proposition – the work done by a system undergoing a reversible change equals the decrease in the free-energy of the system. Thus the free-energy change of a system due to a change in an intensive environmental variable (such as voltage, pressure, temperature, ligand concentration, etc.) is directly estimable through the measurement of the conjugate extensive (charge, volume, entropy, bound ligands, etc.). The median measure (median voltage, median ligand concentration) is simply a convenient transformation of the free-energy change, enabling straightforward comparisons to gauge the energetic perturbation of the system.

Net free energy change for combined ligand and voltage-dependent activation

So far we have seen that the charge-voltage and the ligand binding curve, gives an accurate estimate of the total free-energy change associated with the full-scale activation of a voltage-dependent and a ligand dependent process, respectively. How does one estimate the net free-energy change when the channels are regulated by both voltage and ligand?

Consider a protein with dual sensitivity to voltage and a ligand (X). It exists in N different conformational states, each of which has an associated charge (or valence), q_i, as well as a variable n_i, which depicts the number of molecules of ligand X bound to the conformational state. The probability distribution of states, and thus the free-energy of the system, $\overline{G}$, will now be sensitive to voltage as well as ligand. $\overline{Q}$ is the mean gating

charge of the entire ensemble and equals to $\sum_i q_i P_i(V,x)$,where P_i (V, x) is the occupancy of the i[th] state at voltage V and ligand concentration, x. Similarly, $\overline{X}$ is the average number of bound ligands.

The differential change in free-energy in such a system will be:

$$d\overline{G} = \left(\frac{\partial \overline{G}}{\partial V}\right)_x dV + \left(\frac{\partial \overline{G}}{\partial \ln x}\right)_V d\ \ln x \ldots (14)$$

In Eq. 14, the subscript in each partial differential indicates the parameter held constant during the differentiation. Using our previous descriptions in Eq. 14, it can be shown that:

$$d\overline{G} = -\overline{Q}(V,x)\,dV - k_B T\,\overline{X}(V,x) d\ln x \ldots (15)$$

Suppose we measure the QV curve at a particular ligand concentration. Integrating the area under the curve will yield a measure of the net free-energy change that has occurred due to movement of all the gating-charges at the given ligand concentration:

$$\overline{G}(V_2,x) - \overline{G}(V_1,x) = -\int_{V_1}^{V_2} \overline{Q}(V,x)\,dV \ldots (16a)$$

This free-energy change is the work done to change the distribution of states by changing only voltage, while ligand concentration is maintained constant. It is important to note that although ligand concentration is maintained constant, thermodynamic linkage dictates that the average number of bound ligands to the protein changes with voltage, the only exception being the trivial situation when charge movement and ligand binding are completely energetically independent. A similar relationship can be derived for the ligand induced transformation at constant voltage, that is:

$$\overline{G}(V, x_2) - \overline{G}(V, x_1) = -k_B T \int_{x=x_1}^{x=x_2} \overline{X}(V, x)\, d \ln x \quad \ldots (16b)$$

As in the previous case, binding of ligand will lead to charge movement in the protein, despite voltage being maintained constant.

To deconstruct the free-energy changes associated with charge movement and ligand binding in such a system we look at the thermodynamic cycle shown in Fig. 2. Our initial reference state (S_{ref}) is the one where all the gating charges are in the resting state with no bound ligands. The final state of the system (S_{final}) is where all the gating charges have translocated to activated state and the channel is fully liganded. We are specifically interested in evaluating the free-energy difference between S_{final} and S_{ref} i.e. $\overline{G}(V \to \infty, x \to \infty) - \overline{G}(V \to -\infty, x = 0)$

The net free energy of activation of this system can be calculated in two different ways. In the first pathway, all the gating-charges are moved (step Ia) and subsequently the ligands are allowed to bind (step Ib), while in the second pathway, we first saturate the system with ligands (step IIa) and then allow the translocation of the gating-charges (step IIb). Each of these steps are associated with a free-energy change and, therefore, the net free-energy change associated with the full-scale activation of the protein is $\Delta G_{Ia} + \Delta G_{Ib} = \Delta G_{IIa} + \Delta G_{IIb} = \overline{G}(V \to \infty, x \to \infty) - \overline{G}(V \to -\infty, x = 0)$.

We first consider the free-energy estimation strategy along Path I. From our previous discussion, ΔG_{Ia} is estimable from the QV curve for the channel at zero ligand concentration, while ΔG_{Ib} can be calculated from the ligand binding curve obtained at highly depolarizing voltages. Thus the total free-energy change in the system, ΔG_{net}, can be obtained as:

$$\Delta G_{net} = \Delta G_{Ia} + \Delta G_{Ib} = -\int_{-\infty}^{\infty} \overline{Q}\,(V, x=0)\, dV - k_B T \int_{0}^{\infty} \overline{X}\,(V \to \infty, x)\, d\ln x \quad \text{... (17)}$$

The first integral in Eq.17 is the area under the QV curve at zero ligand concentration while the second is the area under the ligand binding curve at highly depolarized voltages, when all charge has moved. Similarly the free-energy estimation along the second pathway can be accomplished as:

$$\Delta G_{net} = \Delta G_{IIa} + \Delta G_{IIb} = -k_B T \int_{0}^{\infty} \overline{X}\,(V \to -\infty, x)\, d\ln x - \int_{-\infty}^{\infty} \overline{Q}\,(V, x \to \infty)\, dV$$

In the preceding equation the first integral is the area under the ligand binding curve at highly hyperpolarized voltages while the second integral is the area under the QV curve at saturating ligand concentrations. The chemical component of this free-energy change, ΔG_C^{net}, can be extracted by calculation of median variables. In summary,

$$\Delta G_C^{net} = Q_{\max} V_M \,|_{x=0} + k_B T\, N_{\max} \ln x_m \,|_{V \to \infty} = Q_{\max} V_M \,|_{x \to \infty} + k_B T\, N_{\max} \ln x_m \,|_{V \to -\infty} \quad \text{... (18)}$$

Voltage-dependence of ligand occupancy from charge-voltage curves

As shown in the previous section, if we measure the ligand binding curves at various voltages and the charge-voltage curves at various ligand concentrations, we can directly map the free-energy landscape for dual regulation by ligand and voltage. While the QV curves can, in most cases, be measured at different ligand concentrations, estimating the ligand binding curve at very high or very low voltages is not straightforward. In this section, we describe how this information can be extracted from principles of linkage thermodynamics.

Since the free-energy, $\overline{G}$, being a state function, the differential, $d\overline{G}$, (from Eq. 14) is exact. The result is following relation:

$$\frac{\partial^2 \overline{G}}{\partial \ln x \, \partial V} = \frac{\partial^2 \overline{G}}{\partial V \, \partial \ln x} \quad \ldots (19a)$$

or

$$\frac{\partial \overline{Q}}{\partial \ln x} = k_B T \frac{\partial \overline{X}}{\partial V} \quad \ldots (19b)$$

The differentials depicted in Eqs. 19a and 19b are reminiscent of Maxwell's thermodynamic relations. We multiply both sides of Eq. 19b with dV and perform the integration, i.e.:

$$k_B T \int_{V \to -\infty}^{V \to \infty} d\overline{X} = \int_{V \to -\infty}^{V \to \infty} \frac{\partial \overline{Q}(V, x)}{\partial \ln x} dV \quad \ldots (20a)$$

This integral equation can be re-written as:

$$k_B T \{ \overline{X}(V \to \infty, x) - \overline{X}(V \to -\infty, x) \} = \frac{\partial}{\partial \ln x} \int_{V \to -\infty}^{V \to \infty} \overline{Q}(V, x) \, dV = -Q_{\max} \frac{\partial V_M(x)}{\partial \ln x} \quad \ldots (20b)$$

Eq. 20b tells us that gradient of median voltage of activation with respect to the natural logarithm of the ligand concentration is linearly related to the change in the number of ligands bound to protein, due to change in voltage.

While it may be experimentally challenging to obtain ligand binding curves at different voltages, obtaining a single ligand binding curve in absence of membrane potential (0 mV) is relatively simpler. By using this reference binding curve and Q-V curves at different ligand concentrations it is possible to obtain entire ligand binding surface. Once again we look at Eq. 20a and integrate between finite limits, i.e.:

$$k_B T \int_{V_{ref}}^{V} d\overline{X} = \frac{\partial}{\partial \ln x} \int_{V_{ref}}^{V} \overline{Q}(V, x) \, dV = k_B T \{ \overline{X}(V, x) - \overline{X}(V_{ref}, x) \} \quad \ldots (21)$$

The right side of Eq.21 is the change in the ligand occupancy due to change in voltage from V_{ref} to V. This can be obtained by computing the gradient of the area under the QV curve, between V_{ref} and V, with respect to ln *x*. Since V is arbitrary and $\overline{X}(V_{ref}, x)$ (the ligand binding curve at a reference voltage) is available, we can potentially generate the entire ligand binding surface. Similarly, ligand dependence of Q-V curve can also be obtained once a reference Q-V curve and ligand binding curves at different voltages are generated.

Free-energy of interaction between voltage- and ligand-dependent pathways

In the bimodal systems considered here, a change in the QV curve due to changes in ligand concentration is due to energetic coupling of the voltage-dependent and ligand-dependent pathways. How can the strength of this energetic linkage be estimated? Under zero ligand conditions, the area under the QV curve is the work done to move all the charges when all the ligand binding sites are unoccupied (ΔG_{Ia}). Under saturating ligand conditions, the area bound by the QV curve is the work done to move all the charges when all the ligand binding sites are occupied (ΔG_{IIb}). The difference between the two energy measures is thus the energetic connectivity between the voltage-dependent and the ligand-dependent processes. Mathematically the net free-energy of interaction, $\Delta G_{V-X}^{\text{int}}$, between the ligand dependent and voltage dependent pathways is:

$$\Delta G_{V-X}^{\text{int}} = \Delta G_{IIb} - \Delta G_{Ia} = -\left(\int_{-\infty}^{\infty} \overline{Q}(V, x \to \infty)\, dV \; - \; \int_{-\infty}^{\infty} \overline{Q}(V, 0)\, dV \right) \quad \text{... (22)}$$

Thus the change in the areas under the QV curve between fully saturating and zero ligand concentrations gives a measure of the energetic connectivity between the voltage- and

ligand-dependent pathways. Specifically, if the maximum charge translocated in the voltage-dependent activation pathway is unchanged due to the ligand, Eq. 22 can be re-written as:

$$\Delta G_{V-X}^{\text{int}} = Q_{\max}(V_M|_{x\to\infty} - V_M|_{x=0}) = Q_{\max}\Delta V_M \ldots (23a)$$

This principle is illustrated for a hypothetical channel gated by voltage and ligand (Fig. 3a). As shown in Fig. 3b, the area between the QV curves measured at zero and fully saturating ligand concentrations, equals the area of the rectangle bound by the median voltage axes of the two QV curves. This area is the energetic facilitation afforded by ligand binding on the voltage-dependent activation pathway of the protein.

A similar relation can be derived for the ligand binding curve as well, wherein $\Delta G_{V-X}^{\text{int}}$ is estimated from the difference in the areas ligand binding curves obtained at highly depolarized (all gating-charge has moved) and hyperpolarized (all charges in resting configuration) voltages (Fig. 3c). This is a consequence of the thermodynamic cycle in Fig. 2: $\Delta G_{IIb} - \Delta G_{Ia} = \Delta G_{Ib} - \Delta G_{IIa}$. Thus in terms of the ligand binding curves, $\Delta G_{V-X}^{\text{int}}$ will be:

$$\Delta G_{V-X}^{\text{int}} = k_B T N_{\max} \ln\left(\frac{x_m|_{V\to\infty}}{x_m|_{V\to-\infty}}\right) \ldots (23b)$$

Eqs. 22, 23a and b have an important historical context to understand which we transform Eq. 22 as:

$$\Delta G_{V-X}^{\text{int}} = -\int_{-\infty}^{\infty}\frac{\partial}{\partial \ln x}\int_{-\infty}^{\infty}\overline{Q}(V,x)dV\,d\ln x = -\int_{-\infty}^{\infty}\int_{-\infty}^{\infty}\frac{\partial \overline{Q}(V,x)}{\partial \ln x}dV\,d\ln x \ldots (24)$$

The partial differential under the double integral on the left of Eq. 24 is an example of hetero-tropic linkage functions (Wyman, 1984; Gill et al., 1985; Wyman and Gill, 1990),

which have been the cornerstone of Wyman's linkage theory (Wyman, 1964b) and have been used to understand the cross-regulation of enzyme activity by multiple modulators. Our derivation that the double integral of the linkage function is an energetic measure of cooperativity (or linkage) in the system is one example of its utility. In general, the reason why such a mathematical formulation reflects cooperativity in a system can be understood by evaluating the partial differential in terms of the microscopic state/system variables:

$$\frac{\partial \overline{Q}\,(V,x)}{\partial \ln x} = \sum\nolimits_i q_i\, n_i\, P_i - \left(\sum\nolimits_i q_i\, P_i\right)\left(\sum\nolimits_i n_i\, P_i\right) = \overline{qn} - \overline{Q}.\overline{X} \quad \text{... (25)}$$

Noting the functional expression on the right of Eq. 25 it can be realized the linkage function is actually a measure of the covariance between gating-charge movement and ligand binding. If the two processes are strongly interdependent, the covariance will be higher and in the case of independent processes, the covariance will be zero.

RESULTS

Ligand binding curves as an estimate of total free-energy change in ligand gated ion channels

The first major conclusion of our thermodynamic treatment is that total free-energy change associated with saturating a macromolecule with a ligand is estimable from the ligand binding curve, via extraction of the median ligand activity ($\ln x_m$) and the maximum number of ligands that can bind to the macromolecule. This is fundamentally different from the Hill-equation based metrics to characterize the free-energy responses in ligand gated ion channels (Nache et al., 2008; Gleitsman et al., 2009). We consider two ligand-gated channels, the cyclic nucleotide gated (CNG) channels and the

hyperpolarization activated cyclic nucleotide gated (HCN) channels, both of whose direct ligand binding curves have been measured using a fluorescent ligand (Biskup et al., 2007; Kusch et al., 2010; Kusch et al., 2012). Kinetic models of activation of these channels have been developed using constraints from direct ligand binding and ionic current measurements. We compare the free-energy estimate obtained directly from the kinetic model parameters and the median metric, extracted from the simulated ligand binding curves.

In both these channels there are four ligand binding sites. In the reported models, cooperativity in the different ligand binding steps are asymmetric – the second and fourth steps of ligand binding show positive coupling, while the third step shows negative coupling. The ligand dependent activation of these channels can be described by a 10-state model with five closed and five open states, each of the five states being unique in the number of bound ligands (Fig. 4a) (Biskup et al., 2007; Kusch et al., 2012). Our initial reference state for both the channels is the closed state with zero ligands bound and the final state of the channel is the open state with all the ligand binding sites occupied with ligands. Using the equilibrium model parameters, we simulated the binding curves of both channels and extracted their median ligand concentrations (Fig. 4b). For the CNG channel, the median metric comes out to be ~ -29.4 kcal/mol that is nearly identical to the kinetic model based free-energy change estimate from state C_0 to O_4. This estimate is very different from the estimates derived by fitting the Hill-equation to the ligand binding curve (or the simulated dose response curve) (Table 1). Similarly for the HCN channel, the median metric and the kinetic model yield matching estimates of the total free-energy change for ligand-dependent activation of the channel. The simulations clearly

demonstrate the utility of the median metric and its applicability even when ligand binding steps are energetically asymmetric.

It is important to consider the limiting states of the ensemble while inferring energetics from these measurements. For the CNG channel model this is not a complication because P_O at zero ligand is very small while it is approximately one under saturating ligand concentration. On the other hand, for HCN channels, the minimum Po in absence of ligand is 0.55 (from kinetic models). Since the C to O transition is ligand independent, even in complete absence of ligand all the channels are not in C_0 state. As described in Chapter three (Chowdhury and Chanda, 2012a), we can apply equivalent correction factors to estimate the complete free energy of activation of ligand-dependent pathway. Thus, the net expression for the work done is saturating the channel with the ligand is:

$$\Delta G_C = N_{\max} RT \ln x_m - RT \ln P_O^{\max} + RT \ln (1 - P_O^{\min}) \quad \text{... (26)}$$

where $P_O^{\max}$ is the open probability at saturating ligand concentration and $P_O^{\min}$ is the open probability at zero ligand concentration. The first of the two correction factors ($-RT \ln P_O^{\max}$) accounts for the fact that at saturating ligand concentrations there might be some closed states with relatively large occupancy while the second ($RT \ln (1 - P_O^{\min})$) accounts for the fact that at zero ligand concentration, there might be substantial occupancy of the open states of the channel. For the case of the wild type HCN channel model, this correction factor amounts to ~ 0.5 kcal/mol which is much smaller than the median metric estimate alone. However, this might be an important consideration to accurately describe the activation energies of deleterious mutations.

Generating ligand binding curves at different voltages in allosteric ion channels dually modulated by voltage and ligand

Another important utility of the linkage principles described in the theory section is the ability to generate ligand binding curves at different voltages by measuring the QV curves at multiple ligand concentrations and one reference ligand binding curve (at zero voltage). Here, we test this idea using the BK channel for which well-described kinetic models are available (Rothberg and Magleby, 1998; Horrigan and Aldrich, 1999; Horrigan et al., 1999; Rothberg and Magleby, 2000; Horrigan and Aldrich, 2002; Niu and Magleby, 2002). We consider the two-tier HA model (Fig. 5a) with four identical voltage-sensing domains, each of which have an intrinsic activation constant, J_0 $J_0$and a voltage-dependence, z_J. The pore has an intrinsic activation constant L_0 L_0 and an intrinsic voltage-dependence, z_L. The equilibrium constant of activation of voltage-sensor (J) and that of the pore (L) are assumed to have an exponential voltage-dependence ($I = I_0 \exp(z_I FV/RT)$, where I = J or L). In absence of calcium, the voltage-dependent activation of the channel can be described by a 10-state MWC-type allosteric scheme (Cox et al., 1997; Cui et al., 1997; Talukder and Aldrich, 2000), wherein the pore is capable of opening but with reduced potency at very low voltages and depolarization induced activation of the voltage-sensing domains progressively facilitates channel opening. This facilitation is described by an interaction parameter, D. To explain the calcium regulation, it is assumed that there exists a single calcium binding site in each of the subunit, each with a dissociation constant K_D. The binding equilibrium constant is described as: x/K_D. Calcium binding can facilitate the opening of the pore, via an interaction described by the parameter, C. It could also facilitate activation of the voltage-

sensing domain (within the same subunit), via an interaction parameter, E. This model of channel activation has been shown to accurately describe the steady-state and kinetic properties of channel gating over a wide range of voltages and ligand concentrations and hence will be the primary model on which we test our derivations.

We simulated the QV curves at different ligand concentrations using the parameters described by Horrigan and Aldrich (Horrigan and Aldrich, 2002). To estimate the ligand-dependent change in ligand occupancy at a particular voltage (200 mV), we evaluate the area bounded by V=0 and V=200 axes and the Q-V curve at each ligand concentration (Fig. 5b). By plotting these areas at closely spaced ligand intervals (Fig. 5c), we can obtain the gradient of this area with respect to ligand concentrations (Fig. 5d). This gradient gives us the change in ligand occupancy at a given ligand concentration due to change in voltage (Eq. 26). When this plot is added to the reference binding curve, we generate a ligand binding curve at 200 mV (Fig. 5e). This procedure can be repeated at various voltages to obtain voltage-dependent ligand binding curves.

Using such a method of estimation, the total free-energy change associated with full-scale activation of the BK channel is estimated as ≈ -24 kcal/mol. This value is nearly identical to that estimated from the model parameters (Table 2). It is to be noted that the reference binding curve used in Fig. 5e is inferred directly from the kinetic model – direct calcium binding curves for the BK channel has not yet been measured, although calcium induced conformational changes in purified preparations of calcium binding domains have been spectroscopically monitored (Yusifov et al., 2010).

The principle utility of the formulation shown in Fig. 5 is that it allows us to estimate the total free-energy of activation of the channel. It is important to remember

that, standard biochemical assays of ligand binding are performed over time-scales much longer than those of electrophysiological recordings. This may allow the proteins to populate slowly-accessible long-lived desensitized states (Colquhoun, 1998) that are not normally detectable during the time scale of electrophysiology measurements. The median metric extracted from such binding curves, would incorporate the free-energy contributions of such transitions, along with the energetic changes occurring during the early channel activation transitions. Thus to estimate the free-energy energy of activation (i.e. the transition from the first closed state, where all voltage sensors are resting and all ligand binding sites are unoccupied to state final open, conducting state, where all voltage sensors are activated and all ligand bind sites are occupied) one needs to incorporate a correction factor related to the maximum open probability at saturating ligand concentrations and very high voltages, measured at very long time scales. The final free-energy equation(s) in this scenario will be:

$$\Delta G_C^{net} = Q_{\max} V_M \,|_{x=0} + k_B T\, N_{\max} \ln x_m \,|_{V\to\infty} - k_B T \ln P_O(V \to \infty, x \to \infty, t \to \infty) \quad \ldots \quad (27a)$$

$$\Delta G_C^{net} = Q_{\max} V_M \,|_{x\to\infty} + k_B T\, N_{\max} \ln x_m \,|_{V\to-\infty} - k_B T \ln P_O(V \to -\infty, x \to \infty, t \to \infty) \quad \ldots \quad (27b)$$

where, $t \to \infty$ indicates that the measurements are made on a very long time scale. The P_O based correction factors added to Eq. 27a and b are likely to be very important as desensitization in several instances drastically reduces P_O (in some cases almost to baseline levels), especially at long time scales. Unless these limiting P_Os are measured accurately, which might be quite difficult, the free-energy estimates obtained from Eq. 27 will be highly inaccurate. It is to be noted that for the kind of systems to which this discussion directly pertains to (e.g. BK channels) the existence of such deep desensitized states have not yet been reported. This issue however may be more pertinent for the cys-

loop receptor channels, which are not directly voltage-dependent and are not the systems towards which our current discussion is geared towards.

Energetic interdependence of voltage and ligand induced transitions in bimodal allosteric ion channels

To obtain the interaction energy between the ligand and voltage-dependent pathways, we generated QV curves at zero and fully saturating calcium concentrations using the parameters described by the HA model (Horrigan and Aldrich, 2002). Thereafter each of the parameters were varied over several orders of magnitude and in each case we extracted the median voltage at V_M at zero calcium (V_M (x=0)) and at saturating calcium concentrations (V_M (x_{sat})) from the simulated QV curves. For this system, $Q_{max} = 4z_J + z_L$. We plotted $Q_{max}F\Delta V_M$ ($\Delta V_M = V_M(x_{sat}) - V_M(x=0)$) against different values of K_D, J_0, L_0 and D (Fig. 6a). The plot shows that this free-energy metric, $Q_{max}F\Delta V_M$ is completely independent of the ligand binding affinity, intrinsic stability of the voltage-sensing and pore domains as well as the voltage-sensor and pore coupling.

Next, we simulated the QV curves for three characteristic model parameters provided by HA (Fits A, B and C) at multiple calcium concentrations and plotted the V_M values at those ligand concentrations (Fig. 6b). Fit B was chosen as the best fit by Horrigan and Aldrich based on multiple tests. Interestingly, the V_M versus ln *x* plots show that each of the fits generate characteristically different features. When only the interaction terms of the ligand binding domains (parameters C and E) were modified for Fit B to match those in Fit A, a different curve was generated. Strikingly, the V_M values converge at limiting ligand concentrations as long as the interaction terms between the

two sets of model parameters are the same. Next we plotted $Q_{max}F\Delta V_M$ against different values of the parameters C and E (Fig. 6c). The planar 3D surface generated shows that $Q_{max}F\Delta V_M$ is linearly related to interaction energies of the ligand binding domain with the voltage-sensor and the pore even when they are varied over several orders of magnitude.

Are these numerical simulations consistent with our theoretical proposition? To understand this we first write the partition function for this system:

$$Z = (1 + J + K + JKE)^4 + L(1 + JD + KC + JKCDE)^4 \quad \text{... (28)}$$

Under zero calcium conditions, K = 0 and Eq. 28 reduces to:

$$Z(x=0) = (1+J)^4 + L(1 + JD)^4$$

$Q_{max}FV_M$ (x=0) is the measure of the non-electrical free-energy change associated with full-scale voltage-dependent activation of the channel. Thus:

$$Q_{max}FV_M(x=0) = -RT\ln\left(\frac{\lim_{V\to\infty} Z(x=0)}{\lim_{V\to-\infty} Z(x=0)}\right) + Q_{max}FV = -RT\ln\left(J_0^4 D^4 L_0\right)$$

At saturating calcium conditions, Eq. 28 reduces to:

$$Z(x\to\infty) = K^4(1 + JE)^4 + LK^4C^4(1 + JDE)^4$$

The median metric will now yield the following free-energy measure:

$$Q_{max}FV_M(x\to\infty) = -RT\ln\left(\frac{\lim_{V\to\infty} Z(x\to\infty)}{\lim_{V\to-\infty} Z(x\to\infty)}\right) + Q_{max}FV = -RT\ln\left(J_0^4 D^4 C^4 E^4 L_0\right)$$

From this analysis it is easily seen that the net change in the median voltage of charge movement will be given by:

$$Q_{max}F\Delta V_M = Q_{max}FV_M(x\to\infty) - Q_{max}FV_M(x=0) = -RT\ln(C^4E^4) \quad \text{... (29)}$$

The conclusion is that the net displacement of the QV curve upon ligand binding is solely determined by the interaction of the ligand binding domain with the voltage-sensor and the pore.

These simulations illustrate our theoretical results and highlight the crucial utility of QV curve measurements in understanding ligand-dependent gating of polymodal systems such as the BK channels. The model of the BK channel considered here, to some extent, is restrictive since it assumes that there exists a single ligand binding site per subunit of the channel which is allowed to interact with the voltage-sensor only of the same subunit (Bao et al., 2002; Shi et al., 2002; Xia et al., 2002; Magleby, 2003). In the Chapter Addendum we show that our overall relationship is valid even when there is more than a single binding site per subunit of the protein.

A striking outcome of Eq. 29 is that for a constant value of C and E, Q_{max} and ΔV_M will be inversely related. For the two sets of parameters (Fit B and B`), we plotted z_J, the intrinsic voltage dependence of voltage-sensors with respect to ΔV_M (Fig. 6d). The curves clearly show the net sensitivity of the QV curve (due to ligand concentrations) reduces as z_J increases. Furthermore, if z_J is large the V_M shifts due to changes in coupling interactions are attenuated. This can be mathematically proven by differentiating Eq. 29 with respect to z_J for a constant value of C and E:

$$\frac{\partial \Delta V_M}{\partial z_J} = \frac{4RT \ln(C^4 E^4)}{F} \frac{1}{(4z_J + z_L)^2} \quad \text{... (30)}$$

Eq. 30 demonstrates that the total gating charge on the channel can influence its sensitivity to ligands. Significantly, the estimated total gating charge of BK channels is ~2.5 e_o (Ma et al., 2006) , which is much lower than that of a canonical voltage-gated ion

channels such as the Shaker Kv channel (Schoppa et al., 1992; Aggarwal and MacKinnon, 1996; Seoh et al., 1996)).

Linkage relationships in a hyperpolarization and ligand activated channel with a voltage-independent pore

In this section, we consider the hyperpolarization activated, cyclic nucleotide gated HCN channels in which the pore is believed to be intrinsically voltage-independent and negative coupling with the four identical voltage-sensing domains causes it to close as the voltage-sensors activate (Altomare et al., 2001; Chen et al., 2007). However, ligand binding favors channel opening like the BK channel.

To address such a system we modify the thermodynamic cycle (Fig. 7). We chose the closed channel state as a reference state which in this case is predominant at high voltages and zero ligand concentration. This was necessitated by the fact that the ligand binding domain and voltage-sensors are oppositely coupled to the pore unlike BK channels. The final state of the system is the open state where all ligand binding sites are saturated with ligand and all voltage-sensors are deactivated. As shown in Fig. 7, this transformation can be achieved via two paths. Applying the principles that we have detailed in the previous sections on this thermodynamic cycle our primary energy-linkage equation is:

$$\Delta G_{V-X}^{\text{int}} = -Q_{\max} F \Delta V_M = -RT\, N_{\max} \ln\left(\frac{x_m\,|_{V\to\infty}}{x_m\,|_{V\to-\infty}}\right)$$

However, unlike the BK channels the HCN channels the Po does not approach unity at hyperpolarizing conditions in absence of ligand. This means that an ensemble of states is populated under these conditions. To account for this multiplicity of states, we

add a correction term to the interaction energy for HCN channels.

$$\Delta G_{V-X}^{\text{int}}\ (corr.) = -Q_{\max} F \Delta V_M + RT \ln P_O\ (V_{\min}, x_{\min}) \ldots (31)$$

The correction factor used in Eq. 31 is equivalent to that shown in Eq. 26 for the ligand dependent activation. In the wild-type channel, the Po value is zero or unity under all other limiting conditions of voltage and ligand. However, many mutations compromise the channel ability to fully close or fully open and thus the Po values at each of the four limiting conditions have to be taken into account to calculate the net interaction energy for the voltage- and ligand-dependent pathway. Thus, extending Eq. 31 for the thermodynamic cycle shown in Fig. 7, we can write a general from of net interaction energy between the two pathways is:

$$\Delta G_{V-X}^{\text{int}} = -Q_{\max} F \Delta V_M + RT \ln\left(\frac{P_O(V_{\min}, x_{\min})(1 - P_O(V_{\max}, x_{\max})}{P_O(V_{\min}, x_{\max})(1 - P_O(V_{\max}, x_{\min})}\right) \ldots (32)$$

where V_{min} and V_{max} are the highly hyperpolarizing and depolarizing limits respectively and x_{min} and x_{max} are the zero and saturating ligand concentrations respectively.

For HCN2 channels, ligand binding curves have been measured at multiple voltages using confocal microscopy combined with voltage clamp fluorimetry. However, to the best of our knowledge, the QV curves for the same subtype is not available (although Q-V curves for spHCN channels have been reported (Mannikko et al., 2002; Mannikko et al., 2005)). Using the binding curves reported in Kusch et al. 2010 , our thermodynamic relationships (Eq. 23a, 23b and 32) allow us to predict that the net interaction energy between the ligand binding domain and other domains for HCN2 channels is nearly -3 kcal/mol (Table 3). Furthermore, from the kinetic model for ligand induced activation of the HCN2 channel, the net interaction between the ligand-binding

domains and the pore can be estimated to be ≈ -2.2 kcal/mol. This implies that the net energetic coupling the voltage-sensors and the ligand binding domains is weak (~ -0.8 kcal/mol). This is consistent with the notion that cAMP binding to the HCN channels do not affect the voltage-dependent transitions but modifies the final, voltage-independent closed-open transition (Craven and Zagotta, 2004; Shin et al., 2004). It is to be noted however that the coupling associated with ligand binding domains in the HCN2 channels is not completely symmetric (Ulens and Siegelbaum, 2003) – some steps (second and fourth) show positive coupling while the others (third) shows negative coupling (Kusch et al., 2012). Hence the relative small interaction energy estimates may be the result of the net balance of interaction energies. It should be possible to test this prediction directly by measuring the QV curves at different ligand concentrations and using Eqs. 23a and b to calculate ΔG^{int}_{V-x}.

DISCUSSION

In Chapter three, we have shown that the net free-energy associated with voltage-dependent activation of an ion channel can be estimated by extracting the median voltage of activation from the QV curve using the relation:

$$\Delta G_C = Q_{\max} F V_M$$

This relationship is analogous to Wyman's thermodynamic description of ligand binding equilibrium (Wyman, 1967) which when applied to ligand-dependent ion channels, yields the relation:

$$\Delta G_C = N_{\max} RT \ln x_m$$

Thus for ligand gated ion channels, the total work done to drive the channels to activated conformation can be obtained by measuring the median ligand activity and the maximum number of bound ligands.

Here, we extend these thermodynamic principles to develop the free-energy relationships in ion channels dually modulated by voltage and ligand. For these systems the net free-energy change for activation by both ligand and voltage is:

$$\Delta G_C^{net} = Q_{\max} V_M \mid_{x=0} + k_B T\, N_{\max} \ln x_m \mid_{V\to\infty} = Q_{\max} V_M \mid_{x\to\infty} + k_B T\, N_{\max} \ln x_m \mid_{V\to-\infty}$$

Thus, using the Q-V curves at zero ligand concentrations and ligand binding curves at depolarizing conditions, we can determine the net free energy for activation of a voltage and ligand activated channel. The thermodynamic cycle (Fig. 2) dictates that we can also obtain the same information by measuring the Q-V curves at saturating ligand concentration and ligand binding curves at hyperpolarizing conditions.

While Q-V curves at zero and saturating ligand concentrations can be obtained, measuring ligand binding curves at various holding potentials is not straightforward. Recent technological developments have allowed us to directly estimate the ligand binding curves for certain ion channels but this approach has not been extended to many other voltage and ligand activated ion channels. Here, we derive another thermodynamic relationship which allows us to estimate the ligand curves at various potentials by using a single reference ligand binding curve. Accordingly, the ligand occupancy at various voltages and ligand concentrations is:

$$\overline{X}(V,x) = \overline{X}(V_{ref},x) + \frac{1}{RT}\frac{\partial}{\partial \ln x}\int_{V_{ref}}^{V} \overline{Q}(V,x)\, dV$$

If we obtain ligand occupancy at a particular voltage and ligand concentration, $\overline{X}(V_{ref}, x)$, then Q-V curves for this channel at various ligand concentrations will allow us to generate the entire ligand binding surface. This formulation is further illustrated in Fig. 5. Typically ligand binding curves are measured biochemically using detergent solubilized protein preparations which lack voltage-gradient (Szallasi et al., 1999; Jordt and Julius, 2002; Picollo et al., 2009; Piscitelli et al., 2010; Yusifov et al., 2010). In such cases, V_{ref} is 0 mV and this ligand binding curve can serve as a reference. Similarly, using multiple ligand binding curves at different voltages, we can also obtain Q-V curves at multiple ligand concentrations as long as a single reference Q-V curve is available.

These thermodynamic relationships need some qualifications. The median metric of net free-energy change of polymodal channel (Eq. 18) incorporates all the sources of free-energy change in the system including the (true) binding energies of the ligands, the relative stabilities of the voltage-sensors and the pore as well as interactions between them. In case the channel undergoes inactivation/desensitization, its free-energy contribution is also linearly incorporated in the median metric. This free-energy metric allows us to characterize the net energetic effect of a site specific perturbation (which includes its effect on the free-energies of all transitions accompanying the “full-scale” activation of the protein) without any assumptions about the nature and connectivity of intermediate states. Under conditions, correction factors have to be considered which can be obtained by using open probability measurements.

Possibly the most important thermodynamic relationship that we propose here is that the difference between V_M of the QV curves, measured at saturating and zero ligand concentrations, directly yields as estimate of the interaction energy between the voltage-

dependent and the ligand dependent pathways of the channel. This interaction energy can also be estimated from the shift in the ligand binding curve between hyperpolarizing and depolarizing voltages:

$$\Delta G_{V-X}^{\text{int}} = Q_{\max} F \Delta V_M = RT\, N_{\max} \ln\left(\frac{x_m|_{V\to\infty}}{x_m|_{V\to-\infty}}\right)$$

This relationship is independent of the number of possible intermediates and the nature of connectivity between them. This is an important experimental advantage, since identification of allosteric pathways in the complex polymodal ion channels most often requires tedious and complex model fitting procedures. For instance, in the Horrigan and Aldrich model for BK channels, ligand binding involves four identical and independent binding sites. However, additional ligand binding sites have been described some of which also interact with each other (Bao et al., 2002; Shi et al., 2002; Xia et al., 2002; Magleby, 2003; Sweet and Cox, 2008; Zhou et al., 2012). By measuring the ΔV_M value and total gating charge, we can estimate the interaction energies of the binding sites with the voltage-dependent pathways as was shown for BK and HCN channels in Tables 2 and 3. This approach can be also used to identify sites which mediate coupling interactions between voltage and ligand dependent pathways. Note that in case the channel undergoes slowly developing desensitization transitions during binding measurements (not observed in the time scale of gating current measurements), correction factors, related to the limiting P_O values (as described in Eq. 27) need to be incorporated with the median ligand concentration measures.

It is important to note that this energy metric is a *de facto* measure of interaction energy only in systems, which are allosteric in nature. For instance, in BK channels,

voltage-sensor activation, ligand binding and pore opening are independent equilibria but they interact with each other allosterically. To ascertain whether such an allosteric framework is applicable, two conditions have to be satisfied. First, Q_{max} of the protein is independent of ligand concentration such that irrespective of ligand concentration, all the charges can be moved if sufficiently large voltage is applied. Second, the shift in the QV curve saturates at both high and low ligand concentrations. If either condition is not fulfilled, it would imply that certain transitions are under the obligatory control of the ligand and occur only in the presence of ligand. Similar conditions apply to ligand binding phenomenon wherein the maximum possible occupancy is independent of voltage and the shifts in ligand binding curves saturate at limiting voltages. Additionally, in allosteric systems where ligand binding processes are directly voltage-dependent due to the interaction of the ligand with the membrane electric field, Q_{max} for the voltage-dependent transitions might change with ligand concentration and the effect of ligand on Q_{max} (in addition to V_M) must be taken into consideration in the calculations described.

The median method of interaction energy has the advantage that it can provide an estimate of interaction energy in a relatively straightforward manner. Other methods such as the χ-value analysis (Chowdhury and Chanda, 2010) can also provide an estimate of interaction energies but these measurements require limiting conditions where the signal to noise is low. The BK channels, for instance, have a large single channel conductance, which makes it possible to obtain these estimates at potentials where the Po values are less than 10^{-8}. Most other ion channels have approximately 10 fold lower single channel conductances which makes such measurements under limiting conditions a challenging proposition. To eschew potential incorrect experimental application of our

thermodynamic relationships it must be emphasized that these relationships may be applied directly using only QV curves or the direct ligand binding curves and not the more commonly used conductance-voltage or dose-response curves. Channel open probability measurements sample only the states which are conducting and thus cannot be used directly as the conjugate extensives to extract the energetic details of the system, as described here.

Allosteric voltage-dependent ion channels such as the BK, HCN and KCNQ channels are known to be acutely sensitive to ligands, such as calcium, cyclic nucleotides, PIP_2, etc. However all of these channels are believed to have a much lower Q_{max} than the Shaker K_V channels (Craven and Zagotta, 2006; Ma et al., 2006; Miceli et al., 2012) despite having a large number of positively charged residues on their S4 segments. Additionally, experimental evidence have been reported wherein mutation of a gating charge residue in the S4 segment of BK channel increased the channel's sensitivity to calcium (Cui and Aldrich, 2000). This mutual reciprocity may initially seem to be obvious, considering a simplified two-state process where the single transition is directly influenced by voltage and ligand. Nevertheless it is unclear why this inverse correlation should hold in multi-state allosteric systems where voltage and ligand act through different pathways. Furthermore, quantification of such correlations, using the simplified two-state process based calculations, is at best empirical. Our generalized thermodynamic analysis shows that if the interaction energy remains unchanged, changes in ligand concentration will cause greater shifts in the Q-V curves if the gating charge is reduced. In other words, even if the interaction energy between two pathways is modest, the voltage-dependent activation will appear to be very sensitive to ligand concentration as

long as the total gating charge is small. This implies that for proper physiological function of these polymodal channels, both the charge and interaction energies associated with the ligand binding domains have to be optimized. Thus, a low value of Q_{max}, observed in many polymodal allosteric channels, may provide an evolutionary advantage, which renders channel gating highly sensitive to specific ligands.

CHAPTER CONTENT

Significant portions of this chapter (text, figures and tables) are adapted from: "Chowdhury, S., and Chanda, B., *Free-energy relationships in ion channels activated by voltage and ligand.* The Journal of General Physiology, 2013, 141(1):11-28"

FIGURES

Figure 1. Median ligand activity of an arbitrary three-step ligand binding process.

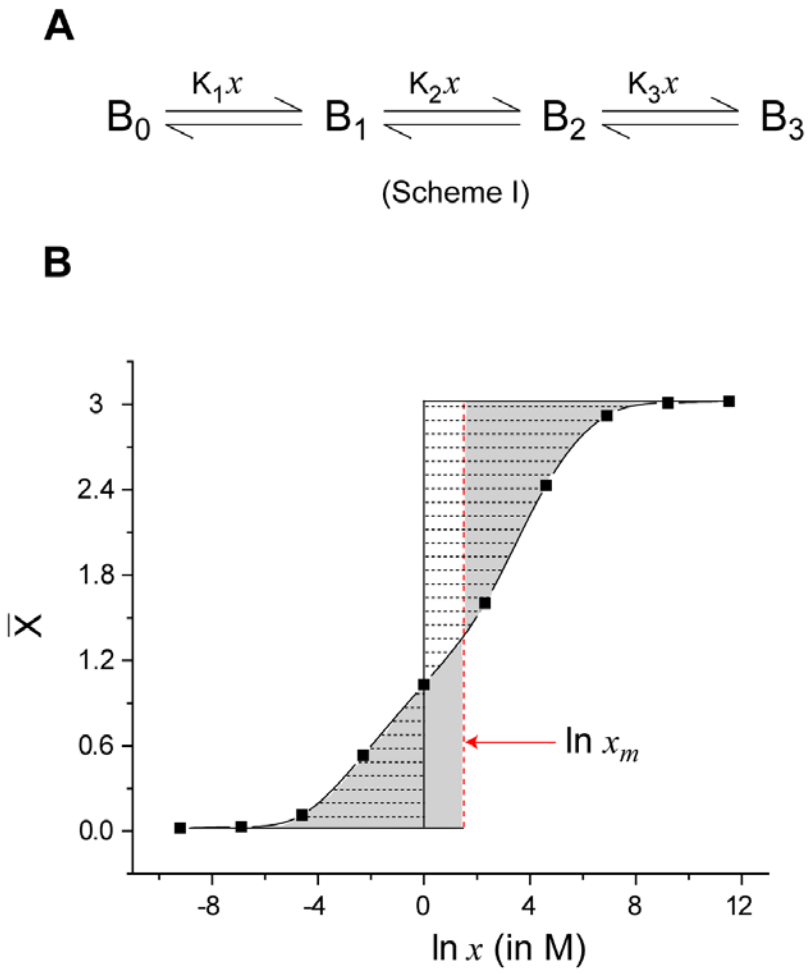

(A) A three-step sequential ligand binding process (N_{max} = 3) where B_i represents the state of the protein with 'i' ligands bound (i = 0,1,2 and 3) and K_j is the equilibrium constant for the j^{th} step of the process (j = 1, 2 or 3). In each step a single molecule of the ligand binds to the protein, B. **(B)** The ligand binding curve for Scheme I generated using arbitrary values of K_j (K_1 = 0.01 M^{-1}, K_2 = 0.1 M^{-1}, K_3 = 10 M^{-1}). The area between the binding curve and the ln x = 0 axis (demarcated by horizontal dashed lines) represents the integral, $\int_0^{N_{max}} \ln x \, d\bar{X}$. By virtue of the integration, the area on the right of the ln x = 0

axis (solid black vertical line) is negative and that on its right is positive. The sum of these areas (taking their signs into consideration) is a measure of total free-energy associated with saturating the protein with the ligands (= $\Delta\bar{G}_c/RT$, where $\Delta\bar{G}_c = -RT\ln(K_1K_2K_3)$). The vertical red dashed line is the median ligand activity axis. By its definition, the two regions on either side of the ln x_m axis, are equal in area. Eq. 11 implies that the region demarcated by the horizontal dashed lines and the rectangle defined by the ln x = 0, ln x_m, $\bar{X} = 0$ and $\bar{X} = N_{max}$ lines are equal in area and both give a measure of $\Delta\bar{G}_c$.

Figure 2. A thermodynamic cycle for a channel dually modulated by voltage and ligand.

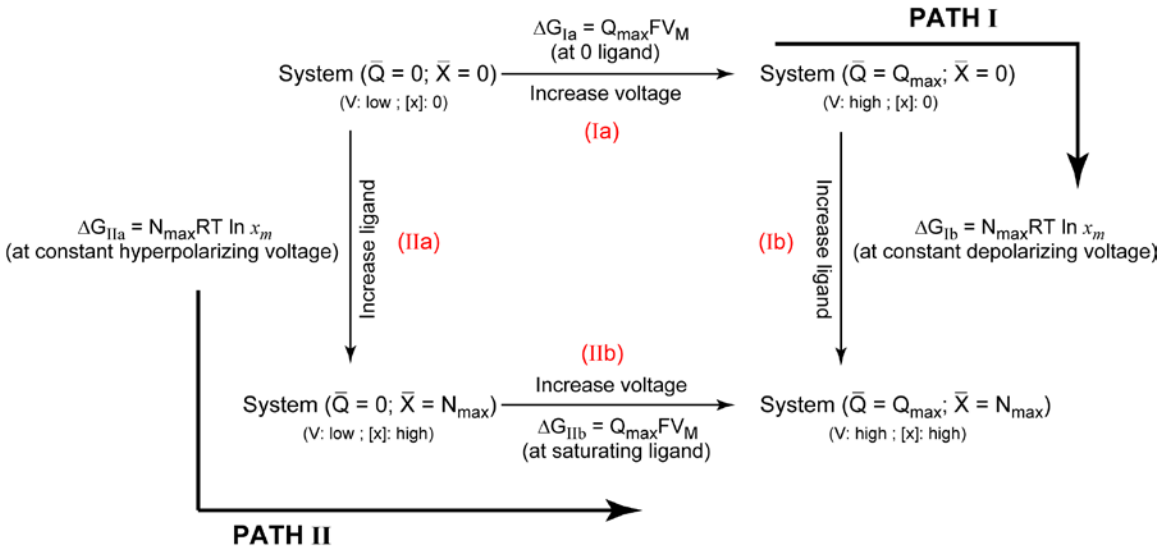

The reference state of the system is that in which all gating charges are in resting position and all ligand binding sites are unoccupied (at hyperpolarizing voltages and zero ligand concentration). The final state of the system is where all gating charges have moved and all ligand binding sites are occupied by the ligand (depolarizing voltages and saturating ligand concentrations). The free-energy difference between these two states can be calculated by two different ways. In **Path I**, in Q-V is measured at zero ligand concentration followed by ligand binding curve at highly depolarized voltages. In **Path II**, ligand binding curve is measured at hyperpolarizing voltages whereas the Q-V curve is measured at saturating ligand concentration. The free energy expressions for each of the steps is shown alongside.

Figure 3. Energetic linkage between the voltage-dependent and ligand-dependent pathways.

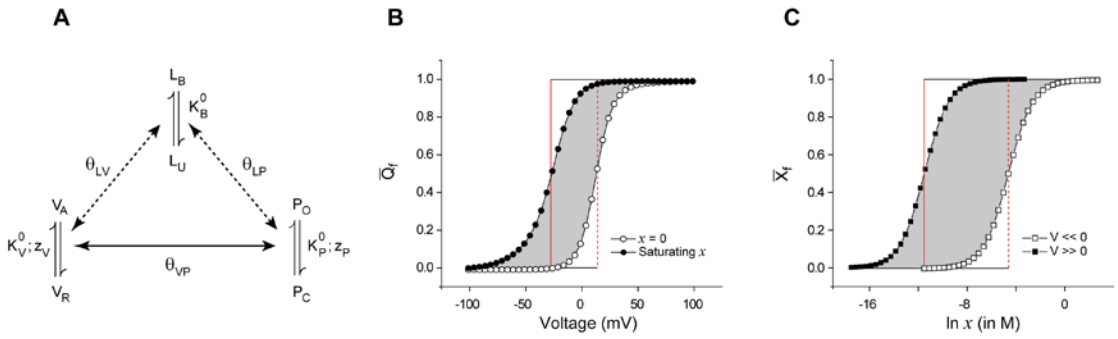

(A) A allosteric model of a hypothetical ion channel with a single voltage-sensing and ligand binding domain. The voltage-sensor exists in two states (V_R and V_A) and the intrinsic equilibrium constant for activation is K_V^0 which has voltage dependence of z_V. The pore unit has an intrinsic activation constant and intrinsic voltage-dependence given by, K_P^0 and z_P respectively. The ligand binding domain has an intrinsic binding affinity of K_B^0. All the three "structural units" are allosterically coupled to each other via interactions represented by the terms, θ_{VP}, θ_{BV} and θ_{BP}. The model parameters are K_V^0 = 0.1, K_P^0 = 0.01, K_B^0 = 100 M^{-1}, θ_{VP} = 100, θ_{BV} = 1, θ_{BP} = 1000, z_V = 2.5, z_P = 1.5. **(B)** Simulated fractional gating charge displacement (Q_f vs V) curves for this system at saturating (open circles) and zero (closed circles) ligand concentrations. The red dashed line is the V_M axis for each of the curves and the shaded area is equal to area of the rectangle bound the two V_M axes. This area when scaled by Q_{max} of the system ($=z_P+z_V$), gives the net energetic facilitation of the voltage-dependent pathway by the ligand and is equal to $-k_BT\ln(\theta_{BV}\theta_{BP})$. **(C)** The fractional ligand binding curves (X_f vs ln x) at very low (closed circles) and very high voltages (open circles) and the red vertical lines are the corresponding ln x_m axes. The area of the shaded region is equal to area of the rectangle

bound the two ln x_m axes which when scaled by N_{max} of the system (equals to 1 in this case) and k_BT , gives the net energetic facilitation of the ligand-dependent pathway by voltage and is equal to $-k_BT\ln(\theta_{BV}\theta_{BP})$. Note that the two shaded in area in **(B)** and **(C)** after the appropriate scaling will be equal.

Figure 4. Comparison of median estimates of free-energy change in CNG and HCN channels.

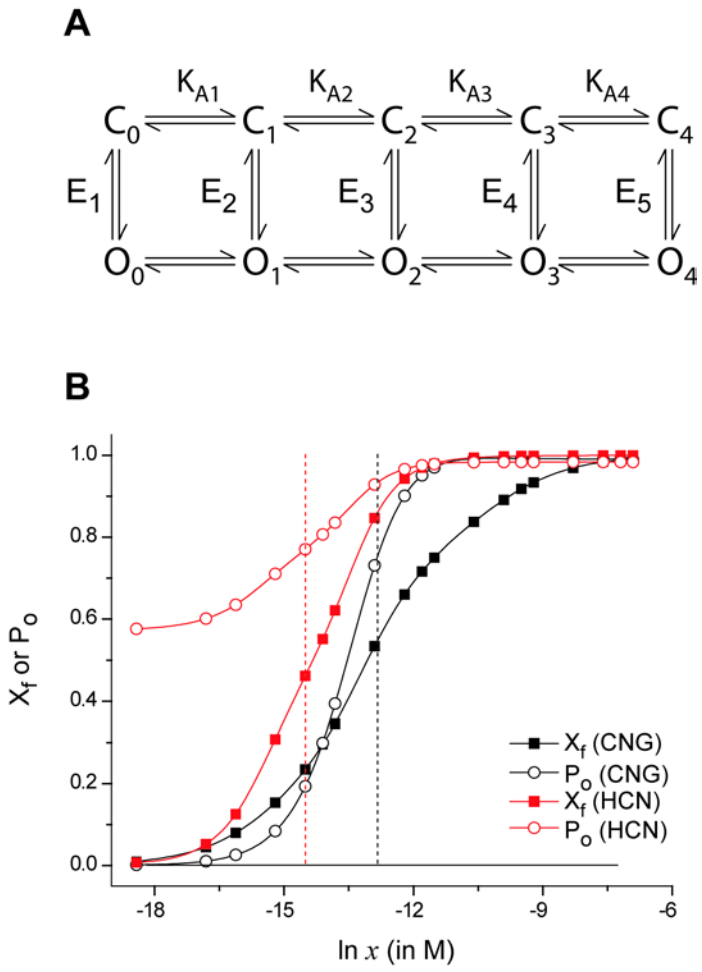

(A) The proposed model of the ligand induced activation pathway of the CNG and HCN channels. There are 5 open and closed states (labeled O_i and C_i, (i=0, 1, 2…,4), where 'i' represents the number of ligands bound to state). K_{Ai} (i=1, 2, 3 or 4) indicate the step-wise binding affinities of the ligand in the closed state. E_i (i=1, 2,..,5) represents the closed-open equilibrium constant for a unique ligation state of the channel. For the CNG channel, each state is considered to have a multiplicity of 4!/(4-i)!i! (i=0,1,2,…,4) while for the HCN channel, each of the states are considered to be unique (multiplicity = 1). **(B)**

Using the model parameters provided in (Biskup et al., 2007)(for the CNG channel) and (Kusch et al., 2012)(for the HCN channel), the steady-state open probability curves (open symbols) and the fractional binding curves (closed symbols) were generated. The vertical dashed lines represent the median ligand concentration axes for the CNG (black) and HCN (red) channels. For the HCN channels, these curves represent the channel response at -130 mV.

Figure 5. Generating ligand binding curves at different voltages using QV curves at different ligand concentrations

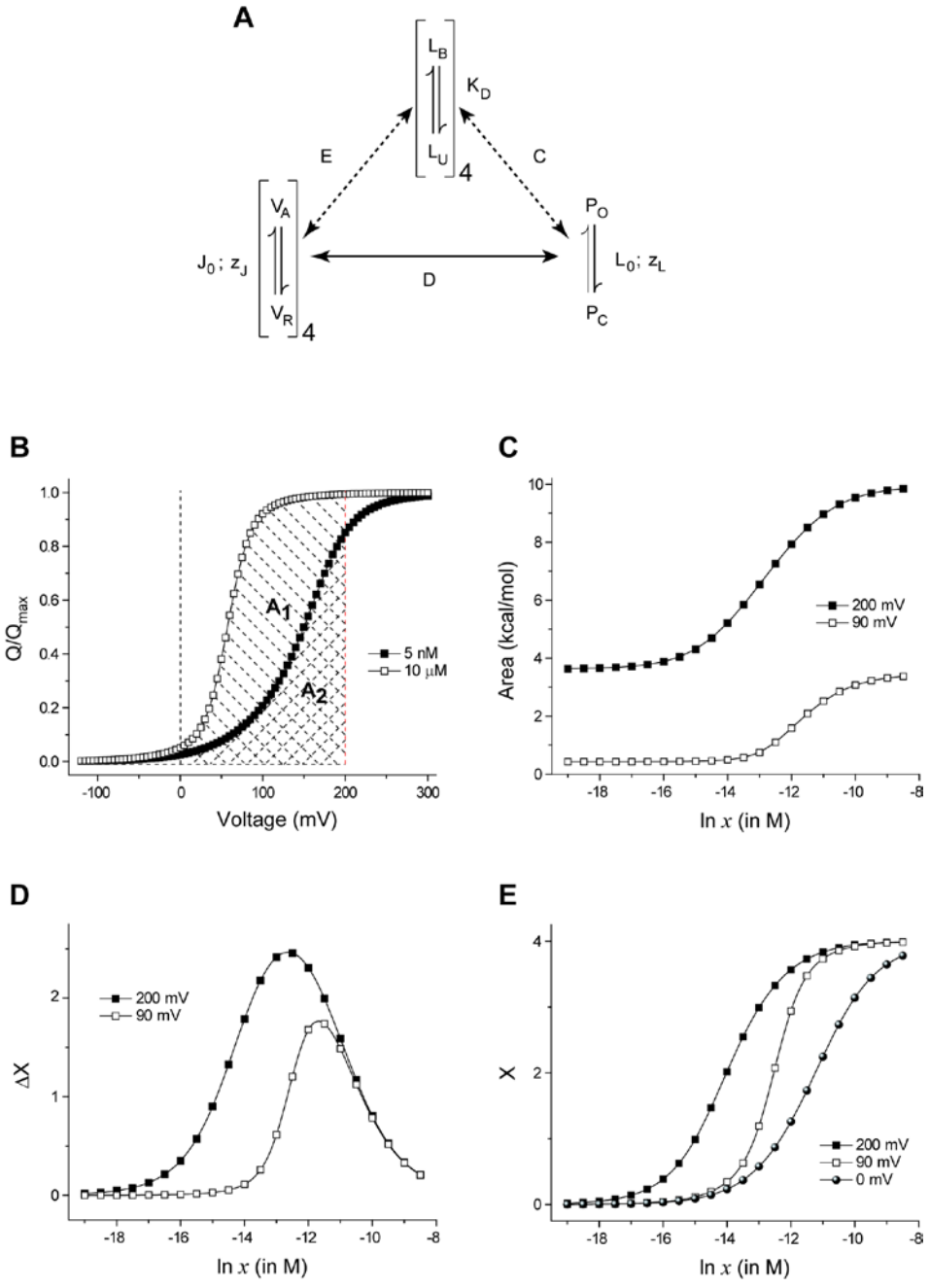

(A) The allosteric model proposed for the BK channel (Horrigan and Aldrich, 2002). There are four voltage-sensing domains, four ligand binding sites (one per subunit) and a

single pore. Each of the voltage-sensors and the ligand binding sites are allosterically linked to the pore. Each ligand-binding site is coupled to a single voltage-sensor (in the same subunit). J_0 and L_0 are the voltage-independent components of the equilibrium constants of activation of the voltage-sensor and the pore respectively. z_J and z_L reflect the voltage-dependence of activation of each voltage-sensor and the pore. K_D is the dissociation constant of each of the ligand binding sites. The voltage-sensor and pore coupling is described by the cooperativity parameter, D. E and C depict the cooperativity parameters describing coupling of the ligand binding sites with the voltage-sensors and pore respectively. The best fit estimates of these parameters (Fit B(Horrigan and Aldrich, 2002)) are: $J_0 = 0.0319$, $K_D = 0.000011$, $L_0 = 9.8\times10^{-7}$, C = 8, D = 25, E = 2.4, $z_J = 0.58$, $z_L = 0.3$. **(B)** QV curves at two ligand concentrations, for the model shown in **(A)**. The cross-hashed area (A_2) is the area under the QV curve at 5 nM ligand, between 0 and 200 mV. The area under the QV curve at 10 μM ligand, between 0 and 200 mV is the total shaded area ($A_1 + A_2$). **(C)** The area under the QV curve between 0 and 200 (or 90) mV is plotted against ligand concentration. As the ligand concentration increases, the QV curve shifts left and this area increases as depicted in **(B)**. **(D)** The change in ligand occupancy of the protein due to increasing voltage from 0 to 200 (or 90) mV is plotted against different ligand concentrations. Note that in the intermediate ligand concentrations (ln x between -15 and -10), changing voltage brings about a large change in the mean number of ligands bound to the protein, even though the ligand concentration is unchanged. **(E)** The linkage-equation derived ligand binding curve at 200 and 90 mV obtained by adding ΔX vs. ln x curves for individual voltages to the reference ligand

binding curve. In this case, the reference binding curve was generated by using the model parameters.

Figure 6. Dependence of the shift of QV curves due to ligand concentration on different parameters of an allosteric model.

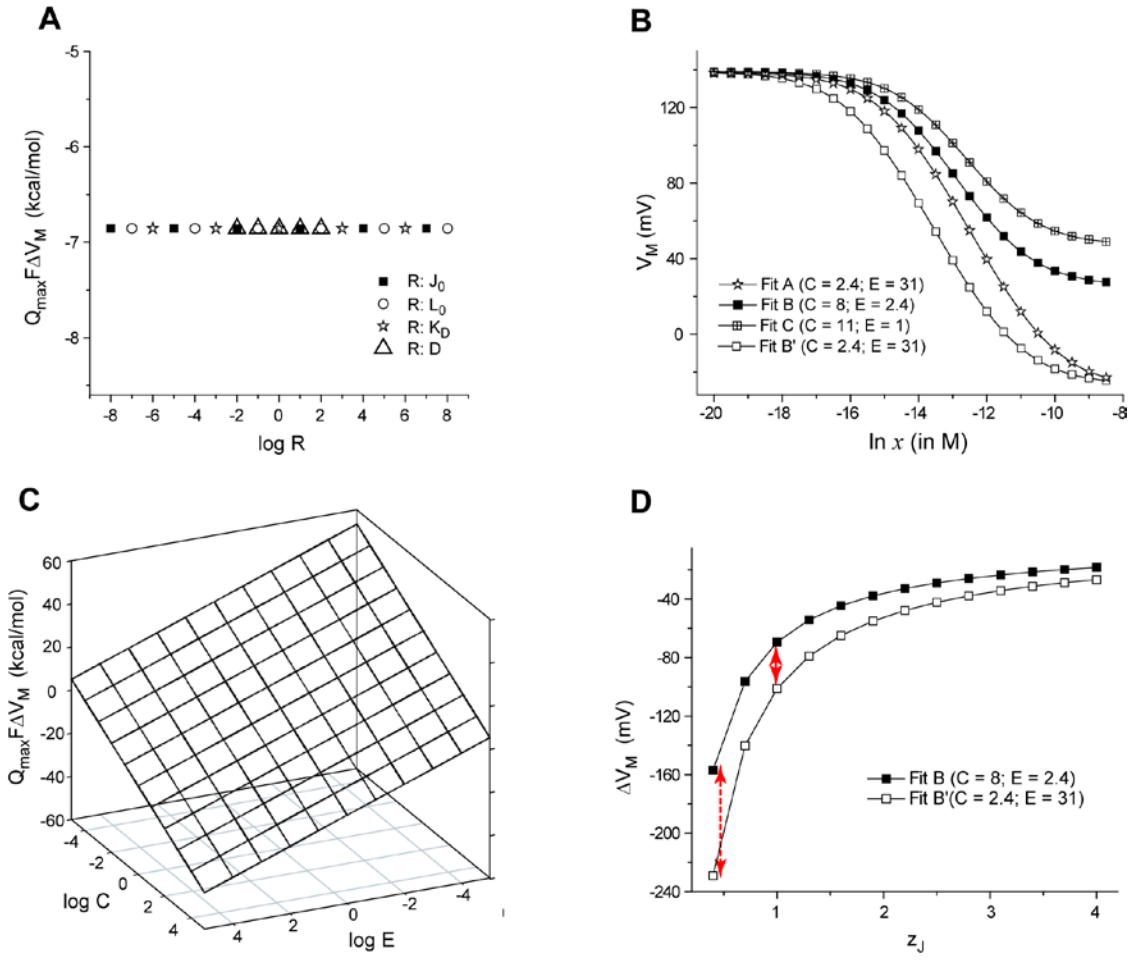

(A) $Q_{max}F\Delta V_m$ is plotted against the (logarithm of the) a subset of parameter values for the allosteric model of the BK channel (Fig. 5a). In each case, a single parameter of the model was changed, while the others were maintained at the control (Fit B) values. Symbol correspond to different parameters that were varied. For all the four equilibrium parameters tested (J_0, L_0, K_D and D), $Q_{max}F\Delta V_m$ remains constant at -6.8 kcal/mol. **(B)**

V_M of the simulated QV curves is plotted against ligand concentrations for four sets of the BK channel model parameters as described by Horrigan and Aldrich (2002): for Fit A: $J_0 = 0.03807$, $K_D = 0.000032$, $L_0 = 2\times10^{-6}$, C = 2.4, D = 18.4, E = 31, $z_J = 0.55$, $z_L = 0.4$; for Fit B: $J_0 = 0.0319$, $K_D = 0.000011$, $L_0 = 9.8\times10^{-7}$, C = 8, D = 25, E = 2.4, $z_J = 0.58$, $z_L = 0.3$; for Fit C: $J_0 = 0.0319$, $K_D = 0.000011$, $L_0 = 9.8\times10^{-7}$, C = 11, D = 25, E = 1, $z_J = 0.58$, $z_L = 0.3$; for Fit B`, Same as Fit B except the coupling terms C = 2.4 and E = 31. **(C)** $Q_{max}F\Delta V_M$ was evaluated through simulations for values of C and E, varying over several orders of magnitude, and is plotted against log C and log E. **(D)** A plot of $\Delta V_M$ with respect $z_J$ for Fits B and B`.

Figure 7. Thermodynamic cycle for a hyperpolarization and ligand activated ion channels.

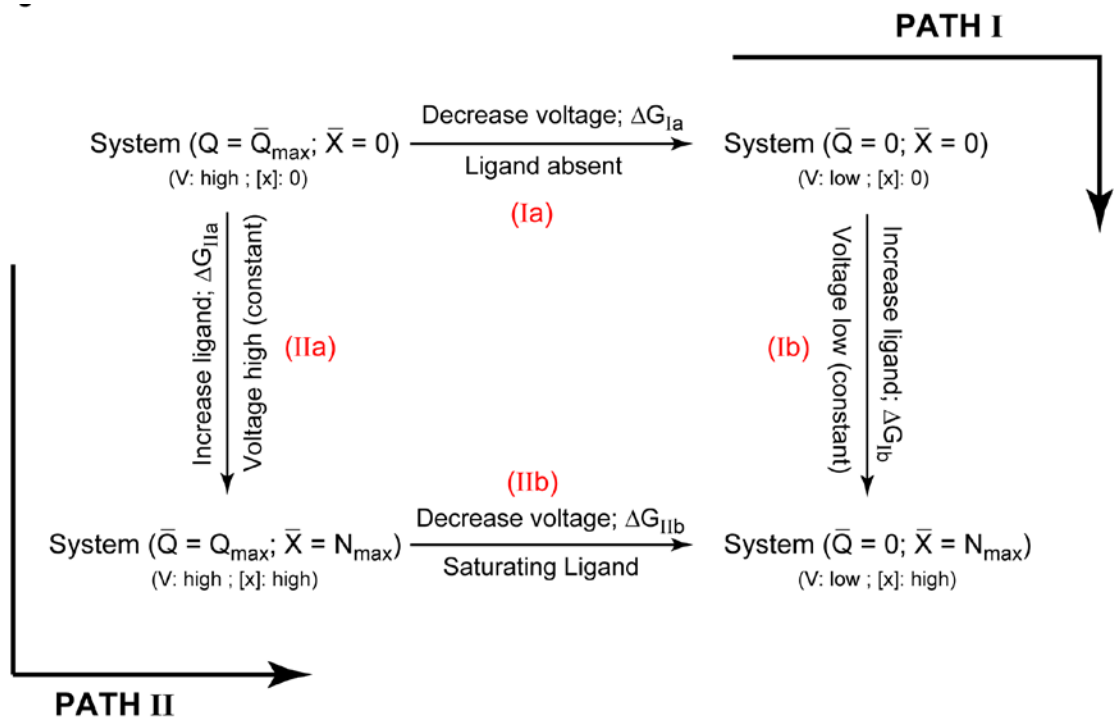

In this case, our reference state is where all the gating charges are in activated conformation and all the ligand binding sites are unoccupied (at depolarizing voltages and zero ligand concentration). The choice of reference state is based on the considerations of type of coupling between voltage- and ligand dependent pathways. The final state of the system is where all the gating charges are in the resting conformation and ligand binding sites are saturated. This state will be preferred when the voltage is low and the ligand concentration is high. As in the previous thermodynamic cycle, the net free energy of activation of this channel can be calculated by two alternate paths.

Table I. Comparison of free-energy estimates of CNG and HCN channel obtained from dose-response curves, binding curves and kinetic models.

Free-energy estimation method			**Free-energy estimate**			
Response	Fitting function	Para-meters	CNG		HCN	
			Values	ΔG_C (kcal/mol)	Values	ΔG_C (kcal/mol)
DRC[a]	$P_O^{\min} + \frac{P_O^{\max} - P_O^{\min}}{1 + (x_{1/2}/x)^H}$	$x_{1/2}$	1.65 μM	-7.7	0.54 μM	-8.3
		H	1.9		1.3	
BC[b]	$\frac{1}{1 + (x_{1/2}/x)^H}$	$x_{1/2}$	2.3 μM	-7.5	0.54 μM	-8.4
		H	0.75		1.14	
BC[c]	$N_{max}\, RT \ln x_m \; + \; C_F$	x_m	2.42 μM	29.4 (-30[d])	0.45 μM	-33.6 (-33.8[d])
		N_{max}	4		4	
		C_F	0		-0.5	

The table lists the estimates of free-energy change of ligand-dependent activation of CNG channel and HCN channel (at -130 mV) calculated by different methods. [a] The simulated dose-response curve (DRC, relative open probability curve) is fitted with a Hill-equation, normalized to account for non-zero open probabilities at zero ligand concentration i.e. $P_O^{\min}$ (and non-unity open probabilities at saturating ligand concentrations $P_O^{\max}$). ΔG_C is calculated as $RT\ln x_{1/2}$. [b] The simulated binding curve (BC) is fitted with the Hill-equation and ΔG_C is calculated as $RT\ln x_{1/2}$. [c] From the simulated binding curve (BC) the median ligand concentration is extracted. C_F is the correction factor in Eq. 26 (informed by $P_O^{\min}$

and $P_O^{\max}$). [d] ΔG_C estimates of the net free-energy difference between the first closed state (C_0) and the last open state (O_5) ($-RT \ln K^0_{C_0 \to O_5}$) obtained from the kinetic model parameters (Fig. 4a).

Table II. Energetic parameters for the BK channel gating model

Energetic Parameter	**Value**
$V_M\ (x = 0)$ [a]	138.6 mV
$V_M\ (x \rightarrow \infty)$ [b]	30.7 mV
$x_m\ (V \rightarrow -\infty)$ [c]	14.7 μM
$x_m\ (V \rightarrow \infty)$ [d]	0.83 μM
$Q_{max} F V_M \mid_{x=0} + RT\, N_{max} \ln x_m \mid_{V \rightarrow \infty}$ [e]	-24.1 kcal/mol
$Q_{max} F V_M \mid_{x \rightarrow \infty} + RT\, N_{max} \ln x_m \mid_{V \rightarrow -\infty}$ [f]	-23.9 kcal/mol
ΔG_{model} [g]	-24.6 kcal/mol
$Q_{max} F \Delta V_M$ [h]	-6.7 kcal/mol
$-RT\, N_{max} \ln\left(\frac{x_m \mid_{V \rightarrow \infty}}{x_m \mid_{V \rightarrow -\infty}}\right)$ [i]	-6.5 kcal/mol
$\Delta G_{int}\,(\text{model})$ [j]	-6.8 kcal/mol

[a, b] V_m values were extracted from QV curves simulated in the absence and saturation concentrations of ligand (x = 75 μM) using parameters of Fit B of the Horrigan and Aldrich model. [c, d] The ligand binding curves at very high (300 mV) and very low (-150

mV) voltages, were deduced using the linkage method (Eq. 21), using the binding curve at 0 mV (directly simulated from the model) as the reference curve. [e] The free-energy change along Path I of thermodynamic cycle, $\Delta G_{Ia} + \Delta G_{Ib}$. [f] The free-energy change along Path II of thermodynamic cycle, $\Delta G_{IIa} + \Delta G_{IIb}$. [g] ΔG_{model} is directly obtained from the model parameters: $-RT\left\{\left(\frac{J_0 CDE}{K_D}\right)^4 L_0\right\}$. [h]Energetic connectivity calculated as: $\Delta G_{IIb} - \Delta G_{Ia}$. [i] Energetic connectivity calculated as: $G_{Ib} - \Delta G_{IIa}$. [j] Energetic connectivity evaluated from the model parameters: $-RT\ln(CE)^4$.

Table III. Energetic parameters for the HCN channel

Parameter	**Parameter Value**
x_m (V → –∞) (V = -160 mV) [a]	0.54 μM
x_m (V → ∞) (V = -30 mV) [b]	1.72 μM
$-RT\,N_{\max}\ln\left(\frac{x_m\,\vert_{V\to\infty}}{x_m\,\vert_{V\to-\infty}}\right)+C_F$ [c]	-3.0 kcal/mol
ΔG_{int} (ligand-pore) [d]	-2.2 kcal/mol

[a,b] The median ligand concentrations at very low and high were approximated to the EC_{50} values of the ligand binding curves reported in (Kusch et al., 2010). [c] The interaction energy between the ligand-binding domain and the rest of the protein and C_F is the correction factor (Eq. 31). The following limiting values were used in calculating C_F: $P_O(V_{min}, x_{min}) = 0.58$; $P_O(V_{min}, x_{max}) = 1$; $P_O(V_{max}, x_{max}) = P_O(V_{max}, x_{min}) = 0$. [d] Interaction between the ligand binding domains are the pore domain calculated from the HCN channel model parameters proposed in (Kusch et al., 2012) (Fig. 4a) (= $-RT\ln(E_5/E_1)$).

ADDENDUM

We consider here the case of a channel with a single pore domain that is allosterically coupled to 'm' identical voltage-sensors (one in each subunit). There are 'n' binding sites per subunit (in different subunits, the i^{th} binding sites have the same ligand binding affinities but within the same subunit, the different sites have different binding affinities. Each of the voltage-sensors have an equilibrium constant J_0 and an intrinsic voltage-dependence, z_J. The pore domain has an intrinsic activation constant L_0 and an intrinsic voltage-dependence, z_L. The equilibrium constant of activation of voltage-sensor (J) and that of the pore (L) are assumed to have an exponential voltage-dependence (as described for the other models considered in this study). The voltage-dependent activation of the channel in zero calcium conditions is described by a 2 X m-state MWC-type allosteric scheme. Activation of each voltage-sensor facilitates the opening of the pore through interactions described by D. The i^{th} binding site of the channel has a binding affinity K_i (i = 1, 2, …n). The i^{th} binding site interacts with the j^{th} voltage sensor, the interaction being described by E_{ij} (j = 1, 2,…m), while its interaction with the pore is described the parameter C_i. The binding sites within the same subunit do not necessarily interact equally with the pore or the voltage-sensors, but the same binding site in different subunits interact equally with the pore and the voltage-sensors (i.e. C_i and E_{ij} is the same for the i^{th} binding site in different subunits, but C_i may or may not equal C_k and E_{ij} may or may not equal E_{kj}).

For this system, at zero calcium, the median metric would be related to the overall free-energy change of the system as:

$$Q_{max} F V_M (x = 0) = -RT \ln J_0^m D^m L_0 \quad \text{... (A.1)}$$

where Q_{max} is mz_J+z_L. Under saturating calcium concentration, at very low voltages, all the ligand binding sites will be occupied to start with. Upon full translocation of gating-charge, the activated voltage-sensors and the open pore begin to interact with the ligand binding sites. These interactions along with the change in energy due to voltage-dependent pathway will govern the free-energy change associated with voltage-dependent activation under saturating ligand concentrations. Thus the median metric at very high calcium ligand concentrations will yield the following equation:

$$Q_{max}FV_M(V \to \infty) = -RT \ln J_0^m D^m L_0 \prod_{i=1}^{n} \left(C_i \prod_{j=1}^{n} E_{ij} \right)^m \quad \text{... (A.2)}$$

Hence the displacement of the QV along the voltage-axis will be:

$$Q_{max}FV_M(V \to \infty) = -RT \ln \prod_{i=1}^{n} \left(C_i \prod_{j=1}^{n} E_{ij} \right)^m \quad \text{... (A.3)}$$

This equation imposes a constraint on the maximum gating-charges transferred, maximum number of ligand binding sites (= mn), ΔV_M and change in the median ligand concentrations due to increase in voltage. The linkage relations that we describe also remain valid in this situation.

CHAPTER SIX

Deconstructing Thermodynamic Parameters from Site-specific Observables in voltage-dependent allosteric ion channels: χ value Analysis

INTRODUCTION

Biological macromolecules often accomplish diverse functions by undergoing a series of conformational changes that are mediated by cooperative interactions between structural domains (Pauling, 1935; Monod and Jacob, 1961). A ligand binding domain, for instance, may transfer its stabilization energy upon ligand binding to an effector domain or another ligand binding domain (Perutz, 1970; Perutz and Greer, 1970). This long-range propagation of energy within a protein molecule has been widely studied in multi-subunit allosteric proteins such as the hemoglobin (Szabo and Karplus, 1972; Perutz et al., 1998; Eaton et al., 1999) and the nicotinic acetylcholine receptor (Changeux and Edelstein, 2005). Classical theories such as the Monod-Wyman-Changeux (MWC) model (Monod et al., 1965b) and the Koshland-Nemethy-Filmer (KNF) model (Koshland et al., 1966) have been developed to provide a simple mechanistic understanding of biological cooperativity.

The most important difference between the various cooperative theories is their treatment of interaction terms and the microscopic equilibrium constants associated with the individual domains or subunits (Edelstein, 1971; Hammes and Wu, 1971). According to the MWC model, cooperativity arises out of a pre-existing equilibrium between two

conformational states, which differ in their ligand binding affinities. The binding of a ligand shifts the equilibrium towards the high affinity state(s). The KNF model, on the other hand, is based on step-wise changes in protein conformation on ligand binding. Interactions between neighboring ligand bound subunits induce a conformational change that alters the binding affinity of other unoccupied sites. The main descriptor of protein conformation in these models is a single observable representative of a global conformational change in the protein (global observable) such as enzyme activity, binding site occupancy, or, in the case of ion channels, the channel open probability. These are frequently state-dependent functions of the whole protein and thus, such global parameters cannot uniquely define the microscopic thermodynamic terms associated with local conformational transitions (Di Cera, 1998a). In order to make the analysis more tractable, these models impose geometry and/or symmetry constraints thereby reducing the number of independent terms (Jackson, 2006). Thus, the interpretation of the underlying thermodynamics is model specific and, perhaps, restrictive.

In this study, we propose a methodology to quantify the energetic effects of mutations on allosteric communication between protein domains in macromolecules, using site-specific information. Site-specific measurements have increasingly become the method of choice because of their ability to provide information about the local conformation and constrain the values of microscopic terms associated with a structural unit. This approach relies on spectroscopic (fluorescence spectroscopy (Weber, 1997), EPR (Hubbell et al., 2000) and NMR (Tochtrop et al., 2002)), biochemical (cysteine and blocker accessibility (Armstrong, 1969; Akabas et al., 1992; Stauffer and Karlin, 1994)) and electrophysiological (Armstrong and Bezanilla, 1974; Chandler et al., 1975)

measurements to monitor the time and stimulus dependent changes in the local structure. To interpret the effect of protein engineering on the energetics of a macromolecular process, we have formulated an approach based on a set of site-specific parameters referred to as χ values. The macromolecule was modeled as an ensemble of an arbitrary number of interacting structural units where each unit is capable of undergoing a single conformational transition. We have considered that the conformational transitions of the individual units are voltage-dependent. We demonstrate that the χ value analysis can assess the effect of mutations on local thermodynamic parameters of an arbitrarily complex system and, more importantly, allows us to probe site-specific energetic linkage between structural domains.

THEORY and RESULTS

Theory for a coupled three-particle ensemble

Let us consider a simple system consisting of three non-identical particles (Fig. 1). Each of the three particles can exist in two conformations, activated and resting (referred as the microstate of a particle). The transition between the resting and activated microstates is influenced by an external variable which here is taken to be voltage. At low voltage, each particle prefers to remain in the resting conformation whereas at a high voltage, the particles prefer to remain in their activated microstates. The conformational change of each particle is associated with an intrinsic activation constant, $\widehat{K}$. Since the activation process of each of the particles is driven by voltage, the intrinsic activation constants should be voltage dependent and their voltage dependence can be expressed as (Stevens, 1978).

$$\widehat{K}_i = \widehat{K}_i^0 e^{q_i FV\beta} \ldots (1)$$

where $\widehat{K}_i^0$ is voltage independent and represents the contribution of chemical interactions to the intrinsic activation constant (referred to as the intrinsic chemical activation constant) of the i^{th} particle, 'q_i' indicates the voltage dependence of its activation, V is the voltage, F is the Faraday constant and $\beta = 1/RT$. For positive 'q_i', $\widehat{K}_i$ increases with voltage.

The coupling between any two particles of the system is assumed to be mediated by pairwise state-dependent interactions or "coupling factors", which are specified as:

$$\theta_{i_{S_1} j_{S_2}} = e^{-G_{i_{S_1} j_{S_2}} \beta} \ldots (2)$$

where $G_{i_{S_1} j_{S_2}}$ indicates the free-energy of interaction between the i^{th} particle in microstate s_1 and j^{th} particle in microstate s_2 (s_1 and s_2 can be 0 or 1 corresponding to the resting or activated microstate respectively). Thus for each pair of particles we have four interaction terms, which may be non-identical, describing the coupling between them. We assume that these coupling interaction energies are independent of the external stimulus (i.e. voltage in our case).

This three-particle system can exist in 8 possible macrostates. Each macrostate of the system is a unique combination of individual particles in different microstates. The energy of each macrostate is the sum of the intrinsic energies of all the particles in their given microstates and the net coupling energy between them. The canonical partition function for this system, $\widehat{\mathbf{Z}}$, is:

$$\widehat{\mathbf{Z}} = \theta_{1_0 2_0}\theta_{1_0 3_0}\theta_{2_0 3_0} + \widehat{K}_1\theta_{1_1 2_0}\theta_{1_1 3_0}\theta_{2_0 3_0} + \widehat{K}_2\theta_{1_0 2_1}\theta_{1_0 3_0}\theta_{2_1 3_0} + \widehat{K}_3\theta_{1_0 2_0}\theta_{1_0 3_1}\theta_{2_0 3_1}$$
$$+ \widehat{K}_1\widehat{K}_2\theta_{1_1 2_1}\theta_{1_1 3_0}\theta_{2_1 3_0} +$$
$$\widehat{K}_1\widehat{K}_3\theta_{1_1 2_0}\theta_{1_1 3_1}\theta_{2_0 3_1} + \widehat{K}_2\widehat{K}_3\theta_{1_0 2_1}\theta_{1_0 3_1}\theta_{2_1 3_1} + \widehat{K}_1\widehat{K}_2\widehat{K}_3\theta_{1_1 2_1}\theta_{1_1 3_1}\theta_{2_1 3_1} \ldots (3)$$

$\widehat{\mathbf{Z}}$ can be normalized by dividing eqn. 3 with $\theta_{1_0 2_0}\theta_{1_0 3_0}\theta_{2_0 3_0}$ and substituting the following normalized parameters:

$$K_i = \widehat{K}_i \prod_{j=1, j\neq i}^{N=3} \frac{\theta_{i_1 j_0}}{\theta_{i_0 j_0}} \ldots (4a)$$

$$\theta_{ij} = \frac{\theta_{i_0 j_0}\theta_{i_1 j_1}}{\theta_{i_1 j_0}\theta_{i_0 j_1}} \ldots (4b)$$

K_i is the apparent activation constant of particle 'i' (hereafter referred to simply as 'i'), θ_{ij} is the macroscopic coupling factor between 'i' and 'j'. The normalized canonical partition function can now be expressed as:

$$\boldsymbol{Z} = 1 + K_1 + K_2 + K_3 + K_1K_2\theta_{12} + K_2K_3\theta_{23} + K_1K_3\theta_{13} + K_1K_2K_3\theta_{12}\theta_{23}\theta_{13} \ldots (5)$$

Such normalized parameters simplify the partition function describing a coupled system and have been widely used in Wyman's linkage theory and other theoretical descriptions of coupled systems (Wyman, 1967). In addition, the thermodynamic terms have exact correspondence to the number of free parameters that can be extracted experimentally. However, K_i is $\widehat{K}_i$ normalized by the interaction energies of 'i' with the resting state of other particles and is not the true intrinsic equilibrium constant of the particle. Perturbations that alter the ground state interaction energies would affect all the normalized thermodynamic parameters. This may be incorrectly interpreted as the mutation having varied effects. Thus, it is important to consider the explicit interaction terms that contribute to the apparent equilibrium constants when interpreting the effects of mutation. Both K_i and $\widehat{K}_i$ have the same voltage dependence because the coupling factors are voltage independent:

$$K_i = K_i^0 e^{q_i FV\beta} \ldots (6)$$

where $K_i^0 = \widehat{K}_i^0 \prod_{j=1, j\neq i}^{N} \frac{\theta_{i_1 j_0}}{\theta_{i_0 j_0}}$.

The θ_{ij} terms in Eq. 5 are measures of the energy difference between "like-state" interactions between 'i' and 'j' ($\theta_{i_0 j_0}$ and $\theta_{i_1 j_1}$) and the "cross-interactions" between them ($\theta_{i_1 j_0}$ and $\theta_{i_0 j_1}$). It is a measure of coupling energy and reflects the stability of the two particles when they are in the "like" microstates, relative to their "unlike" microstates.

From the linkage theory (Wyman, 1965) we see that the probability of 'i' to be in microstate 's' (P_{is}) will depend on the Boltzmann weights of all the macrostates where 'i' is in the microstate 's'. Thus, P_{11} will be determined by all the macrostates where particle 1 is in the activated conformation:

$$P_{11} = \frac{\partial \ln \boldsymbol{Z}}{\partial \ln K_1} = \frac{z(1,1,1) + z(1,1,0) + z(1,0,0) + z(1,0,1)}{\boldsymbol{Z}} \ldots (7)$$

where $z(s_1, s_2, s_3)$ is the Boltzmann weight of the macrostate (s_1, s_2, s_3). However, at very low voltages P_{11} would be dominated by the Boltzmann weight of the macrostate (1,0,0) and it would become $z(1,0,0)/\boldsymbol{Z}$. A simple physical interpretation of this behavior is that at very low voltages the probability of finding two (or more) particles simultaneously in activated microstate is much smaller than the probability of a single activated particle. This can be mathematically illustrated by taking the ratios of the Boltzmann weights of the macrostates (1,1,1), (1,1,0) and (1,0,1) to z(1,0,0):

$$\frac{z(1,1,0)}{z(1,0,0)} = K_2 \ldots (8a)$$

$$\frac{z(1,0,1)}{z(1,0,0)} = K_3 \ldots (8b)$$

$$\frac{z(1,1,1)}{z(1,0,0)} = K_2 K_3 \theta_{23} \ldots (8c)$$

Both K_2 and K_3 are small at low voltages (Eq. 1) and, therefore, the ratios defined in the above equations will become negligible. In other words, the magnitude of the z(1,0,0) term will be much larger than z(1,0,1), z(1,1,0) and z(1,1,1). In contrast, at high voltages P_{11} would be simplified to $z(1,1,1)/\boldsymbol{Z}$. When similar approximations are applied to the probability of particle 1 being in the resting conformation, we find that at very low voltages, P_{10} is $z(0,0,0)/\boldsymbol{Z}$ whereas at very high potentials, P_{10} is $z(0,1,1)/\boldsymbol{Z}$.

We define a new parameter, ε_i (referred to as the "coupled equilibrium constant") as:

$$\varepsilon_i = \frac{P_{i1}}{P_{i0}} \dots (9)$$

which is the ratio of the probability of 'i' in the activated microstate to its probability in the resting microstate. At intermediate potentials, the coupled equilibrium constant depends on all the parameters of the system. The coupled equilibrium constant for the 1st particle is expressed as:

$$\varepsilon_1 = \frac{K_1K_2K_3\theta_{12}\theta_{23}\theta_{13} + K_1K_2\theta_{12} + K_1 + K_1K_3\theta_{13}}{1 + K_3 + K_2 + K_2K_3\theta_{23}} \dots (10)$$

Each of the apparent intrinsic equilibrium constants is an exponential function of voltage. Thus $\ln \varepsilon_1$ would be a highly non-linear function of voltage. At extreme voltages where only few macrostates are thermodynamically relevant, the expression for ε_i $(i = 1, 2, 3)$ greatly simplifies. For example, the coupled equilibrium constant for particle 1 at very low and high voltages would be given by:

$$\varepsilon_{1-} = \left[\frac{P_{11}}{P_{10}}\right]_- \cong \frac{z(1,0,0)}{z(0,0,0)} = K_1 \dots (11a)$$

$$\varepsilon_{1+} = \left[\frac{P_{11}}{P_{10}}\right]_+ \cong \frac{z(1,1,1)}{z(0,1,1)} = K_1\theta_{12}\theta_{13} \dots (11b)$$

These equations show that at extreme voltages ε_{1+} and ε_{1-} are essentially single exponential functions of voltage and thus a plot of $\ln \varepsilon$ vs. V would be linear at extreme voltages.

The above treatment for a coupled three-particle system can be applied to multi-domain proteins. Each particle represents a structural or functional domain, whose voltage-dependent conformational dynamics can be monitored using site-specific measurements. We can calculate the probability of activation of the domain and compute the extremal ε values for each of the three structural units. Combining equations 6 and 11a,b the extremal ε values for particle 1 in a three-particle system can be expressed as:

$$\ln \varepsilon_{1-} = q_1 F\beta V + \ln K_1^0 \ldots (12)$$

for low voltages. For very high voltages, the equation is:

$$\ln \varepsilon_{1+} = q_1 F\beta V + \ln(K_1^0 \theta_{12} \theta_{13}) \ldots (13)$$

From the above equations, we see that the linear plots of $\ln \varepsilon_{1+}$ and $\ln \varepsilon_{1-}$ with respect to V have the same slope, $q_1 F\beta$, which reflects the intrinsic voltage-dependence of activation of particle 1. The two plots, however, differ in their constant terms $\ln K_1^0$ and $\ln(K_1^0 \theta_{12} \theta_{13})$, which we hereafter refer to as χ_{1-} and χ_{1+} respectively (Fig. 3a).

Next, we extended our analysis to a system of N non-identical particles (see Addendum). The general expressions for the χ values of the '*i*' in an N- particle system, are:

$$\varepsilon_{i-} = \ln(K_i^0) \ldots (14)$$

$$\varepsilon_{i+} = \ln\left(K_i^0 \prod\nolimits_{j=1, j\neq i}^{N} \theta_{ij}\right) \ldots (15)$$

We introduce another parameter, χ_i^{diff}, which is the difference of the two χ values:

$$\chi_i^{diff} = \chi_{i+} - \chi_{i-} = \ln\left(\prod_{j=1,j\neq i}^{N} \theta_{ij}\right) \ldots (16)$$

χ_i^{diff} is a measure of the energy difference between all the like-state direct interactions associated with '*i*' and its cross-interactions. Since χ_i^{diff} depends only on the coupling factors directly associated with '*i*', it can be used to deduce the thermodynamic effect of a site-specific mutation in an allosteric system. If a mutation perturbs any of the coupling factors directly associated with '*i*', then χ_i^{diff} changes whereas if the mutation alters any of the intrinsic chemical activation constants or coupling factors between other particles then χ_i^{diff} remains unchanged. Thus by direct measurement of a single experimental parameter one could potentially identify whether a perturbation specifically alters the coupling or the intrinsic stability of the structural unit. In addition, the free energy of perturbation on coupling, ΔG_P is:

$$\Delta G_P = RT\left(\chi_{Mutant}^{diff} - \chi_{WT}^{diff}\right) \ldots (17)$$

It is important to note that χ_i^{diff} is the net macroscopic interaction energy. If χ_i^{diff} is greater than zero, then '*i*' is positively coupled to system as a whole whereas if it is negative then '*i*' is negatively coupled to the system. Its absence, however, does not necessarily establish that '*i*' is independent of other particles in the system. It signifies that the positive interaction of '*i*' with some particles in the system equals its negative interaction with others. But '*i*' may still be coupled to the rest of the system. This can be easily illustrated by considering the three particle system where φ_{12} equals to $1/\varphi_{13}$ and therefore, the χ_1^{diff} is zero. Fig. 2b shows that the $ln\,\varepsilon$ vs voltage plot is not linear (except at the extremities) indicating that particle 1 is coupled to the other particles in the

system. Perturbation of the intrinsic stability of particle 2 alters the behavior of particle 1 at intermediate potentials as expected in a coupled system.

Apart from identifying whether a mutation affects the coupling associated with a specific structural unit, this approach could also provide useful information about state-dependence of the interactions. Remembering that the parameters in Eqns. 14-16 are normalized (Eqns. 4a,b), we expand them to arrive at the following expressions:

$$\chi_{i-} = \ln\left(\frac{\widehat{K_i}^{0}\prod_{j=1,j\neq i}^{N}\theta_{i_1 j_0}}{\prod_{j=1,j\neq i}^{n}\theta_{i_0 j_0}}\right) \ldots (18)$$

$$\chi_{i+} = \ln\left(\frac{\widehat{K_i}^{0}\prod_{j=1,j\neq i}^{N}\theta_{i_1 j_1}}{\prod_{j=1,j\neq i}^{n}\theta_{i_0 j_1}}\right) \ldots (19)$$

These generalized expressions help us observe some important features of the χ values. First, both the χ values of a particle depend on its intrinsic chemical activation constant. Second, the χ values of a particle depend only on the interactions directly associated with it – the coupling factors between two particles have no effect on the χ values of a third particle. Third, the χ values do not depend on the same coupling factors – χ_{i-} depends on the interactions of 'i' with the resting state of the other particles while χ_{i+} depends on its interactions with the activated state of the other particles. Suppose we use a probe to monitor the conformational dynamics of the i^{th} structural unit of the protein from which we extract its χ values (at high and low voltages).

A generalized equation for χ-value in terms of the probability of activation of a specific structural unit (P_A) can be obtained as follows. At extreme voltages:

$$\ln \varepsilon = qF\beta V + \chi \ldots (20)$$

$qF\beta$ is the slope of the lnε vs V plot at extreme voltages. Thus Eq. 20, may be re-written as:

$$\ln \varepsilon = \left(\frac{\partial \ln \varepsilon}{\partial V}\right) V + \chi \ldots (21)$$

Eq. 21 can be converted into an exact differential as:

$$-\frac{\chi}{V^2} = -\frac{\ln \varepsilon}{V^2} + \frac{1}{V}\frac{\partial \ln \varepsilon}{\partial V} = \frac{\partial}{\partial V}\left(\frac{\ln \varepsilon}{V}\right) \ldots (22)$$

Thus a standard expression for the χ-values is:

$$\chi_{\pm} = \lim_{V \to \pm\infty} -V^2 \frac{\partial}{\partial V}\left\{\frac{\ln\left(\frac{P_A}{1-P_A}\right)}{V}\right\} \ldots (23)$$

where V is the voltage. If upon mutation, χ_i^{diff} changes then the mutation affects a coupling factor directly associated with '*i*'. If the change in χ_i^{diff} is due to only χ_{i-} changing, then we can attribute the effect of the mutation to the alteration of a coupling factor associated with '*i*' and the resting state of another particle. Conversely, if only the χ_{i+} changes it can be concluded that the mutation affects only the coupling factor(s) associated with '*i*' and the activated state of other particles. If, however, both χ_{i-} and χ_{i+} values change and the changes are equal ($\Delta\chi_{i-} = \Delta\chi_{i+}$ and $\Delta\chi_i^{diff} = 0$) then the primary effect of the perturbation is on the intrinsic chemical activation constant of the particle.

Although Eq. 23 describes a system-independent mathematical expression relating the χ values to the probability of activation of a particle, it may not be always practical for experimental implementation since it involves taking derivatives of noisy data traces. A better approach may be to fit the data points at extremities in the $\ln \varepsilon$ vs V plots (Fig. 2) to a straight line and extrapolating it to 0 mV. How do we ascertain that we have reached such extreme conditions? According to Eqns. 12 and 13, the slopes at the

both extremities should be identical and are related to intrinsic voltage dependence of the structural unit. This criterion can be used as a practical method to identify the linear regime suitable for extracting the χ values.

Systems with identical structural units

Suppose in the N-particle system, there are multiple (N_i) copies of particle 'i' (labeled as 'i' through '$i + N_i - 1$'). To illustrate the χ value approach for this system, we can show that:

$$\frac{\partial \ln z_{i\_}}{\partial \ln K_i} = \frac{\partial \ln z_{i_+}}{\partial \ln K_i} = 1 \ldots (24)$$

where $z_{i\_}$ is the Boltzmann weight of the macrostate where all particles but a single copy of 'i' are resting and z_{i_+} is the Boltzmann weight of the macrostate where all particles but a single copy of 'i' are activated. The probability of activation of structural unit 'i' in this case is:

$$P_{i1} = \frac{1}{N_i}\frac{\partial \ln \boldsymbol{Z}}{\partial \ln K_i} \ldots (25)$$

At very low potentials, $\boldsymbol{Z}$ can be approximated as:

$$\boldsymbol{Z} \approx z(0,0,\ldots,0) + N_i z_{i\_} \ldots (26)$$

where $z(0,0,\ldots,0)$ is the Boltzmann weight of the macrostate where all particles are resting. In eqn. 21 we have assumed that all macrostates where any one of the N_i copies of 'i' is activated, while all the remaining particles are resting, are identical in energy. Using Eqn. 26 in Eqn.25, along with Eqn. 23, we get, $P_{i1} = z_{i\_}/\boldsymbol{Z}$. Furthermore, at very low voltages, $P_{i0} = z(0,0,\ldots,0)/\boldsymbol{Z}$ and $\varepsilon_{i\_}$ turns out to be $z_{i\_}/z(0,0,\ldots,0)$. Thus $\varepsilon_{i\_}$ is essentially K_i. Similarly, at very high voltages, by approximating $\boldsymbol{Z}$ as:

$$\boldsymbol{Z} \approx z(1,1,\ldots,1) + N_i z_{i_+} \ldots (27)$$

we can show that ε_{i+} would remain the same as before and the resultant χ value can still be expressed by Eq. 15. It is important to note that in the expression for χ_{i+}(for this system), the running variable 'j' samples all the remaining particles of the system – the ones which are different from 'i' as well as its $N_i - 1$ replicates. Consequently χ_i^{diff} would depend on all the macroscopic coupling factors associated with 'i' – interaction terms with its identical copies as well as all non-identical particles of the system. Thus the χ value analysis can be applied to completely or partially homomeric systems as well as heteromeric systems.

Numerical simulations to demonstrate the χ-value approach

To illustrate our theory, we carried out numerical simulations for a model that approximates a voltage-dependent sodium channel (Fig. 2). The channel consists of four non-identical voltage-sensing domains (labeled as particles 1 to 4). The four pore segments associate to form the ion permeation pathway which is represented as a single structural unit (particle 5). Voltage-dependent conformational dynamics of these discrete structural units can be tracked using a site-specific probe. For example, in voltage-gated sodium channels, fluorescence probes have been used to measure the dynamics of each of the four voltage-sensors while ionic current measurements have long been used to probe the conformational status of the pore domain (Chanda and Bezanilla, 2002). In the model, that we use for our simulations, we assume that each of voltage sensors is coupled to the pore domain through four state-dependent interaction terms ($\theta_{i_0 5_0}, \theta_{i_1 5_0}, \theta_{i_0 5_1}, \theta_{i_1 5_1}$ - where i represents a voltage-sensor, i = 1, 2, 3 or 4). The four voltage sensors do not

directly interact with each other. Numerical simulations were performed using mostly arbitrary values of the thermodynamic parameters whose initial values are listed in Table1. The initial values of $\widehat{K}_1^0$ and $\widehat{K}_5^0$, the intrinsic chemical activation constants of domain I (DI) voltage-sensor and the pore respectively, and the coupling factors between them were chosen to be close to that obtained from previous modeling data (Muroi et al., 2010). The remaining thermodynamic parameters were randomly distributed around these values. Each of the explicit thermodynamic terms in the system were separately varied over several orders of magnitude and the ε values of DI voltage sensor (ε_1) were calculated over a large range of voltage, from which both its χ values were obtained. The numerical simulations were performed using MATLAB 2008b (The Mathworks). The simulations were independently verified by calculating the χ^{diff} values using Eq. 16.

Representative plots for $\ln \varepsilon_1$ vs V in response to perturbation of different thermodynamic parameters of the system are shown in Fig. 3c-f. Three phases are clearly visible in these plots – at very low voltages the plot is linear, at intermediate voltages it becomes non-linear and finally at very voltages the plot is linear again. χ_{1-} and χ_{1+} are extracted from these traces by extrapolating the respective linear segments to the y-axis (V=0). Clearly, as $\widehat{K}_1^0$ is increased (Fig. 3c) both the χ-values increase, maintaining a constant χ_1^{diff}. When $\theta_{1_0 5_0}$, the interaction between the resting DI voltage-sensor and the resting pore, is increased (Fig. 3d), the χ_{1+} value remains unchanged, as seen by the convergence of the different traces at very high voltages. However, χ_{1-} shows a graded decrease (indicated by a decrease in the saturating values of $\ln \varepsilon_1$) and as a result, χ_1^{diff} also increases. Figures 3e and 3f show the $\ln \varepsilon_1$ vs V traces in response to perturbation of $\widehat{K}_5^0$, and $\theta_{2_0 5_0}$(the interaction between resting DII voltage-sensor and the resting pore),

respectively. While there are some deviations between the different traces (in both figures) at intermediate voltages, they all converge at saturating voltages, indicating that these perturbations affect neither χ_{1-} nor χ_{1+} (and thus not even χ_1^{diff}). These simulations provide a clear picture of the χ-value analysis – χ_{1+} depends only on $\widehat{K}_1^0$ and the direct interactions of particle 1 with the activated state of other particles and χ_{1-} depends only on $\widehat{K}_1^0$ and the direct interactions of particle 1 with the resting state of other particles. χ_1^{diff} depends only on the direct interactions of particle 1 with the other particles of the system (Fig. 4). Thus experimentally observing the changes in these three parameters in response to a mutation, we can identify whether the mutation affects the intrinsic stability of a structural unit or its interaction with other structural units of the protein and in the case of the latter we could obtain useful information about the state dependence of the interaction as well.

DISCUSSION

The above analysis shows that a site-specific observable in an allosteric protein can be described, under limiting conditions, by a small set of thermodynamic parameters. These thermodynamic terms are directly related to the structural unit under observation. This approach, which we refer to as the χ value analysis, relies on measuring the probability of activation of individual structural units under limiting conditions where the system dynamics can be approximated to a two-state process. This allows us to determine the effects of site-specific mutations in macromolecular systems without *a priori* assumptions about the nature of allosteric connectivity. χ values of a structural unit of a protein can be obtained experimentally by probing its conformational changes using site-

specific measurements such as EPR or fluorescence spectroscopy. Our theory allows us to incorporate such site-specific observables to gain valuable insight into the thermodynamics of elementary conformational changes in a protein, as opposed to a single global observable (e.g. fraction of ligand bound sites). This approach is reminiscent of the analysis used to study the allosteric thermodynamics of calcium and voltage-activated potassium channels, within the framework of specific cooperative models (Horrigan et al., 1999). In that case, driving the system to extreme conditions greatly simplify the equations making it possible to assign values to specific parameters upon fitting the experimental data to the model.

The term χ^{diff} introduced in eqn. 14 has an important physical meaning in relation to Wyman's linkage theory. It reflects how easily a domain can activate when all the other domains are in their activated conformations relative to the case when all the remaining domains are resting. Wyman showed that the difference between the final and initial asymptotes of a Hill plot represents the net global cooperativity parameter. This parameter is a measure of the total interaction energy between different allosterically linked sites of a macromolecule. Estimates of such macroscopic interaction parameters have been frequently obtained using experimental observables which report the global states of a macromolecule. The lnε vs V plot is similar to the Hill plot and hence χ^{diff} is related in significance to the net global cooperativity parameter. But, lnε vs V plots are obtained using site-specific measurements. Thus χ^{diff} would yield an estimate for net stabilization energy associated with a local site of a macromolecule as opposed to a global parameter which has contributions from several different sites embedded within it. Obtaining energetic parameters such as χ^{diff} would be indispensible in gaining a

thorough understanding of thermodynamic principles governing local conformational dynamics – for example, χ^{diff} for a specific voltage-sensor of the voltage-gated sodium channels can tell us what fraction of the net free-energy change associated with the voltage-sensor activation is derived from interaction with other structural units in the protein.

Protein thermodynamics and structure are intimately related. Inferences can be drawn about protein structure, if we are able to relate the effect of mutations to perturbations of specific thermodynamic terms. Our theory posits that if a subunit does not form a direct energetic contact with a second subunit, then no amount of perturbation of the second subunit would affect the χ parameters of the first. In our simulations the χ values of the DI voltage-sensor remained invariant when the thermodynamic parameters of all the indirectly linked segments were varied over many orders of magnitude (Fig. 4). Therefore, if in an actual experiment the χ values of the DI voltage-sensor remain unaltered in response to systematic perturbations throughout the DII voltage-sensor, then we can conclude that the DI and DII voltage-sensors are unlikely to share a common structural interface through which they interact directly.

In order to deconstruct the thermodynamic perturbation caused by a mutation using χ value analysis it is necessary that we are able to make measurements under conditions where the lnε vs V plots become linear. If the voltage dependence of the constituent domains is small, the extreme voltages necessary to evoke a linear response might become experimentally infeasible. Again, if the coupling factors are voltage-dependent, then the approximations that simplify the expressions for coupled equilibrium constants may not be valid. Also, the limiting slopes at high and low voltages may be

different if the coupling terms have different voltage-dependencies. Extraction of the χ values might become difficult in these situations. Also in cases where two structural units are extremely tightly coupled, it might not be possible to experimentally probe one structural unit separately from the other. In our description, the conformational dynamics of every structural unit is treated as a single step transition. In many instances, the activation of specific structural units may involve multiple transitions (Zagotta et al., 1994a; Schoppa and Sigworth, 1998; Lecar et al., 2003). In such cases, if the site-specific probe monitors the final conformational state, then the χ value analysis becomes valid because the intermediate non-activated microstates can be lumped together rendering an effective single-step transition. However, it is important to remember that the energetics extracted using the χ value analysis is relative to these intermediate states rather than the absolute ground state and uncertainties associated with these intermediate states could introduce significant errors in χ value estimation/interpretation.

Despite these limitations, the χ value could prove to be a powerful analytical tool to dissect the thermodynamic parameters using site-specific measurements. When combined with site-directed mutagenesis, this approach could help us understand the role of protein structure in determining thermodynamics and function. Other methods based on measurements of global observable such as functional mutant cycle analysis have been used to extract interaction energies between specific sites in proteins but their applicability is limited by strict constraints (Horovitz and Fersht, 1990) and prone to yielding false interactions as described in Chapter four of this thesis. While our analysis was based on the assumption that the transitions are voltage-dependent, similar equations can be developed if the conformational transitions depend on other stimuli such as ligand.

Therefore, χ value analysis can be applied to wider class of proteins including proteins activated by ligand and other cofactors.

CHAPTER CONTENT

Significant portions of this chapter (text, figures and tables) are adapted from: "Chowdhury, S., and Chanda, B., *Deconstructing thermodynamic parameters of a coupled system from site-specific observables*. Proceedings of the National Academy of Sciences U S A, 2010, 2;107(44):18856-61"

FIGURES

Figure 1 Coupled model for a three-particle system.

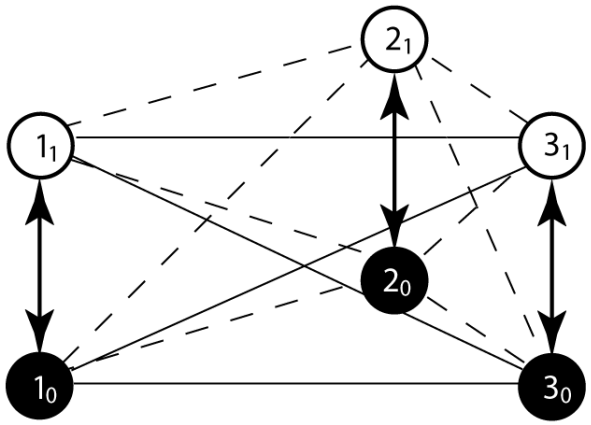

A system of three particles, 1, 2 and 3, each of which can exist in two conformations: i_0 (resting state of '*i*') and i_1 (activated state of '*i*'). Vertical double arrowed lines indicate the intrinsic activation constants of the particles. All the three particles are thermodynamically linked to each other via four state-dependent pairwise coupling factors, as described in the text. These are depicted by the horizontal and diagonal lines connecting the two particle microstates.

Figure 2: Hypothetical model of a voltage-dependent sodium channel.

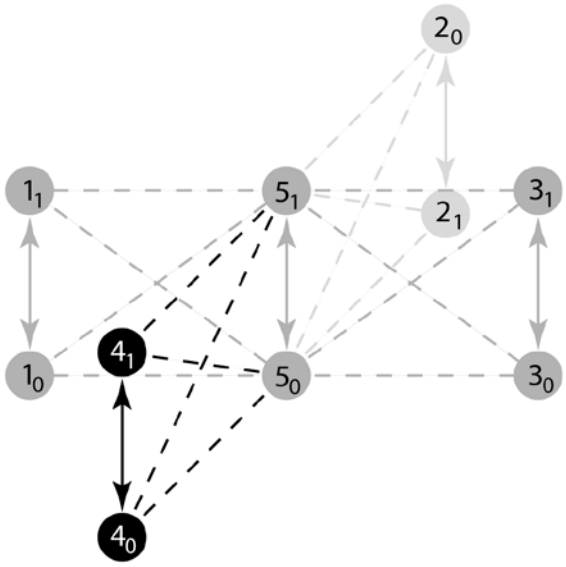

The model represents a voltage-dependent sodium channel. Particles 1 through 4 represent the four non-identical voltage-sensing domains of the ion channel, each capable of existing in two conformations: resting (designated as i_0) and activated (designated as i_1) (i = 1, 2, 3 or 4). The central pore domain, designated as particle 5, can also exist in two conformations: open (5_1) or closed (5_0). The vertical double arrowed solid lines represent the intrinsic activation constants for the conformational change of the particles. The diagonal and horizontal lines represent the microstate dependent pairwise coupling factors between the particles: the diagonal lines indicate the cross-interactions between particles which are in unlike states, while the horizontal lines represent the like interactions between particles in the same microstate. Each of the voltage-sensing domains is directly coupled to the pore, but none of the voltage-sensors interact with each other directly.

Figure 3. Simulations of the lnε vs V plots.

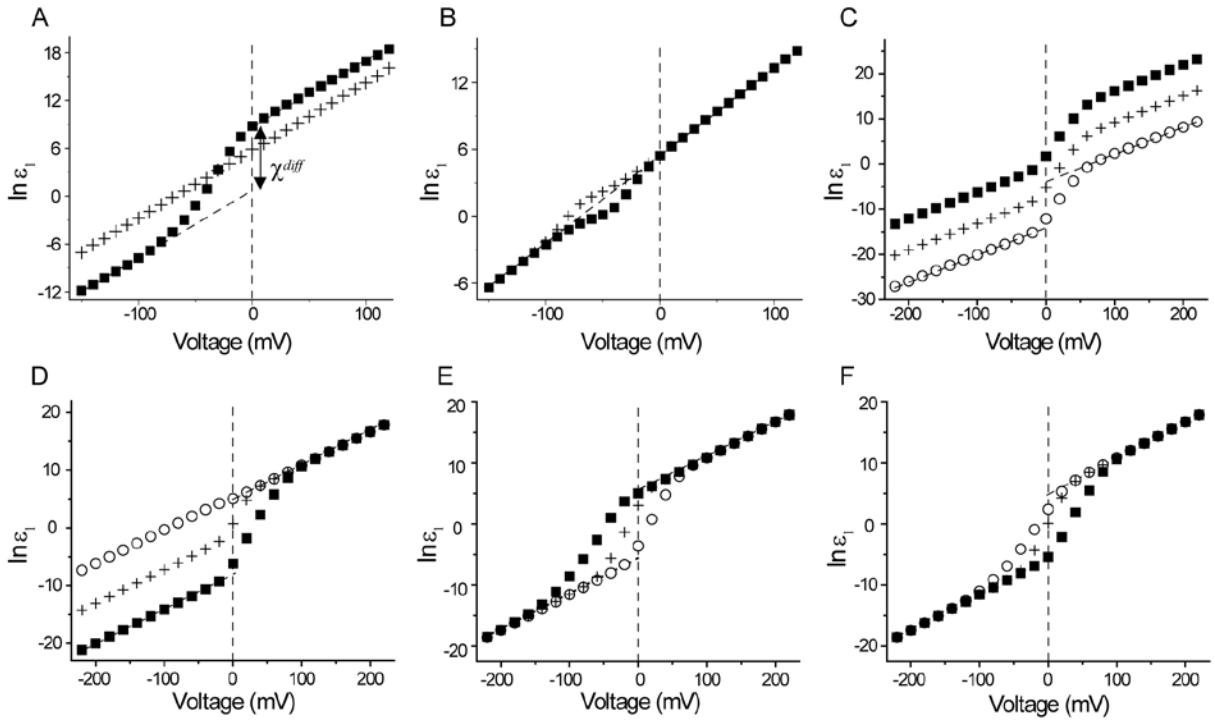

(A) The plot of lnε vs V for a three particle system in the presence (■) or absence (+) of interactions between the three particles. The extrapolation of the linear segments at low and high voltages to the V=0 axis (vertical dashed line) gives the respective χ values. Difference between these intercepts (χ values) is the χ^{diff} parameter. **(B)** The lnε vs V for a three particle system where χ^{diff} for a specific particle is zero (■). Although the χ^{diff} is zero, perturbation of the intrinsic equilibrium constant of another particle alters lnε vs V plot (+). **(C)-(F)** $\ln \varepsilon_1$ vs V plots for the DI voltage-sensor (particle 1) of the model of the voltage-dependent sodium channel (Figure S1) in response to perturbation of different parameters of the model. The intrinsic chemical activation constant of particles 1, $\widehat{K}_1^0$ **(C)**, and 5, $\widehat{K}_5^0$ **(E)**, were varied over 6 orders of magnitude: $\log \widehat{K}_i^0$ = -3 (○), 0 (+), 3(■) (i = 1 or 5). Interaction between resting states of particles 1 and 5, $\theta_{1_o 5_o}$

(D), and that between resting states of particles 2 and 5, $\theta_{2_0 5_0}$ **(F),** were varied over 6 orders of magnitude $\log \theta_{i_0 5_0}$ = -3 (○), 0 (+), 3(■) (i = 1 or 2). Vertical dashed line corresponds to the voltage axis at 0 mV. Extrapolating the linear segments of the traces (at high and low voltages) to this axis, gives the corresponding χ values.

Figure 4. Change in the χ values ($\Delta\chi = \chi^{Mutant} - \chi^{WT} \equiv \chi^{Perturbed} - \chi^{Initial}$) of a particle in response to perturbation of different model parameters.

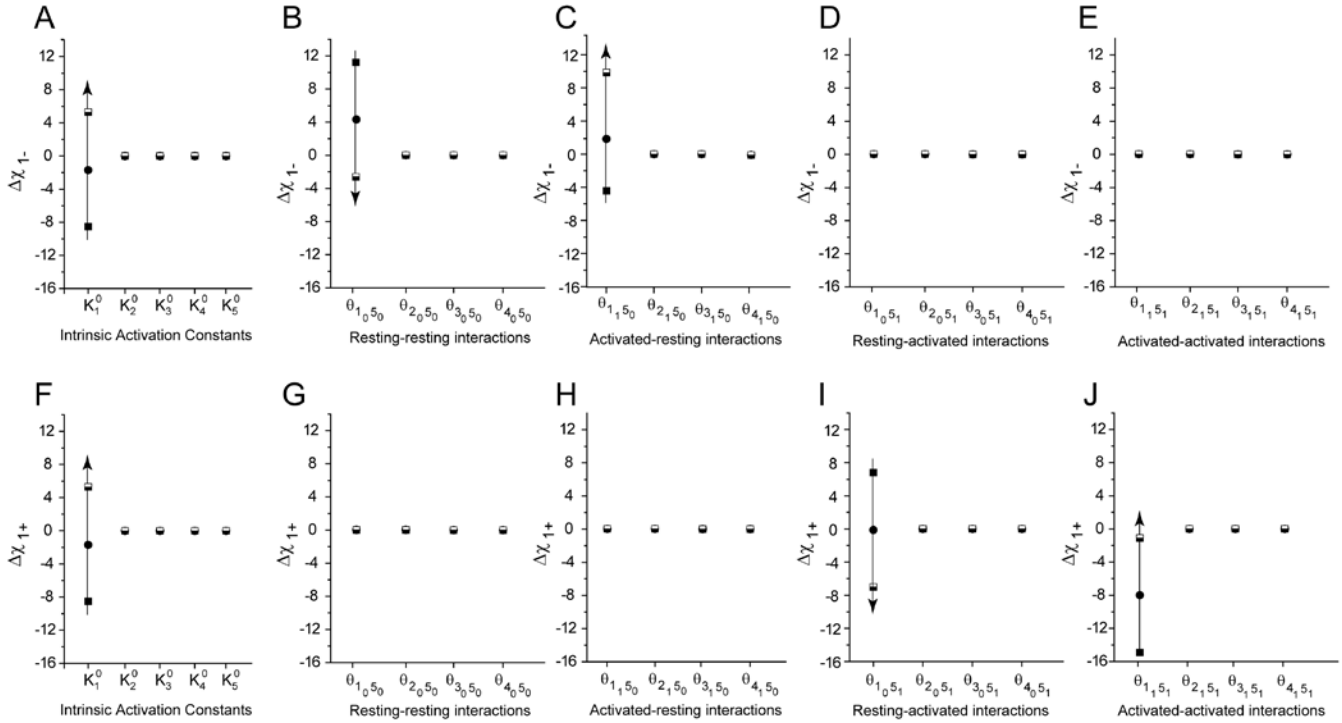

Simulations were performed using the model of sodium channel as described in Figure S1. Each of the model parameters were perturbed one at a time (while retaining the control values for the rest of the parameters) and the changes in the values of χ_{1-} **(A)-(E)** and χ_{1+} **(F)-(J**), relative to their control (initial) values are shown. Resting-resting and activated-activated state interactions imply the "like" state interactions between two particles which are in the same microstate. The "resting-activated" interaction implies the interaction between resting particle 1 and another particle that is activated. The "activated-resting" interaction implies that between an activated particle 1 and another particle that is resting. The arrows point towards increasing value of the thermodynamic parameter.

Table 1. Parameter values used for simulation of sodium channel model

Parameter	Value
$\widehat{K}_1^0$	5
q_1	1.5
$\widehat{K}_2^0$	10
q_2	1.5
$\widehat{K}_3^0$	20
q_3	2
$\widehat{K}_4^0$	1
q_4	1
$\widehat{K}_5^0$	0.001
q_5	0.5
$\theta_{1_0}\theta_{5_0}$	75
$\theta_{1_1}\theta_{5_0}$	0.05
$\theta_{1_0}\theta_{5_1}$	1
$\theta_{1_1}\theta_{5_1}$	30
$\theta_{2_0}\theta_{5_0}$	50
$\theta_{2_1}\theta_{5_0}$	0.05
$\theta_{2_0}\theta_{5_1}$	0.01
$\theta_{2_1}\theta_{5_1}$	50
$\theta_{3_0}\theta_{5_0}$	100
$\theta_{3_1}\theta_{5_0}$	5
$\theta_{3_0}\theta_{5_1}$	0.5
$\theta_{3_1}\theta_{5_1}$	20
$\theta_{4_0}\theta_{5_0}$	75
$\theta_{4_1}\theta_{5_0}$	10
$\theta_{4_0}\theta_{5_1}$	1
$\theta_{4_1}\theta_{5_1}$	15

The table lists the parameters and their values used for the numerical solution of the model sodium channel. These parameters were used to calculate three extreme values of $\ln \varepsilon$ to check the parity between the numerical simulations and the expected (calculated) values of $\ln \varepsilon$.

ADDENDUM

We consider an N-particle system, in which each of the particles undergoes a voltage dependent transition from its resting to activated microstate, and each particle interacts with every other the particle of the system through four state-dependent interactions as described for the three particle system. For any particle 'i' in this system, we define the particle matrix, $\bar{S}_i$, which is a 1x2 vector, with the intrinsic chemical factors as its elements,

$$\bar{S}_i = [\omega_{i0} \quad \omega_{i1}] \ldots (A.1)$$

where the intrinsic chemical factor of 'i' in a specific conformation $'s'$ is:

$$\omega_{is} = e^{-G_{is}\beta} \ldots (A.2)$$

The system can exist in 2^n possible macrostates and therefore, we can write a 1×2^n vector where each element represents the intrinsic chemical factor of a macrostate of this system. This system matrix, $\overline{\Lambda}$, can be defined as:

$$\overline{\Lambda} = \bigotimes_{i=1}^{n} \bar{S}_i \ldots (A.3)$$

where $\bigotimes$ indicates the Kronecker* product of all the particle matrices. The elements of the system matrix $\overline{\Lambda}$ do not include the contributions of the interaction energies between the particles. To incorporate the coupling interaction terms, we define another 1×2^n coupling vector, $\bar{C}$, where each element indicates the stabilization conferred to an individual macrostate of the system by the pairwise interactions.

To denote every macrostate of this N-particle system we use an N-dimensional variable $\nu_k(x_1^k, x_2^k, x_3^k, \ldots, x_{n-1}^k, x_n^k)$. The components of ν_k are x_i^k, (i = 1, 2,…,n), which indicate the microstate of the i^{th} particle in the k^{th} macrostate of the system (k = 1, 2,

…,2^n). x_i^k is 1 or 0 ($\forall\, i,k$) and indicates whether the i^{th} particle is in the activated or resting conformation. The k^{th} element of $\overline{\Lambda}$ corresponds to the macrostate ν_k and can be expressed as:

$$\Lambda_k = \prod_{i=1}^{n} \omega_{ix_i^k} \ldots (A.4)$$

The net coupling factor for the N-particle system in the k^{th} macrostate will be:

$$C_k = \prod_{i=1}^{n} \prod_{j=1, j\neq i}^{i} \theta_{i_0 j_0}^{(1-x_i^k)(1-x_j^k)} \theta_{i_1 j_1}^{x_i^k x_j^k} \theta_{i_0 j_1}^{(1-x_i^k)x_j^k} \theta_{i_1 j_0}^{x_i^k (1-x_j^k)} \ldots (A.5)$$

Λ_k and C_k are the k^{th} elements in the system matrix, $\overline{\Lambda}$ and the coupling matrix, $\bar{C}$ respectively. Thus, the Boltzmann weight of the k^{th} macrostate, ν_k, becomes:

$$z(\nu_k) = \Lambda_k C_k \ldots (A.6)$$

The Boltzmann weights of all the macrostates of the system can be collectively represented in the form of a 1x2^n matrix, $\bar{\zeta}$, whose k^{th} element is $z(\nu_k)$:

$$\bar{\zeta} = [z(\nu_1)\ z(\nu_2)\ z(\nu_3) \ldots \ldots z(\nu_{2^n-1})\ z(\nu_{2^n})] = [\overline{\Lambda} \circ \bar{C}] \ldots (A.7)$$

where [$\circ$] indicates the Hadamard[†] product of the two matrices.

The canonical partition function for the entire system is:

$$\widehat{\boldsymbol{Z}} = \sum_k z(\nu_k) = \overline{\Lambda}.\overline{C^T} \ldots (A.8)$$

The probability of the i^{th} particle being in the activated conformation as:

$$P_{i1} = \frac{\sum_k x_i^k z(\nu_k)}{\widehat{\boldsymbol{Z}}} \ldots (A.9)$$

And the probability of the i^{th} particle being in the resting conformation can be expressed as:

$$P_{i0} = \frac{\sum_k (1-x_i^k) z(\nu_k)}{\widehat{\boldsymbol{Z}}} \ldots (A.10)$$

At extreme potentials these probability terms would also be dominated by a single macrostate of the system – at low voltages the macrostate where 'i' is activated and all others are resting would dominate P_{i1}, and the macrostate where all particles are resting would dominate P_{i0}. At high voltages P_{i1} would be dominated by the macrostate where all particles are activated, while P_{i0} would be dominated by the macrostate where only 'i' is resting and all the others are activated. With these approximations the χ parameters for 'i' in an N- particle system can be easily derived in the explicit or normalized forms.

FOOTNOTES

***** Consider matrices, $\overline{A} = (a_{ij})$ of ordern m x n and $\overline{B} = (b_{kl})$ of the order p x q. The Kronecker product of the two matrices is given by $\overline{A} \otimes \overline{B} = (a_{ij}\overline{B})_{ij}$ where $a_{ij}\overline{B}$ is of the order p x q and $\overline{A} \otimes \overline{B}$ is of the order mp x nq.

† Consider matrices, $\overline{A} = (a_{ij})$ of ordern m x n and $\overline{B} = (b_{kl})$ of the order p x q. The Hadamard product of the two matrices is given by $[\overline{A} \circ \overline{B}] = (a_{ij}b_{ij})_{ij}$ where $a_{ij}b_{ij}$ is a scalar and $[\overline{A} \circ \overline{B}]$ is of the order p x q.

CHAPTER SEVEN

A molecular framework for temperature-dependent gating of ion channels.

Introduction

The ability to rapidly sense and respond to thermal stimuli is essential for an organism's survival. Not surprisingly, adaptive evolution has led to the emergence of specialized temperature sensing mechanisms enabling organisms to quickly sense and respond to noxious temperature stimuli. In higher organisms this role is performed by members of a specialized family of ion channels - the TRP channels (Clapham, 2003; Patapoutian et al., 2003; Dhaka et al., 2006; Ramsey et al., 2006). Members of this family of membrane proteins enable ions to flux across the membrane when triggered by changes in temperature (Caterina et al., 1997; McKemy et al., 2002; Peier et al., 2002a; Peier et al., 2002b; Xu et al., 2002; Story et al., 2003; Cao et al., 2013a). However, the molecular mechanisms by which temperature controls the functional state of the channel pore remain poorly understood. While it has been suggested that temperature-dependent gating in heat- and cold-sensing channels involves extensive conformational rearrangements (Brauchi et al., 2004; Yang et al., 2010; Yao et al., 2010, 2011), to date there is no consensus regarding the identity of this "temperature-sensing" domain. Recently, Clapham and Miller pointed out (Clapham and Miller, 2011) that, in principle, small number of sites in the protein may account for most of the temperature-sensitivity in TRP channels whose overall membrane architecture is remarkably similar to typical voltage-dependent ion channel (Long et al., 2007; Cao et al., 2013b; Liao et al., 2013). Although TRP channels serve as physiological thermal sensors (Bautista et al., 2007;

Dhaka et al., 2007), they are not the only ones that are highly sensitive to temperature. Several other ion channels, such as H_V (DeCoursey and Cherny, 1998), hERG (Vandenberg et al., 2006), K2P (Maingret et al., 2000), ClC (Pusch et al., 1997) and Anoactamins (Cho et al., 2012) are known to be strongly modulated by changes in temperature. Moreover, several pathological mutations in the voltage-gated sodium channels (Na_V) have been identified, which enhance the temperature dependence of the Na_V channel activity (McClatchey et al., 1992; Sugiura et al., 2000; Han et al., 2007; Dib-Hajj et al., 2008). Thus it raises an important question – is there a general mechanism which underlies temperature dependent gating of channels?

The design principle

A central functional characteristic of temperature modulated voltage-dependent ion channels is that upon changing the temperature, their relative open-probability *vs* voltage (P_OV) relationships (which are similar to the normalized conductance-voltage relationships) shift along the voltage axis (Voets et al., 2004). For heat sensing channels, such as TRPV1, the P_OV curves shift left when the temperature is increased, reflecting that channel opening is energetically facilitated at elevated temperatures (Fig. 1a, top panel). The reverse is true for cold sensing channels, such as TRPM8 (Fig. 1a, bottom panel), where increase in temperature makes it harder for the channels to open and causes rightward shifts in their P_OV curves. Such phenotypic effects of temperature on channel gating are strongly reminiscent of heat or cold induced unfolding of proteins. Classical calorimetric studies of protein folding have firmly established that the 'hydrophobic effect' plays a central role in governing the sensitivity of protein folds to changes in temperature. Unfolding of a protein bares its hydrophobic core to the surrounding

aqueous media, which leads to structural reorganization of water molecules and changes in their dynamic properties, around hydrophobic surfaces of the unfolded state (Schellman et al., 1981; Makhatadze and Privalov, 1993; Privalov and Makhatadze, 1993). Such a process is frequently associated with large changes in an important thermodynamic parameter, the specific heat capacity (Baldwin, 1986; Privalov and Gill, 1988), which is what ultimately shapes the free-energy change *vs* temperature (ΔG *vs* T) profile of the folding/unfolding process. As shown in Fig. 1b, non-zero 'change in specific heat capacity' (ΔC_P) of any arbitrary process results in the ΔG *vs* T profile becoming curved, following the equation:

$$\Delta G(T) = \Delta H_C + \Delta C_P(T - T_C) - T\Delta C_P \ln(T/T_C) \dots (1)$$

where, T_C is the temperature at which the profile switches in its monotonicity and ΔH_C is the enthalpy change of the process at T_C. The sign of ΔC_P governs the sign of the curvature (i.e. concavity *vs* convexity) of the profile while its absolute value determines the magnitude of the curvature. Thermodynamic investigations of ΔC_P associated with protein folding have revealed that solvation of hydrophobic residues is associated with a positive ΔC_P while that of polar/charged residues is associated with a negative ΔC_P (Makhatadze et al., 1990; Makhatadze and Privalov, 1990, 1994). This key observation formed the basis of our heuristic approach to design a temperature modulated ion channel.

The Shaker K_V channel is a model voltage-dependent ion channel, whose voltage-dependent gating has been extensively studied using electophysiological (Zagotta et al., 1994a; Schoppa and Sigworth, 1998), spectroscopic (Pathak et al., 2007) and biochemical techniques (Ahern and Horn, 2005; Xu et al., 2013). Of primary interest to us was the fact that its gating is only slightly modulated by change in temperature (Rodriguez and

Bezanilla, 1996; Rodriguez et al., 1998). Upon lowering the temperature from 28°C to 8°C, the kinetics of activation and deactivation of its ionic currents are modestly decelerated (Fig. 2a and b), its P_OV curve is right-shifted by less than 5mV and there is a slight reduction its steepness (Fig. 2c). The relative insensitivity of the P_OV curve of the Shaker K_V channel, to a 20°C change in temperature, complemented with the wealth of structural and functional information available for it and its homologs, made it an excellent template to implement our engineering approach and thereby test our theories about the physical origins of temperature dependent gating.

Voltage-dependent conformational changes of the Shaker K_V channel, underlying its transition between closed and open states, lead to changes in water accessibility in different parts of the protein (Larsson et al., 1996; Liu et al., 1997; Starace et al., 1997; Krepkiy et al., 2009; Jensen et al., 2010; Jensen et al., 2012; Krepkiy et al., 2012). We reasoned that substitution of key residues, in regions which undergo increased solvation when channels open, with hydrophobic residues will confer a positive ΔC_P to the overall gating process while polar residues at similar locations will confer a negative ΔC_P. Such substitutions should thus sensitize voltage dependent gating to changes in temperature but the temperature sensing phenotype (i.e. cold or heat sensing) will depend on the polarity of the perturbation. Conversely, perturbations at sites which undergo desolvation during channel opening, should also sensitize to temperature, although, hydrophobic and polar substitutions will now confer negative and positive ΔC_P respectively.

We chose to target sites within the voltage-sensing domain (VSD) of the Shaker K_V channel and perturb them to design a temperature-sensitive K_V channel. Our choice of the VSD over the pore domain was prompted by two factors. First, accessibility studies

of thiol-modifying reagents and protons to substituted cysteines and histidines, respectively, in the VSDs, complemented with computational models of hydrated VSDs, suggest the presence of water accessible crevices within the VSD (Fig. 3a) which undergo structural reorganization when the channel opens (Nguyen and Horn, 2002; Schonherr et al., 2002; Starace and Bezanilla, 2004; Li et al., 2014b). Such processes would likely be associated with changes in accessibility of residues in the VSD. Second, the VSD, in general appears to be more resilient to perturbations than the pore domain as suggested by previous perturbation studies which have reported that polar perturbations in the pore domain frequently compromises functional expression of channels (Hackos et al., 2002).

The specific sites within the VSD to be perturbed in this study were chosen based on two considerations. We reasoned that polar sites buried within the proteinaceous core of the VSD are likely to be the primary determinants of water occupancy in the voltage-sensing crevices. To identify such sites, using the structure of the VSD of the K_V1.2/2.1 paddle chimera (PDB-ID: 2R9R chain B), we computed the fractional buried surface area of each residue within the voltage-sensor (2R9R residue numbers: 159-310), using VMD using a probe-radius of 1.4 Å (Fig. 3b). Residues for which the buried fractions were > 0.8 (relative to the total surface area of the respective amino-acid sidechains) were classified as buried residues. Next, we computed the polarity conservation index (PCI) of each of the sites in the VSD. PCI of each site is essentially reflects the enrichment of polar/hydrophobic residues at a given site, based on evolutionary information. For the polarity conservation index (PCI) calculation, a previously reported multiple sequence alignment of 360 K_V channel homologs (Lee et al., 2009) was used to compute the gap-

corrected position specific frequency of each amino acid (a) and each position of the alignment (i), $f_i^{(a)}$ (gap-correction normalizes the raw frequency scores at each position of the alignment with $1 - f_i^{(gap)}$). This was subsequently used to compute the polarity conservation index (PCI) of each site as: $\sum_{(a)} h_{(a)} f_i^{(a)}$, where the summation is over all 20 amino acids and $h_{(a)}$ indicates the hydrophobicity score of the amino acid (a), according to the the Hessa von-Heijne (H-vH) scale. For each site, PI > 1 reflects a strong enrichment of highly polar/charged residues, PI between 0.3 and 1 reflects an enrichment of polar residues, while PI < -0.3 suggests an enrichment of highly hydrophobic residues. Our candidate sites were those with fractional buried surface area > 0.8 and PI > 0.3. Eight sites located in the S1-S3 segments of the VSD for which the fractional buried surface area > 0.8 and PCI > 0.3 were selected for experimental analysis (Fig. 3a and b).

RESULTS

Influence of residues in S1-S3

We first targeted three sites, S240, E293 and Y323, in the S1, S2 and S3 segments respectively, of which E293 lies in the intracellular crevice of the voltage-sensor while the other two sites reside in the extracellular crevice (Fig. 3a). Each of the three sites were individually mutated to residues of varying polarity, beginning with a hydrophobic residue (Fig. 4a-c, top panel) and leading on to more polar residues (Fig. 4a-c, lower panels). The relative-open probability vs voltage ($P_O V$) relationships of each of the mutants, were measured at two different temperatures, 8°C and 28°C (Fig. 4a-c**,** blue and red curves respectively). The temperature dependent shifts of the $P_O V$ curves were quantified by calculating median voltage of channel opening (V_M) at each temperature.

Raw ionic current traces for some of the mutants are shown in Fig. 5. Several of these mutations significantly altered the temperature dependence of ionic current activation/deactivation and some of them resulted in large shifts in the P_OV curves. For instance, upon heating (from 8°C to 28°C), the E293I mutant results in a ~20mV rightward shift in the P_OV curve (Fig. 4b, top panel) while the Y323I mutant causes a ~30mV leftward shift. The change in the median voltage of channel opening due to heating ($\Delta V_M = V_M(28°C) - V_M(8°C)$) due to the different perturbations at each of the three sites are summarized in Fig. 4d, where ΔV_M due to each perturbation is plotted against the hydrophobicity of the perturbing residue (H-vH scale (Hessa et al., 2005)). For the S240 site (Fig. 4d, left panel), ΔV_M is not correlated with the hydrophobicity. However, for the E293 site (Fig. 4d, center panels) we observe a strong negative correlation, i.e. upon increasing the polarity, the E293 mutants switch from being cold sensitive to heat sensitive. Conversely, the strong positive correlation observed with the Y323 mutants (Fig. 4d, left panel) indicates that increasing the polarity of the site causes the channel to switch from being heat to cold sensitive. Furthermore, we also observe that the V_M, at 28°C, for the different mutations at each of the three sites are also correlated with hydrophobicity (Fig. 4e). For the S240 and Y323 sites (Fig. 4e, left and right panels), the positive correlation observed in the V_Ms (at 28°C) of different mutations suggests that it becomes harder to open the channels when the sites are occupied by polar residues, while for the E293 site (Fig. 4e, center panel), the negative correlation implies it is easier to open the channel when the site is occupied by a polar residue (although the Gln mutant is an outlier).

How can we rationalize these results? For the Y323 site, the positive correlations of V_M (at 28°C) and ΔV_M with hydrophobicity suggests that channel activation results in, at least partial, desolvation of this site. A hydrophobic residue at such a site would thus confer a negative ΔC_P to channel gating while a polar residue would impart a positive ΔC_P. In a similar way, the negative correlations observed for the different mutants at the E293 site imply conformational changes at or around this site results in increased solvation of this site in the activated/open state of the channel. Hydrophobic residues at this position will thus result in a positive ΔC_P and polar residues will result in a negative ΔC_P. Consistent with the ΔG vs T profile, depicted in Fig. 1b, in the given temperature range of 8°C to 28°C, channel gating with positive ΔC_P (desolvation of a polar residue, as with Y323T/Q, or solvation of a non-polar residue, E293I) will render the channel cold sensitive while a negative ΔC_P (desolvation of a non-polar residue Y323I or solvation of a polar residue, E293Q/H). For the S240 site, although V_M is correlated with polarity, ΔV_M is not. This could arise in instances wherein although the site undergoes a change in polarity of the environment, it does not undergo extensive solvation/desolvation on account of being located in water inaccessible nooks and corners of the protein.

Other sites in the VSD, S233 (in S1), E283 (in S2), N313, D316 and T326 (all in S3), were perturbed with two different mutations, each. Perturbations at E283 and D316 (to Ile and Val) did not yield functionally expressing channels (Table 1) or their P_OV curves do not exhibit temperature dependent shifts (Fig. 6a-c). It is however interesting to note that for the sites in the internal crevice of the VSD (S233, E293 and N313), hydrophobic mutations makes channel opening (at 28°C) less favorable, relative to polar mutations (Fig. 6d). In contrast, for the sites in the external crevice (S240, Y323 and

T326), the hydrophobic mutation renders channel opening more favorable relative to the polar mutation (Fig. 6d). These results indicate that during channel opening there are mutually complementary changes in the structural organization of the intracellular and extracellular crevices (for instance, changes in the volumes of the crevices) that cause an overall change in the polarity of the crevice environment, although only few of these residues truly determine the energetics of solvation and thereby modulate the temperature dependent behavior of channel gating.

Influence of hydrophobic residues in S4

Membrane depolarization triggers complex motions of the S4 helix which in part comprises vertical displacement, rotation about its helical screw axis, change in tilt (relative to the membrane plane) and still remains an active area of investigation. The S4 charges likely remain water accessible in both the resting and active conformations of the VSD as indicated by proton accessibility studies (Starace et al., 1997; Starace and Bezanilla, 2001, 2004). Lu and colleagues have recently demonstrated that the hydrophobic residues intervening the principle gating charges of the channel become exposed to a more polar environment when the channel activates (Xu et al., 2010). Such state-dependent changes in polarity at these sites make them suitable candidates to test for temperature-dependence. We created three hextuplet mutants, where the six uncharged residues interspersing the gating charge determining residues were simultaneously mutated to Ile, Met or Ala. Measurements of the P_OV curves of each of these mutants (Fig. 7a-c) showed that decreasing the polarity of the perturbation left shifts the P_OV curves of the channel (at 28°C) and concomitantly renders the channel

more heat sensitive (Fig. 7d). Next, we generated three quadruplet mutants, where the four uncharged residues between the first and third gating charge (R362 and R368 respectively) were simultaneously mutated to Ile, Met or Ala. The P_OV curves of these three mutants (Fig. 7e-g) followed the overall trend of the heat sensitivities of the hextuplets, with the Ala mutant exhibiting the most left shifted GV curve (at 28°C) and the largest heat sensitivity (~28mV) (Fig. 7h). Interestingly though, the V_M of the P_OV curves at 28°C somewhat loose the strong polarity correlation observed with the hextuplet substitutions. These observations imply that upon channel activation there is an increase in average solvation of these sites.

To test the position dependence of the hydrophobic residues in S4, we mutated each intervening pair to create three sets of doublets (X2Top, X2Mid and X2Bot). The top doublets (X2Top, where X is the perturbed amino acids) were joint perturbations of the two residues between the first and second gating charge; the middle (X2Mid) and bottom doublets (X2Bot), involved simultaneous perturbations of the two residues between the second and third or third and fourth gating charges, respectively. Perturbations were made to four different amino acids, namely, Ile, Met, Ala and Ser, and in each of the twelve cases we measured the ΔV_M due a change in temperature from 8°C to 28°C (Fig. 8**)**. Many of the doublet perturbations strongly sensitize the P_OV curves to temperature. In particular, for the S2Bot mutant (Fig. 8d, right panel) a 20°C change in temperature results in ~75mV shift in the P_OV curves. Upon correlating these functional effects with the polarity of perturbation, we find that the temperature dependent shifts of the P_OV curves (ΔV_M) exhibited a positive correlation with the hydrophobicity of perturbation for only the Top and Bottom doublets (Fig. 8e). Interestingly however, at

28°C, the V_M of the different perturbations shows polarity correlation only for the Middle doublets (Fig. 8f).

How can these results be reconciled? The results of the X2Mid doublets are similar to that observed for the S240 site (Fig. 2d and e, left panels) and a similar explanation might apply to the X2Mid perturbations. For the Top and Bottom doublets, although we observe a polarity correlated ΔV_M, the absence of any correlation in V_M indicates that these sites are involved in interactions with different parts of the protein which influence the energetic consequences of the perturbations at these sites. For instance, the I364 (in the top doublet) has been proposed to be interacting with residues in the S3b segment of the paddle (Xu et al., 2013) while V369 (in the bottom doublet) is a site which may be involved in electromechanical coupling of the VSD with the pore domain (Smith-Maxwell et al., 1998b, a). Raw ionic current traces for three heat sensitive mutants, generated via perturbation of the S4 hydrophobic residues, are shown in Fig. 9, which show the substantial changes in the kinetics of channel activation/deactivation.

Another important point to note is that, in the cases of the hextuplet, quadruplet and doublet perturbations where we see a polarity correlated temperature-sensitization of channel gating, unlike the 323 and 293 sites, there is no switch in temperature-sensitivity across the spectrum of perturbations. These observations can be reconciled with our original hypothesis if we consider that the perturbations are not only introducing new ΔC_p components but in some cases they can also subtract pre-existing ΔCp components associated with channel gating. Say, the contributions of different residues to the net ΔCp associated with channel gating can be written as:

$$\Delta C_{P,net} = \Delta C_{P(+)} + \Delta C_{P(-)} + \Delta C_{P(0)} \quad \ldots(2)$$

where $\Delta C_{P(+)}$ and $\Delta C_{P(-)}$ denotes the contribution of amino acids which respectively increase or decrease the $\Delta C_{P,net}$ during channel opening. $\Delta C_{P(0)}$ represents all the other amino acids which do not contribute to the $\Delta C_{P,net}$. Since the wild type Shaker K+ channel does not exhibit any temperature-dependent shift in its relative open probability, $\Delta C_{P,net}$ associated with its gating is zero implying $\Delta C_{P(+)}$ and $\Delta C_{P(-)}$ are equal in magnitude.

Now consider a site which undergoes solvation during channel activation, which natively was responsible for $\Delta C_{P(0)}$. When such a site is occupied by a polar residue, it solvation in the activated state will lead to a negative ΔC_P and lead to heat sensitivity (Fig. 10a). Conversely when the site harbors a non-polar residue, its solvation will lead to a positive ΔC_P and thus cold sensitivity (Fig. 10a). This would be the case for our 293 site.

A different scenario arises when we consider a site, which undergoes solvation when the channel activates and contributes to $\Delta C_{P(+)}$ component. At such a site, a non-polar residue (whose solvation is associated with a positive ΔC_P) will not alter the net ΔC_P of channel gating and the channel will remain temperature insensitive. However, replacing a polar residue at such a side will reduce the $\Delta C_{P(+)}$ component which means that the net ΔC_P is dominated by $\Delta C_{P(-)}$ term, effectively making the process in heat sensitive (Fig. 10b). In both the scenarios, polar residues at the two sites lead to heat sensitivity, however increasing the hydrophobicity in the first case causes a switch in the temperature sensing phenotype of the channel while in the second case, and it simply compromises the heat sensing phenotype of the channel.

Enhancement of temperature sensitivity

The change in ΔG of gating, due change in temperature, is directly proportional to the ΔC_P of gating (Eq. 1). The proportionality posits that an increase in ΔC_P will render the channel more temperature sensitive. Through our targeted perturbations described we have identified several mutations in Shaker K_V channel which robustly enhance the temperature sensitivity of the channel, causing >25mV shifts in the P_OV curves of the channel. We asked the question, can we further enhance the temperature sensitivity of the Shaker K_V channel by combining two temperature sensitizing perturbations?

The mutations, Y323I and S2mid (doublet serine mutant, V366S/I367S) individually result in ~30mV and ~10mV leftward shifts in GV upon heating. We generated a combination mutant, Y323I/S2mid and measured its GV curves at 28°C and 8°C. This mutant caused a massive shift leftward shift of ~56mV upon heating (Fig. 11a). The magnitude of shift observed in this mutant was significantly larger than the additive effects of the individual perturbations. Next, we generated a second mutant by combining the perturbations Y323I and M6 (the S4 hextuplet methionine mutant, Fig. 11b). The resultant mutant also exhibited robust heat sensitivity to the extent that we were unable to reliably measure the full P_OV curve of the mutant at 8°C. Hence for the Y323I/M6 mutant, we measured the P_OV curves at 28°C and 15°C (Fig. 11b). For this heat sensitive mutant, the shift in the P_OV curve was ~36mV. For both the Y323I amd M6 mutants, the P_OV curves shift by ~30mV for a 20°C change in temperature. The fact that the combination mutant results in a similar ΔV_M but in response to a smaller change in temperature strongly suggests the two perturbations significantly enhance the temperature sensitivity of the channel.

An important hallmark of temperature modulation of channel gating is that change in temperature directly alters the magnitude of ion flux through the channel. To gauge the extent of temperature sensitization of our engineered heat sensitive channels we performed temperature ramp experiments. To this end, oocytes expressing wild-type or mutant channels were voltage-clamped at -120mV and subjected to temperature ramps between 28°C and 8°C, wherein temperature was changed at the rate of 1°C/15sec. Every 15 seconds, ionic currents were elicited by a 100ms depolarizing pulse to -20mV, which is close to the V_M of the wild-type Shaker K_V channel (at 28°C). For the wild-type channel (Fig. 12a), our temperature ramp protocol shows that a 20°C decrease in temperature causes ~2.2 fold reduction in the current. This change in current levels in all likelihood arises largely due to the change in single channel conductance of the channel (Rodriguez and Bezanilla, 1996; Rodriguez et al., 1998). In comparison, in the case of the two of the strongly heat sensitized mutants, S2Bot (i.e. V369S/F370S) and Y323I/M6, the same change in temperature led to a ~30 fold reduction in the current, in each case (Fig. 12b and c). A semi-logarithmic plot of the fraction of current at each temperature (relative to current at 28°C) *vs* temperature, for each of the two mutants (Fig. 12e and f) shows a steep temperature dependence in both cases, strikingly different from that observed for the wild-type Shaker K_V channel. In the temperature range of 10°C - 14°C, Q_{10} value of the outward currents elicited by the 100ms depolarizing pulses at -20mV is 18.3 and 15.5 for the S2Bot and Y323I/M6 mutants respectively (which are comparable to those reported for thermoTRPs), while that for the wild-type Shaker K_V channel is ~1.8 which reflects the strongly enhanced heat sensitivity of the two mutants. The results of these experiments convincingly demonstrate that relatively few amino acid

substitutions (2 in S2Bot and 7 in Y323I/M6, per subunit) in a protein subunit of more 600 amino acids, can result is massive alterations in the temperature sensing phenotype of the channel. Such an observation engenders the view that modest structural changes in critical parts of a channel undergoing state dependent changes in solvation may underlie the temperature responsiveness of the channel.

Role of the gating charges in S4

It has been proposed that the voltage-sensitivity of the channel is inversely proportional to its temperature sensitivity such that strongly temperature sensitive channels such as the thermoTRPs have low voltage dependence while the K_V channels, which are steeply voltage-dependent, exhibit low temperature sensitivity. The argument for such a proposition arises from thermodynamic relationships which show that a shift in the voltage-dependent activation curves of a channel, ΔV_M, is governed by the ratio $f(\Delta S, \Delta C_P)/z$, where '$f(\Delta S, \Delta C_P)$' is a function of the change in entropy and heat capacity of channel gating and 'z' is its apparent voltage-sensitivity (Voets et al., 2004; Latorre et al., 2007). The equations describing the temperature dependence of V_M of channel opening are:

$$V_M(T) = \{\Delta H_C + \Delta C_P(T - T_C) - T\Delta C_P \ln(T/T_C)\}/zF \ldots (3a)$$

or in the case where ΔC_P is 0:

$$V_M(T) = \frac{(\Delta H - T\Delta S)}{zF} \ldots (3b)$$

where ΔH and ΔS are enthalpy and entropy change associated with channel gating (these parameters are temperature independent when ΔC_P is 0).

Such a principle, does not limit itself to temperature sensitivity of the channel but to other modes of sensitivities (such as ligand, pressure, etc.) and has been discussed in detail in Chapter Five. Thus as the voltage-sensitivity of the channel is compromised (say by neutralizing of the gating-charge determining residues which leads to lowering of 'z') the sensitivity of the channel to changes in temperature is enhanced. To test this principle, we generated eight mutants in which the four S4 charges (R362, R365, R368 and R371), were individually mutated to Ala and Gln (or Asn for R368). The P_OV curves of each of these mutants were virtually non-responsive to changes in temperature (Fig. 13) except for R365A, which shows mild cold sensitization (~10mV shift).

The lack of temperature sensitization due to the arginine point mutations might arise due to two reasons. The first possibility is that, single charge neutralized channels are still significantly voltage-sensitive to mask any possible temperature sensitivity of the channel. The second possibility is that innate temperature sensitivity of the channel of channel gating, governed by its ΔS and ΔC_P (i.e. the function '*f*'), is so small that reduction in the channel's voltage-sensitivity has no effect on its temperature sensitivity. To test this hypothesis we introduced the R368N and R371Q mutations in the background of the heat sensitive Y323I mutation and recorded the P_OV curves of the two combination mutants. Strikingly both mutants were significantly more heat sensitive than the Y323I mutant alone (Fig. 14a and b). To further investigate this charge-dependent enhancement of temperature sensitivity, we combined the R371Q mutant with the modestly heat sensitive S2Mid mutant and the modestly cold sensitive Y323Q mutant and assessed the temperature dependent shifts in their P_OV curves. As in previous instances, the modestly heat sensitive mutant was rendered significantly more heat

sensitive by the R371Q neutralization (Fig. 14c) while the modestly cold sensitive mutant became significantly more cold sensitive in the background of the R371Q mutant (Fig. 14d).

We plotted the magnitude of temperature dependent shifts in the P_OV curves due to each of the three mutants (namely, Y323I, Y323Q and S2mid) when introduced in the background of a charge neutralized channel (i.e. R371Q or R368N) against the shifts due to same mutants when introduced in the background of the native channel (wild-type Shaker K_V) (Fig. 14e). The linear relationship of the plot has a regression slope of ~ 2. This implies that in each of the four cases, charge neutralization (R368N or R371Q) doubles the temperature dependent shifts in the GV curves. Such a charge dependent effect is in complete agreement with the thermodynamic predictions, described in the simulated V_M *vs* temperature profiles shown in Fig. 14f. For two processes with identical ΔG *vs* T profiles, the V_M *vs* T profiles will be more curved (and/or steep) for the process which has a lower voltage-sensitivity. As a result, although both systems have identical ΔG *vs* T profiles, the functional activity of the system with a lower voltage-sensitivity will be altered to a greater degree than that with a higher voltage-sensitivity. These results therefore underline the crucial role played by the voltage-sensing charges of the channel in indirectly modulating the temperature sensitivity of the channel.

DISCUSSION

Despite intensive effort, the molecular basis of temperature-sensitivity remains an enigma. Miller and Clapham recently pointed out (Clapham and Miller, 2011) the importance of specific heat capacity change accompanying channel gating as a primary

determinant for temperature dependence of ion channel activity. However, measuring ΔC_P of channel gating of the natively temperature sensitive channels (e.g. thermoTRPs) is a formidable challenge because of two fundamental reasons. First, an accurate estimate of ΔG of gating, at different temperatures, necessarily requires experimental measurements of either the conjugate displacements associated with a stimulus or heat exchange during gating, both of which are non-trivial. Second, accurate ΔG estimates need to be obtained at temperatures close to T_C (the temperature at which the monotonicity of the ΔG *vs* T profile switches) because, further away from T_C, ΔG *vs* T profiles become quasi-linear and ΔC_P cannot be accurately calculated. To date, non-monotonicity of ΔG vs T curves have not been observed which would suggest that the T_C is likely to be outside the experimentally accessible temperature range.

To test the role of ΔC_P on temperature-dependent gating of ion channel, we have developed a model system that allows us to modulate the ΔC_P associated with the gating process in a somewhat well-defined manner and test its effects on channel gating. Our approach exploits the prior knowledge that ΔC_P of solvation of polar and non-polar residues are opposite in sign and during voltage-dependent activation certain regions of the Shaker potassium channel undergo changes in water accessibility (Fig. 15). We identify multiple positions on voltage-sensing domain at which perturbations introduce large temperature dependent shifts on the channel activation curves, in a polarity correlated fashion. It is clear, however, that in some instances, temperature dependent effects on gating do not parallel polarity and this might be due to multiple reasons. First, $P_O V$ (or conductance-voltage) curves do not reflect the full energetics of channel activation of multi-state systems (Chowdhury and Chanda, 2012a, 2013) and may not

accurately recapitulate temperature dependent changes in free-energy. Second, the substituted side-chains may become partially solvent accessible which would reduce their contribution to ΔC_P of solvation. Finally, the properties of the water molecules in the crevices may be different from that of the bulk water which could result in anomalous heat capacity changes. Despite these caveats, our results show that relatively few mutations (1 to 7 per subunit) can profoundly alter the temperature sensing phenotype of the channel (as exhibited by the Y323I, S2Bot, Y323I-S2mid, Y323I-M6 mutants) implying that large conformational changes in the protein is not a pre-requisite for strong temperature dependent gating.

Our experiments also shed light on the major influence of voltage-sensing charges on temperature dependence of P_OV curves. Although an inverse relationship between voltage and temperature sensitivity of a channel has been proposed earlier in the context of TRP channels (Voets et al., 2004; Latorre et al., 2007), direct experimental evidence in support of such a hypothesis has been lacking, in part due to the uncertainty regarding the identity of gating charges in the thermoTRPs. However, the charge carrying residues in the Shaker K_V channel are well known which enables us to directly test this hypothesis. Gating-charge neutralizations in the wild-type channels do not exhibit temperature-sensitive responses whereas when introduced in the background of heat- or cold-sensitized mutants, the resultant mutants exhibit substantially enhanced temperature sensitivity highlighting the crucial but indirect role of charges on temperature gating.

In conclusion, through the characterization of the relative open-probability *vs* voltage relationships of several targeted mutants of Shaker K_V channel, at two different temperatures, we have elucidated some of the fundamental physical principles underlying

temperature modulation of voltage-dependent gating. The idea that relatively modest conformational changes which lead to change in solvation of residues can massively enhance the temperature sensitivity of the channel is important as it implies that a specialized temperature sensing domain might not be a necessary requirement for temperature dependent gating. This is a crucial point as traditionally voltage and ligand gated ion channels harbor specialized structural domains which serve as stimulus sensors. Temperature dependent gating of natively heat or cold sensing ion channels could thus arise out of small conformational changes occurring in different parts which lead to overall large heat capacity changes. Consistent with such a proposition, perturbations at different locations of the TRPV1 channel has been shown to alter its temperature dependent gating. Our findings illustrate an alternate mechanism wherein temperature sensitivity is conferred by multiple temperature-sensing microdomains distributed over the whole channel rather than a distinct temperature-sensing domain.

FIGURES

Figure 1. ΔC_P sign governs the temperature-sensitivity of channel gating.

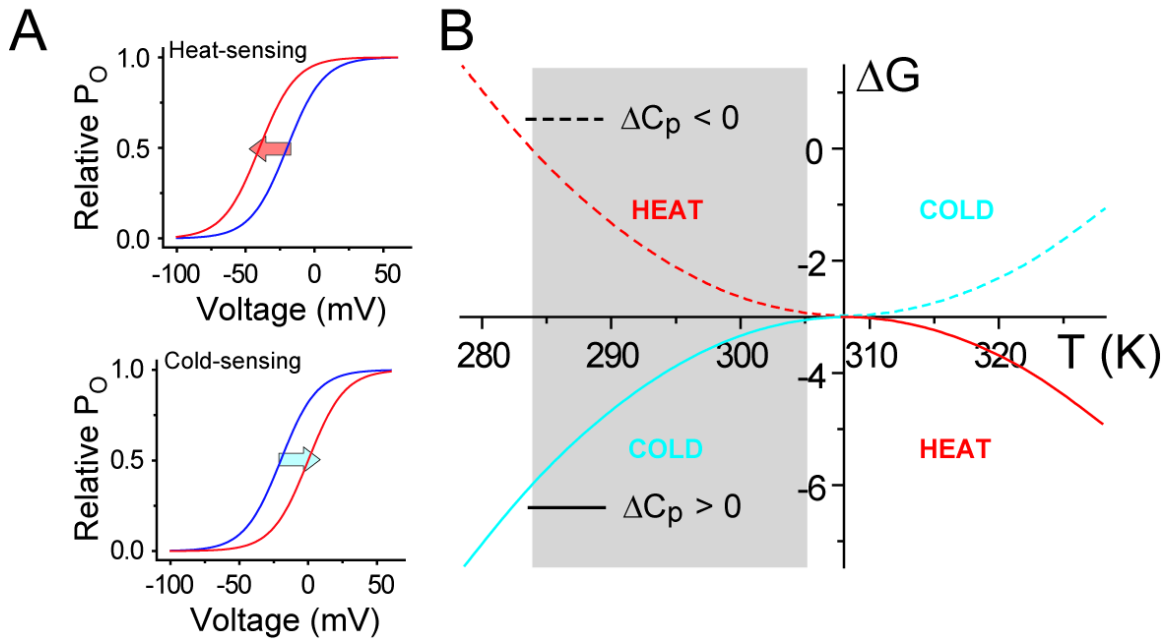

(A) and (B) Arbitrary relative open probability *vs* voltage curves for a heat-sensing channel **(A)** and a cold-sensing channel **(B)** at two temperatures (red: high temperature, blue: low temperature). Arrows indicate the shifts in the curve on heating. **(C)** ΔG *vs* T profiles simulated using **Eq. 1** for two processes, one with a positive ΔC_P (= 3 kcal/mol) (solid curve) and the other with a negative ΔC_P (= -3 kcal/mol) (dotted curve), with ΔH_C = -3 kcal/mol and T_C = 308K in both cases. The heat sensing and cold sensing regimes of the curves are indicated by the red and blue colors respectively.

Figure 2. Temperature sensitivity of wild-type Shaker K_V channel.

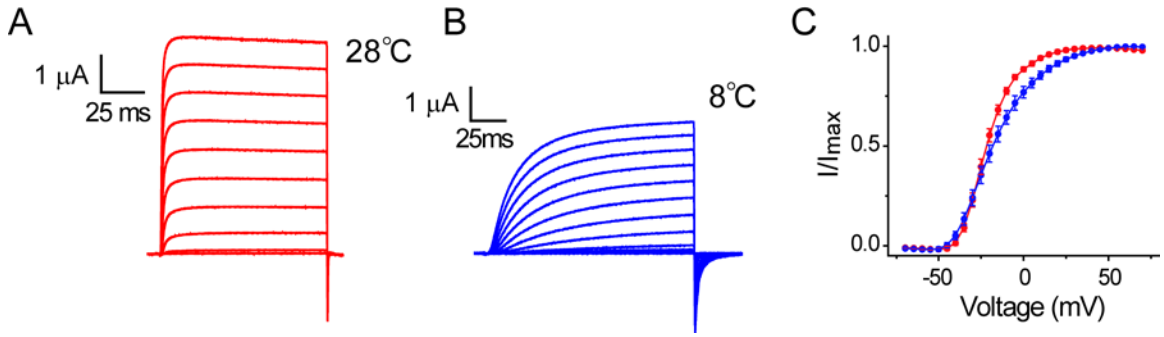

(A), (B) Representative ionic currents at 28°C **(A)** and 8°C **(B)** from an oocyte expressing wild-type Shaker K_V channel, elicited by depolarizing voltage pulses from -60 to +60mV, in 10mV increments, from a holding voltage of -120mV. **(C)** Relative open probability *vs* voltage curve of the wild-type Shaker K_V channel at 28°C (red) and 8°C (blue) (measured from tail currents).

Figure 3. Identification of buried sites of high polarity conservation index (PCI).

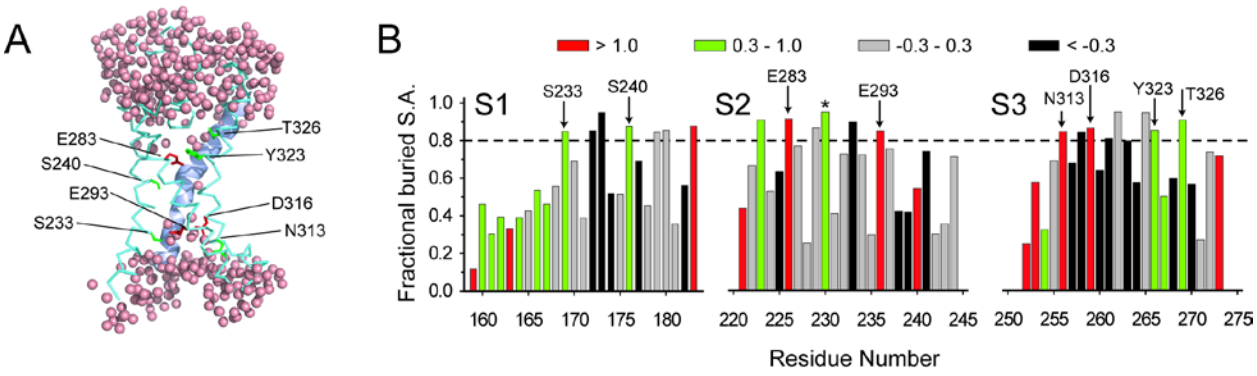

(A) A model of a hydrated voltage-sensor, deduced from the crystal structure of the $K_V1.2/2.1$ paddle chimera and molecular dynamics simulations, showing occupancy of water within the crevices of the voltage-sensor. Sites target by mutagenesis in this study are indicated. **(B)** Fractional buried surface area of different residues in the transmembrane segments S1-S3. The dotted horizontal lines indicates the cut-off for buried surface areas. The bars are colored according to the polarity index of the residue position, deduced from an alignment of 360 K_V channel sequences. The site marked with an asterisk (in S2), while satisfies our criteria, is a hydrophobic residue in the Shaker K_V channel, and was not investigated in this study.

Figure 4. Perturbations at crevice facing residues of S1-S3 segments sensitize the relative open-probability curves to temperature.

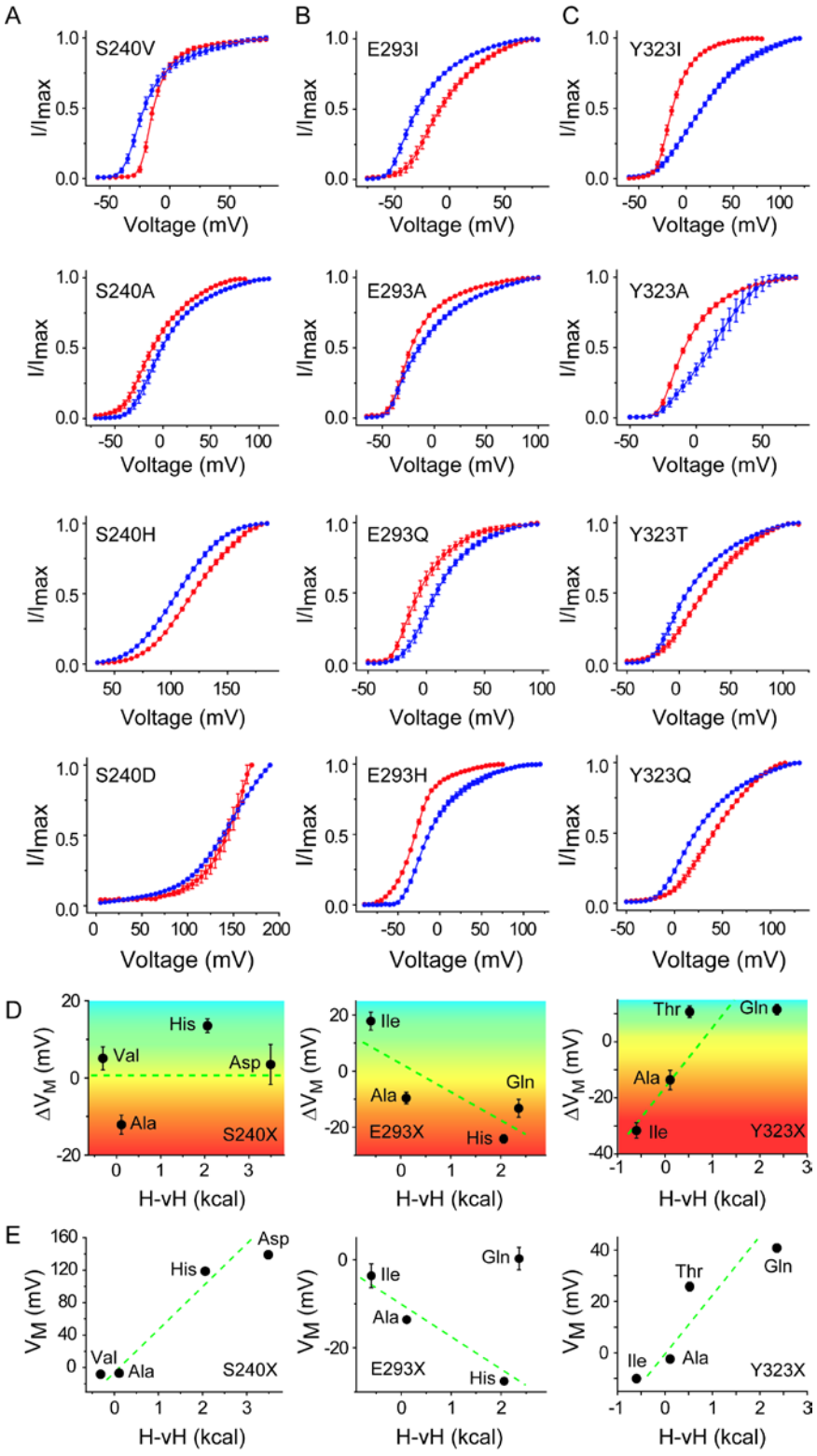

Relative open-probability *vs* voltage-curves for different perturbations at sites S240 **(A)**, E293 **(B)** and Y323 **(C)** mutant, deduced from measurements of tail currents at 5mV voltage intervals. Unless otherwise mentioned, in all cases blue curves indicate measurements at 8°C while red curves indicate measurements at 28°C. The mutation corresponding to each panel is listed in the top left corner of each panel. **(D)** Correlation of temperature dependent change in the median voltage of channel opening (ΔV_M) with the polarity of perturbation for sites S240 **(left panel)**, E293 **(middle panel)**, Y323 **(right panel)**. **(E)** Correlation of median voltage of channel opening (V_M) at 28°C, with the polarity of perturbation for sites S240 **(left panel)**, E293 **(middle panel)**, Y323 **(right panel)**. **(F)-(H)** Relative open-probability *vs* voltage-curves for a hydrophobic mutation (**top panel**) and a polar mutation (**bottom panel**) at sites S233 **(F)**, N313 **(G)** and T326 **(H)** mutants, at 28°C (red) and 8°C (blue).

Figure 5. Ionic currents of mutations at crevice facing sites in S1-S3.

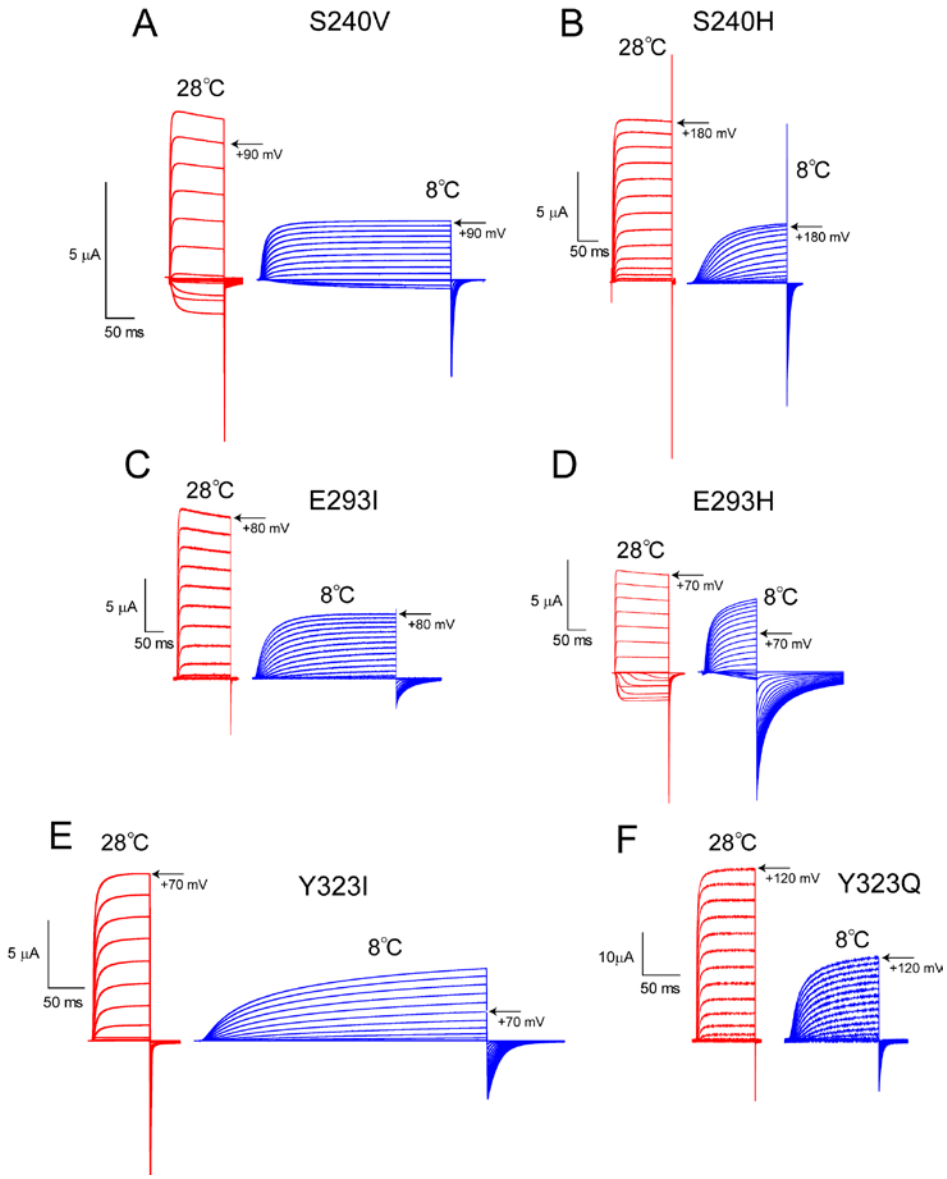

Representative ionic currents at 28°C **(red)** and 8°C **(blue)** from single oocytes expressing mutant channels, elicited by depolarizing voltage pulses in 10mV increments ($V_{Holding}$ = -120mV). In each set of traces, the arrow points to the current response at the indicated voltage. The mutants corresponding to these raw current traces are: S240V **(A)**, S240H **(B)**, E293I **(C)**, E293H **(D)**, Y323I **(E)** and Y323Q **(F)**.

Figure 6. Comparison of effects of perturbations at external and internal crevices.

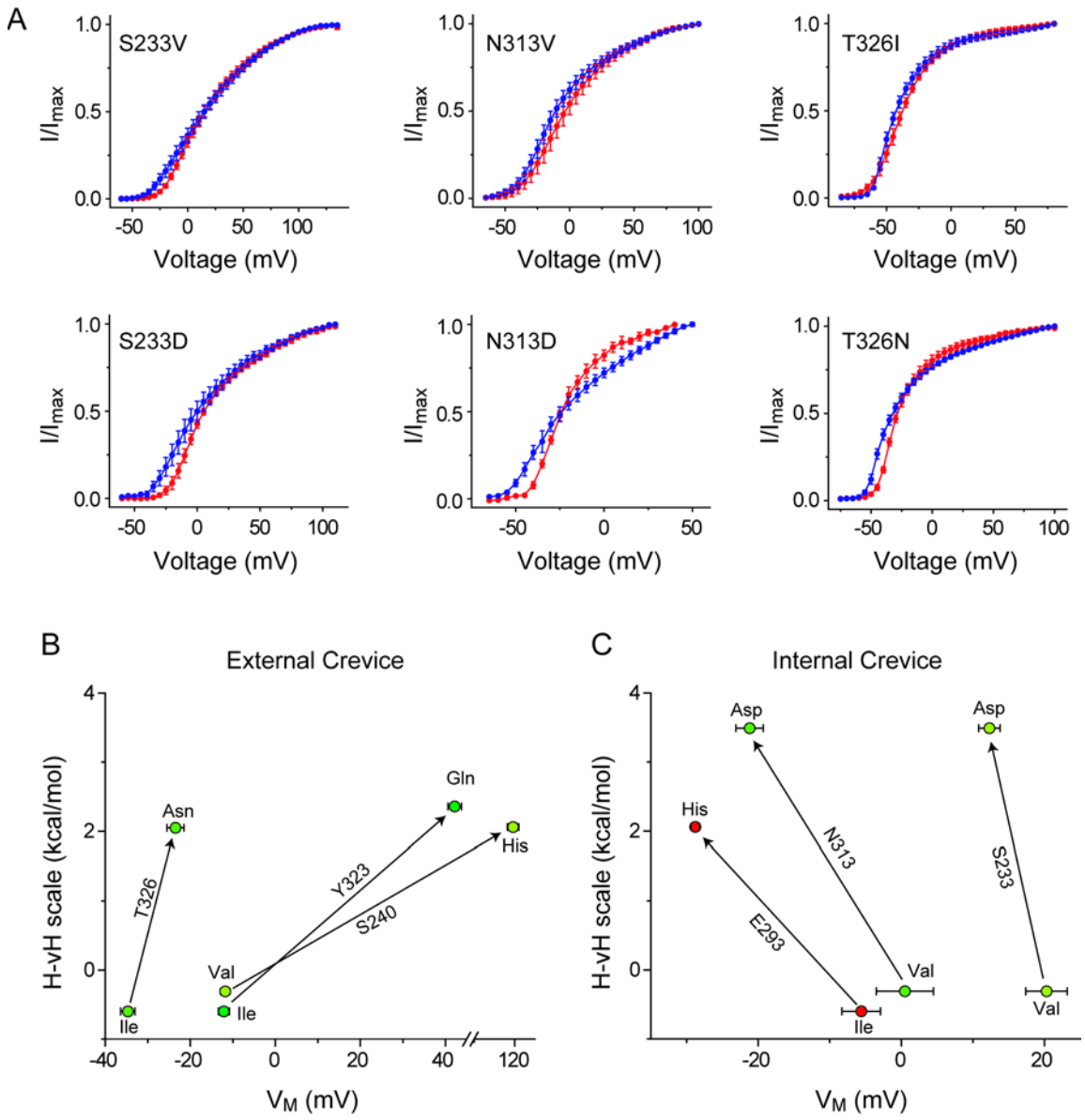

(A) The relative open-probability *vs* voltage curve at 28°C (red) and 8°C (blue) for hydrophobic perturbations (top row) and polar perturbations (bottom row) at sites S233 (left), N313 (center) and T326 (right). **(B)** For three sites in the external crevice, T326, Y323 and S240, the polarity of the perturbation is plotted against the V_M, at 28°C, of each mutant. Arrows connect the two perturbations at the same site (written alongside the arrow) and indicate the change in V_M in response to a change in polarity. As indicated,

increase in polarity shifts the V_M rightward in all three cases. **(C)** Same as **(B)**, except that three sites, S233, 283, N313, reside in the internal crevice – for each of these sites increase in polarity shifts the V_M leftward.

Figure 7. Effect of hextuplet and quadruplet mutations at hydrophobic residues in S4 segment.

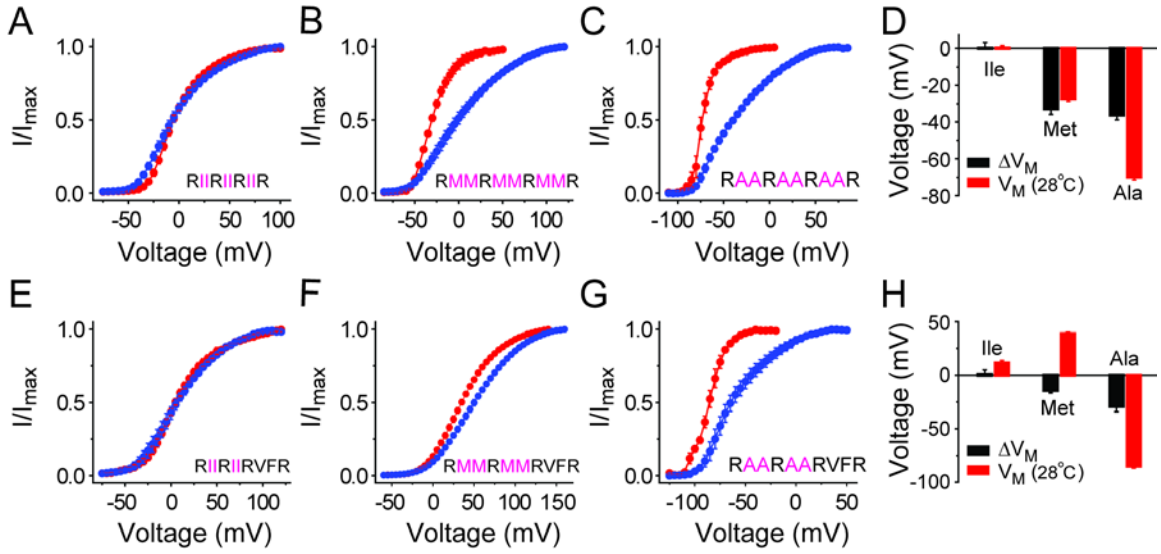

(A)-(C) Relative open-probability *vs* voltage curves, at two temperatures (28°C, red and 8°C, blue) for hextuplet mutations in the S4 segment where six residues are simultaneously mutated to Ile **(A)**, Met **(B)** or Ala **(C)**. **(D)** The V_M (at 28°C) and ΔV_M due to a 20° change in temperature for the hextuplet mutations to Ile, Met and Ala are represented as bar graphs. **(E)-(G)** Relative open-probability *vs* voltage curves, at two temperatures (28°C, red and 8°C, blue) for quadruplet mutations in the S4 segment where four residues are simultaneously mutated to Ile **(E)**, Met **(F)** or Ala **(G)**. **(H)** The V_M (at 28°C) and ΔV_M due to a 20° change in temperature for the quadruplet mutations to Ile, Met and Ala are represented as bar graphs.

Figure 8. Effect of doublet mutations at hydrophobic residues in S4 segment.

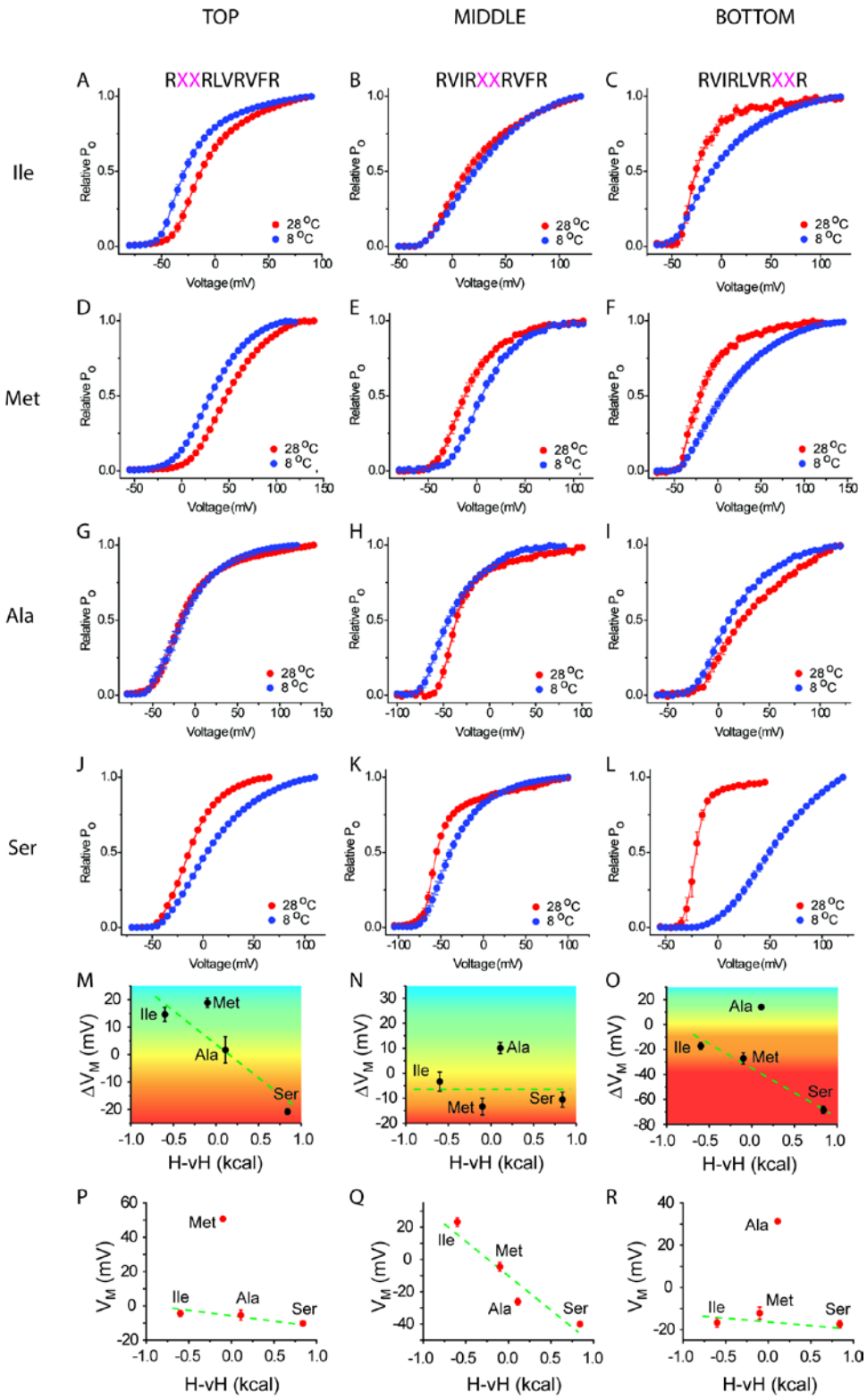

(A)-(L) Relative open-probability *vs* voltage curve at 28°C (red) and 8°C (blue) for doublet perturbations – top row **(A)-(C)** are Ile perturbations, upper middle row; **(D)-(F)** are Met perturbations; lower middle row are **(G)-(I)** Ala perturbations; bottom row **(G)-(I)** are Ala perturbations. The first column (**(A), (D), (G) and (J))** represent the top doublets, the second (**(B), (E), (H) and (K)**) and the third (**(C), (F), (I) and (L)**) columns represent the middle and bottom doublets respectively. **(M)-(O)** Correlation of temperature dependent change in the median voltage of channel opening (ΔV_M) with the polarity of perturbations for the Top (**M**), Middle (**N)** and Bottom (**O**) doublet mutations. **(P)-(R)** Correlation of median voltage of channel opening (V_M) at 28°C with the polarity of perturbations for the Top (**P**), Middle (**Q)** and Bottom (**R**) doublet mutations.

Figure 9. Raw ionic currents of mutations of hydrophobic residues in S4.

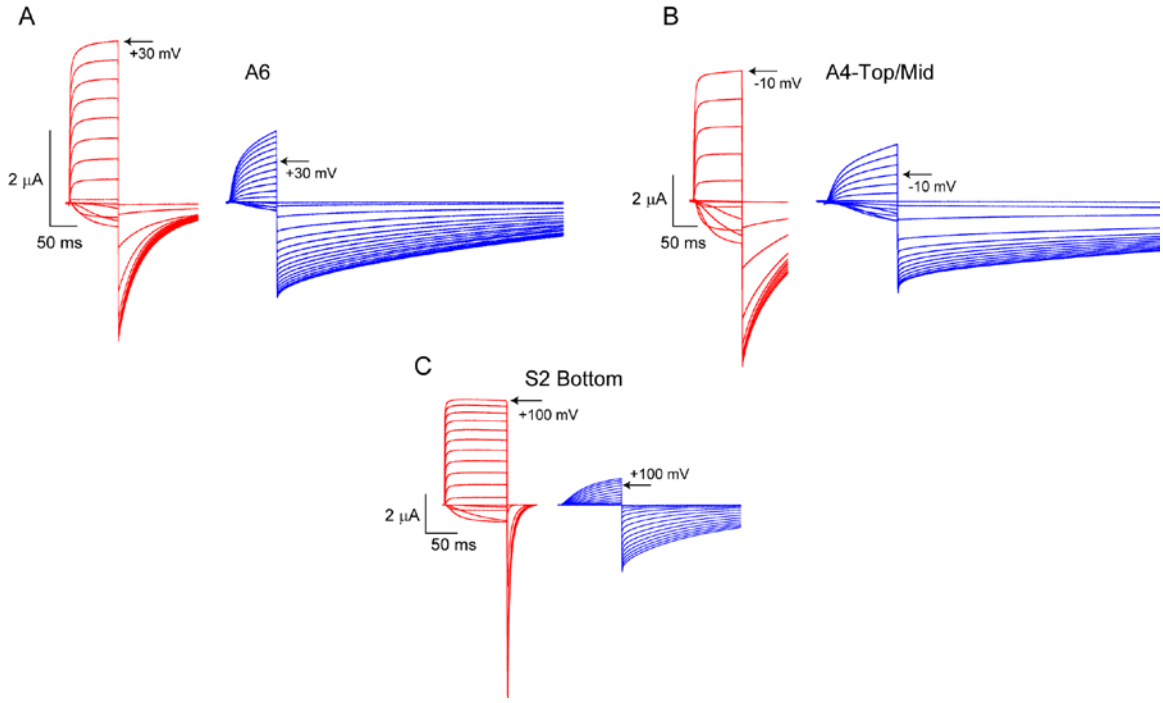

Representative ionic currents at 28°C **(red)** and 8°C **(blue)** from single oocytes expressing mutant channels, elicited by depolarizing voltage pulses in 10mV increments ($V_{Holding}$ = -120mV). In each set of traces, the arrow points to the current response at the indicated voltage. The mutants corresponding to these raw current traces are: the hextuplet Ala mutant, A6 **(A)**, the quadruplet Ala mutant, A4 **(B)** and the bottom doublet Ser mutant, S2Bot **(C)**.

Figure 10. Polarity correlated of ΔG *vs* T profiles for different perturbations at a site undergoing solvation during channel activation.

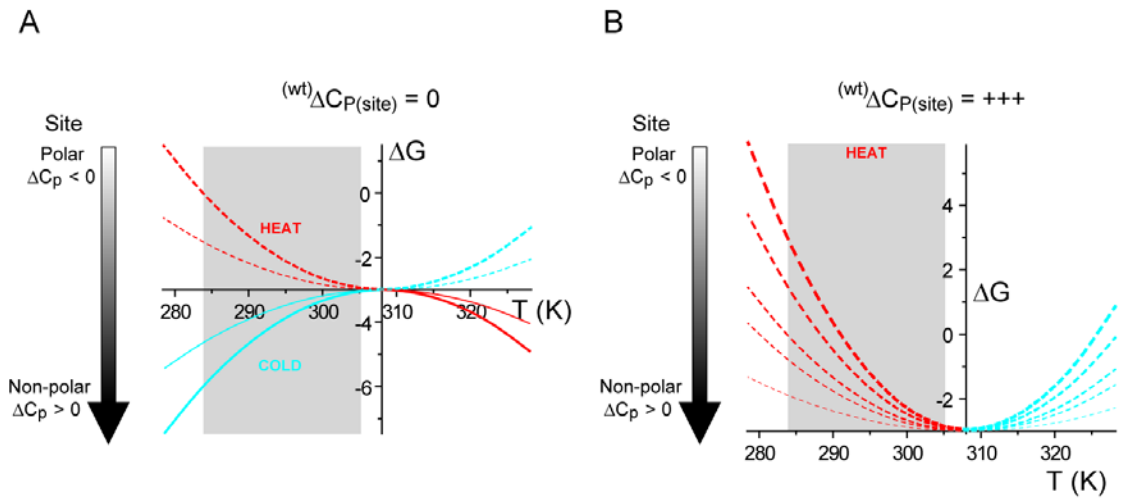

(A) At a site which in the native channel contributes to $\Delta Cp_{(0)}$, polar perturbations lead to heat sensitivity (gray region) and increasing the hydrophobicity progressively renders the channel cold sensitive **(B)** At a site, which in the native channel contributes to $\Delta Cp_{(+)}$, residues of relatively high polarity causes heat sensitivity while those of relatively high hydrophobicity attenuate the heat sensitivity but do not necessarily switch the temperature sensing phenotype of the channel.

Figure 11. Enhancement of heat sensitivity conferred by combining S3 and S4 perturbations.

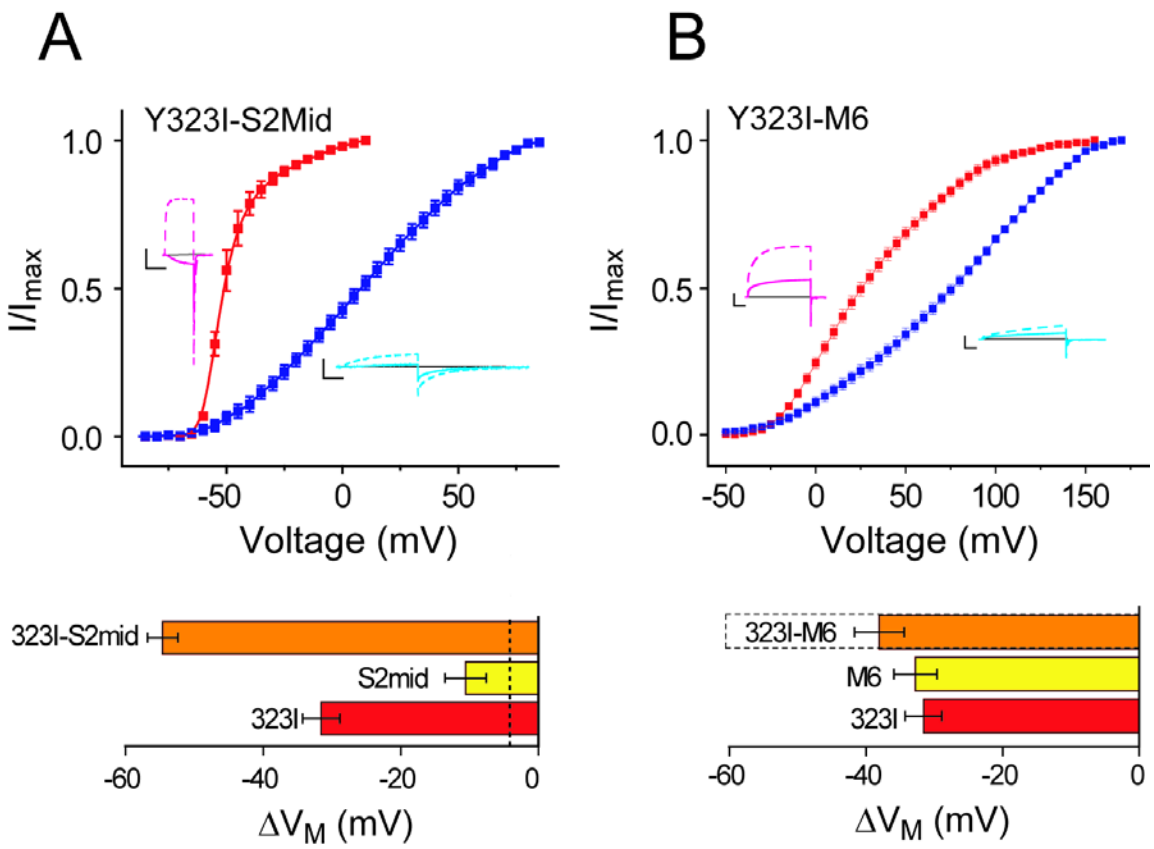

(A) Relative open-probability *vs* voltage-curves for the mutant Y323I-S2mid at 28°C and 8°C. Horizontal bar plot below shows the temperature dependent shifts (ΔV_M) of the mutant (orange), compared with that of Y323I (red) and S2mid (yellow). Inset shows raw ionic currents for the mutant at two temperatures (magenta: 28°C and cyan: 8°C), at two voltages each (one is at a voltage close to V_M, at the respectively temperatures, and the other is at saturating voltages) – scale bars correspond to 2 μA and 100 ms. **(B)** Relative open-probability *vs* voltage-curves for the mutant Y323I-M6 at 28°C and 15°C. Horizontal bar plot below show the shifts in the median voltage of activation (ΔV_M) for Y323I-M6 (orange), Y323I (red) and M6 (yellow). For the Y323I and M6 the shifts

correspond to 20°C change in temperature while for the Y323I-M6 the orange bar corresponds to a 13°C change in temperature (the dotted bar corresponds to the shift of the mutant for a 20°C change in temperature expected from a linear extrapolation of the experimental result). Inset shows raw ionic currents for the mutant at two temperatures (magenta: 28°C and cyan: 8°C), at two voltages each (one is at a voltage close to V_M, at the respectively temperatures, and the other is at saturating voltages) – scale bars correspond to 2 μA and 100 ms.

Figure 12. Temperature sensitivity of mutants evaluated by heat-ramps.

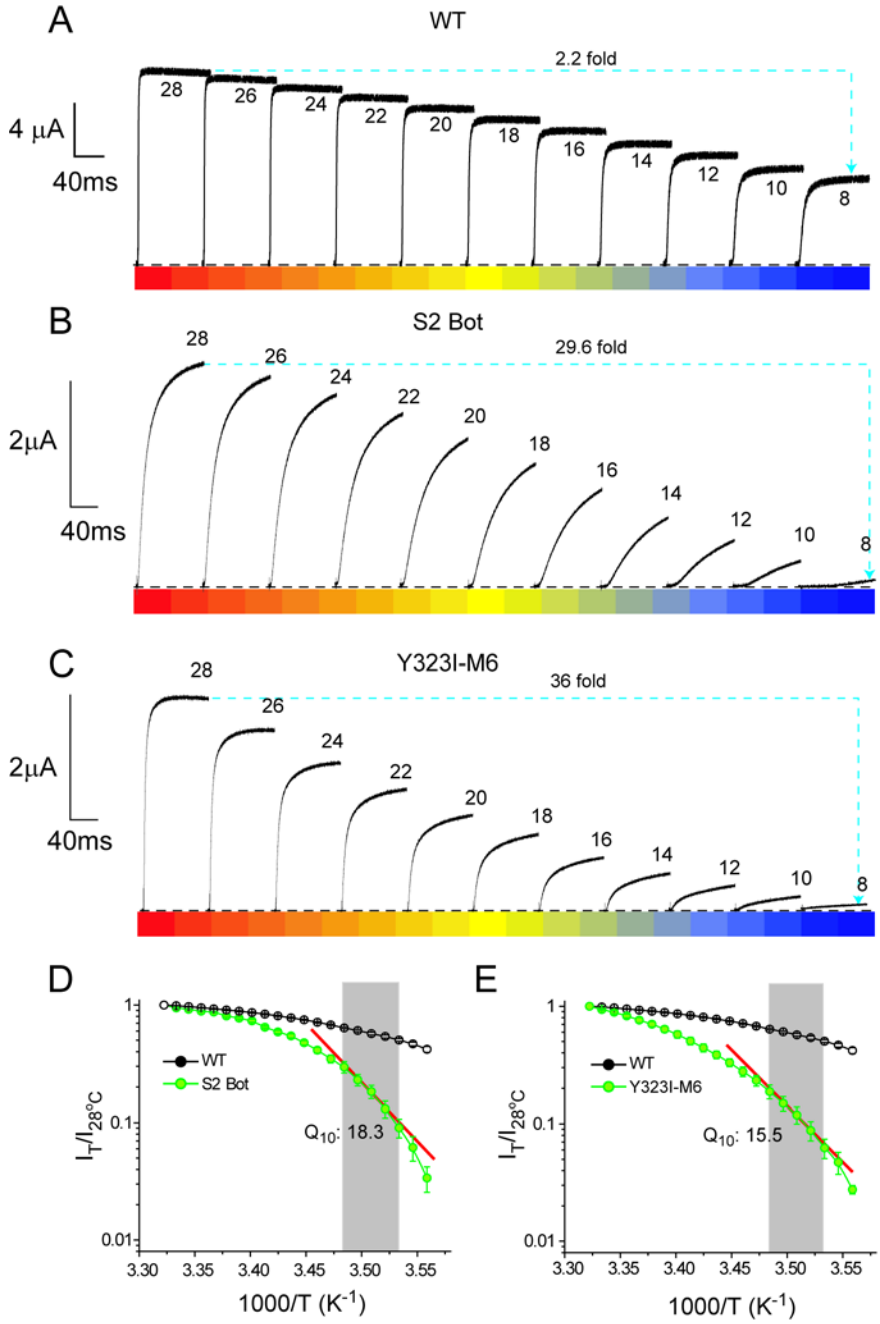

(A)-(C) Outward currents in response to 100ms depolarizing pulses from -120mV to -20mV at different temperatures for WT **(A)**, S2Bot (V369S/F370S) **(B)** and Y323I-M6 **(C)**. The temperature corresponding to each current trace is written alongside. Zero current level is denoted by the dashed line. The heat legend in each case shows the

gradient in temperature (from 28°C to 8°C). **(D) and (E)** Semi-logarithmic plots of fractional current at different temperatures, measured over 28°C to 8°C, at 1°C intervals, for S2Bot **(D)** and Y323I-M6 **(E)** compared with that of the wild-type channel. Shaded region indicates the 10° - 14°C temperature regime over which the Q_{10} value was calculated.

Figure 13. Effect of gating-charge point mutations on temperature sensitivity.

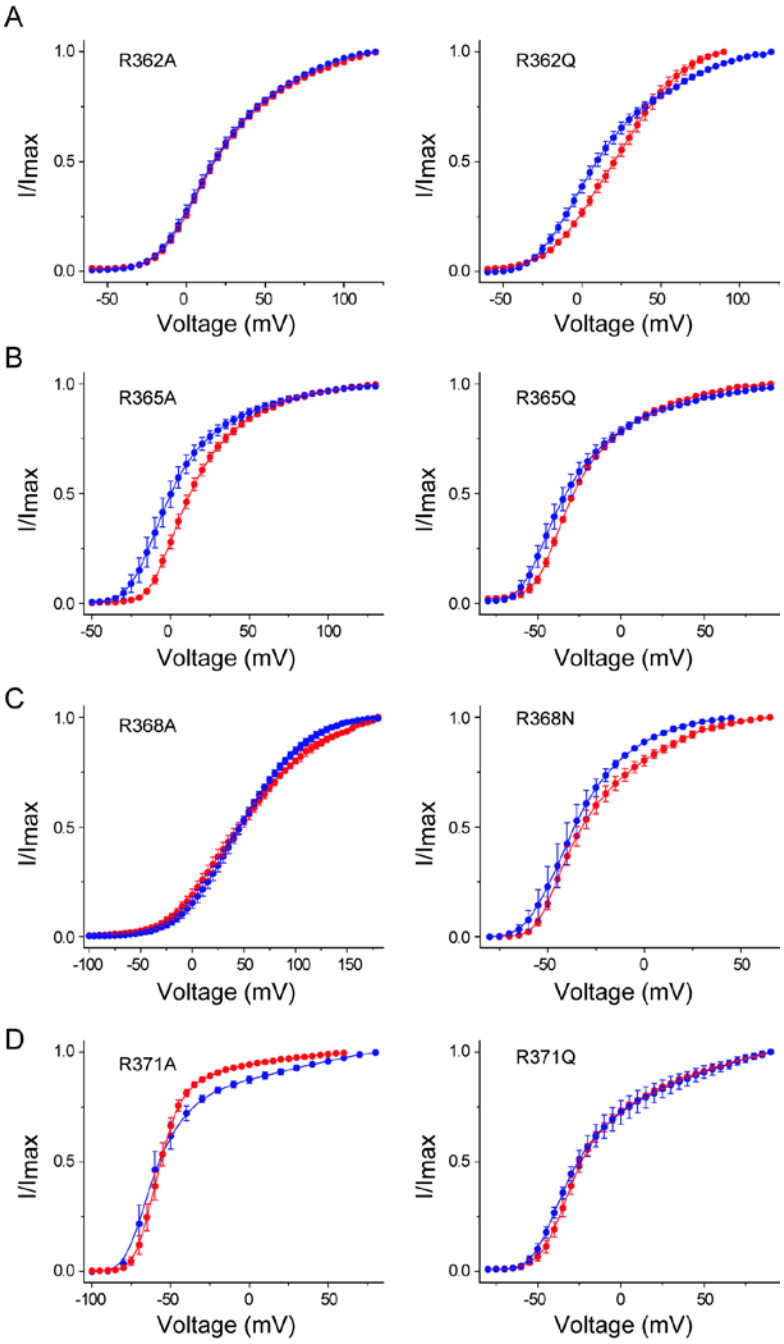

Relative open-probability *vs* voltage curves, at 28°C (red) and 8°C (blue) for charge neutralization mutations at R362 **(A)**, R365 **(B)**, R368 **(C)** and R371 **(D)**. All left panels are Ala mutations and all right panels are polar mutations (N for R368 and Q for the others).

Figure 14. Influence of voltage-sensing charges on temperature sensitivity.

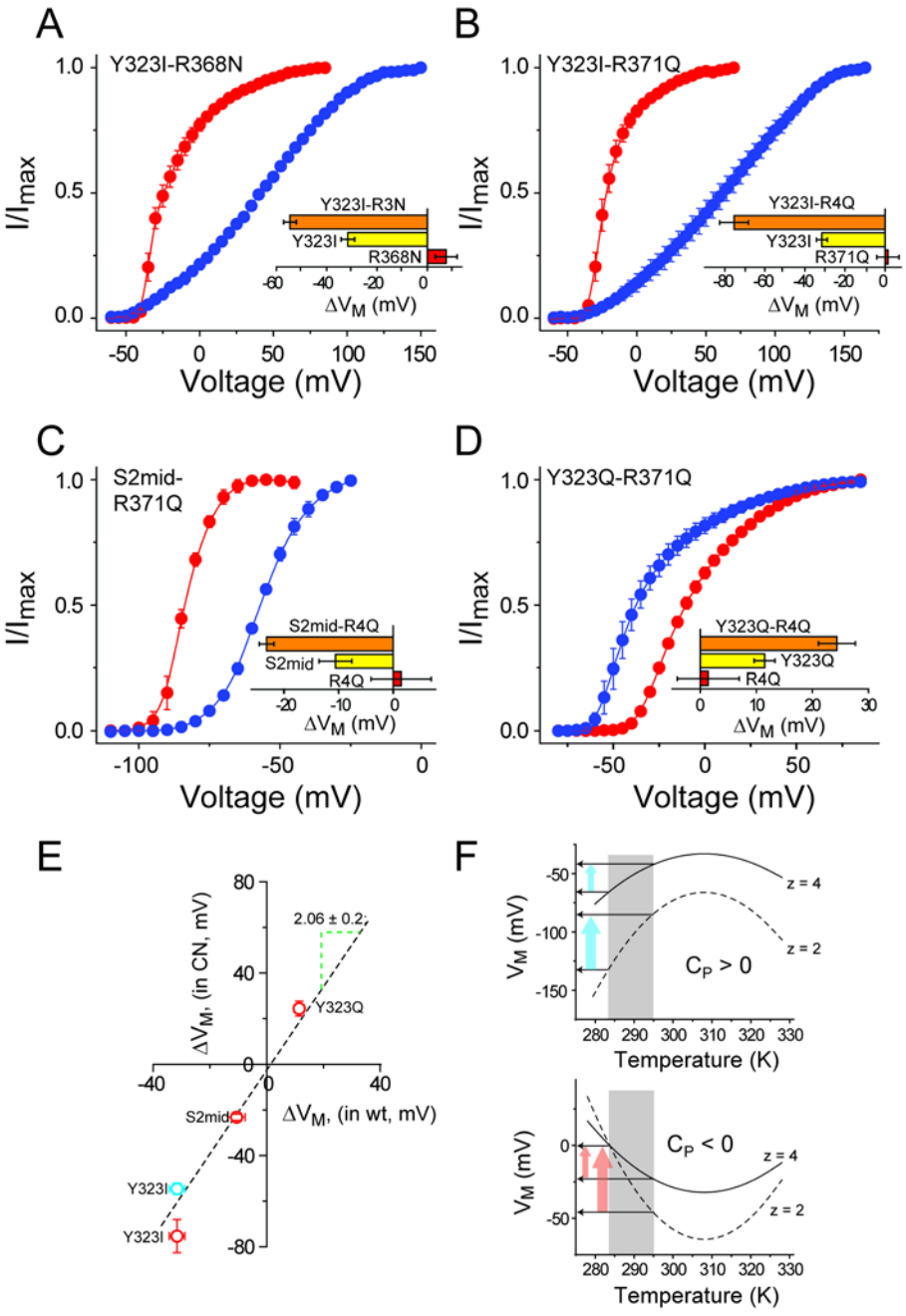

(A)-(D) The relative open-probability *vs* voltage curves of a temperature sensitizing mutant (Y323I, **(A), (B)**; S2mid **(C)**; Y323Q **(D)**) in the background of a charge neutralizing mutant (R368N, **(A)**; R371Q, **(B)-(D)**). In each case the inset shows the temperature induced ΔV_M for the charge neutralizing mutant in red, the temperature

sensitizing mutant in yellow and the combination mutant in orange. **(E)** ΔV_M for each of the temperature sensitizing mutants (Y323I, S2mid, Y323Q) in the background of a gating charge neutralization mutant (R368N (blue circle) or R371Q (red circles)) plotted against ΔV_M for each of the temperature sensitizing mutants (Y323I, S2mid, Y323Q) in the background of the native channel. The dotted line represents the regression line through the points, which has a slope of 2.06 ± 0.2. **(F)** Simulated V_M *vs* temperature profile for a cold sensitive process ($\Delta C_P > 0$, top panel) and a heat sensitive process ($\Delta C_P < 0$, bottom panel), deduced from **Eq. 3a**. In each case, dotted curves indicate the profiles for a process with low voltage-sensitivity and solid curves represent a process with high voltage-sensitivity. Arrows indicate the change in the change in V_M due to change in temperature.

Figure 15. State-dependent change in solvation is a possible mechanism of temperature dependent gating.

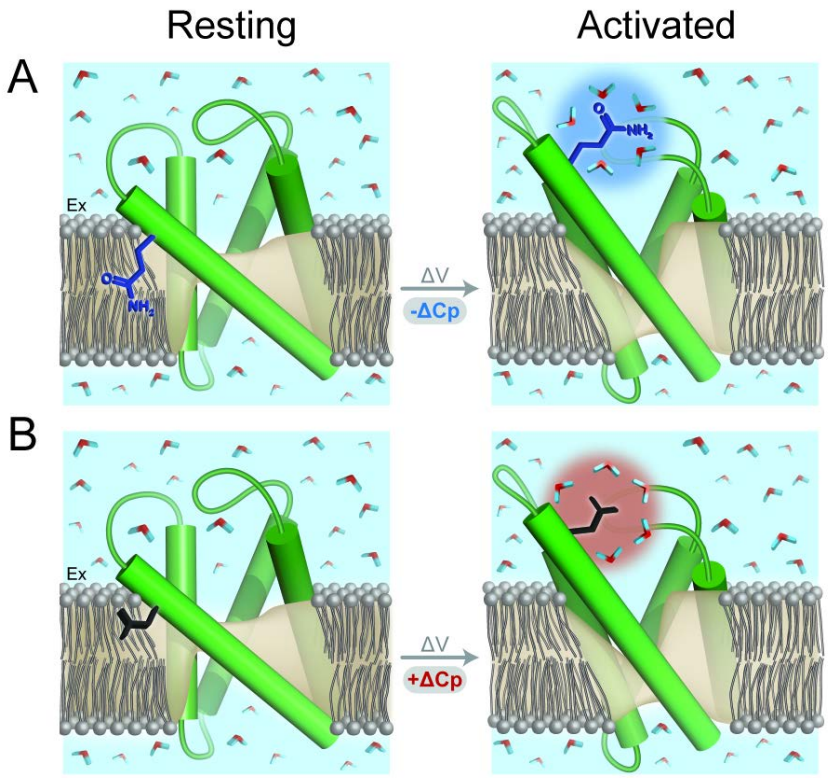

The cartoons **(A) and (B)** depict the voltage-sensors in resting and activated conformations. Voltage-dependent change in the VSD is associated with a change in solvation of a residue. When the residue is polar **(A)**, activation will be conferred a negative ΔC_P (indicated by the red halo around the hydration shell) and when the residue is non-polar **(B)**, activation will be conferred a positive ΔC_P (indicated by the blue halo around the hydration shell). The opposite signs of ΔC_P in the two cases will lead to one of them ((**A)**) being heat sensitive and the other ((**B)**) being cold sensitive.

Table 1. Effect of mutations on the relative $P_O V$ curves at two temperatures.

Mutant	V_M (s.e.) 28°C (in mV)	n	V_M (s.e.) 8°C (in mV)	n	ΔV_M (s.e.) (in mV)	z_{HT} (s.e.) / z_{LT}(s.e.)
WT	-20.6 (1.7)	4	-15.9 (2.1)	5	-4.7 (2.7)	2.83 (0.14) / 2.08 (0.15)
S1-S3 crevice facing mutants						
S233I	×		×		×	×
S233V	21.8 (2.9)	6	21.1 (3.9)	7	0.7 (4.9)	1.17 (0.05) / 1.04 (0.04)
S233D	16.6 (1.5)	4	9.1 (4.6)	4	7.5 (4.8)	1.29 (0.09) / 1.16 (0.01)
S240I	×		×		×	×
S240V	-8.2 (1.2)	5	-13.3 (2.7)	4	5.1 (2.9)	3.44 (0.3) / 2.06 (0.20)
S240A	-6.9 (1.4)	5	5.2 (2.0)	4	-12.1 (2.4)	1.36 (0.09) / 1.35 (0.07)
S240H	118.7 (1.4)	4	105.1 (1.2)	4	13.6 (1.8)	1.35 (0.04) / 1.41 (0.06)
S240D	131.0 (5.0)	4	130.0 (1.4)	3	1.0 (5.2)	1.48 (0.12) / 1.07 (0.05)
E283I	×		×		×	×
E283V	×		×		×	×
E293I	-3.6 (2.7)	4	-21.5 (1.7)	8	17.9 (3.2)	1.42 (0.08) / 1.57 (0.03)
E293A	-13.6 (0.7)	4	-4.0 (1.9)	4	-9.6 (2.0)	1.70 (0.16) / 1.25 (0.05)
E293Q	0.2 (2.6)	6	13.5 (2.0)	5	-13.3 (3.3)	1.81 (0.19) / 1.66 (0.15)
E293H	-27.6 (0.6)	4	-3.4 (1.3)	4	-24.2 (1.4)	1.87 (0.02) / 1.33 (0.11)
N313V	3.3 (4.0)	6	0.8 (4.2)	6	2.5 (5.8)	1.28 (0.08) / 1.18 (0.08)
N313D	-15.7 (1.9)	4	-16.3 (3.3)	5	0.6 (3.8)	2.32 (0.22) / 1.44 (0.04)
D316I	×		×		×	×
D316V	×		×		×	×
Y323I	-9.9 (1.3)	4	21.6 (2.4)	4	-31.5 (2.7)	2.49 (0.06) / 1.02 (0.03)
Y323A	-2.4 (0.9)	4	11.2 (3.3)	4	-13.6 (3.4)	2.04 (0.15) / 1.69 (0.25)
Y323T	25.8 (1.7)	6	15.1 (1.2)	5	10.7 (2.1)	1.20 (0.09) / 1.30 (0.04)

Y323Q	40.8 (1.6)	6	29.3 (0.9)	5	11.5 (1.8)	1.23 (0.06) / 1.17 (0.04)
T326I	-30.7 (1.7)	5	-32.0 (1.6)	5	1.3 (2.3)	1.79 (0.19) / 1.93 (0.25)
T326N	-18.4 (2.0)	5	-18.1 (2.0)	5	-0.3 (2.8)	1.85 (0.27) / 1.36 (0.06)
Hydrophobic residues in S4						
I6	0.1 (1.4)	9	0.0 (2.7)	10	0.1 (3.0)	1.68 (0.05) / 1.33 (0.08)
M6	-27.2 (1.5)	4	5.6 (2.8)	4	-32.8 (3.2)	2.17 (0.29) / 0.91 (0.05)
A6	-69.8 (1.7)	4	-33.6 (2.0)	4	-36.2 (2.6)	3.74 (0.11) / 1.11 (0.02)
I4	11.2 (2.4)	5	10.2 (3.0)	4	1.2 (3.8)	1.23 (0.05) / 1.05 (0.09)
M4	38.7 (1.5)	6	52.9 (1.9)	4	-14.2 (2.4)	1.21 (0.03) / 0.95 (0.01)
A4	-84.9 (1.7)	3	-55.8 (4.7)	4	-29.1 (5.0)	2.98 (0.08) / 1.37 (0.12)
I2Top	-4.4 (1.7)	7	-18.9 (1.9)	12	14.5 (2.5)	1.45 (0.15) / 1.53 (0.09)
M2Top	50.8 (1.4)	5	31.9 (1.0)	5	18.9 (1.7)	1.33 (0.04) / 1.3 (0.07)
A2Top	-5.4 (3.0)	7	-7.0 (3.7)	4	1.6 (4.8)	1.23 (0.08) / 1.25 (0.07)
S2Top	-10.2 (0.8)	3	10.6 (0.7)	3	-20.8 (1.1)	1.91 (0.09) / 1.19 (0.03)
I2Mid	23.2 (2.8)	4	26.5 (2.6)	5	-3.3 (3.8)	1.16 (0.04) / 1.16 (0.02)
M2Mid	-4.5 (2.8)	5	8.9 (1.9)	5	-13.4 (3.4)	1.52 (0.08) / 1.46 (0.07)
A2Mid	-26.2 (2.2)	5	-36.2 (0.6)	4	10.0 (1.9)	1.79 (0.18) / 1.45 (0.55)
S2Mid	-40.1 (1.4)	7	-29.5 (2.6)	4	-10.6 (3.0)	1.75 (0.14) / 1.28 (0.01)
I2Bot	-16.7 (2.2)	5	0.6 (1.8)	4	-17.3 (2.8)	2.18 (0.39) / 1.09 (0.08)
M2Bot	-12.1 (2.8)	4	15.0 (3.5)	7	-27.1 (4.5)	1.65 (0.18) / 0.98 (0.04)
A2Bot	31.3 (0.9)	4	17.3 (1.6)	4	14.0 (1.8)	1.06 (0.09) / 1.32 (0.07)
S2Bot	-17.4 (1.7)	5	51.1 (2.4)	4	-68.5 (2.9)	4.49 (0.39) / 1.21 (0.04)
Combination mutants						
Y323I/ S2Mid	-46.3 (1.9)	3	8.1 (2.5)	5	-54.4 (3.1)	3.97 (0.72) / 1.08 (0.06)
Y323I/M6	32.4 (2.4)	8	70.5 (2.7)	7	-38.1 (3.6)	1.04 (0.04) / 0.78 (0.02)
S4 charge mutants						

R362A	24.9 (1.5)	6	23.5 (2.1)	7	1.4 (2.6)	1.23 (0.02) / 1.18 (0.02)
R362Q	19.8 (1.9)	5	17.1 (4.6)	5	2.7 (5.0)	1.33 (0.10) / 1.16 (0.17)
R365A	19.9 (1.9)	7	9.3 (3.2)	6	10.6 (3.7)	1.58 (0.06) / 1.38 (0.17)
R365Q	-19.0 (0.6)	4	-21.3 (3.6)	3	2.3 (3.6)	1.52 (0.09) / 1.27 (0.02)
R368A	50.7 (3.2)	7	47.9 (2.8)	5	2.8 (4.3)	0.8 (0.04) / 0.84 (0.05)
R368N	-24.1 (2.6)	4	-31.6 (3.5)	3	7.5 (4.4)	1.63 (0.12) / 1.84 (0.20)
R371A	-50.3 (1.8)	11	-45.1 (1.7)	4	-5.2 (2.5)	2.69 (0.24) / 1.52 (0.3)
R371Q	-12.0 (1.8)	8	-13.5 (5.2)	3	1.5 (5.5)	1.38 (0.07) / 1.26 (0.14)
Y323I/ R368N	-14.3 (2.3)	5	40.3 (1.1)	4	-54.6 (2.5)	1.94 (0.12) / 0.91 (0.06)
Y323I/ R371Q	-15.1 (2.1)	6	60.3 (6.9)	4	-75.4 (7.2)	2.78 (0.24) / 0.81 (0.03)
S2Mid/ R371Q	-80.2 (1.1)	3	-57.0 (0.8)	4	-23.2 (1.3)	5.28 (0.71) / 3.29 (0.27)
Y323Q/ R371Q	-3.0 (1.6)	6	-27.4 (2.9)	3	24.4 (3.3)	1.58 (0.06) / 1.56 (0.11)

The table lists the median voltage of channel opening (V_M) of each of the mutants of the Shaker K_V channel at 28°C and 8°C (except for Y323I/M6, where the V_M values are those at 28°C and 15°C). The standard error associated with each V_M is reported in parenthesis. 'n' indicates the number of replicates (independent measurements in oocytes) used to obtain the V_M at each temperature. ΔV_M is the change in V_M between the high and the low temperature ($\Delta V_M = V_M(28°C) - V_M(8°C)$, or for the Y323I/M6 mutant: $\Delta V_M = V_M(28°C) - V_M(15°C)$). The standard error associated with ΔV_M was calculated as: $\sqrt{\delta V_M^2(28°C) + \delta V_M^2(8°C)}$, where δV_M is the standard error associated with each V_M measurement. The last column reports the steepness of the relative $P_O V$ curves at the high and low temperatures (z_{HT} and z_{LT} respectively), with their respective

standard errors in parenthesis. The steepness of each curve is its 'Boltzmann slope' obtained by fitting a Boltzmann equation to the curve. Mutants were classified as temperature sensitive if $|\Delta V_M| > 3\,\delta V_M$ and are colored red or blue depending on whether they are heat or cold sensitive respectively.

AUTHORSHIP NOTE

This project was designed by Sandipan Chowdhury and Dr. Baron Chanda. All molecular biology was done by Sandipan Chowdhury. Electrophysiological experiments were performed by Sandipan Chowdhury and Dr. Brian W. Jarecki (equal contribution). Sequence analyses and generation of a structural model of the hydrated voltage-sensor was performed by Sandipan Chowdhury.

CHAPTER EIGHT

Conclusions and Future Directions

Understanding the energetics of channel activation

Gating mechanisms of voltage-gated ion channels and its different homologs have been studied actively for more than half-a-century. Experimental strategies employed to their study have involved electrophysiology, biochemistry, crystallography and spectroscopy and they have articulated important rules and principles governing voltage-dependent activity of the proteins. Although, our understanding of the structural details of gating has become quite mature in the past decade, there are several important questions to be answered, many of which cannot be simply addressed via structural inspection.

One of these important questions is to determine the mechanism of electromechanical coupling i.e. how the voltage-sensor activation leads to opening of the channel pore. Search for molecular determinants of electromechanical coupling have to a large extent focused on a region of the polypeptide chain, known as the S4-S5 linker, which covalently links the voltage-sensors to the pore domain. Initial evidence of the role of this region in coupling came from studies on a leucine heptad motif found in this region which when perturbed results in large modification of channel gating (McCormack et al., 1991b; McCormack et al., 1993). In a remarkable experiment (Lu et al., 2002), Lu et. al. were able to confer voltage-sensitivity to channels which natively feature only the pore domains by fusing them to the voltage-sensing domains derived from the Shaker potassium channels. They showed that complementarity of the S4-S5 linker region with the C-terminal end of the S6 transmembrane segment was crucial for

cross-talk between the voltage-sensor and pore. Various perturbation studies have examined the functional effects of mutations in the S4-S5 linker regions on the voltage-dependent opening in different members of this superfamily (Sanguinetti and Xu, 1999; Chen et al., 2001; Tristani-Firouzi et al., 2002; Decher et al., 2004; Ferrer et al., 2006; Soler-Llavina et al., 2006; Labro et al., 2008; Muroi et al., 2010; Van Slyke et al., 2010; Labro et al., 2011; Wall-Lacelle et al., 2011). In many early studies, attributes such as rightward shifts in conductance-voltage curves, slowed kinetics of channel opening and increased deactivation rates were used to identify sites involved in coupling voltage-sensor and pore. Despite the incontrovertible importance of the S4-S5 linker-S6 interface in electromechanical coupling, direct estimation of the interaction energies between the residues constituting the interface has been lacking, in part due to absence of accurate experimental methodologies to quantify such interactions. In this light, the free-energy estimation techniques described in this Thesis ('Generalized Interaction energy Analysis' or GIA) can prove to be very useful in determining the molecular interactions underlying electromechanical coupling.

Apart from careful consideration of some of the caveats to GIA application, it must be mentioned that the non-additive energies computed using mutant cycles generally involve mutations to Alanine. Ideally, removal of the sidechain should be accomplished by a Glycine substitution but the possibility that Glycine, by virtue of its ultra-flexibility, can distort protein structures, renders Alanine as the preferred choice of perturbing residue. Thus, the non-additive energies actually report the "excess" contribution of a specific interaction partner to the free-energy of activation of a protein, relative to an Ala-Ala pair. In other words, if the putative interaction energies are assayed

using Valine as the perturbing residue, then the deduced interaction energies quite possibly would be different. This occurs because the perturbing residue might interact as well and this contribution might also influence the experimentally inferred non-additive energies. This caveat must also be kept in mind while comparing interaction energies between different pairs which are not equidistant in the protein structures.

The Shaker K_V channel, natively is an inactivating channel, in which inactivation proceeds via binding of an N-terminal peptide to the open pore. Deletion of this peptide fragment creates a channel which does not undergo inactivation on the same time scale as the native channels. By comparing the gating-charge displacement curves of the inactivating and non-inactivating Shaker channels, it should be possible to deduce key information about the energetics of channel inactivation. Such an application might be especially important to study inactivation mechanisms for the Na_V channels, where inactivation proceeds via interaction of a specific intracellular loop with different parts of the channel.

It must be mentioned that while gating currents are relatively easy to measure experimentally for the Shaker K_V channels (and several of its mammalian orthologs) because of a known non-conducting channel mutant (W434F in particular), in other more distant families, gating current measurements are significantly more challenging. In eukaryotic sodium channels, gating currents are most frequently measured in the presence of a channel blocking toxin (tetrodotoxin or saxitoxin), which has been shown in some instances to modify voltage-sensor activation (Capes et al., 2012). Thus, gating currents measured from toxin blocked channels might not be representative of voltage-dependent charge displacement of native, unblocked channels. In other channels, such as the

mammalian HCN channels, channel expression seems to be the limiting factor preventing measurement of gating currents. Gating currents are ~200-500 fold smaller in magnitude than ionic currents and much higher levels of expression of functional channels are required to measure them. One possible strategy to circumvent this limitation is to optimize the codon of the channel gene for heterologous expression, which has been shown to elevate expression levels of many proteins (and ion channels) in different expression systems. Another challenge encountered in gating current measurements, as seen in the case of BK channels, is that large membrane depolarization (>160 mV) is necessary to saturate the charge-displacement curves (Horrigan and Aldrich, 1999). Under such conditions, the endogenous leak currents often become large which contaminates the gating current measurement. One of the principle origins of such a leak current is the calcium activated chloride channels (CaCC) and thus it might be helpful to measure gating currents in the presence of CaCC blockers (suchs as niflumic acid, DIDS or MONNA). Clearly, measurement of gating currents is not as trivial as measuring ionic currents and with the development of standardized strategies to measure gating currents it will be possible to calibrate free-energies of activation of different voltage-gated ion channels.

Although much of the discussion has been explicitly geared towards voltage-gated ion channels, the thermodynamic principles described in this thesis are readily transferrable to ligand gated ion channels. As discussed in Chapter three, the median ligand activity of the channel, deduced from direct ligand binding curves (not dose response curves) is a measure of the total work done to saturate the channel with the ligand – which includes the energetic changes accompanying ligand binding, channel

opening, allosteric interactions, etc. Ligand gated channels such as the pentameric Cys-loop receptors, tetrameric ionotropic glutamate receptors, trimeric P2X receptors and acid sensing ion channels – all undergo rapid and almost complete desensitization in response to sustained applications of their specific agonists. Thus the energetics of channel desensitization will also be incorporated (linearly) into the free-energy change measure, deduced from the median ligand activity (from direct ligand binding curves). As mentioned in the case of VGICs, our ability to specifically block channel desensitization would allow us to probe the energetic contributions of residues and residue-level interactions to the channel activation and desensitization directly, by measuring the direct ligand binding curves of the native channel and the channel in which desensitization is blocked. For example in the GluA2 receptor, application of the drug cyclothiazide or a Leu to Tyr substitution (Sun et al., 2002) at a specific site in the extracellular ligand binding domain can almost completely eliminate channel desensitization. These perturbations also lead to large shifts in the agonist ligand binding curves of the channel (Hall et al., 1993; Kessler et al., 1996) which might reflect the energetic changes associated with channel desensitization. For ligand dependent process, the stoichiometry of protein:ligand association is unlikely to change as easily as Q_{max} of voltage-gated channel activation, in response to mutations, and thus measurements of ligand binding curves will be sufficient to deduce to free-energy changes in channels and their mutants. However, one principle difficulty associated with estimation of the median ligand activity is that the number of points on the curve (ligand concentrations at which binding is assayed) need to be large. Fitting of a Hill-equation to a binding curve can be performed even with as few three points, however to estimate the median ligand activity, we need to

calculate the area between the binding curve and the ordinate axis. Since area is evaluated numerically (using approximations such as the trapezoid rule implemented in this thesis), insufficiency of the number of points on the curve can introduce serious errors in the median ligand activity measurements. This might make the experiments, relatively more tedious to perform. Despite these challenges, our ability to deduce energetic changes from direct experimental measurements, with relatively few assumptions about the channel gating behavior, could reveal important insights into the molecular driving forces underlying the structural transitions accompanying channel opening and closing.

Energetic features of allosteric gating in polymodal ion channels

Gating of many VGICs is influenced by other stimuli such as calcium concentrations (in the BK channels) which are crucial for their physiological activity. Understanding the energetic origins of modulation by a secondary stimulus is a very challenging problem, owing to the large number of discrete channel states which must be accounted for in a realistic model of channel gating. Using a thermodynamic cycle analysis we have shown that the energetic linkage between the voltage and the ligand dependent pathways can be ascertained by measuring the gating charge displacement curves at zero and saturating ligand concentrations. In many of the polymodal ion channels, based on functional studies (such as cross-linking effects on channel activity) or structural inspection of the channel or its homologs, it has been suggested that the ligand regulatory domains, although in most cases are covalently linked to channel gates, share important interfaces with the transmembrane core (such as the S4 or the S4-S5 linker) which could underlie its regulatory activity (Horrigan and Ma, 2008; Kowal et al.,

2014). The approach that we describe could thus be directly used to probe the energetic contributions of these interfaces. When combined with the χ-value analysis, the above strategy can be used to deconstruct different energetic linkage pathways within a polymodal allosteric protein. For instance, within the framework of nested allosteric models of polymodal channel gating, the Hill-transformed $P_O V$ curves (in total absence of the ligand) yields the interaction energy of the pore domain with all the voltage-sensors. Next, by measuring the P_O *vs* [ligand] curves, over a wide range of ligand concentrations and at a constant hyperpolarizing voltage, we can extract the interaction energy between the pore and the ligand binding domains. From the gating charge measurements, we can obtain the net interaction of the pore and the voltage-sensor with the ligand binding domains, which can thus be parsed to obtain the voltage-sensor coupling energy with the ligand binding domain itself.

Although, not explicitly discussed in Chapter five, these ideas can be directly extended to study the pharmacology of ligand gated ion channels. Members of the cys loop receptors, for instance, have been known to be very important targets for general anesthesia. Action of many of these drugs are believed to be allosteric in nature. However it is not clearly known whether these drugs exert their effects by modulating ligand binding and/or gating and molecular mediators of such functional coupling remain poorly understood. In such instances, measuring direct ligand binding curves in absence and presence of saturating concentrations of the drug would allow us to quantify the energetic coupling between the structural transitions associated with the binding of the channel agonist and binding of the drug. These strategies might help us understand the mechanisms of action of different drugs at a molecular and energetic level.

Molecular principles of temperature modulation of voltage-dependent gating

Temperature is an important modulator of activity of different proteins. Studies on different voltage-gated ion channels (such as the K_V, Na_V channels) have shown temperature accelerates the activation, deactivation and inactivation kinetics of the channel but has small effects on the relative open-probability *vs* voltage relationships. These effects have often been reconciled using Arrhenius plots which provide an estimate of the transition energy barriers during each process. In many pathological mutations, linked to inherited diseases, the kinetics of the different steps become significantly more temperature sensitive and the steady state activation curves of mutant channels exhibit temperature dependent shifts along the voltage-axis. However, till date, such effects have not been reconciled under a molecular framework.

TRP channels are an evolutionarily related, although distant, member of the VGIC superfamily. Their transmembrane topology is very similar to that of the VGICs as has been recently demonstrated in the high resolution electron-microscopy structures of the TRPV1 channel (Cao et al., 2013b; Liao et al., 2013). These channels often have additional domains appended at their N and C termini, both of which are cytoplasmic. Some members of the TRP channel family exhibit exquisite temperature sensitivity – temperature change causes large shifts in their conductance voltage-relationships (7-10 mV/°C) and causes large increase in the ion flux through the channels (which cannot be explained by simply the change in the single channel conductance of the channel (Brauchi et al., 2004; Matta and Ahern, 2007)). Owing to their large temperature sensitivity and structural similarities with the prototypical members of the Shaker K_V

channel, they have become model temperature sensitive ions on which different models of temperature sensation are investigated. Some of the central questions in such an area are – What is the mechanism of temperature sensitivity? Is there a specific domain of the protein which confers temperature sensitivity to the channel? What might be the nature of the structural changes in these putative temperature sensing domains underlying temperature sensation? Is the temperature sensing domain conserved in the different members of the TRP channels? What are the differences in the temperature sensing behavior of the heat and cold activated ion channels?

A lot of effort has been invested in probing these molecular mechanisms in the TRP channels, principally via mutating different parts of the protein and assaying the temperature dependent activity of the mutants (Brauchi et al., 2006; Voets et al., 2007; Grandl et al., 2008; Grandl et al., 2010; Yang et al., 2010; Cordero-Morales et al., 2011; Yao et al., 2011). However, such an approach cannot determine whether the perturbations which lead to loss of temperature modulation do so by abolishing temperature sensation or coupling between the temperature sensing domain and channel gating.

Of particular interest to us was the question – how particular channels, of conserved architecture, have evolved to become more temperature sensitive? To answer this question, we embarked on a heuristic approach to design a temperature sensing ion channel based on a template of a voltage-gated ion channel, whose steady state responses innately exhibit very little temperature sensitivity. We asked, is it possible to semi-rationally engineer mutations in a model voltage-gated ion channel and systematically design a temperature modulated channel? By correlating the nature of the amino acid

perturbation to the temperature sensing phenotype of the channel we can potentially understand a great deal about how native temperature sensitive ion channels operate.

Our studies show that at several positions in the voltage-sensing domain of the Shaker K_V channel, perturbations render the channel extremely temperature sensitive. We find that the heat sensing phenotype and the magnitude of temperature sensitive at some locations are correlated with the polarity of the perturbation. An interpretation of these results is that temperature sensitivity arises due to state dependent changes in the solvation of specific sites. Solvation is accompanied by changes in the specific heat capacity which in turn causes the channels to become temperature sensitive.

A second important conclusion of our study is demonstration of the crucial, yet indirect, role played by the voltage-sensing charges in modulation of temperature dependent gating. We show that neutralization of voltage-sensing charges significantly enhance (almost doubles) the magnitude of temperature dependent shifts of the conductance-voltage relationships produced by site-specific perturbations, although in the native channel they exert very little effect. This observation is a direct consequence of the thermodynamic linkage principles (as described in Chapter five). Thus, as discussed earlier in the context of temperature sensitivity or sensitivity to a secondary stimulus, large number of voltage sensing charge compromises the ability of the channel to be modulated by other stimuli. As an evolutionary principle most polymodal channels will likely have low innate voltage sensitivity.

The ability to impart temperature sensitivity to a native temperature insensitive channel with relatively few mutations have an additional implication – local state dependent changes in solvation of amino acids, associated with channel gating, might

confer sufficient ΔC_P to channel gating so as to make them very temperature sensitive. In other words, it is not necessary for a channel to house a specialized temperature sensing domain for it to be temperature sensitive. Rather, the "temperature sensor" could be "distributed" over the global structure of the protein, where small solvation changes during channel gating confer the channel its remarkable temperature sensitivity.

In this study, temperature sensitization has been assayed using the conductance voltage relationships, which as indicated in the previous chapters, do not yield an accurate estimate of the energetics of activation. It will be very useful to measuring the gating charge displacement curves for some of the temperature sensitizing mutants and determine whether the polarity correlated trends extend to the QV curves as well. This will provide a strong thermodynamic foundation to the observations of this study.

It will be very interesting to determine whether the ideas etched in our studies extend to the thermo-TRPs. Perturbations at sites, previously identified to be important for temperature dependent gating in TRPV1 (or TRPV3) channels (Grandl et al., 2008; Grandl et al., 2010), may exhibit polarity correlated effects on the temperature sensitivity of the channel. This will provide support to our conclusion and indicate that solvation correlated phenomena also underlies temperature dependent gating of natively temperature sensitive ion channels.

Miller and Clapham (Clapham and Miller, 2011) formally introduced the concept of specific heat capacity change on temperature modulation of channel gating. Their ideas, much like ours, emerge directly from the laws of thermodynamics. However, our hypothesis differs from theirs' in a crucial way. We posit that heat and cold sensitivity arises because of a change in the sign of ΔC_P – both the heat and cold sensing ion

channels will have a large ΔC_P of gating but in one case it will be positive and in the other it will be negative. The "Miller-Clapham hypothesis" however claims that heat and cold sensing channels have the same sign of ΔC_P, however they differ in their T_C (see Fig. 1). Due to the non-monotonicity in the ΔG *vs* T profiles, a difference in the T_Cs between the profiles implies that over a given temperature, ΔG will be decreasing with T in one instance and increasing in the other. While such a hypothesis is elegant it will be virtually impossible to demonstrate its validity without estimation of the T_C. Since T_C might well extend into temperature ranges, physiologically and experimentally inaccessible, it might be very difficult to prove this hypothesis. Even if Miller-Clapham hypothesis is proven to be correct, identifying the molecular determinants of T_C, which is responsible for heat-sensitivity of TRPV1 and cold sensitivity of TRPM8, in the physiological temperature ranges, will be a crucial and challenging problem.

It must also be mentioned that the principles of temperature modulation explored in this Thesis does not limit itself to channels with shared membrane topology. Anoctamins are another class of voltage and calcium activated chloride channels, which have been described to be very temperature sensitive (Cho et al., 2012). Additionally, slow deactivation of the ClC family of chloride channels is also known to exhibit large temperature sensitivity (Q_{10} ~ 40) (Pusch et al., 1997). We posit that solvation desolvation phenomenon leads to change in ΔC_P of gating in these channels as well causing them to be temperature sensitive. In the ClC channels, NMR studies of cytoplasmic domains have been shown to exhibit large backbone rearrangements with temperature. It would be quantify the energetics of such rearrangements, calorimetrically

(say using Isothermal Titration Calorimetrically) and extract the ΔC_P of such conformational changes.

Figure 1. Miller and Clapham hypothesis of heat and cold sensitivity

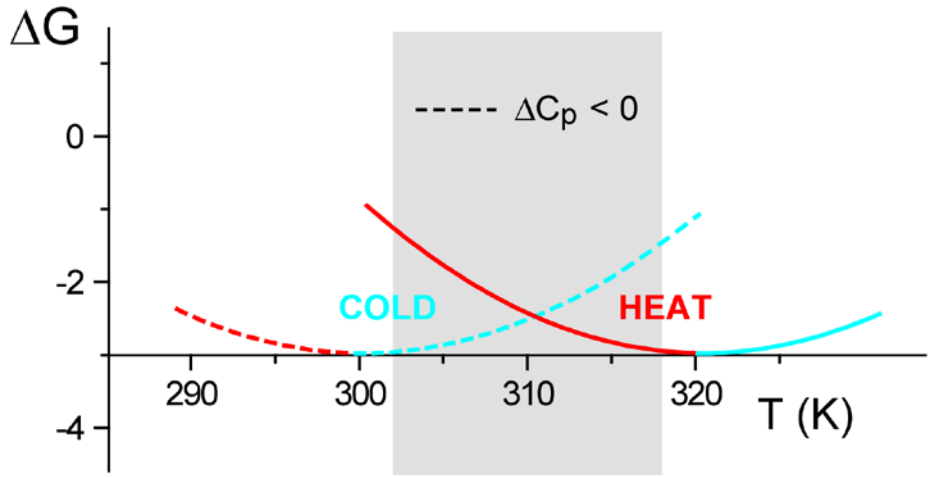

In the two simulated ΔG *vs* T profiles, representing the temperature dependent free-energy change of channel gating, ΔH_C and ΔC_P are identical but the T_C is different. As a consequence in the temperature range of 300-320 K, in one case (T_C = 300K), the channel exhibits cold sensitivity and in the other case (T_C = 320 K) the channel exhibits heat sensitivity.

APPENDIX I

Identification of clusters of conserved residues in a protein structure

In this appendix, an informatics approach is employed to identify groups of structurally contiguous, evolutionary conserved residues, which was based on a graph-theoretical approach previously demonstrated previously (Kannan and Vishveshwara, 1999). Using the structure of the K_V1.2/2.1 paddle chimera (PDB-id: 2R9RB) (Long et al., 2007), we first derived the adjacency matrix, **A**, for the residues in the transmembrane segments of the protein. **A** is a square matrix whose elements, a_{ij}, were calculated as:

$$a_{ij} = 100\frac{N_{ac}(i,j)}{Norm(i)}$$

where N_{ac}(i,j) is the number of interatomic contacts between the side-chains of residues 'i' and 'j', an atomic contact being defined only when two atoms are within 4.5Å of each other. Norm(i) is a parameter which depends on the specific type of residue at position 'i' – it is related to the size of the specific amino acid. The Norm() values used for our purposes were the same as those reported previously (Kannan and Vishveshwara, 1999).A higher value of a_{ij} suggests an increased possibility that the two residues are interacting. By this formulation, **A** is not a symmetric matrix (since Norm(i) ≠ Norm(j), unless residues 'i' and 'j' are identical). Furthermore, since the channel is homotetrameric, there are 4 possible values for N_{ac}(i,j), depending on whether the residues are in the same or neighboring subunits. For our calculations we used the maximum of the four possible values for N_{ac}(i,j) to generate **A**. Once **A** is obtained, we generate a symmetric version of the adjacency matrix, **S** (with elements s_{ij}), as follows:

$$s_{ij} = \begin{cases} 0 \;\; when\; |i-j| \leq 5 \\ \max(a_{ij}, a_{ji}) \;\; when\; |i-j| > 5 \; and \; \max(a_{ij}, a_{ji}) \geq lim \\ 0 \;\; when\; |i-j| > 5 \; and \; \max(a_{ij}, a_{ji}) < lim \end{cases}$$

where ‘lim’ is a cut-off value for the adjacency scores, used to ‘neutralize’ residue pairs with a low number of inter-atomic contacts. For our purpose, we used a value of 7 for the limiting cut-off score. Additionally, the condition, $|i-j| \leq 5$ implies that scores were evaluated only for residues which are more than 5 residues apart in primary sequence. The result of this calculation is shown in Fig. 1 as a heat map. We can make out that residues in certain regions of the protein (for instance, the S4-S5 linker and the S6 tail) are more tightly packed against each other than other regions. While most of the clusters comprise of residues within the same of the protein, the red and the cyan cluster, each contains residues from different subunits.

Using the elements of the symmetric adjacency matrix as weights, the different residues of the protein were clustered into groups such that residues within each group have high inter-residue contact scores while residues between groups have relatively low inter-residue contact scores. Clustering was performed using the ClusterOne program (Nepusz et al., 2012). Each cluster was constrained to comprise at least 5 amino acids and show strong clustering density (i.e. high degree of interconnectivity). Application of this approach shows that the 259 residues of the channel (residue numbers 158-417 corresponding to 2R9RB) can be first reduced into a graph with 109 nodes (each corresponding to a residue) and 98 edges (each edge indicating a connection, the ‘strength’ of which is reflecting by its adjacency score), which can be further subdivided into 6 clusters (Fig. 2a), three of which are mapped onto the structure of the paddle chimera (Fig. 2b). While most of the clusters comprise of residues within the same of the protein, the red and the cyan cluster, each contains residues from different subunits.

For the sequence conservation calculation we used an alignment of ~ 360 K_V channel sequences (Lee et al., 2009). For each position of the alignment we computed the conservation entropy (Halabi et al., 2009) (c.e.(i)) as follows:

$$c.e.(i) = \sum_{j=1}^{20} f_j^i \ln\left(\frac{f_j^i}{f_j^b}\right)$$

where f_j^i is the frequency of amino acid 'j' at position 'i' of the sequence alignment and f_j^b is the background frequency of the amino acid (deduced from the non-redundant database of the protein) and the summation runs over all 20 amino acids. The f_j^b values previously reported by Halabi et al. (2009) were used here. c.e.(i) indicates the 'enrichment' of a particular site in amino acids with respect to a background distribution of amino acids. We also calculated the frequency of occurrence of each amino acid in the multiple sequence alignment (as described previously) and found it to be close to the background frequency distribution suggesting sufficient sampling of sequence for conservation analyses.

For each cluster, the mean and standard deviation of the conservation entropy scores were evaluated as:

$$\mu_{c.e.}(i) = \frac{\sum_{j=1}^{n_i} c.e.(j)}{n_i}$$

$$\sigma_{c.e.}(i) = \sqrt{\frac{\sum_{j=1}^{n_i}\{c.e.(j) - \mu_{c.e.}(i)\}^2}{n_i - 1}}$$

where n_i is the number of residues constituting the cluster and the summations (over 'j') are performed over the residues constituting the cluster ('i'). These two parameters reflect the average conservation score of the residues constituting a cluster ($\mu_{c.e.}$) and the

standard deviation of the conservation scores of the residues in the cluster ($\sigma_{c.e.}$). A cluster with a high $\mu_{c.e}$ and low $\sigma_{c.e.}$ indicates that all the residues comprising it are strongly conserved (as opposed to one with a high $\mu_{c.e}$ and high $\sigma_{c.e.}$ which indicates that the cluster comprises both strongly and poorly conserved residues) and is likely to be crucial for channel function.

Of the six clusters, three (red, yellow and green) are constituted by sites which exhibit high evolutionary conservation (Fig. 3a). The red cluster is particularly significant since it is formed by residues – I384, R394, E395, V476 and Y485 (numbered according to the Shaker K_v sequence) – all at the intracellular interface between the S4-S5 linker and S6 helices. Fig. 3b-f shows the distribution of the different amino acids at each of the five sites deduced from the sequence alignment. In comparison with the distribution of the amino acids in the total multiple sequence alignment (which closely follows the background distribution of amino acids in the non-redundant protein database), we find that the sites are strongly are strongly enriched in specific amino acids, which accounts for high conservation scores at each of these sites.

Figure 1. The symmetric adjacency matrix derived from the paddle chimera structure.

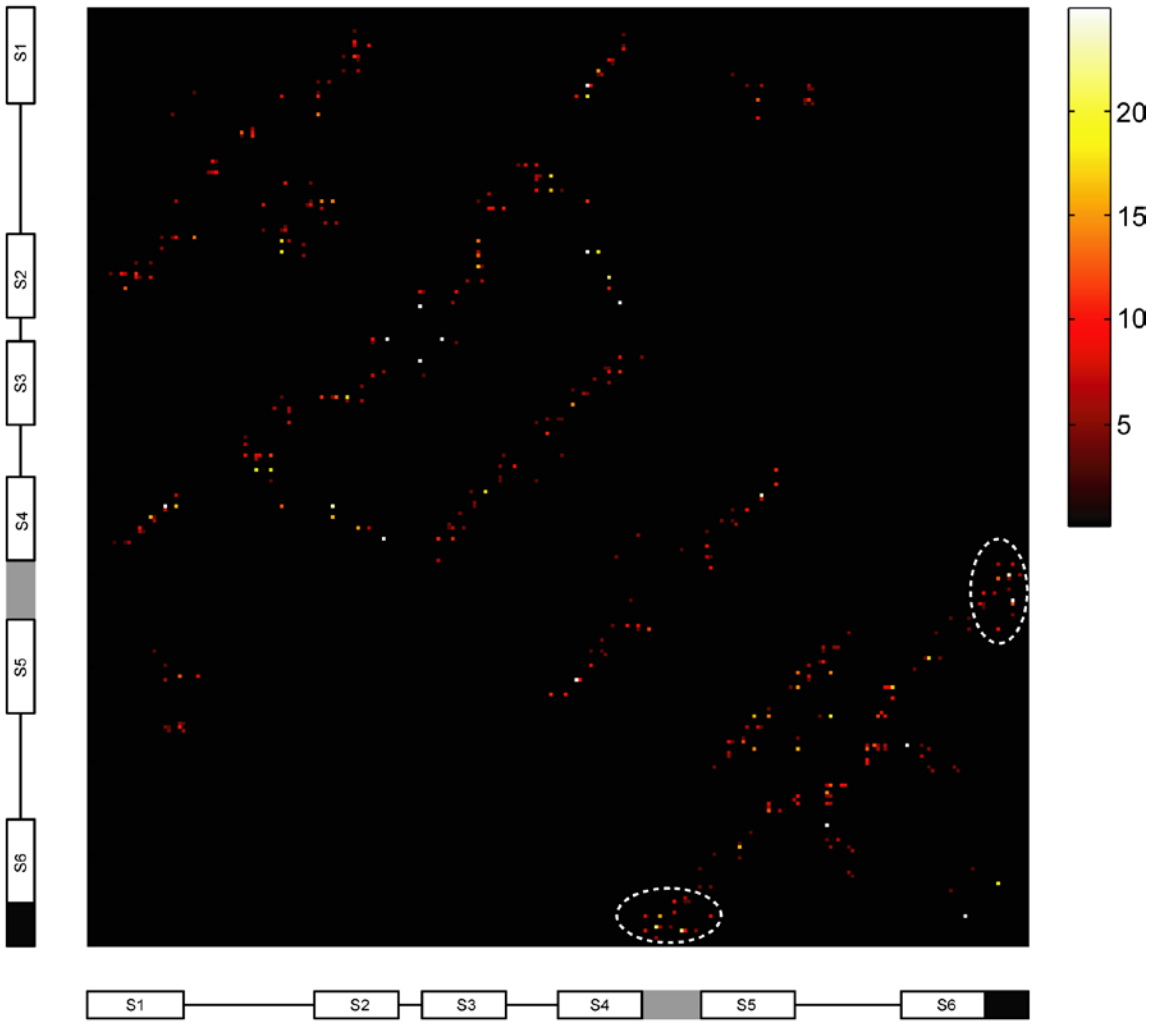

A heat map showing the symmetric adjacency matrix (**S**) showing the proximity scores between residues within the S1-S6 segments, deduced from the paddle chimera structure (residues 158-417). The proximity scores are colored from black to white according to the color bar. The locations of the different helical segments are shown along the axes of the matrix, with the S4-S5 linker helix in gray and the tail end of the S6 helix in black.

Within the matrix, the elements which depict the contacts between the S4-S5 linker and the S6 tail are shown within the dotted white ellipse.

Figure 2. Clusters of contiguous residues in the paddle chimera structure

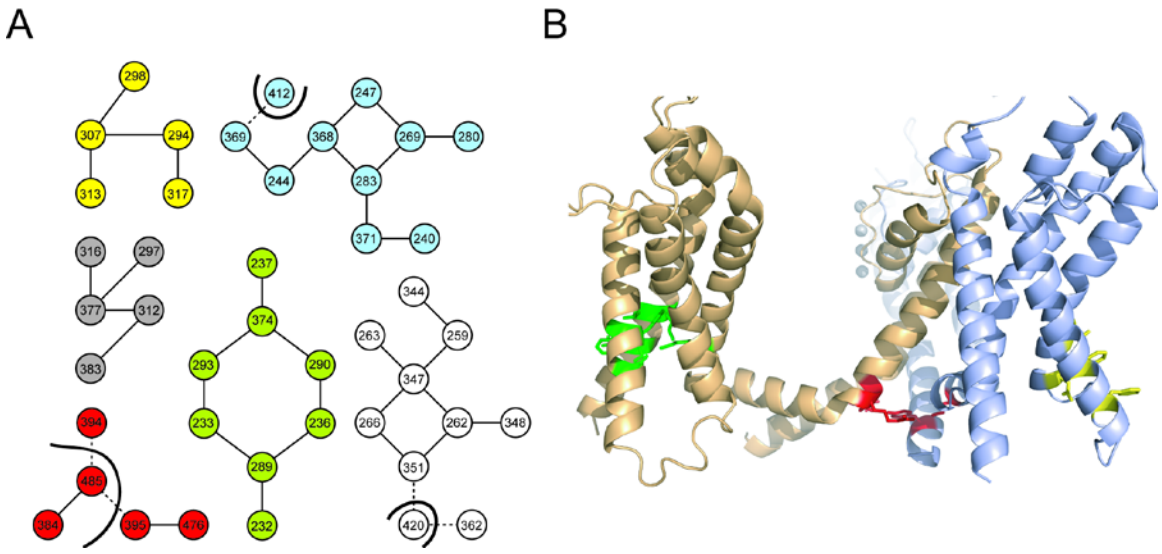

(A) The full adjacency matrix transforms the protein structure into a 'graph' was clustered to find groups of residues with high inter-residue contact density, which identifies 6 clusters. In each cluster, the circles (or nodes) represent an amino acid residue, numbered according to the Shaker K_V channel sequence (based on an alignment of Shaker and the paddle chimera, **Fig. 4**). The lines between the nodes (or edges) depict whether the two nodes have a proximity score greater than the cut-off. In the yellow, grey and green clusters, all residues are within the same subunit. In the cyan, white and red clusters, not all residues are in the same subunit – residues which belong to different subunits are marked by black curved lines. The edges are solid for intra-subunit contacts and dashed for inter-subunit contacts. **(B)** The green, yellow and red clusters are mapped on the structure of the K_V channel, with the residues colored according to the cluster in (B). For clarity, the intra-subunit green and yellow clusters, which are housed in the voltage-sensing domains, are shown on different subunits. The red cluster lies at the intracellular interface between the two subunits.

Figure 3. Conservation of residues constituting an intersubunit network

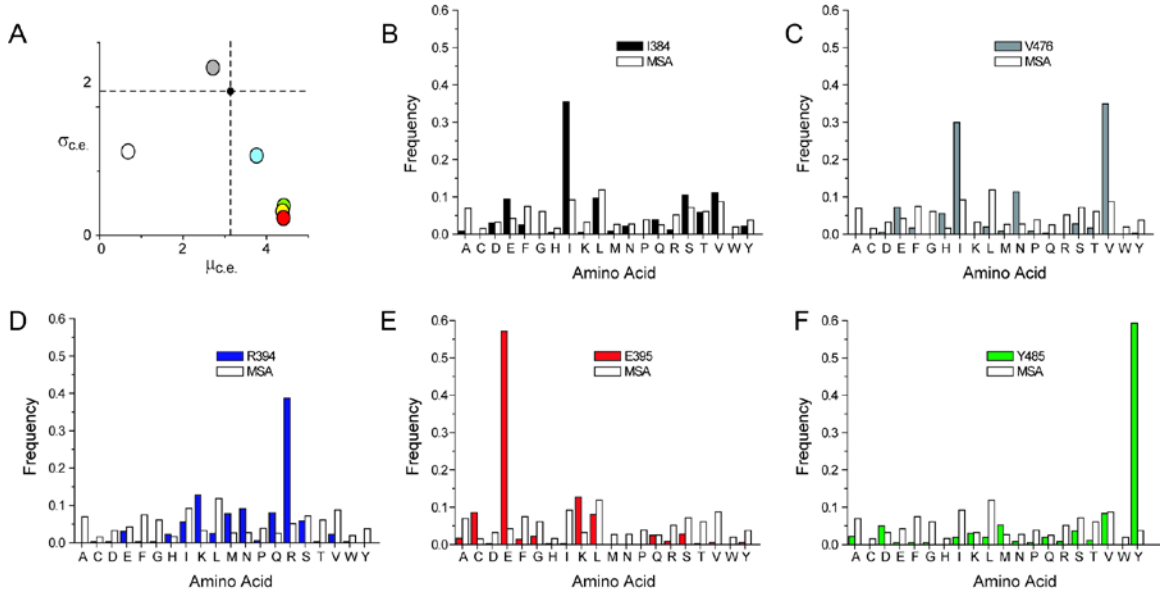

(A) For each of the 6 clusters, the standard deviation of the conservation entropy of the residues of a cluster ($\sigma_{c.e.}$) is plotted against the mean conservation entropy of the residues of the same cluster ($\mu_{c.e.}$), derived from the multiple sequence alignment (MSA). Each circle, represents a cluster and is colored according to (B). The black circle indicates the $\sigma_{c.e.}$ and $\mu_{c.e.}$ for all the residues of the protein (paddle chimera (2R9RB) residues 158-417). **(B)-(F)** The frequency distribution of amino acids, at positions corresponding to each of the five residues of the inter-subunit red cluster, derived from the MSA, is compared against the frequency distribution of amino acids in the overall MSA. The enrichment of particular amino acids at these positions underlie the high $\mu_{c.e.}$ and low $\sigma_{c.e.}$ for the red cluster.

Figure 4. Alignment of Shaker K_V and the K_V1.2/2.1 paddle chimera

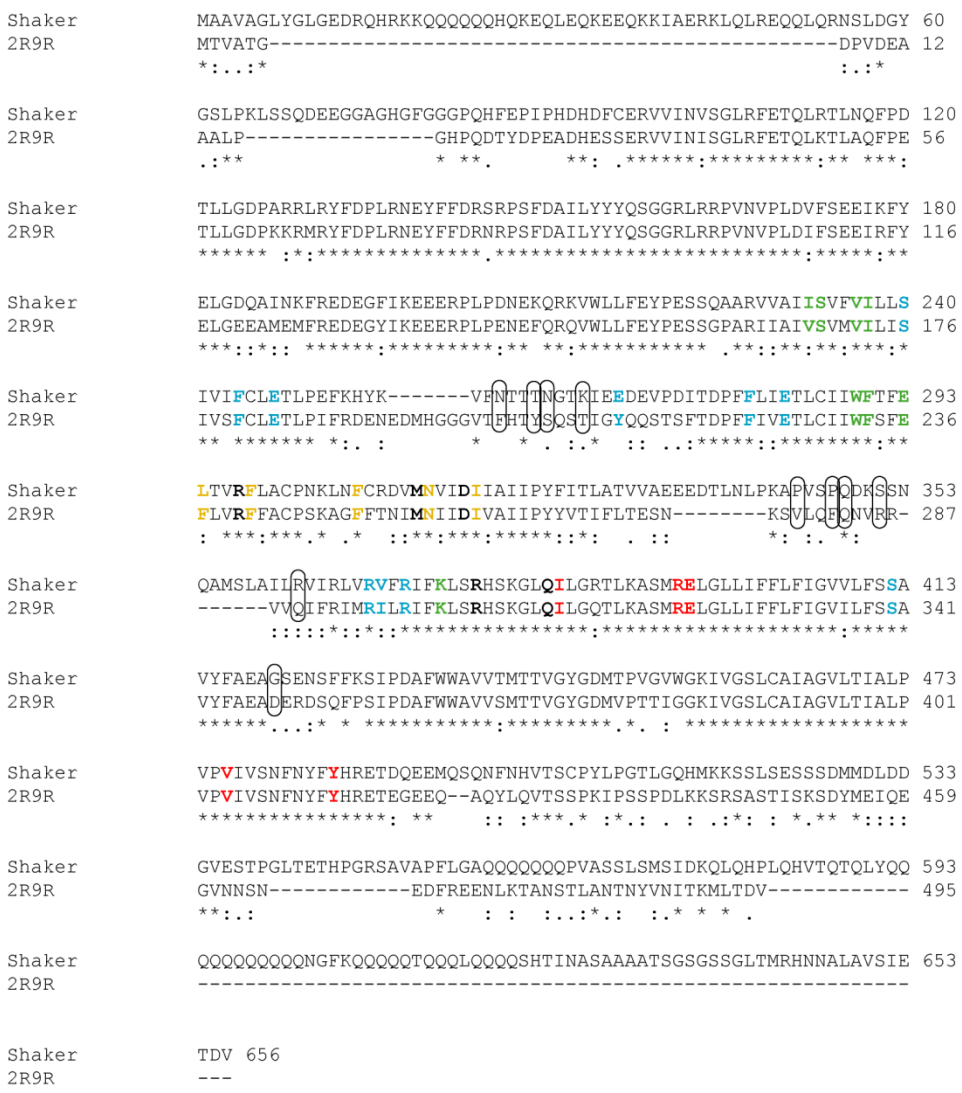

Residues corresponding to each cluster are colored according to the color scheme in Fig. 2a, except for the gray cluster (marked in bold-black in the alignment) and the white cluster (marked by vertical tubes).

REFERENCES

Ackers, G.K., and F.R. Smith. 1985. Effects of site-specific amino acid modification on protein interactions and biological function. *Annu Rev Biochem*. 54:597-629.

Aggarwal, S.K., and R. MacKinnon. 1996. Contribution of the S4 segment to gating charge in the Shaker K+ channel. *Neuron*. 16:1169-1177.

Ahern, C.A., and R. Horn. 2004. Specificity of charge-carrying residues in the voltage sensor of potassium channels. *J Gen Physiol*. 123:205-216.

Ahern, C.A., and R. Horn. 2005. Focused electric field across the voltage sensor of potassium channels. *Neuron*. 48:25-29.

Akabas, M.H., D.A. Stauffer, M. Xu, and A. Karlin. 1992. Acetylcholine receptor channel structure probed in cysteine-substitution mutants. *Science*. 258:307-310.

Alabi, A.A., M.I. Bahamonde, H.J. Jung, J.I. Kim, and K.J. Swartz. 2007. Portability of paddle motif function and pharmacology in voltage sensors. *Nature*. 450:370-375.

Almers, W. 1978. Gating currents and charge movements in excitable membranes. *Rev Physiol Biochem Pharmacol*. 82:96-190.

Altomare, C., A. Bucchi, E. Camatini, M. Baruscotti, C. Viscomi, A. Moroni, and D. DiFrancesco. 2001. Integrated allosteric model of voltage gating of HCN channels. *J Gen Physiol*. 117:519-532.

Armstrong, C.M. 1969. Inactivation of the potassium conductance and related phenomena caused by quaternary ammonium ion injection in squid axons. *J Gen Physiol*. 54:553-575.

Armstrong, C.M., and F. Bezanilla. 1973. Currents related to movement of the gating particles of the sodium channels. *Nature*. 242:459-461.

Armstrong, C.M., and F. Bezanilla. 1974. Charge movement associated with the opening and closing of the activation gates of the Na channels. *J.Gen.Physiol*. 63:533-552.

Asamoah, O.K., J.P. Wuskell, L.M. Loew, and F. Bezanilla. 2003. A fluorometric approach to local electric field measurements in a voltage-gated ion channel. *Neuron*. 37:85-97.

Baldwin, R.L. 1986. Temperature dependence of the hydrophobic interaction in protein folding. *Proc Natl Acad Sci U S A*. 83:8069-8072.

Banerjee, A., and R. MacKinnon. 2008. Inferred motions of the S3a helix during voltage-dependent K+ channel gating. *J Mol Biol*. 381:569-580.

Bao, L., A.M. Rapin, E.C. Holmstrand, and D.H. Cox. 2002. Elimination of the BK(Ca) channel's high-affinity Ca(2+) sensitivity. *J Gen Physiol*. 120:173-189.

Batulan, Z., G.A. Haddad, and R. Blunck. 2010. An intersubunit interaction between S4-S5 linker and S6 is responsible for the slow off-gating component in Shaker K+ channels. *J Biol Chem*. 285:14005-14019.

Bautista, D.M., J. Siemens, J.M. Glazer, P.R. Tsuruda, A.I. Basbaum, C.L. Stucky, S.E. Jordt, and D. Julius. 2007. The menthol receptor TRPM8 is the principal detector of environmental cold. *Nature*. 448:204-208.

Bernstein, J. 1902. Untersuchungen zur Thermodynamik der bioelectrischen Ströme. Erster Theil. *Pflügers Archiv*. 92:521-562.

Bernstein, J. 1912. Electrobiologie. . Vieweg, Braunschweig.

Bezanilla, F. 2000. The voltage sensor in voltage-dependent ion channels. *Physiol Rev*. 80:555-592.

Bezanilla, F., E. Perozo, and E. Stefani. 1994. Gating of Shaker K+ channels: II. The components of gating currents and a model of channel activation. *Biophys J*. 66:1011-1021.

Biskup, C., J. Kusch, E. Schulz, V. Nache, F. Schwede, F. Lehmann, V. Hagen, and K. Benndorf. 2007. Relating ligand binding to activation gating in CNGA2 channels. *Nature*. 446:440-443.

Bosmans, F., M.F. Martin-Eauclaire, and K.J. Swartz. 2008. Deconstructing voltage sensor function and pharmacology in sodium channels. *Nature*. 456:202-208.

Brauchi, S., P. Orio, and R. Latorre. 2004. Clues to understanding cold sensation: thermodynamics and electrophysiological analysis of the cold receptor TRPM8. *Proc Natl Acad Sci U S A*. 101:15494-15499.

Brauchi, S., G. Orta, M. Salazar, E. Rosenmann, and R. Latorre. 2006. A hot-sensing cold receptor: C-terminal domain determines thermosensation in transient receptor potential channels. *J Neurosci*. 26:4835-4840.

Broomand, A., and F. Elinder. 2008. Large-scale movement within the voltage-sensor paddle of a potassium channel-support for a helical-screw motion. *Neuron*. 59:770-777.

Campos, F.V., B. Chanda, B. Roux, and F. Bezanilla. 2007. Two atomic constraints unambiguously position the S4 segment relative to S1 and S2 segments in the closed state of Shaker K channel. *Proc Natl Acad Sci U S A*. 104:7904-7909.

Cao, E., J.F. Cordero-Morales, B. Liu, F. Qin, and D. Julius. 2013a. TRPV1 channels are intrinsically heat sensitive and negatively regulated by phosphoinositide lipids. *Neuron*. 77:667-679.

Cao, E., M. Liao, Y. Cheng, and D. Julius. 2013b. TRPV1 structures in distinct conformations reveal activation mechanisms. *Nature*. 504:113-118.

Capes, D.L., M. Arcisio-Miranda, B.W. Jarecki, R.J. French, and B. Chanda. 2012. Gating transitions in the selectivity filter region of a sodium channel are coupled to the domain IV voltage sensor. *Proc Natl Acad Sci U S A*. 109:2648-2653.

Carter, P.J., G. Winter, A.J. Wilkinson, and A.R. Fersht. 1984. The use of double mutants to detect structural changes in the active site of the tyrosyl-tRNA synthetase (Bacillus stearothermophilus). *Cell*. 38:835-840.

Caterina, M.J., M.A. Schumacher, M. Tominaga, T.A. Rosen, J.D. Levine, and D. Julius. 1997. The capsaicin receptor: a heat-activated ion channel in the pain pathway. *Nature*. 389:816-824.

Catterall, W.A. 2000. From ionic currents to molecular mechanisms: the structure and function of voltage-gated sodium channels. *Neuron*. 26:13-25.

Chanda, B., O.K. Asamoah, R. Blunck, B. Roux, and F. Bezanilla. 2005. Gating charge displacement in voltage-gated ion channels involves limited transmembrane movement. *Nature*. 436:852-856.

Chanda, B., and F. Bezanilla. 2002. Tracking voltage-dependent conformational changes in skeletal muscle sodium channel during activation. *J Gen Physiol*. 120:629-645.

Chandler, W.K., M.F. Schneider, R.F. Rakowski, and R.H. Adrian. 1975. Charge movements in skeletal muscle. *Philos.Trans.R.Soc.Lond B Biol.Sci.* 270:501-505.

Changeux, J.P., and S.J. Edelstein. 2005. Allosteric mechanisms of signal transduction. *Science*. 308:1424-1428.

Chen, J., J.S. Mitcheson, M. Tristani-Firouzi, M. Lin, and M.C. Sanguinetti. 2001. The S4-S5 linker couples voltage sensing and activation of pacemaker channels. *Proc Natl Acad Sci U S A*. 98:11277-11282.

Chen, S., J. Wang, L. Zhou, M.S. George, and S.A. Siegelbaum. 2007. Voltage sensor movement and cAMP binding allosterically regulate an inherently voltage-independent closed-open transition in HCN channels. *J Gen Physiol*. 129:175-188.

Chen, X., Q. Wang, F. Ni, and J. Ma. 2010. Structure of the full-length Shaker potassium channel Kv1.2 by normal-mode-based X-ray crystallographic refinement. *Proc Natl Acad Sci U S A*. 107:11352-11357.

Cho, H., Y.D. Yang, J. Lee, B. Lee, T. Kim, Y. Jang, S.K. Back, H.S. Na, B.D. Harfe, F. Wang, R. Raouf, J.N. Wood, and U. Oh. 2012. The calcium-activated chloride channel anoctamin 1 acts as a heat sensor in nociceptive neurons. *Nat Neurosci*. 15:1015-1021.

Chowdhury, S., and B. Chanda. 2010. Deconstructing thermodynamic parameters of a coupled system from site-specific observables. *Proc Natl Acad Sci U S A*. 107:18856-18861.

Chowdhury, S., and B. Chanda. 2012a. Estimating the voltage-dependent free energy change of ion channels using the median voltage for activation. *J Gen Physiol*. 139:3-17.

Chowdhury, S., and B. Chanda. 2012b. Perspectives on: conformational coupling in ion channels: thermodynamics of electromechanical coupling in voltage-gated ion channels. *J Gen Physiol*. 140:613-623.

Chowdhury, S., and B. Chanda. 2013. Free-energy relationships in ion channels activated by voltage and ligand. *J Gen Physiol*. 141:11-28.

Clapham, D.E. 2003. TRP channels as cellular sensors. *Nature*. 426:517-524.

Clapham, D.E., and C. Miller. 2011. A thermodynamic framework for understanding temperature sensing by transient receptor potential (TRP) channels. *Proc Natl Acad Sci U S A*. 108:19492-19497.

Cole, K.S., and H.J. Curtis. 1939. Electrical impedence of the squid giant axon during activity. *Journal of general physiology*. 22:649-670.

Cole, K.S., and J.W. Moore. 1960. Potassium ion current in the squid giant axon: dynamic characteristic. *Biophys J*. 1:1-14.

Colquhoun, D. 1998. Binding, gating, affinity and efficacy: the interpretation of structure-activity relationships for agonists and of the effects of mutating receptors. *Br J Pharmacol*. 125:924-947.

Cordero-Morales, J.F., E.O. Gracheva, and D. Julius. 2011. Cytoplasmic ankyrin repeats of transient receptor potential A1 (TRPA1) dictate sensitivity to thermal and chemical stimuli. *Proc Natl Acad Sci U S A*. 108:E1184-1191.

Cox, D.H., J. Cui, and R.W. Aldrich. 1997. Allosteric gating of a large conductance Ca-activated K+ channel. *J Gen Physiol*. 110:257-281.

Craven, K.B., and W.N. Zagotta. 2004. Salt bridges and gating in the COOH-terminal region of HCN2 and CNGA1 channels. *J Gen Physiol*. 124:663-677.

Craven, K.B., and W.N. Zagotta. 2006. CNG and HCN channels: two peas, one pod. *Annu Rev Physiol*. 68:375-401.

Cuello, L.G., V. Jogini, D.M. Cortes, and E. Perozo. 2010. Structural mechanism of C-type inactivation in K(+) channels. *Nature*. 466:203-208.

Cui, J., and R.W. Aldrich. 2000. Allosteric linkage between voltage and Ca(2+)-dependent activation of BK-type mslo1 K(+) channels. *Biochemistry*. 39:15612-15619.

Cui, J., D.H. Cox, and R.W. Aldrich. 1997. Intrinsic voltage dependence and Ca2+ regulation of mslo large conductance Ca-activated K+ channels. *J Gen Physiol*. 109:647-673.

Day, M.L., S.J. Pickering, M.H. Johnson, and D.I. Cook. 1993. Cell-cycle control of a large-conductance K+ channel in mouse early embryos. *Nature*. 365:560-562.

DeCaen, P.G., V. Yarov-Yarovoy, T. Scheuer, and W.A. Catterall. 2011. Gating charge interactions with the S1 segment during activation of a Na+ channel voltage sensor. *Proc Natl Acad Sci U S A*. 108:18825-18830.

DeCaen, P.G., V. Yarov-Yarovoy, E.M. Sharp, T. Scheuer, and W.A. Catterall. 2009. Sequential formation of ion pairs during activation of a sodium channel voltage sensor. *Proc Natl Acad Sci U S A*. 106:22498-22503.

DeCaen, P.G., V. Yarov-Yarovoy, Y. Zhao, T. Scheuer, and W.A. Catterall. 2008. Disulfide locking a sodium channel voltage sensor reveals ion pair formation during activation. *Proc Natl Acad Sci U S A*. 105:15142-15147.

Decher, N., J. Chen, and M.C. Sanguinetti. 2004. Voltage-dependent gating of hyperpolarization-activated, cyclic nucleotide-gated pacemaker channels: molecular coupling between the S4-S5 and C-linkers. *J Biol Chem*. 279:13859-13865.

DeCoursey, T.E., K.G. Chandy, S. Gupta, and M.D. Cahalan. 1984. Voltage-gated K+ channels in human T lymphocytes: a role in mitogenesis? *Nature*. 307:465-468.

DeCoursey, T.E., and V.V. Cherny. 1998. Temperature dependence of voltage-gated H+ currents in human neutrophils, rat alveolar epithelial cells, and mammalian phagocytes. *J Gen Physiol*. 112:503-522.

del Camino, D., and G. Yellen. 2001. Tight steric closure at the intracellular activation gate of a voltage-gated K(+) channel. *Neuron*. 32:649-656.

Depaula, J., and P.W. Atkins. 2010. Physical Chemistry. 9.ed. W H Freeman & Company.

Dhaka, A., A.N. Murray, J. Mathur, T.J. Earley, M.J. Petrus, and A. Patapoutian. 2007. TRPM8 is required for cold sensation in mice. *Neuron*. 54:371-378.

Dhaka, A., V. Viswanath, and A. Patapoutian. 2006. Trp ion channels and temperature sensation. *Annu Rev Neurosci*. 29:135-161.

Di Cera, E. 1998a. Site-Specific Thermodynamics: Understanding Cooperativity in Molecular Recognition. *Chem.Rev*. 98:1563-1592.

Di Cera, E. 1998b. Site-Specific Thermodynamics: Understanding Cooperativity in Molecular Recognition. *Chem Rev*. 98:1563-1592.

Di Cera, E., and Z.Q. Chen. 1993. The binding capacity is a probability density function. *Biophys J*. 65:164-170.

Di Cera, E., S.J. Gill, and J. Wyman. 1988. Binding capacity: cooperativity and buffering in biopolymers. *Proc Natl Acad Sci U S A*. 85:449-452.

Dib-Hajj, S.D., Y. Yang, and S.G. Waxman. 2008. Genetics and molecular pathophysiology of Na(v)1.7-related pain syndromes. *Adv Genet*. 63:85-110.

Ding, S., and R. Horn. 2002. Tail end of the s6 segment: role in permeation in shaker potassium channels. *J Gen Physiol*. 120:87-97.

Dolmetsch, R. 2003. Excitation-transcription coupling: signaling by ion channels to the nucleus. *Sci STKE*. 2003:PE4.

Eaton, W.A., E.R. Henry, J. Hofrichter, and A. Mozzarelli. 1999. Is cooperative oxygen binding by hemoglobin really understood? *Nat.Struct.Biol.* 6:351-358.

Edelstein, S.J. 1971. Extensions of the allosteric model for haemoglobin. *Nature*. 230:224-227.

Favre, I., E. Moczydlowski, and L. Schild. 1996. On the structural basis for ionic selectivity among Na+, K+, and Ca2+ in the voltage-gated sodium channel. *Biophys J*. 71:3110-3125.

Ferrer, T., J. Rupp, D.R. Piper, and M. Tristani-Firouzi. 2006. The S4-S5 linker directly couples voltage sensor movement to the activation gate in the human ether-a'-go-go-related gene (hERG) K+ channel. *J Biol Chem*. 281:12858-12864.

Gagnon, D.G., and F. Bezanilla. 2010. The contribution of individual subunits to the coupling of the voltage sensor to pore opening in Shaker K channels: effect of ILT mutations in heterotetramers. *J Gen Physiol*. 136:555-568.

Gamal El-Din, T.M., G.Q. Martinez, J. Payandeh, T. Scheuer, and W.A. Catterall. 2013. A gating charge interaction required for late slow inactivation of the bacterial sodium channel NavAb. *J Gen Physiol*. 142:181-190.

Garcia, M.L., M. Garcia-Calvo, P. Hidalgo, A. Lee, and R. MacKinnon. 1994. Purification and characterization of three inhibitors of voltage-dependent K+ channels from Leiurus quinquestriatus var. hebraeus venom. *Biochemistry*. 33:6834-6839.

Gill, S.J., B. Richey, G. Bishop, and J. Wyman. 1985. Generalized binding phenomena in an allosteric macromolecule. *Biophys Chem*. 21:1-14.

Gleitsman, K.R., J.A. Shanata, S.J. Frazier, H.A. Lester, and D.A. Dougherty. 2009. Long-range coupling in an allosteric receptor revealed by mutant cycle analysis. *Biophys J*. 96:3168-3178.

Gonzalez, C., E. Rosenman, F. Bezanilla, O. Alvarez, and R. Latorre. 2000. Modulation of the Shaker K(+) channel gating kinetics by the S3-S4 linker. *J Gen Physiol*. 115:193-208.

Gonzalez, C., E. Rosenman, F. Bezanilla, O. Alvarez, and R. Latorre. 2001. Periodic perturbations in Shaker K+ channel gating kinetics by deletions in the S3-S4 linker. *Proc Natl Acad Sci U S A*. 98:9617-9623.

Goodey, N.M., and S.J. Benkovic. 2008. Allosteric regulation and catalysis emerge via a common route. *Nat Chem Biol*. 4:474-482.

Grandl, J., H. Hu, M. Bandell, B. Bursulaya, M. Schmidt, M. Petrus, and A. Patapoutian. 2008. Pore region of TRPV3 ion channel is specifically required for heat activation. *Nat Neurosci*. 11:1007-1013.

Grandl, J., S.E. Kim, V. Uzzell, B. Bursulaya, M. Petrus, M. Bandell, and A. Patapoutian. 2010. Temperature-induced opening of TRPV1 ion channel is stabilized by the pore domain. *Nat Neurosci*. 13:708-714.

Gupta, S., and A. Auerbach. 2011. Mapping heat exchange in an allosteric protein. *Biophys J*. 100:904-911.

Guy, H.R., and P. Seetharamulu. 1986. Molecular model of the action potential sodium channel. *Proc Natl Acad Sci U S A*. 83:508-512.

Hackos, D.H., T.H. Chang, and K.J. Swartz. 2002. Scanning the intracellular S6 activation gate in the shaker K+ channel. *J Gen Physiol*. 119:521-532.

Hagiwara, S. 1966. Membrane properties of the barnacle muscle fiber. *Ann N Y Acad Sci*. 137:1015-1024.

Hagiwara, S., M.P. Henkart, and Y. Kidokoro. 1971. Excitation-contraction coupling in amphioxus muscle cells. *J Physiol*. 219:233-251.

Hagiwara, S., and Y. Kidokoro. 1971. Na and Ca components of action potential in amphioxus muscle cells. *J Physiol*. 219:217-232.

Hagiwara, S., and S. Nakajima. 1966. Effects of the intracellular Ca ion concentration upon the excitability of the muscle fiber membrane of a barnacle. *J Gen Physiol*. 49:807-818.

Hagiwara, S., and N. Saito. 1959. Voltage-current relations in nerve cell membrane of Onchidium verruculatum. *J Physiol*. 148:161-179.

Halabi, N., O. Rivoire, S. Leibler, and R. Ranganathan. 2009. Protein sectors: evolutionary units of three-dimensional structure. *Cell*. 138:774-786.

Hall, R.A., M. Kessler, A. Quan, J. Ambros-Ingerson, and G. Lynch. 1993. Cyclothiazide decreases [3H]AMPA binding to rat brain membranes: evidence that AMPA receptor desensitization increases agonist affinity. *Brain Res*. 628:345-348.

Hammes, G.G., and C.W. Wu. 1971. Relaxation spectra of aspartate transcarbamylase. Interaction of the native enzyme with carbamyl phosphate. *Biochemistry*. 10:2150-2156.

Han, C., A. Lampert, A.M. Rush, S.D. Dib-Hajj, X. Wang, Y. Yang, and S.G. Waxman. 2007. Temperature dependence of erythromelalgia mutation L858F in sodium channel Nav1.7. *Mol Pain*. 3:3.

Heginbotham, L., Z. Lu, T. Abramson, and R. MacKinnon. 1994. Mutations in the K+ channel signature sequence. *Biophys J*. 66:1061-1067.

Henrion, U., J. Renhorn, S.I. Borjesson, E.M. Nelson, C.S. Schwaiger, P. Bjelkmar, B. Wallner, E. Lindahl, and F. Elinder. 2012. Tracking a complete voltage-sensor cycle with metal-ion bridges. *Proc Natl Acad Sci U S A*. 109:8552-8557.

Hessa, T., H. Kim, K. Bihlmaier, C. Lundin, J. Boekel, H. Andersson, I. Nilsson, S.H. White, and G. von Heijne. 2005. Recognition of transmembrane helices by the endoplasmic reticulum translocon. *Nature*. 433:377-381.

Hille, B. 1971. The permeability of the sodium channel to organic cations in myelinated nerve. *J Gen Physiol*. 58:599-619.

Hille, B. 1972. The permeability of the sodium channel to metal cations in myelinated nerve. *J Gen Physiol*. 59:637-658.

Hille, B. 1973. Potassium channels in myelinated nerve. Selective permeability to small cations. *J Gen Physiol*. 61:669-686.

Hille, B. 2001a. Ion Channels of Excitable Membranes. Sinauer Associates, Sunderland.

Hille, B. 2001b. Ion Channels of Excitable Membranes, Third Edition. Sinauer Associates, Sunderland, MA.

Hirschberg, B., A. Rovner, M. Lieberman, and J. Patlak. 1995. Transfer of twelve charges is needed to open skeletal muscle Na+ channels. *J Gen Physiol*. 106:1053-1068.

Hodgkin, A.L., and A.F. Huxley. 1952a. The components of membrane conductance in the giant axon of Loligo. *J Physiol*. 116:473-496.

Hodgkin, A.L., and A.F. Huxley. 1952b. Currents carried by sodium and potassium ions through the membrane of the giant axon of Loligo. *J Physiol*. 116:449-472.

Hodgkin, A.L., and A.F. Huxley. 1952c. The dual effect of membrane potential on sodium conductance in the giant axon of Loligo. *J Physiol*. 116:497-506.

Hodgkin, A.L., and A.F. Huxley. 1952d. Movement of sodium and potassium ions during nervous activity. *Cold Spring Harb Symp Quant Biol*. 17:43-52.

Hodgkin, A.L., and A.F. Huxley. 1952e. A quantitative description of membrane current and its application to conduction and excitation in nerve. *J Physiol*. 117:500-544.

Holmgren, M., K.S. Shin, and G. Yellen. 1998. The activation gate of a voltage-gated K+ channel can be trapped in the open state by an intersubunit metal bridge. *Neuron*. 21:617-621.

Hong, K.H., and C. Miller. 2000. The lipid-protein interface of a Shaker K(+) channel. *J Gen Physiol*. 115:51-58.

Horovitz, A., E.S. Bochkareva, O. Yifrach, and A.S. Girshovich. 1994. Prediction of an inter-residue interaction in the chaperonin GroEL from multiple sequence alignment is confirmed by double-mutant cycle analysis. *J Mol Biol*. 238:133-138.

Horovitz, A., and A.R. Fersht. 1990. Strategy for analysing the co-operativity of intramolecular interactions in peptides and proteins. *J Mol Biol*. 214:613-617.

Horrigan, F.T., and R.W. Aldrich. 1999. Allosteric voltage gating of potassium channels II. Mslo channel gating charge movement in the absence of Ca(2+). *J Gen Physiol*. 114:305-336.

Horrigan, F.T., and R.W. Aldrich. 2002. Coupling between voltage sensor activation, Ca2+ binding and channel opening in large conductance (BK) potassium channels. *J Gen Physiol*. 120:267-305.

Horrigan, F.T., J. Cui, and R.W. Aldrich. 1999. Allosteric voltage gating of potassium channels I. Mslo ionic currents in the absence of Ca(2+). *J Gen Physiol*. 114:277-304.

Horrigan, F.T., and Z. Ma. 2008. Mg2+ enhances voltage sensor/gate coupling in BK channels. *J Gen Physiol*. 131:13-32.

Hoshi, T., W.N. Zagotta, and R.W. Aldrich. 1994. Shaker potassium channel gating. I: Transitions near the open state. *J Gen Physiol*. 103:249-278.

Hubbell, W.L., D.S. Cafiso, and C. Altenbach. 2000. Identifying conformational changes with site-directed spin labeling. *Nat Struct Biol*. 7:735-739.

Humphrey, W., A. Dalke, and K. Schulten. 1996. VMD: visual molecular dynamics. *J Mol Graph*. 14:33-38, 27-38.

Islas, L.D., and F.J. Sigworth. 2001. Electrostatics and the gating pore of Shaker potassium channels. *J Gen Physiol*. 117:69-89.

Jackson, M.B. 2006. Molecular and Cellular Biophysics Cambridge University Press, Cambridge. 111-141 pp.

Jardetzky, O. 1966. Simple allosteric model for membrane pumps. *Nature*. 211:969-970.

Jensen, M.O., D.W. Borhani, K. Lindorff-Larsen, P. Maragakis, V. Jogini, M.P. Eastwood, R.O. Dror, and D.E. Shaw. 2010. Principles of conduction and hydrophobic gating in K+ channels. *Proc Natl Acad Sci U S A*. 107:5833-5838.

Jensen, M.O., V. Jogini, D.W. Borhani, A.E. Leffler, R.O. Dror, and D.E. Shaw. 2012. Mechanism of voltage gating in potassium channels. *Science*. 336:229-233.

Jordt, S.E., and D. Julius. 2002. Molecular basis for species-specific sensitivity to "hot" chili peppers. *Cell*. 108:421-430.

Kalia, J., and K.J. Swartz. 2013. Exploring structure-function relationships between TRP and Kv channels. *Sci Rep*. 3:1523.

Kannan, N., and S. Vishveshwara. 1999. Identification of side-chain clusters in protein structures by a graph spectral method. *J Mol Biol*. 292:441-464.

Kessler, M., A. Arai, A. Quan, and G. Lynch. 1996. Effect of cyclothiazide on binding properties of AMPA-type glutamate receptors: lack of competition between cyclothiazide and GYKI 52466. *Mol Pharmacol*. 49:123-131.

Kitaguchi, T., M. Sukhareva, and K.J. Swartz. 2004. Stabilizing the closed S6 gate in the Shaker Kv channel through modification of a hydrophobic seal. *J Gen Physiol*. 124:319-332.

Koshland, D.E., Jr., G. Nemethy, and D. Filmer. 1966. Comparison of experimental binding data and theoretical models in proteins containing subunits. *Biochemistry*. 5:365-385.

Kowal, J., M. Chami, P. Baumgartner, M. Arheit, P.L. Chiu, M. Rangl, S. Scheuring, G.F. Schroder, C.M. Nimigean, and H. Stahlberg. 2014. Ligand-induced structural

changes in the cyclic nucleotide-modulated potassium channel MloK1. *Nat Commun*. 5:3106.

Krepkiy, D., K. Gawrisch, and K.J. Swartz. 2012. Structural interactions between lipids, water and S1-S4 voltage-sensing domains. *J Mol Biol*. 423:632-647.

Krepkiy, D., M. Mihailescu, J.A. Freites, E.V. Schow, D.L. Worcester, K. Gawrisch, D.J. Tobias, S.H. White, and K.J. Swartz. 2009. Structure and hydration of membranes embedded with voltage-sensing domains. *Nature*. 462:473-479.

Kusch, J., C. Biskup, S. Thon, E. Schulz, V. Nache, T. Zimmer, F. Schwede, and K. Benndorf. 2010. Interdependence of receptor activation and ligand binding in HCN2 pacemaker channels. *Neuron*. 67:75-85.

Kusch, J., S. Thon, E. Schulz, C. Biskup, V. Nache, T. Zimmer, R. Seifert, F. Schwede, and K. Benndorf. 2012. How subunits cooperate in cAMP-induced activation of homotetrameric HCN2 channels. *Nat Chem Biol*. 8:162-169.

Labro, A.J., I.R. Boulet, F.S. Choveau, E. Mayeur, T. Bruyns, G. Loussouarn, A.L. Raes, and D.J. Snyders. 2011. The S4-S5 linker of KCNQ1 channels forms a structural scaffold with the S6 segment controlling gate closure. *J Biol Chem*. 286:717-725.

Labro, A.J., A.L. Raes, A. Grottesi, D. Van Hoorick, M.S. Sansom, and D.J. Snyders. 2008. Kv channel gating requires a compatible S4-S5 linker and bottom part of S6, constrained by non-interacting residues. *J Gen Physiol*. 132:667-680.

Lacroix, J.J., and F. Bezanilla. 2011. Control of a final gating charge transition by a hydrophobic residue in the S2 segment of a K+ channel voltage sensor. *Proc Natl Acad Sci U S A*. 108:6444-6449.

Lacroix, J.J., H.C. Hyde, F.V. Campos, and F. Bezanilla. 2014. Moving gating charges through the gating pore in a Kv channel voltage sensor. *Proc Natl Acad Sci U S A*. 111:E1950-1959.

Larsson, H.P., O.S. Baker, D.S. Dhillon, and E.Y. Isacoff. 1996. Transmembrane movement of the shaker K+ channel S4. *Neuron*. 16:387-397.

Latorre, R., S. Brauchi, G. Orta, C. Zaelzer, and G. Vargas. 2007. ThermoTRP channels as modular proteins with allosteric gating. *Cell Calcium*. 42:427-438.

Lecar, H., H.P. Larsson, and M. Grabe. 2003. Electrostatic model of S4 motion in voltage-gated ion channels. *Biophys J*. 85:2854-2864.

Ledwell, J.L., and R.W. Aldrich. 1999. Mutations in the S4 region isolate the final voltage-dependent cooperative step in potassium channel activation. *J Gen Physiol*. 113:389-414.

Lee, S.Y., A. Banerjee, and R. MacKinnon. 2009. Two separate interfaces between the voltage sensor and pore are required for the function of voltage-dependent K(+) channels. *PLoS Biol*. 7:e47.

Lee, W.Y., and S.M. Sine. 2005. Principal pathway coupling agonist binding to channel gating in nicotinic receptors. *Nature*. 438:243-247.

Li-Smerin, Y., D.H. Hackos, and K.J. Swartz. 2000a. alpha-helical structural elements within the voltage-sensing domains of a K(+) channel. *J Gen Physiol*. 115:33-50.

Li-Smerin, Y., D.H. Hackos, and K.J. Swartz. 2000b. A localized interaction surface for voltage-sensing domains on the pore domain of a K+ channel. *Neuron*. 25:411-423.

Li-Smerin, Y., and K.J. Swartz. 1998. Gating modifier toxins reveal a conserved structural motif in voltage-gated Ca2+ and K+ channels. *Proc Natl Acad Sci U S A*. 95:8585-8589.

Li-Smerin, Y., and K.J. Swartz. 2001. Helical structure of the COOH terminus of S3 and its contribution to the gating modifier toxin receptor in voltage-gated ion channels. *J Gen Physiol*. 117:205-218.

Li, Q., S. Wanderling, M. Paduch, D. Medovoy, A. Singharoy, R. McGreevy, C.A. Villalba-Galea, R.E. Hulse, B. Roux, K. Schulten, A. Kossiakoff, and E. Perozo. 2014a. Structural mechanism of voltage-dependent gating in an isolated voltage-sensing domain. *Nat Struct Mol Biol*. 21:244-252.

Li, Q., S. Wanderling, P. Sompornpisut, and E. Perozo. 2014b. Structural basis of lipid-driven conformational transitions in the KvAP voltage-sensing domain. *Nat Struct Mol Biol*. 21:160-166.

Liao, M., E. Cao, D. Julius, and Y. Cheng. 2013. Structure of the TRPV1 ion channel determined by electron cryo-microscopy. *Nature*. 504:107-112.

Liu, Y., M. Holmgren, M.E. Jurman, and G. Yellen. 1997. Gated access to the pore of a voltage-dependent K+ channel. *Neuron*. 19:175-184.

Long, S.B., E.B. Campbell, and R. Mackinnon. 2005a. Crystal structure of a mammalian voltage-dependent Shaker family K+ channel. *Science*. 309:897-903.

Long, S.B., E.B. Campbell, and R. Mackinnon. 2005b. Voltage sensor of Kv1.2: structural basis of electromechanical coupling. *Science*. 309:903-908.

Long, S.B., X. Tao, E.B. Campbell, and R. MacKinnon. 2007. Atomic structure of a voltage-dependent K+ channel in a lipid membrane-like environment. *Nature*. 450:376-382.

Lopez, G.A., Y.N. Jan, and L.Y. Jan. 1991. Hydrophobic substitution mutations in the S4 sequence alter voltage-dependent gating in Shaker K+ channels. *Neuron*. 7:327-336.

Lu, Z., A.M. Klem, and Y. Ramu. 2002. Coupling between voltage sensors and activation gate in voltage-gated K+ channels. *J Gen Physiol*. 120:663-676.

Ma, Z., X.J. Lou, and F.T. Horrigan. 2006. Role of charged residues in the S1-S4 voltage sensor of BK channels. *J Gen Physiol*. 127:309-328.

Magleby, K.L. 2003. Gating mechanism of BK (Slo1) channels: so near, yet so far. *J Gen Physiol*. 121:81-96.

Maingret, F., I. Lauritzen, A.J. Patel, C. Heurteaux, R. Reyes, F. Lesage, M. Lazdunski, and E. Honore. 2000. TREK-1 is a heat-activated background K(+) channel. *EMBO J*. 19:2483-2491.

Makhatadze, G.I., S.J. Gill, and P.L. Privalov. 1990. Partial molar heat capacities of the side chains of some amino acid residues in aqueous solution. The influence of the neighboring charges. *Biophys Chem*. 38:33-37.

Makhatadze, G.I., and P.L. Privalov. 1990. Heat capacity of proteins. I. Partial molar heat capacity of individual amino acid residues in aqueous solution: hydration effect. *J Mol Biol*. 213:375-384.

Makhatadze, G.I., and P.L. Privalov. 1993. Contribution of hydration to protein folding thermodynamics. I. The enthalpy of hydration. *J Mol Biol*. 232:639-659.

Makhatadze, G.I., and P.L. Privalov. 1994. Hydration effects in protein unfolding. *Biophys Chem*. 51:291-304; discussion 304-299.

Mannikko, R., F. Elinder, and H.P. Larsson. 2002. Voltage-sensing mechanism is conserved among ion channels gated by opposite voltages. *Nature*. 419:837-841.

Mannikko, R., S. Pandey, H.P. Larsson, and F. Elinder. 2005. Hysteresis in the voltage dependence of HCN channels: conversion between two modes affects pacemaker properties. *J Gen Physiol*. 125:305-326.

Marty, A. 1981. Ca-dependent K channels with large unitary conductance in chromaffin cell membranes. *Nature*. 291:497-500.

Matta, J.A., and G.P. Ahern. 2007. Voltage is a partial activator of rat thermosensitive TRP channels. *J Physiol*. 585:469-482.

McClatchey, A.I., P. Van den Bergh, M.A. Pericak-Vance, W. Raskind, C. Verellen, D. McKenna-Yasek, K. Rao, J.L. Haines, T. Bird, R.H. Brown, Jr., and et al. 1992. Temperature-sensitive mutations in the III-IV cytoplasmic loop region of the skeletal muscle sodium channel gene in paramyotonia congenita. *Cell*. 68:769-774.

McCormack, K., L. Lin, and F.J. Sigworth. 1993. Substitution of a hydrophobic residue alters the conformational stability of Shaker K+ channels during gating and assembly. *Biophys J*. 65:1740-1748.

McCormack, K., M.A. Tanouye, L.E. Iverson, J. Lin, M. Ramaswami, T. McCormack, J.T. Campanelli, M.K. Mathew, and B. Rudy. 1991a. A role for the hydrophobic residues in the voltage-dependent gating of Shaker K^+ channels. *Proc Natl Acad Sci U S A*. 88:2931-2935.

McCormack, K., M.A. Tanouye, L.E. Iverson, J.W. Lin, M. Ramaswami, T. McCormack, J.T. Campanelli, M.K. Mathew, and B. Rudy. 1991b. A role for hydrophobic residues in the voltage-dependent gating of Shaker K+ channels. *Proc Natl Acad Sci U S A*. 88:2931-2935.

McKemy, D.D., W.M. Neuhausser, and D. Julius. 2002. Identification of a cold receptor reveals a general role for TRP channels in thermosensation. *Nature*. 416:52-58.

Miceli, F., E. Vargas, F. Bezanilla, and M. Taglialatela. 2012. Gating currents from Kv7 channels carrying neuronal hyperexcitability mutations in the voltage-sensing domain. *Biophys J*. 102:1372-1382.

Milescu, M., F. Bosmans, S. Lee, A.A. Alabi, J.I. Kim, and K.J. Swartz. 2009. Interactions between lipids and voltage sensor paddles detected with tarantula toxins. *Nat Struct Mol Biol*. 16:1080-1085.

Monks, S.A., D.J. Needleman, and C. Miller. 1999. Helical structure and packing orientation of the S2 segment in the Shaker K+ channel. *J Gen Physiol*. 113:415-423.

Monod, J., and F. Jacob. 1961. Teleonomic mechanisms in cellular metabolism, growth, and differentiation. *Cold Spring Harb Symp Quant Biol*. 26:389-401.

Monod, J., J. Wyman, and J.P. Changeux. 1965a. On the Nature of Allosteric Transitions: A Plausible Model. *J Mol Biol*. 12:88-118.

Monod, J., J. Wyman, and J.P. Changeux. 1965b. ON THE NATURE OF ALLOSTERIC TRANSITIONS: A PLAUSIBLE MODEL. *J.Mol.Biol*. 12:88-118.

Muroi, Y., M. Arcisio-Miranda, S. Chowdhury, and B. Chanda. 2010. Molecular determinants of coupling between the domain III voltage sensor and pore of a sodium channel. *Nat Struct Mol Biol*. 17:230-237.

Nache, V., J. Kusch, C. Biskup, E. Schulz, T. Zimmer, V. Hagen, and K. Benndorf. 2008. Thermodynamics of activation gating in olfactory-type cyclic nucleotide-gated (CNGA2) channels. *Biophys J*. 95:2750-2758.

Nelson, M.T., and J.M. Quayle. 1995. Physiological roles and properties of potassium channels in arterial smooth muscle. *Am J Physiol*. 268:C799-822.

Nepusz, T., H. Yu, and A. Paccanaro. 2012. Detecting overlapping protein complexes in protein-protein interaction networks. *Nat Methods*. 9:471-472.

Nguyen, T.P., and R. Horn. 2002. Movement and crevices around a sodium channel S3 segment. *J Gen Physiol*. 120:419-436.

Niu, X., and K.L. Magleby. 2002. Stepwise contribution of each subunit to the cooperative activation of BK channels by Ca2+. *Proc Natl Acad Sci U S A*. 99:11441-11446.

Noceti, F., P. Baldelli, X. Wei, N. Qin, L. Toro, L. Birnbaumer, and E. Stefani. 1996. Effective gating charges per channel in voltage-dependent K+ and Ca2+ channels. *J Gen Physiol*. 108:143-155.

Noda, M., T. Ikeda, H. Suzuki, H. Takeshima, T. Takahashi, M. Kuno, and S. Numa. 1986. Expression of functional sodium channels from cloned cDNA. *Nature*. 322:826-828.

O'Rourke, B. 2004. Evidence for mitochondrial K+ channels and their role in cardioprotection. *Circ Res*. 94:420-432.

Papazian, D.M., T.L. Schwarz, B.L. Tempel, Y.N. Jan, and L.Y. Jan. 1987. Cloning of genomic and complementary DNA from Shaker, a putative potassium channel gene from Drosophila. *Science*. 237:749-753.

Papazian, D.M., L.C. Timpe, Y.N. Jan, and L.Y. Jan. 1991. Alteration of voltage-dependence of Shaker potassium channel by mutations in the S4 sequence. *Nature*. 349:305-310.

Patapoutian, A., A.M. Peier, G.M. Story, and V. Viswanath. 2003. ThermoTRP channels and beyond: mechanisms of temperature sensation. *Nat Rev Neurosci*. 4:529-539.

Pathak, M.M., V. Yarov-Yarovoy, G. Agarwal, B. Roux, P. Barth, S. Kohout, F. Tombola, and E.Y. Isacoff. 2007. Closing in on the resting state of the Shaker K(+) channel. *Neuron*. 56:124-140.

Pauling, L. 1935. The Oxygen Equilibrium of Hemoglobin and Its Structural Interpretation. *Proc Natl Acad Sci U S A*. 21:186-191.

Payandeh, J., T.M. Gamal El-Din, T. Scheuer, N. Zheng, and W.A. Catterall. 2012. Crystal structure of a voltage-gated sodium channel in two potentially inactivated states. *Nature*. 486:135-139.

Payandeh, J., T. Scheuer, N. Zheng, and W.A. Catterall. 2011. The crystal structure of a voltage-gated sodium channel. *Nature*. 475:353-358.

Peier, A.M., A. Moqrich, A.C. Hergarden, A.J. Reeve, D.A. Andersson, G.M. Story, T.J. Earley, I. Dragoni, P. McIntyre, S. Bevan, and A. Patapoutian. 2002a. A TRP channel that senses cold stimuli and menthol. *Cell*. 108:705-715.

Peier, A.M., A.J. Reeve, D.A. Andersson, A. Moqrich, T.J. Earley, A.C. Hergarden, G.M. Story, S. Colley, J.B. Hogenesch, P. McIntyre, S. Bevan, and A. Patapoutian. 2002b. A heat-sensitive TRP channel expressed in keratinocytes. *Science*. 296:2046-2049.

Perozo, E., R. MacKinnon, F. Bezanilla, and E. Stefani. 1993. Gating currents from a nonconducting mutant reveal open-closed conformations in Shaker K+ channels. *Neuron*. 11:353-358.

Perozo, E., L. Santacruz-Toloza, E. Stefani, F. Bezanilla, and D.M. Papazian. 1994. S4 mutations alter gating currents of Shaker K channels. *Biophys J*. 66:345-354.

Perutz, M.F. 1970. Stereochemistry of cooperative effects in haemoglobin. *Nature*. 228:726-739.

Perutz, M.F., and J. Greer. 1970. Stereochemical effects of amino acid substitution in abnormal human haemoglobin. *Biochem.J.* 119:31P.

Perutz, M.F., A.J. Wilkinson, M. Paoli, and G.G. Dodson. 1998. The stereochemical mechanism of the cooperative effects in hemoglobin revisited. *Annu.Rev.Biophys.Biomol.Struct.* 27:1-34.

Phillips, J.C., R. Braun, W. Wang, J. Gumbart, E. Tajkhorshid, E. Villa, C. Chipot, R.D. Skeel, L. Kale, and K. Schulten. 2005. Scalable molecular dynamics with NAMD. *J Comput Chem*. 26:1781-1802.

Picollo, A., M. Malvezzi, J.C. Houtman, and A. Accardi. 2009. Basis of substrate binding and conservation of selectivity in the CLC family of channels and transporters. *Nat Struct Mol Biol*. 16:1294-1301.

Piscitelli, C.L., H. Krishnamurthy, and E. Gouaux. 2010. Neurotransmitter/sodium symporter orthologue LeuT has a single high-affinity substrate site. *Nature*. 468:1129-1132.

Pless, S.A., J.D. Galpin, A.P. Niciforovic, and C.A. Ahern. 2011. Contributions of counter-charge in a potassium channel voltage-sensor domain. *Nat Chem Biol*. 7:617-623.

Privalov, P.L., and S.J. Gill. 1988. Stability of protein structure and hydrophobic interaction. *Adv Protein Chem*. 39:191-234.

Privalov, P.L., and G.I. Makhatadze. 1993. Contribution of hydration to protein folding thermodynamics. II. The entropy and Gibbs energy of hydration. *J Mol Biol*. 232:660-679.

Purohit, P., S. Gupta, S. Jadey, and A. Auerbach. 2013. Functional anatomy of an allosteric protein. *Nat Commun*. 4:2984.

Pusch, M., U. Ludewig, and T.J. Jentsch. 1997. Temperature dependence of fast and slow gating relaxations of ClC-0 chloride channels. *J Gen Physiol*. 109:105-116.

Ramsey, I.S., M. Delling, and D.E. Clapham. 2006. An introduction to TRP channels. *Annu Rev Physiol*. 68:619-647.

Ramu, Y., Y. Xu, and Z. Lu. 2006. Enzymatic activation of voltage-gated potassium channels. *Nature*. 442:696-699.

Ranganathan, R., J.H. Lewis, and R. MacKinnon. 1996. Spatial localization of the K+ channel selectivity filter by mutant cycle-based structure analysis. *Neuron*. 16:131-139.

Rodriguez, B.M., and F. Bezanilla. 1996. Transitions near the open state in Shaker K(+)-channel: probing with temperature. *Neuropharmacology*. 35:775-785.

Rodriguez, B.M., D. Sigg, and F. Bezanilla. 1998. Voltage gating of Shaker K+ channels. The effect of temperature on ionic and gating currents. *J Gen Physiol*. 112:223-242.

Rothberg, B.S., and K.L. Magleby. 1998. Kinetic structure of large-conductance Ca2+-activated K+ channels suggests that the gating includes transitions through intermediate or secondary states. A mechanism for flickers. *J Gen Physiol*. 111:751-780.

Rothberg, B.S., and K.L. Magleby. 2000. Voltage and Ca2+ activation of single large-conductance Ca2+-activated K+ channels described by a two-tiered allosteric gating mechanism. *J Gen Physiol*. 116:75-99.

Roux, B. 1997. Influence of the membrane potential on the free energy of an intrinsic protein. *Biophys J*. 73:2980-2989.

Ruta, V., J. Chen, and R. MacKinnon. 2005. Calibrated measurement of gating-charge arginine displacement in the KvAP voltage-dependent K+ channel. *Cell*. 123:463-475.

Sadovsky, E., and O. Yifrach. 2007. Principles underlying energetic coupling along an allosteric communication trajectory of a voltage-activated K+ channel. *Proc Natl Acad Sci U S A*. 104:19813-19818.

Sanguinetti, M.C., and Q.P. Xu. 1999. Mutations of the S4-S5 linker alter activation properties of HERG potassium channels expressed in Xenopus oocytes. *J Physiol*. 514 (Pt 3):667-675.

Sauer, D.B., W. Zeng, S. Raghunathan, and Y. Jiang. 2011. Protein interactions central to stabilizing the K+ channel selectivity filter in a four-sited configuration for selective K+ permeation. *Proc Natl Acad Sci U S A*. 108:16634-16639.

Schellman, J.A., M. Lindorfer, R. Hawkes, and M. Grutter. 1981. Mutations and protein stability. *Biopolymers*. 20:1989-1999.

Schmidt, D., Q.X. Jiang, and R. MacKinnon. 2006. Phospholipids and the origin of cationic gating charges in voltage sensors. *Nature*. 444:775-779.

Schneider, M.F., and W.K. Chandler. 1973. Voltage dependent charge movement of skeletal muscle: a possible step in excitation-contraction coupling. *Nature*. 242:244-246.

Schonherr, R., L.M. Mannuzzu, E.Y. Isacoff, and S.H. Heinemann. 2002. Conformational switch between slow and fast gating modes: allosteric regulation of voltage sensor mobility in the EAG K+ channel. *Neuron*. 35:935-949.

Schoppa, N.E., K. McCormack, M.A. Tanouye, and F.J. Sigworth. 1992. The size of gating charge in wild-type and mutant Shaker potassium channels. *Science*. 255:1712-1715.

Schoppa, N.E., and F.J. Sigworth. 1998. Activation of Shaker potassium channels. III. An activation gating model for wild-type and V2 mutant channels. *J Gen Physiol*. 111:313-342.

Schreiber, G., and A.R. Fersht. 1995. Energetics of protein-protein interactions: analysis of the barnase-barstar interface by single mutations and double mutant cycles. *J Mol Biol*. 248:478-486.

Seoh, S.A., D. Sigg, D.M. Papazian, and F. Bezanilla. 1996. Voltage-sensing residues in the S2 and S4 segments of the Shaker K+ channel. *Neuron*. 16:1159-1167.

Serrano, L., A. Horovitz, B. Avron, M. Bycroft, and A.R. Fersht. 1990. Estimating the contribution of engineered surface electrostatic interactions to protein stability by using double-mutant cycles. *Biochemistry*. 29:9343-9352.

Shanata, J.A., S.J. Frazier, H.A. Lester, and D.A. Dougherty. 2012. Using mutant cycle analysis to elucidate long-range functional coupling in allosteric receptors. *Methods Mol Biol*. 796:97-113.

Shi, J., G. Krishnamoorthy, Y. Yang, L. Hu, N. Chaturvedi, D. Harilal, J. Qin, and J. Cui. 2002. Mechanism of magnesium activation of calcium-activated potassium channels. *Nature*. 418:876-880.

Shin, K.S., C. Maertens, C. Proenza, B.S. Rothberg, and G. Yellen. 2004. Inactivation in HCN channels results from reclosure of the activation gate: desensitization to voltage. *Neuron*. 41:737-744.

Sigg, D., and F. Bezanilla. 1997. Total charge movement per channel. The relation between gating charge displacement and the voltage sensitivity of activation. *J Gen Physiol*. 109:27-39.

Sigworth, F.J. 1993. Voltage gating of ion channels. *Quarterly Reviews of Biophysics*. 27:1-40.

Smith-Maxwell, C.J., J.L. Ledwell, and R.W. Aldrich. 1998a. Role of the S4 in cooperativity of voltage-dependent potassium channel activation. *J Gen Physiol*. 111:399-420.

Smith-Maxwell, C.J., J.L. Ledwell, and R.W. Aldrich. 1998b. Uncharged S4 residues and cooperativity in voltage-dependent potassium channel activation. *J Gen Physiol*. 111:421-439.

Sokolov, S., T. Scheuer, and W.A. Catterall. 2007. Gating pore current in an inherited ion channelopathy. *Nature*. 446:76-78.

Soler-Llavina, G.J., T.H. Chang, and K.J. Swartz. 2006. Functional interactions at the interface between voltage-sensing and pore domains in the Shaker K(v) channel. *Neuron*. 52:623-634.

Starace, D.M., and F. Bezanilla. 2001. Histidine scanning mutagenesis of basic residues of the S4 segment of the shaker k+ channel. *J Gen Physiol*. 117:469-490.

Starace, D.M., and F. Bezanilla. 2004. A proton pore in a potassium channel voltage sensor reveals a focused electric field. *Nature*. 427:548-553.

Starace, D.M., E. Stefani, and F. Bezanilla. 1997. Voltage-dependent proton transport by the voltage sensor of the Shaker K+ channel. *Neuron*. 19:1319-1327.

Stauffer, D.A., and A. Karlin. 1994. Electrostatic potential of the acetylcholine binding sites in the nicotinic receptor probed by reactions of binding-site cysteines with charged methanethiosulfonates. *Biochemistry*. 33:6840-6849.

Stefani, E., and F. Bezanilla. 1998. Cut-open oocyte voltage-clamp technique. *Methods Enzymol*. 293:300-318.

Stevens, C.F. 1978. Interactions between intrinsic membrane protein and electric field. An approach to studying nerve excitability. *Biophys J*. 22:295-306.

Story, G.M., A.M. Peier, A.J. Reeve, S.R. Eid, J. Mosbacher, T.R. Hricik, T.J. Earley, A.C. Hergarden, D.A. Andersson, S.W. Hwang, P. McIntyre, T. Jegla, S. Bevan, and A. Patapoutian. 2003. ANKTM1, a TRP-like channel expressed in nociceptive neurons, is activated by cold temperatures. *Cell*. 112:819-829.

Sugiura, Y., T. Aoki, Y. Sugiyama, C. Hida, M. Ogata, and T. Yamamoto. 2000. Temperature-sensitive sodium channelopathy with heat-induced myotonia and cold-induced paralysis. *Neurology*. 54:2179-2181.

Sun, Y., R. Olson, M. Horning, N. Armstrong, M. Mayer, and E. Gouaux. 2002. Mechanism of glutamate receptor desensitization. *Nature*. 417:245-253.

Suzuki, H., S. Beckh, H. Kubo, N. Yahagi, H. Ishida, T. Kayano, M. Noda, and S. Numa. 1988. Functional expression of cloned cDNA encoding sodium channel III. *FEBS Lett*. 228:195-200.

Swartz, K.J. 2008. Sensing voltage across lipid membranes. *Nature*. 456:891-897.

Sweet, T.B., and D.H. Cox. 2008. Measurements of the BKCa channel's high-affinity Ca2+ binding constants: effects of membrane voltage. *J Gen Physiol*. 132:491-505.

Szabo, A., and M. Karplus. 1972. A mathematical model for structure-function relations in hemoglobin. *J.Mol.Biol.* 72:163-197.

Szallasi, A., P.M. Blumberg, L.L. Annicelli, J.E. Krause, and D.N. Cortright. 1999. The cloned rat vanilloid receptor VR1 mediates both R-type binding and C-type calcium response in dorsal root ganglion neurons. *Mol Pharmacol*. 56:581-587.

Talukder, G., and R.W. Aldrich. 2000. Complex voltage-dependent behavior of single unliganded calcium-sensitive potassium channels. *Biophys J*. 78:761-772.

Tanabe, T., H. Takeshima, A. Mikami, V. Flockerzi, H. Takahashi, K. Kangawa, M. Kojima, H. Matsuo, T. Hirose, and S. Numa. 1987. Primary structure of the receptor for calcium channel blockers from skeletal muscle. *Nature*. 328:313-318.

Tao, X., A. Lee, W. Limapichat, D.A. Dougherty, and R. MacKinnon. 2010. A gating charge transfer center in voltage sensors. *Science*. 328:67-73.

Tempel, B.L., D.M. Papazian, T.L. Schwarz, Y.N. Jan, and L.Y. Jan. 1987. Sequence of a probable potassium channel component encoded at Shaker locus of Drosophila. *Science*. 237:770-775.

Timpe, L.C., T.L. Schwarz, B.L. Tempel, D.M. Papazian, Y.N. Jan, and L.Y. Jan. 1988. Expression of functional potassium channels from Shaker cDNA in Xenopus oocytes. *Nature*. 331:143-145.

Tiwari-Woodruff, S.K., C.T. Schulteis, A.F. Mock, and D.M. Papazian. 1997. Electrostatic interactions between transmembrane segments mediate folding of Shaker K+ channel subunits. *Biophys J*. 72:1489-1500.

Tochtrop, G.P., K. Richter, C. Tang, J.J. Toner, D.F. Covey, and D.P. Cistola. 2002. Energetics by NMR: site-specific binding in a positively cooperative system. *Proc.Natl.Acad.Sci.U.S.A.* 99:1847-1852.

Tombola, F., M.M. Pathak, and E.Y. Isacoff. 2005. Voltage-sensing arginines in a potassium channel permeate and occlude cation-selective pores. *Neuron*. 45:379-388.

Tristani-Firouzi, M., J. Chen, and M.C. Sanguinetti. 2002. Interactions between S4-S5 linker and S6 transmembrane domain modulate gating of HERG K+ channels. *J Biol Chem*. 277:18994-19000.

Ulens, C., and S.A. Siegelbaum. 2003. Regulation of hyperpolarization-activated HCN channels by cAMP through a gating switch in binding domain symmetry. *Neuron*. 40:959-970.

Van Slyke, A.C., S. Rezazadeh, M. Snopkowski, P. Shi, C.R. Allard, and T.W. Claydon. 2010. Mutations within the S4-S5 linker alter voltage sensor constraints in hERG K+ channels. *Biophys J*. 99:2841-2852.

Vandenberg, C.A., and F. Bezanilla. 1991. A sodium channel gating model based on single channel, macroscopic ionic, and gating currents in the squid giant axon. *Biophys J*. 60:1511-1533.

Vandenberg, J.I., A. Varghese, Y. Lu, J.A. Bursill, M.P. Mahaut-Smith, and C.L. Huang. 2006. Temperature dependence of human ether-a-go-go-related gene K+ currents. *Am J Physiol Cell Physiol*. 291:C165-175.

Villalba-Galea, C.A., W. Sandtner, D.M. Starace, and F. Bezanilla. 2008. S4-based voltage sensors have three major conformations. *Proc Natl Acad Sci U S A*. 105:17600-17607.

Voets, T., G. Droogmans, U. Wissenbach, A. Janssens, V. Flockerzi, and B. Nilius. 2004. The principle of temperature-dependent gating in cold- and heat-sensitive TRP channels. *Nature*. 430:748-754.

Voets, T., G. Owsianik, A. Janssens, K. Talavera, and B. Nilius. 2007. TRPM8 voltage sensor mutants reveal a mechanism for integrating thermal and chemical stimuli. *Nat Chem Biol*. 3:174-182.

Wall-Lacelle, S., M.I. Hossain, R. Sauve, R. Blunck, and L. Parent. 2011. Double mutant cycle analysis identified a critical leucine residue in the IIS4S5 linker for the activation of the Ca(V)2.3 calcium channel. *J Biol Chem*. 286:27197-27205.

Weber, G. 1997. Fluorescence in biophysics: accomplishments and deficiencies. *Methods Enzymol*. 278:1-15.

Winterfield, J.R., and K.J. Swartz. 2000. A hot spot for the interaction of gating modifier toxins with voltage-dependent ion channels. *J Gen Physiol*. 116:637-644.

Wyman, J. 1965. The Binding Potential, a Neglected Linkage Concept. *J Mol Biol*. 11:631-644.

Wyman, J. 1967. Allosteric linkage. *Journal of the American Chemical Society*. 89:2202-2218.

Wyman, J. 1984. Linkage graphs: a study in the thermodynamics of macromolecules. *Q Rev Biophys*. 17:453-488.

Wyman, J., and S.J. Gill. 1990. Binding and linkage: functional chemistry of biological macromolecules. University Science Books, Mill Valley.

Wyman, J., Jr. 1964a. Linked Functions and Reciprocal Effects in Hemoglobin: A Second Look. *Adv Protein Chem*. 19:223-286.

Wyman, J.J. 1964b. Linked functions and reciprocal effects in hemoglobin: A second look. *In* Advances in Protein Chemistry. 223-286.

Xia, X.M., X. Zeng, and C.J. Lingle. 2002. Multiple regulatory sites in large-conductance calcium-activated potassium channels. *Nature*. 418:880-884.

Xu, H., I.S. Ramsey, S.A. Kotecha, M.M. Moran, J.A. Chong, D. Lawson, P. Ge, J. Lilly, I. Silos-Santiago, Y. Xie, P.S. DiStefano, R. Curtis, and D.E. Clapham. 2002. TRPV3 is a calcium-permeable temperature-sensitive cation channel. *Nature*. 418:181-186.

Xu, Y., Y. Ramu, and Z. Lu. 2010. A shaker K+ channel with a miniature engineered voltage sensor. *Cell*. 142:580-589.

Xu, Y., Y. Ramu, H.G. Shin, J. Yamakaze, and Z. Lu. 2013. Energetic role of the paddle motif in voltage gating of Shaker K(+) channels. *Nat Struct Mol Biol*. 20:574-581.

Yang, F., Y. Cui, K. Wang, and J. Zheng. 2010. Thermosensitive TRP channel pore turret is part of the temperature activation pathway. *Proc Natl Acad Sci U S A*. 107:7083-7088.

Yang, N., A.L. George, Jr., and R. Horn. 1996. Molecular basis of charge movement in voltage-gated sodium channels. *Neuron*. 16:113-122.

Yang, N., and R. Horn. 1995. Evidence for voltage-dependent S4 movement in sodium channels. *Neuron*. 15:213-218.

Yang, Y., Y. Yan, and F.J. Sigworth. 1997. How does the W434F mutation block current in Shaker potassium channels? *J Gen Physiol*. 109:779-789.

Yao, J., B. Liu, and F. Qin. 2010. Kinetic and energetic analysis of thermally activated TRPV1 channels. *Biophys J*. 99:1743-1753.

Yao, J., B. Liu, and F. Qin. 2011. Modular thermal sensors in temperature-gated transient receptor potential (TRP) channels. *Proc Natl Acad Sci U S A*. 108:11109-11114.

Yellen, G. 1998. The moving parts of voltage-gated ion channels. *Q Rev Biophys*. 31:239-295.

Yifrach, O., and R. MacKinnon. 2002. Energetics of pore opening in a voltage-gated K(+) channel. *Cell*. 111:231-239.

Yifrach, O., N. Zandany, and T. Shem-Ad. 2009. Examining cooperative gating phenomena in voltage-dependent potassium channels: taking the energetic approach. *Methods Enzymol*. 466:179-209.

Yusifov, T., A.D. Javaherian, A. Pantazis, C.S. Gandhi, and R. Olcese. 2010. The RCK1 domain of the human BKCa channel transduces Ca2+ binding into structural rearrangements. *J Gen Physiol*. 136:189-202.

Zagotta, W.N., T. Hoshi, and R.W. Aldrich. 1994a. Shaker potassium channel gating. III: Evaluation of kinetic models for activation. *J Gen Physiol*. 103:321-362.

Zagotta, W.N., T. Hoshi, J. Dittman, and R.W. Aldrich. 1994b. Shaker potassium channel gating. II: Transitions in the activation pathway. *J Gen Physiol*. 103:279-319.

Zandany, N., M. Ovadia, I. Orr, and O. Yifrach. 2008. Direct analysis of cooperativity in multisubunit allosteric proteins. *Proc Natl Acad Sci U S A*. 105:11697-11702.

Zhang, X., W. Ren, P. DeCaen, C. Yan, X. Tao, L. Tang, J. Wang, K. Hasegawa, T. Kumasaka, J. He, J. Wang, D.E. Clapham, and N. Yan. 2012. Crystal structure of an orthologue of the NaChBac voltage-gated sodium channel. *Nature*. 486:130-134.

Zheng, J., and F.J. Sigworth. 1998. Intermediate conductances during deactivation of heteromultimeric Shaker potassium channels. *J Gen Physiol*. 112:457-474.

Zhou, Y., X.H. Zeng, and C.J. Lingle. 2012. Barium ions selectively activate BK channels via the Ca2+-bowl site. *Proc Natl Acad Sci U S A*.